Modeling and Control of Pharmacological Systems

YLVA WAHLQUIST
DEPARTMENT OF AUTOMATIC CONTROL | LUND UNIVERSITY

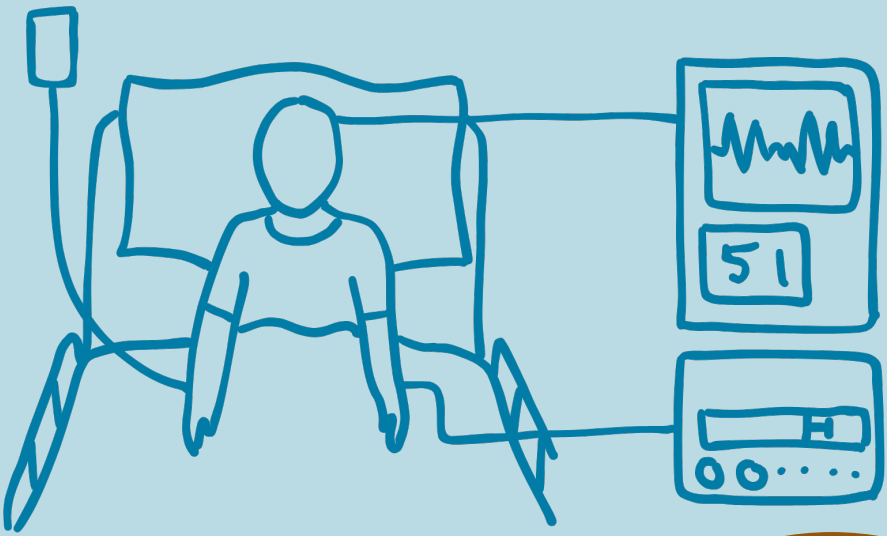

Modeling and Control of Pharmacological Systems

Ylva Wahlquist

LUND
UNIVERSITY

Department of Automatic Control

PhD Thesis TFRT-1148
ISBN 978-91-8104-370-9 (print)
ISBN 978-91-8104-371-6 (web)
ISSN 0280-5316

Department of Automatic Control
Lund University
Box 118
SE-221 00 LUND
Sweden

Printed in Sweden by Media-Tryck.
Lund 2025

Abstract

Personalized patient care has gained increasing attention in recent years. Precise drug dosing is critical for patient safety and good clinical outcomes, especially in intensive care units, where patients often are in critical conditions. Such treatments can include stabilizing blood pressure and heart rate or maintaining safe anesthesia levels. However, the inter-patient variability in the drug response makes finding a dosing regimen that works for all patients challenging. The problem with the most commonly used methods today is that they do not account (at least not sufficiently) for this variability, which can lead to under- or overdosing.

This thesis aims to solve these issues by improving modeling and control strategies for individualized drug dosing. These aims are to: 1) stabilize heart donor hemodynamics to enhance organ quality for transplantation, 2) streamline the identification of covariate models that capture the inter-patient variability in the drug response, and 3) develop control strategies resilient to disturbances and poor measurement signal quality. First, we demonstrate that precise blood pressure control can delay ischemic myocardial contracture in heart donors. However, the controller performance was limited by the inter-patient variability in drug response, which motivated further research on drug modeling. Therefore, we developed a method to automate the covariate modeling process using symbolic regression networks, which enabled us to find simple and interpretable models that capture this variability well. To evaluate the covariate model's performance, we needed to simulate a large dataset, which motivated the development of a fast simulator for pharmacokinetics. Therefore, we developed an efficient simulator that could simulate a large dataset in a fraction of the time compared to current available methods. Returning to the control problem, we proposed combining open- and closed-loop control for anesthesia using a Kalman filter. This allowed for robust control performance even when model errors, disturbances, and poor signal quality were present.

In conclusion, these contributions demonstrate how pharmacological modeling and control can improve drug dosing accuracy and patient safety. Adopting the methods provided in this thesis can lead to safer and more efficient healthcare.

Acknowledgments

Thank you, Kristian, for being a great supervisor and friend. I am glad you convinced me to pursue a PhD and discover how exciting research can be. You are always full of ideas, and during this time, I have learned how to sort the best ones out (no, not all of them are good). Sometimes, it can be hard to keep up with your pace, but I enjoy that there is always something new in the pipeline– new research or a new outdoor activity.

Tore, thank you for being Kristian's calm counterpart. I have always felt welcome at your office if I had any problems, and you always take your time to help me.

Thanks to all of my colleagues at the department. The coffee breaks have been so much fun, and I have learned a lot about things I would never have learned about otherwise. Nils, Martin H, and Albin, thank you for helping me believe in myself and for being close friends. We have had many board game nights and disc golf rounds, and I look forward to many more! Harry, Frida N, Pex, thank you for being considerate and always having time to discuss research or personal matters. Frida H, why did we not realize sooner that we have so much in common? I look forward to getting to know you more. Claudio, thank you for welcoming me into the department and for being a good friend. Jesper, you have taught me a lot about research outside of the automatic control field, and we always have a good time together. I also want to thank Johan Grönqvist for the idea of looking into symbolic regression, which laid the foundation for a major part of this thesis work. To all of the administrative staff at the department: Anders N, Anders B, Mika, Cecilia, and Monika, thank you for always being helpful. Special thanks to Eva who always spreads joy around her.

I want to thank everyone at Igelösa Life Science for the opportunity to be part of such a fantastic working environment. Stig and the late Trygve, thank you for always being willing to share your infinite knowledge and for the opportunity to work with you. And to the rest of the group, thank you for making me feel like part of the team.

I have had the opportunity to visit research groups in Vancouver, Brescia, and Tenerife. Klaske, Sara, and Guy in Vancouver, thank you for welcoming me and making me feel at home in your wonderful city. Michele, Nicola, Antonio, and the others in Brescia, I have enjoyed getting to know and working with you, and I hope to stay in touch. Juan Albino and José in Tenerife, thank you for allowing me to visit, write my thesis, and enjoy beautiful hikes.

Thank you, Martin, for always taking the opposite side of the argument. This has helped me see things from new perspectives.

Last but not least, thanks to my family for all the encouragement and support.

Financial Support This work was supported by the Hans-Gabriel och Alice Trolle-Wachtmeister Foundation for medical research, the Wallenberg AI, Autonomous Systems and Software Program (WASP), and the LMK Foundation. The author is a member of the ELLIIT Strategic Research Area at Lund University.

Contents

Nomenclature

Acronym	Meaning
BD	Brain Death
BIS	Bispectral Index
cDCD	Controlled Donation after Circulatory Death
DBD	Donation after Brain Death
DCD	Donation after Circulatory Death
DoH	Depth of Hypnosis
ECG	Electrocardiogram
ECMO	Extracorporeal Membrane Oxygenation
EEG	Electroencephalogram
EMG	Electromyogram
FOPTD	First Order Plus Time Delay (model)
FWIT	Functional Warm Ischemic Time
IMC	Ischemic Myocardial Contracture
LBM	Lean Body Mass
ML	Machine Learning
MLE	Maximum Likelihood Estimation
MPC	Model Predictive Control
NLME	Nonlinear Mixed Effects
NMB	Neuromuscular Blockade
NRP	Normothermic Regional Perfusion
ODE	Ordinary Differential Equation
PD	Pharmacodynamics
PID	Proportional-Integral-Derivative controller
PK	Pharmacokinetics
TCI	Target-Controlled Infusion
TIVA	Total Intravenous Anesthesia
uDCD	Uncontrolled Donation after Circulatory Death
WAV_{CNS}	Wavelet-based Anesthesia Value for Central Nervous System
WLST	Withdrawal of Life-Sustaining Treatment

1

Introduction

Have you thought about how individuals of different sizes often receive the same drug dose? For example, when visiting the doctor, you might be given the same amount of painkillers as someone twice your size. This "one-size-fits-all" is the standard approach in healthcare. When it comes to painkillers, it might not be a problem. But what if you are undergoing surgery and need anesthesia? Accurate dosing is challenging because each individual reacts differently to the same dose. This variation can depend on age, weight, sex, or underlying diseases [Mould and Upton, 2012]. This is where personalized medicine comes in. Instead of a "one-size-fits-all" approach, personalized medicine aims to tailor the drug dose to each individual. This allows safer treatments and better outcomes for the patient. In personalized medicine, the way to obtain this is by describing the difference in how different individuals respond to the same drug dose, which is called inter-patient variability. This variability is exemplified in Figure 1.1, where four individuals receive the same drug infusion, but their response varies greatly. This variability can be described by models that capture the underlying mechanisms and factors that affect the drug response.

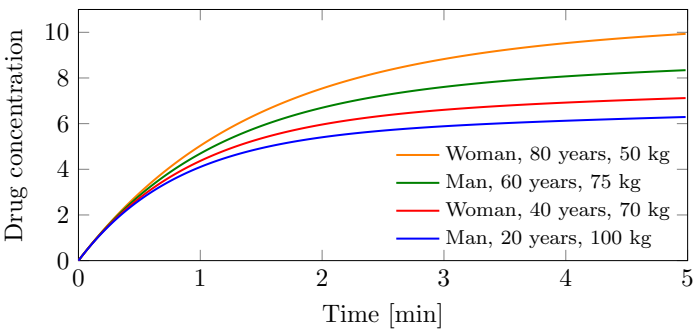

Figure 1.1 Simulation example of inter-patient variability in drug response. The drug concentration in the blood over time is shown for four different individuals, that obtain the same (constant) drug infusion.

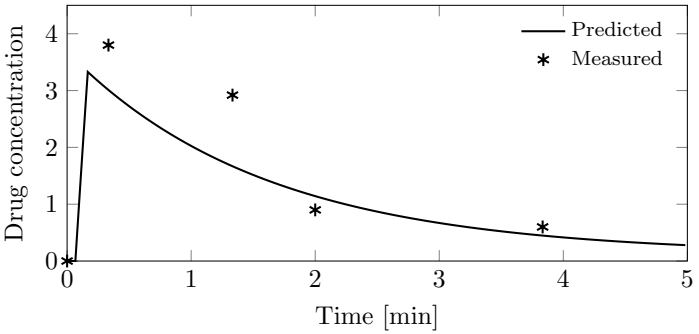

Figure 1.2 Example of model errors in drug response between the model prediction (solid) and actual measurements (markers). The difference comes from that the model was developed to fit a range of individuals, and not for this particular individual.

Individualized drug dosing can be achieved, for example, by using mathematical models and automatic control systems. A model is a simplified representation of a system, often described by mathematical equations. The simplification is related to the intended use of the model, as described by [Mould and Upton, 2012]:

> For example, one scale model of an airplane may be made for testing its aerodynamics in a wind tunnel, while another may be made for visualizing and choosing the exterior colors. Neither of the models is meant to do the job of the real airplane. Furthermore, neither is a "true" model, but each may be fit for its intended purpose.

This quote highlights that all models are simplifications of reality, but still are useful in the right context. This is particularly useful in physiological modeling, where the complexity of the human body makes it impossible to capture all the details in a model. However, modeling the relevant functions of the body can help us understand how it works and interacts with drugs. Therefore, there is a trade-off between model complexity and interpretability, where a model that is too complex can be difficult to interpret and understand, while a model that is too simple might not capture the relevant features of the system.

In pharmacology, models that describe drug absorption, distribution, metabolism, and clinical effect are called pharmacokinetic-pharmacodynamic (PKPD) models. These models are important for understanding how drugs interact with the body and for designing optimal dosing strategies. In these models, patient characteristics, such as age, weight, and other factors, referred to as covariates, are used to improve model predictions [Mould and Upton, 2012; Sahinovic et al., 2018]. The model predictions tell us something about how the patient will respond to a drug dose, which can be used to find the right dose for the individual. For example, a patient with a larger body weight might need a higher dose than a patient with a lower body weight. Inaccurate models can lead to poor dosing decisions, which

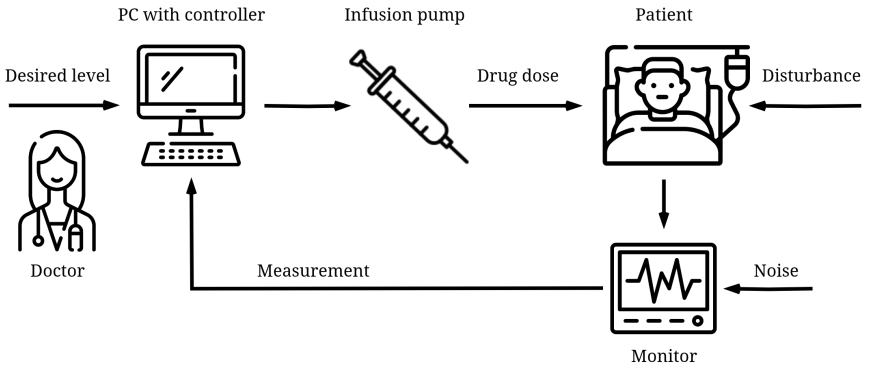

Figure 1.3 Example of closed-loop control of a physiological variable, such as blood pressure or anesthetic depth. The doctor sets the desired level of the variable, and the control system adjusts the drug dose to maintain the desired level. A monitor continuously measures the patient's response and sends this information to the control system. Noise and disturbances affect the patient's response and the estimate of the variable. Icons from `https://www.flaticon.com/free-icons/`.

can be harmful to the patient. An example of where the model prediction does not match the patient's actual response is shown in Figure 1.2, where the model predicts a different drug response than what is actually measured. In this case, the peak concentration is underestimated, which can lead to overdosing.

One challenge in the development of PKPD models is that they are often developed manually in a step-wise manner where covariates are added and removed based on their statistical and clinical significance [Mould and Upton, 2012]. This process is often done by hand, which is both time- and work-intensive. Replacing this manual model development with machine learning methods makes it possible to automate the modeling process and identify models that can capture variability better across patients. Machine learning methods are flexible and are particularly suitable for handling large datasets [Janssen et al., 2022a]. However, these methods often generate black-box models which can be complex and difficult to interpret. This is a limitation in clinical practice, where understandable models are required to guarantee patient safety and to gain clinical acceptance. Again, the trade-off between model complexity and interpretability is important to consider.

If we can measure the patient's drug response in real-time, we can further individualize the drug dosing. For this, automatic control systems can be used to adjust the drug dose based on the patient's response. An example of a closed-loop system for controlling a physiological variable, such as heart rate or blood pressure, is shown in Figure 1.3. The patient's response is monitored continuously and the dose is adjusted accordingly by the control system, commonly implemented on a computer. This allows for individualized and robust drug dosing based on the patient's needs at that moment. It also allows for rapid adjustments to changes in the patient's

condition, which can be crucial in critical care settings [Dumont et al., 2009]. Disturbances, such as surgical interventions, can affect the patient's state and response. For example, if the patient's blood pressure drops during surgery, the control system can rapidly calculate the drug dose needed to stabilize the blood pressure again. This can be difficult to do manually, especially in intensive care units, where the patient's condition can change rapidly.

The control system is sensitive to measurement noise and electric inference from other devices in the operating room [Chan et al., 2012; Pawlowski et al., 2022]. If the measurement signal is poor, for example, due to electric inference, the control system has incorrect information about the patient's state, which can then lead to over- or underdosing. Overdosing can cause undesirable side effects such as hypotension[1] or bradycardia[2], while underdosing can lead to insufficient treatment effects [Bibian et al., 2006]. Therefore, it can be useful to combine PKPD model predictions with measurement feedback for drug dosing, rather than relying purely on the measurement.

In anesthesia, individualized drug dosing is crucial to ensure patient safety. The anesthesiologist continuously adjusts the drug dose to keep the patient unconscious and pain-free during surgery. The patient's response to anesthetic drugs can vary greatly between patients, making it challenging to find the right dose [Bibian et al., 2006; Sahinovic et al., 2018]. Disturbances, such as surgical interventions, affect the level of anesthesia, which motivates the need for an automatic control system that can adjust the drug dose based on the patient's response.

Heart transplantation is a treatment that is often necessary for survival in patients with end-stage heart failure. There is a shortage of donor hearts, and many hearts are discarded because they are not deemed suitable for transplantation. For instance, in Sweden, two-thirds of potential donor hearts are routinely discarded and the situation is similar in other countries [MOD, 2024; Domínguez-Gil, 2021]. This shortage of donor hearts has motivated the introduction of donors after circulatory death (DCD)[3] in several countries[4]. However, DCD donor hearts are more susceptible to ischemic[5] damage compared to the traditional donors after brain death (DBD) [Messer et al., 2016]. Therefore, procurement of DCD donor hearts is performed under tight time constraints. Ischemic myocardial contracture (IMC) can develop when the heart is beating without oxygen, which prevents the heart from being used for transplantation. Few studies have been performed on how to prevent or delay IMC for DCD donor hearts. Here, we investigate how precise drug dosing can stabilize the hemodynamics[6] of the heart donor to prevent IMC and improve the quality of the heart.

[1] Hypotension - low blood pressure.
[2] Bradycardia - low heart rate.
[3] DCD - circulatory death can be determined when the donor has no circulation and no breathing.
[4] DCD for heart transplantation is not yet implemented in Sweden.
[5] Ischemia - Lack of blood to the blood muscle, resulting in shortage of oxygen.
[6] Hemodynamics - what affects the blood flow, such as blood pressure and heart rate.

While the applications of individualized drug control in anesthesia and heart transplantation may seem to differ in scope–from ensuring safe anesthesia in surgery to optimizing donor heart outcomes–both highlight the importance of precision dosing and automatic control systems to address variability in patient responses and optimize therapeutic outcomes. In conclusion, the main challenges in pharmacological modeling and control that are addressed in this thesis are:

- **Inter- and intra-patient variability**, meaning that the patient's drug response can vary between patients and within the same patient over time.
- **Model errors**. There can be a mismatch between the model's prediction and the patient's response, which can lead to over- or underdosing.
- **Unmeasured disturbances**, such as surgical interventions, affect the patient's state and drug response.
- **Noisy or lack of measurements**. The drug concentration at the site of interest can usually not be measured directly but is often estimated from other measurements.

1.1 Research Aims

To address these aforementioned challenges, this thesis aims to improve the modeling and control of pharmacological systems, with a particular focus on precision dosing with accurate models and feedback systems. The main objectives are to:

- study how precision dosing can be used to stabilize hemodynamics in heart donors, thereby reducing ischemic damage to the donated heart and enhancing the quality of the organ for transplantation.
- streamline the model development process for pharmacological models and apply machine learning techniques to create simple, interpretable models that capture inter-patient variability well.
- improve automatic control of drug delivery systems by combining model predictions with measurement feedback to better handle model errors and uncertain measurements.

1.2 Outline

The outline of the thesis is as follows: Chapter 2 provides the background with an introduction to pharmacological models and control. It also presents the two applications that have been studied: heart transplantation and anesthesia. This chapter serves as a background for the papers included in this thesis. Chapter 3 summarizes the included papers and presents the main contributions of this thesis. In Chapter 4, the significance and ethics of the work are discussed, as well as future work. Thereafter, the six included papers are attached as Paper I, Paper II, . . . , and Paper VI.

2

Background

This background chapter provides an overview of the field of pharmacological systems and control and introduces the motivation behind the problems addressed in this thesis. Its purpose is to provide the reader with the necessary background knowledge for the contributed papers that follow in the thesis. The chapter is divided into four sections: Section 2.1 introduces modeling of pharmacological systems, in particular pharmacokinetic-pharmacodynamic (PKPD) modeling and pharmacometrics. Section 2.2 presents control of pharmacological systems. Section 2.3 and Section 2.4 present two applications on which this thesis is based, namely heart transplantation and anesthesia, respectively. These applications are used to illustrate how precision dosing and control can be used to improve patient outcomes in clinical practice.

2.1 Modeling of Pharmacological Systems

The modeling of pharmacological systems is essential in drug development and precision dosing. Mathematical models describe the relationship between drug dose and clinical effect, which can be used to derive drug dosing guidelines, both for manual dosing, in target-controlled infusion (TCI) devices, and in closed-loop control systems. Accurate drug models are crucial for patient safety, as under- or overdosing can lead to severe consequences. In this section, we describe the main concepts of pharmacokinetic (PK) (Section 2.1.1) and pharmacodynamic (PD) modeling (Section 2.1.2). This is the foundation of pharmacometrics, which is a methodology for modeling the variability in drug response between individuals (Section 2.1.3).

2.1.1 Modeling of Pharmacokinetics

Pharmacokinetics (PK) describe the absorption, distribution, and elimination of a drug in the body. The modeling of pharmacokinetics is mainly used to understand the effect of the body on the drug, estimate physiological parameters, and determine accurate drug dosing. The most commonly used models for PK modeling

are low-order compartment models, where the body is divided into parts based on similar properties. For example, organs, tissue, or blood can be grouped as separate compartments. Then, drug transfer rates describe drug diffusion between these compartments.

A one-compartment model is the simplest representation, where a single compartment approximates the entire body. The drug is assumed to be uniformly distributed in the body and is eliminated through a first-order process. For many drugs, a one-compartment model is sufficient to describe pharmacokinetics [Sahinovic et al., 2018]. Multi-compartment models include one or several peripheral compartments connected to the central one. They can be connected in different ways, that is, having different topologies, depending on how the compartments are connected and where the drug is added and eliminated from the system.

Schematic representations of one-, two- and three-compartment (mammillary) models are shown in Figure 2.1. In the case of the three-compartment model, the central compartment typically models blood plasma, and the two peripheral compartments model slow-perfused (e.g., fat) and fast-perfused (e.g., muscle) tissue. The drug is added and eliminated from the central compartment, and non-negative transfer rates k_{ij} [1/time] describe the diffusion of the drug from compartment i to j. In the cases covered in this thesis, the central compartment models blood plasma. In general, the concentrations of the peripheral compartments are not directly measurable, as they rather are a mathematical construct to capture the drug dynamics. However, the concentration of the central compartment can be measured directly from blood samples. These blood samples are typically taken at discrete time points, so the drug concentration is not continuously measured. This is the case for the drugs considered in this thesis, where the analysis is done offline based on blood samples. However, for some applications, such as blood glucose monitoring in diabetes, there are devices for online monitoring, where the blood glucose concentration is measured in real-time.

The suitable topology and number of compartments can be determined from data [Sahinovic et al., 2018]. The most common representations are low-order models, as they typically capture the main properties of the absorption, distribution, and elimination dynamics of the drug. However, increasing the complexity of the model by adding more compartments may result in models that are not practically identifiable from available data. Identifiability is in general a large challenge in PK modeling, as poor input excitation limits the identifiability of the model parameters [da Silva et al., 2014]. Increasing input excitation is usually not possible in clinical practice, as it might risk patient safety which raises ethical concerns.

Another approach to compartmental PK modeling is physiologically-based PK models (PBPK), where all major tissues, such as muscles, brain, heart, kidneys, liver, and lungs, are represented as separate parts, as explained, for example, in [Jones and Rowland-Yeo, 2013]. Then, the parts are directly linked to physiological meaning, in contrary to compartmental models where the compartments lack physiological meaning. However, PBPK modeling is more complex, requires extensive

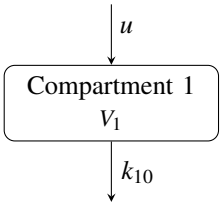

(a) One-compartment model

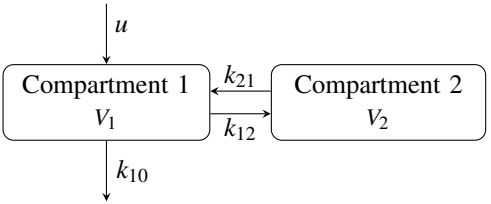

(b) Two-compartment model

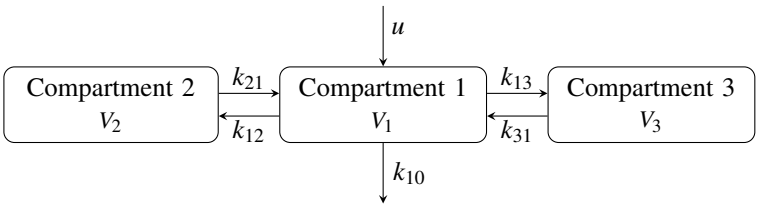

(c) Three-compartment model

Figure 2.1 Schematic illustration of one-, two- and three-compartment models. Compartmental volumes are denoted by V_i and transfer rates between compartments i and j are denoted by k_{ij}. Drug is added and eliminated from the central compartment at rates u and k_{10}, respectively.

data for model development, and does not necessarily improve prediction accuracy compared to compartmental models [Masui et al., 2009].

Mathematically, we can describe the drug concentration in the compartments using ordinary differential equations (ODEs). The relation between drug infusion rate $u(t)$ [mass/time] and drug concentration $x(t)$ [mass/volume] in the one-compartment model (Figure 2.1a) is given by the first-order linear time-invariant (LTI) model:

$$\dot{x} = -k_{10}x + \frac{1}{V_1}u, \tag{2.1}$$

where $\dot{x}$ denotes the time derivative of x, k_{10} [1/time] is the elimination-rate constant, and V_1 [volume] is the volume of distribution. Note that we have left out the

time dependence of the state variable x and input u for readability. Similarly, the two-compartment model (Figure 2.1b) can be described by:

$$\dot{x}_1 = -(k_{10} + k_{12})x_1 + k_{21}x_2 + \frac{1}{V_1}u \tag{2.2a}$$
$$\dot{x}_2 = k_{12}x_1 - k_{21}x_2, \tag{2.2b}$$

where x_1 and x_2 denote the drug concentration of the central and peripheral compartment, respectively. The transfer rate constant from compartment i to j is denoted k_{ij} [1/time] and V_1 denotes the volume of the central compartment.

A state-space representation of the mammillary three-compartment model (Figure 2.1c) is given by:

$$\dot{x}_1 = -(k_{10} + k_{12} + k_{13})x_1 + k_{21}x_2 + k_{31}x_3 + \frac{1}{V_1}u \tag{2.3a}$$
$$\dot{x}_2 = k_{12}x_1 - k_{21}x_2 \tag{2.3b}$$
$$\dot{x}_3 = k_{13}x_1 - k_{31}x_3, \tag{2.3c}$$

where x_1, x_2, and x_3 denote the drug concentration of the central, and the two peripheral compartments respectively.

The PK model can be described either in terms of transfer rates or volumes and clearances. The conversion between these two representations (in terms of the three-compartment model) is:

$$V_2 = \frac{k_{12}}{k_{21}}V_1, \tag{2.4a}$$
$$V_3 = \frac{k_{13}}{k_{31}}V_1, \tag{2.4b}$$
$$CL = k_{10}V_1, \tag{2.4c}$$
$$Q_2 = k_{12}V_2, \tag{2.4d}$$
$$Q_3 = k_{13}V_3, \tag{2.4e}$$

where V_1, V_2, V_3 and CL, Q_2, Q_3 are the compartmental volumes and clearances, respectively.

These PK models can be used to simulate the drug concentration in the body over time. They can be simulated with software tools, such as general solvers for ordinary differential equations (ODEs), or by fixed-step methods for linear systems. Some examples of simulators that can be used to simulate PK dynamics are `ode45` and `lsim` in MATLAB [MathWorks, 2023] and `DifferentialEquations.jl` in Julia [Bezanson et al., 2017].

A challenge in PK modeling is to capture the variability in drug response between individuals. A constant PK model where all compartment volumes and transfer rates are constant over a population will not capture the variability. For example, older people can be more sensitive to the drug, which is not captured by a constant

model. Therefore, it is common to model the PK parameters as a function of patient characteristics such as age and weight, which are referred to as covariates. For example, the central compartment volume V_1 can be modeled as a function f of age and weight:

$$V_1 = f(\text{age}, \text{weight}). \tag{2.5}$$

Modeling of these types of relationships is included in pharmacometrics and will be the topic of Section 2.1.3. These models are used to model the drug variability between patients.

2.1.2 Modeling of Pharmacodynamics

Pharmacodynamics (PD) describes how a drug affects the body, i.e. how the drug concentration relates to the clinical drug effect. Generally, we are interested in the effect of the drug on a specific clinical variable, such as blood pressure or heart rate. A PK model together with the PD model makes up a PKPD model that describes how the drug dose relates to the clinical effect.

PD relationships are commonly described by linear models or sigmoidal Emax models. The linear model assumes a linear relationship between drug concentration C_p [mass/volume] and clinical effect E. The sigmoidal Emax model (also called the Hill model) assumes a nonlinear relationship in which the drug effect increases with concentration and reaches a maximum effect ($E_{\max}$) [Curry and Whelpton, 2017]. If there is a baseline effect E_0 when no drug has been administered, the sigmoidal Emax model is given by

$$E = E_0 + \frac{E_{\max} C_p^{\gamma}}{C_{e50}^{\gamma} + C_p^{\gamma}}. \tag{2.6}$$

where C_{e50} [mass/volume] is the drug concentration at which the effect is half of the maximum effect, shifted by E_0. For example, if $C_p = C_{e50}$, the effect is $E_0 + E_{\max}/2$. The steepness of the dose-response curve is determined by a parameter γ, where a higher value of γ results in a steeper dose-response curve.

Sometimes, an extra single compartment is used to model the delay from blood plasma concentration to clinical effect, i.e., the time it takes for the drug to reach the effect site [Sheiner et al., 1979]. This is called the effect-site compartment and is modeled by

$$\frac{dC_e}{dt} = k_{e0}(C_p - C_e), \tag{2.7}$$

where C_e [mass/volume] is the effect-site concentration and k_{e0} [1/time] is the effect-site rate constant.

The PD parameters are sometimes modeled with a covariate dependence, similar to the PK models. However, this is less common than for PK models. One example where the PD model parameters depend on covariates is the PD model for propofol by [Eleveld et al., 2018], where C_{e50}, k_{e0}, and γ are covariate-dependent. This model is detailed in Section 2.4.

2.1.3 Pharmacometrics

Pharmacometrics is an important tool in drug development and in determining safe dose recommendations for patients [Mould and Upton, 2012]. It can also be used to understand the underlying mechanisms of drug interaction with the body. The main goal of pharmacometrics is to develop models that can estimate the drug concentration in the body and the clinical effect of the drug. This is done by modeling the variability in drug response in a population, which is called population modeling. Population modeling covers both the inter-patient and the intra-patient variability, where the inter-patient variability is the variability between patients and the intra-patient variability is the variability within a patient between a dose and another. Covariates, such as age, weight, or other underlying physiological factors can describe some of the variability, but not all. The remaining variability is described by stochastic models, which will be explained in the following section.

Population PK modeling was first introduced in 1972 by [Sheiner et al., 1972] with the aim of computer-aided therapy for individual drug dosing. This topic remains highly relevant today, as demonstrated in this thesis. Later, in the early 1990s, the methodology was extended to include PD models as well [Stanski and Maitre, 1990]. Modeling requires information about covariates, measurements, and dosing. It is sensitive to the data quality, which limits the predictability of the model.

Population models consist of three components [Mould and Upton, 2012]:

- **Structural models**, such as the compartment models described in Section 2.1.1. These are commonly described by ODEs.
- **Covariate models** (or fixed effects) describe the relationship between covariates and the parameters of the structural model.
- **Stochastic models** (or random effects) describe the remaining variability that the covariate model does not cover.

First, the structural model is determined based on the data, after which the covariate model and the stochastic model are added to describe the variability of the data. Together, the covariate model (fixed effects) and the stochastic model (random effects) make up the nonlinear mixed-effects model (NLME), which is the most common model used in pharmacometrics [Mould and Upton, 2012]. NLME models are used to describe the variability in the data and will be explained in more detail below.

The covariate model aims to describe the relationship between the covariates and the structural model parameters with simple and readable expressions. An example of a covariate model is the linear model with one covariate

$$\theta_i = \theta_{i0} + \theta_{i1} \cdot \text{covariate}, \tag{2.8}$$

where θ_i is the i^{th} structural model parameter (such as central compartment volume V_1), θ_{i0} is the baseline value of the parameter, and θ_{i1} is the effect of the covari-

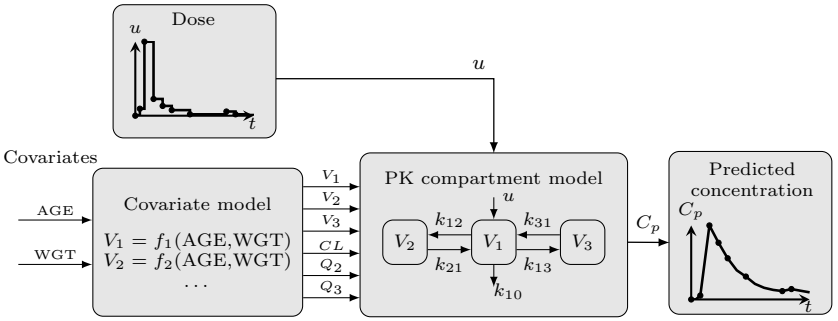

Figure 2.2 Pharmacokinetic (PK) covariate modeling with two covariates (age and weight) and a three-compartment model (see Figure 2.1c for details). The six PK parameters $(V_1, V_2, V_3, CL, Q_2, Q_3)$ are modeled as functions of the covariates and are simulated to estimate plasma concentrations C_p with a given drug administration profile u.

ate on the parameter. The covariate can be, for example, age in years or weight in kilograms.

A more complex covariate model can include nonlinear terms, for example, the effect of the two covariates age and weight on the second compartment volume for propofol, published in [Eleveld et al., 2018] (here presented without random effects):

$$V_2 = \theta_{V_2,1} \cdot \text{WGT} \cdot \exp\left(\text{AGE} - \theta_{V_2,2}\right) \text{ [L]}, \tag{2.9}$$

where $\theta_{V_2,1}$ and $\theta_{V_2,2}$ are covariate model parameters and WGT and AGE are the weight in kilograms and age in years of the patient, respectively.

Figure 2.2 shows an example of how a PK covariate model can be used to simulate drug concentration in the body over time. In this example, there are two covariates (age and weight) and a three-compartment structural model. In the PK covariate model, the six PK parameters are modeled as functions of the covariates. This can be used to simulate and estimate plasma concentrations C_p for a given drug administration profile u.

Identifying the covariate model is a manual iterative process in which components are sequentially added and removed to find the best model fit to the data. This is a very time-consuming process. Typically, this process is based on prior knowledge of the physiology and pharmacology of the drug. The model fit is commonly evaluated using maximum likelihood estimation (MLE), where the best parameters are found by maximizing the likelihood of the data given the model [Mould and Upton, 2012]. In the identification process, both the structure of the covariate model is identified and the parameters (commonly called θ) are estimated.

The stochastic model (random effects) captures the remaining variability that is not covered by the covariates. This variability is commonly modeled by a stochastic variable named η which is assumed to be log-normally distributed across the pop-

ulation. It has zero mean and variance σ^2. An example of a covariate model with a stochastic element is again from [Eleveld et al., 2018], but now with random effects:

$$V_2 = \theta_{V_2,1} \cdot \text{WGT} \cdot \exp\left(\text{AGE} - \theta_{V_2,2}\right) \exp(\eta_{V_2}) \text{ [L]}, \tag{2.10}$$

where η_{V_2} is the stochastic element with $\eta_{V_2} \sim \mathcal{N}(0, \sigma^2_{V_2})$. The stochastic components are commonly modeled as additive or multiplicative. In the case of Equation (2.10), the stochastic element is multiplicative.

The most popular and widely used software for nonlinear mixed-effects modeling is NONMEM [Sheiner and Beal, 1980]. NONMEM is used by pharmaceutical companies and is approved by regulatory agencies for drug development and dosing recommendations. Recently, the Julia package Pumas.jl [Rackauckas et al., 2020] has been developed as an alternative to NONMEM, developed in the efficient Julia programming language [Bezanson et al., 2017], which allows faster model development and parameter estimation. An overview of pharmacometrics for the non-expert is given in [Mould and Upton, 2012].

Machine learning in pharmacometrics In the last 20 years, there has been increasing interest in using machine learning (ML) for pharmacometrics. The focus of ML in pharmacometrics has mainly been on drug concentration predictions directly from data [Brier et al., 1995; Chow et al., 1997; Liu et al., 2015], but also for covariate selection [Janssen et al., 2022b; Sibieude et al., 2021]. For example, neural networks [Janssen et al., 2022c; Sibieude et al., 2022] and random forests [Janssen et al., 2022b] have been used for this. Another example is DeepPumas, which is an ML software for pharmacometrics implemented in Pumas.jl [Rackauckas et al., 2020].

The interest in ML in pharmacometrics has mainly increased due to the availability of large datasets and more powerful computational resources. ML methods can capture complex relationships in the data that are difficult to identify with traditional statistical models. However, these models often lack interpretability, which is a challenge in the regulatory context. Interpretability and explainability are important in healthcare, where the model predictions can have a direct impact on the patient. If these problems are addressed, ML models can be a powerful tool in pharmacometrics. Therefore, using a combination of ML and traditional pharmacometric modeling may be beneficial. ML can be used to speed up model development and process large datasets, while traditional pharmacometric modeling methods can be used to incorporate expert knowledge and to ensure the interpretability of the model. This is the approach taken in Paper III in this thesis. An overview of the possibilities and challenges of ML in pharmacometrics is given in [Janssen et al., 2022a].

2.2 Control of Pharmacological Systems

Precise and fast drug delivery is essential to ensure patient safety. Control of pharmacological systems aims to reach and maintain the desired therapeutic drug effect

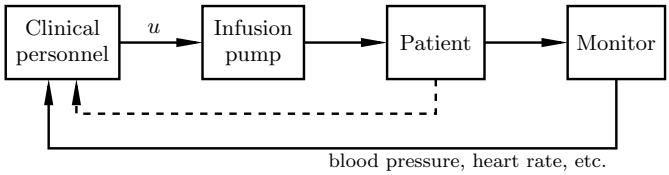

(a) Manual control

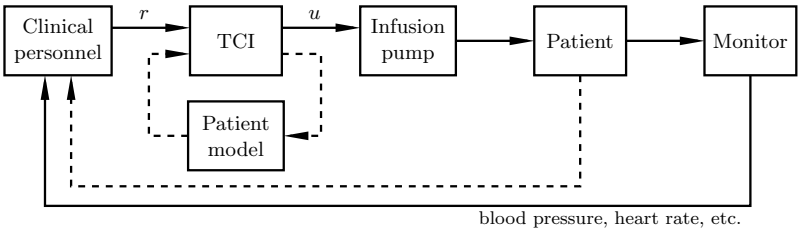

(b) Target-controlled-infusion (TCI)

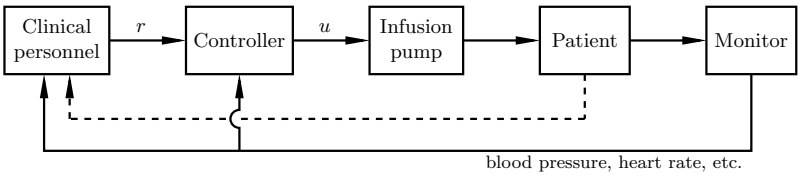

(c) Closed-loop control

Figure 2.3 Dosing strategies for intravenous drugs: (a) manual control, (b) target-controlled infusion (TCI), and (c) closed-loop control. The clinician supervises the system by studying the patient's response (for example, measurements of physical signs such as blood pressure and heart rate) and can adjust the drug dose u (or reference r) if necessary.

as accurately and rapidly as possible. There are several ways to administer drugs, such as orally, intravenously, or by inhalation. Here, we focus on the control of intravenous drugs, where there are three main ways of administration: manual control, target-controlled infusion (TCI), and closed-loop control. These are explained in the following sections and are schematically illustrated in Figure 2.3.

2.2.1 Manual Control

Manual control is the standard practice of drug delivery in many clinical settings. The clinician assesses the patient based on signs such as breathing, sweating, or pupil size, or on clinical measurements such as blood pressure and heart rate, and adjusts the drug dose accordingly, as illustrated in Figure 2.3a. For intravenous drugs, this corresponds to setting an infusion rate or administering a bolus dose. Initially, the clinician administers a dose to reach the desired effect as quickly as possible. This dose is based on the patient's covariates, commonly computed from PKPD models. If the patient's response is not as expected due to patient variability, the clinician must adjust the infusion rate to reach the desired effect. In the presence of unaccounted disturbances, caused for example by surgical interventions, the clinician must change the infusion rate to counteract these disturbances. The clinician must be observant and adjust the drug dose continuously to maintain the desired effect.

The main advantage of manual control is that the clinician uses all available information to adjust the drug dose. However, manual control is prone to be slow and imprecise, as it might take time for the clinician to react to changes in the patient's state and to determine the correct dose to again reach the desired effect. Automatic control systems can be used to assist the clinician in this task, as discussed in the following sections.

2.2.2 Target-Controlled Infusion (TCI)

Target-controlled infusion (TCI) is a method for automatic intravenous drug delivery. It has been used routinely in the clinic for more than 30 years and is today a well-established method for the administration of intravenous drugs. A comprehensive review of the history of TCI systems can be found in [Struys et al., 2016]. TCI systems were originally developed for the administration of the anesthetic drug propofol and are now also used for other drugs, for example, opioids such as remifentanil and alfentanil. The most widely used TCI system is the Diprifusor™(AstraZeneca, London, UK).

In TCI, a dose trajectory is calculated by a computer based on an underlying patient PKPD model and the desired effect-site concentration. The clinician determines a target concentration in the plasma or at the effect site rather than the specific infusion rate, which can be more intuitive for the clinician [Servin, 1998; Russell et al., 1995]. Then, the TCI system computes an optimal infusion rate trajectory based on an underlying patient model to reach this target concentration as quickly as possible without overshooting [Shafer and Gregg, 1992; van Poucke et al., 2004].

At the start of the therapy, the TCI system will compute a bolus of suitable size to reach the desired effect-site concentration as fast as possible, while still staying within the recommended drug administration limits. Then, a constant infusion will maintain the desired effect-site concentration during the maintenance phase. An example of a computed dose trajectory is shown in Figure 2.4 (lower). The predicted

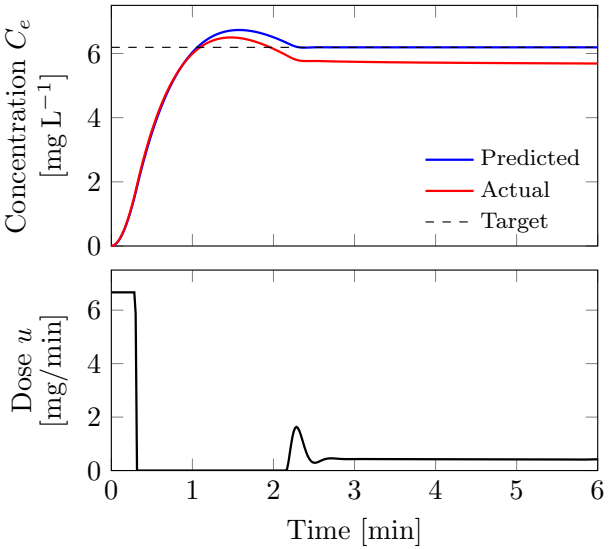

Figure 2.4 Predicted, actual, and reference effect-site concentration C_e (upper). Propofol infusion profile computed by the TCI algorithm (lower), computed based on the patient model corresponding to the blue prediction in the upper plot.

TCI dose trajectory (blue) with the target concentration (dashed, black) is shown in the upper plot of Figure 2.4.

However, TCI is not based on feedback from measurements, but rather is based on the underlying patient model. If the incorporated patient model is not accurate, the TCI system will not optimally deliver drugs, which can result in a static error in drug concentration [Wahlquist et al., 2024]. An example of this is shown in Figure 2.4, where there is a discrepancy between the predicted concentration (blue) and the actual concentration (red), due to model errors (discrepancy between model and patient response). A model error could result in over- or under-dosing of the patient, which can potentially have severe consequences. If the patient responds differently than expected, the clinician can adjust the target concentration to account for this. In this way, the TCI system can be seen as an open-loop feed-forward control system. However, it can be difficult for the clinician to know how to adjust the target concentration, as direct measurements of the actual blood concentration are commonly not available.

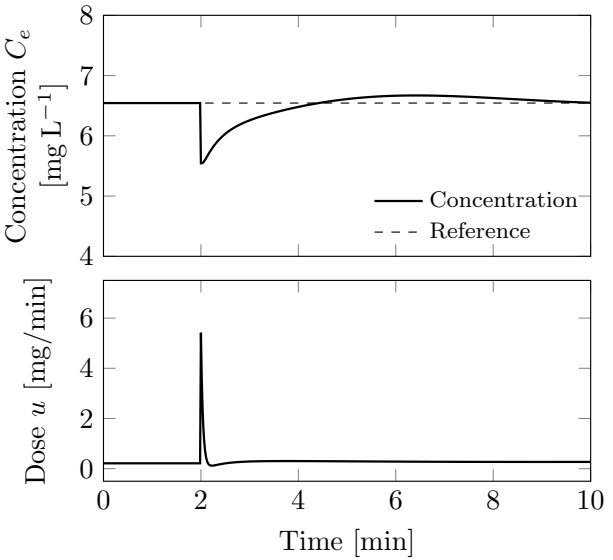

Figure 2.5 Simulation of disturbance rejection with a PID controller to maintain effect-site concentration at a stationary level (upper) with the corresponding dose profile (lower). A negative step disturbance of size one is introduced at $t = 2$ min and the controller adjusts the infusion rate to maintain the desired drug concentration.

2.2.3 Closed-Loop Control

Closed-loop control is an automated method for drug delivery where the drug dose is computed based on a measurement. A schematic illustration of a closed-loop control system is shown in Figure 2.3c. The controller aims to maintain a physiological state, such as blood pressure or drug concentration in the blood. The clinician sets the reference value r (the desired drug concentration) and the controller calculates an infusion rate u that will drive the system to the desired concentration. Although the system may run fully automatic, the clinician must supervise it and interrupt if necessary, for example, if the system is not performing as expected. Closed-loop control of drug delivery has been suggested to improve patient safety and reduce the workload of the clinician [Ghita et al., 2020]. Using measurements allows for the drug to be computed in real-time, which can lead to faster and more accurate drug delivery compared to manual control or TCI. Particularly, the rejection of disturbances can be handled effectively by the controller. This can be obtained also with manual control if the clinician is observant and reacts quickly.

An example of how a control system can reject a disturbance is shown in Figure 2.5. A negative step disturbance is introduced at $t = 2$ min and within two minutes from the start of the disturbance, the main part of the disturbance is rejected by the controller, and the drug concentration is maintained at the desired level.

The measurement could be, for example, blood plasma concentration, blood pressure, heart rate, or other physiological measurements. In some cases, the concentration of interest cannot be measured online and the control system must rely on another measurement that is directly or indirectly affected by the drug concentration. An example in which the measurement of interest can be directly observed is diabetes, in which blood glucose concentration is sampled online. The glucose concentration can then be controlled by infusions of insulin. In contrast, in automatic control of anesthesia, the drug concentration of the anesthetic drug cannot be measured directly at the effect site (i.e., the brain). Instead, an estimate of the hypnotic depth based on the patient's EEG is used as an indirect measurement of the drug concentration. Closed-loop control of anesthesia is further discussed in Section 2.4.

The most common feedback controller, not only of pharmacological systems, is the proportional-integral-derivative (PID) controller because of its simplicity and robustness. In PID control, the infusion rate u is calculated from the control error $e = r - y$, where r is the reference signal and y is the measurement. The ideal PID controller is given by

$$u(t) = K\left(e(t) + \frac{1}{T_i}\int_0^t e(\tau)d\tau + T_d\frac{de(t)}{dt}\right), \tag{2.11}$$

where K is the controller gain, T_i is the integral time constant, and T_d is the derivative time constant. These are tunable controller parameters that determine the speed, stability, and robustness of the control system. For the actual implementation of the PID controller, some modifications such as anti-windup and filtering are needed [Soltesz et al., 2012].

PID control of pharmacological systems has been successfully implemented in clinical settings, such as control of blood glucose concentration in diabetes [Brown Sue A. et al., 2019] and in control of anesthesia [Schiavo et al., 2021]. Other, more advanced, control strategies have also been successfully tested, such as model predictive control (MPC) [Hovorka et al., 2004] and fuzzy logic [Schäublin et al., 1996]. An overview of closed-loop control systems applied to pharmacological systems is given in [Spataru et al., 2024].

There are several available software for closed-loop control in pharmacology, such as the Control-IQ™(Tandem Diabetes Care) for diabetes and Intellivent-ASV™(Hamilton Medical) for ventilation which have been evaluated in clinical trials [Brown Sue A. et al., 2019; Beijers et al., 2014]. However, closed-loop control of pharmacological systems is not yet widely adopted in clinical practice, and several challenges need to be addressed before it can be implemented routinely.

Closed-loop control in pharmacological systems is challenging for multiple reasons. Since the feedback commonly relies on one measurement only, poor signal quality greatly affects control performance. Surgical devices, such as electrocautery devices, can introduce noise in the measurement signal, which can lead to poor control performance [Chan et al., 2012]. Another challenge is the choice of controller and tuning of controller parameters. Poor tuning of controller parameters can lead

to unwanted behaviors such as oscillations, instability, or slow response. A complex control structure is unlikely to be adopted in clinical practice, as it can be difficult to understand by the clinical personnel. However, automated drug delivery is likely to be adopted in the future as more and more online measurements are becoming available in medicine. In Papers V and VI, we investigate how controller performance can be improved when the signal quality of the measurement is poor, by seamlessly moving between TCI and closed-loop control.

2.3 Application: Stabilization of Heart Donors for Transplantation

With the background presented in the previous sections, we now turn our attention to the application of heart transplantation. In this section, we discuss how accurate dosing can be used to stabilize hemodynamics in the heart donor. For this, drug modeling and control systems can be used to maintain normal physiological variables in the donor, for example, blood pressure and heart rate. This is crucial to prevent ischemic damage to the donor heart and to maintain organ viability. First, we present an overview of heart transplantation, with a focus on donation after circulatory death (DCD) (Section 2.3.1). Then we introduce the phenomenon of ischemic myocardial contracture (IMC) (Section 2.3.2) and finally we discuss how hemodynamic stabilization can prevent ischemic damage to the donor heart (Section 2.3.3).

2.3.1 Heart Transplantation

Organ transplantation has saved many lives since the first kidney transplant in 1954. In terms of long-term survival, transplantation is the only option for end-stage organ failure of the liver, lung, and heart. In 2019, 153 863 solid-organ transplants (kidneys, lungs, hearts, livers, pancreas, and small bowels) were performed worldwide in 111 countries. However, this only matches 10 % of the global need [EDQM, 2022].

The first step in the donation process is the identification of potential donors. The clinical personnel determines whether a patient is suitable for donation and the life-sustaining treatment is continued. When the will to donate has been established (commonly through a donation register), organ-protective treatment can begin. This treatment is the first step towards a successful transplantation and can include treatment of hypertension, hypotension, hypothermia, and the detection and correction of metabolic diseases. This treatment must not contradict what is best for the patient [EDQM, 2022; MOD, 2024].

This chapter will focus on the two most common scenarios of organ donation depending on the determination of death: donation after brain death (DBD) and donation after circulatory death (DCD). In particular, the focus will be on DCD for heart transplantation and the current status of organ transplantation in Sweden.

Donation after brain death (DBD) Currently, donation after brain death (DBD) presents the main source of transplantable organs. In a study of transplanted organs in the US during 2021 and 2022, DBD made up 97 % of all deceased donors, and DCD donors represented the other 3 % [Jawitz et al., 2022].

DBD is only performed under certain conditions, where the patient must be in a hospital, have given consent for donation (commonly through the donation register), and be declared brain dead (BD). The definition of brain death, or equivalently death by neurological criteria, has varied over time. Today, the widespread definition is the complete and permanent loss of brain functions. This loss of brain functions is characterized by unresponsive coma with loss of consciousness, loss of brainstem reflexes, and the inability to breathe independently [Greer et al., 2020]. The key factor for diagnosing BD is the irreversibility of brain function, where the absence of brain function must be observed for some time before the patient can be legally declared dead by neurological criteria [Rossetti et al., 2010]. Other tests for confirming BD include neurologic tests, for example, checking for spontaneous breathing and brainstem reflexes such as the pupillary light reflex [EDQM, 2022].

Donation after circulatory death (DCD) The shortage of transplantable organs has led to the (re)introduction of donation after the circulatory determination of death (DCD). DCD patients can be categorized into one of the four categories depending on the circumstances of the circulatory arrest:

- **Category I**: Uncontrolled DCD (uDCD). The patient suffers an unexpected circulatory arrest and no resuscitation is attempted.
- **Category II**: Uncontrolled DCD (uDCD). The patient suffers an unexpected circulatory arrest and resuscitation is attempted but failed.
- **Category III**: Controlled DCD (cDCD). Withdrawal of life-sustaining treatment (WLST) is performed in a planned setting in the hospital, leading to circulatory arrest.
- **Category IV**: Circulatory arrest while brain dead. The patient is declared brain dead and suffers a circulatory arrest.

The most common categories for DCD are categories II and III. Uncontrolled DCD (category I and II) is subject to the damaging effect of warm ischemia, as circulatory arrest does not take place in a controlled setting in an ICU but rather under unclear circumstances. However, with strict selection criteria, these donors are often healthy before circulatory arrest, usually resulting in good-quality organs. Controlled DCD (category III) takes place in the form of WLST when it has been determined that continuous organ support is no longer in the patient's best interest [EDQM, 2022]. Most cDCD donors have suffered acute brain damage similar to DBD donors, with a high risk of developing total brain infarction after WLST. A

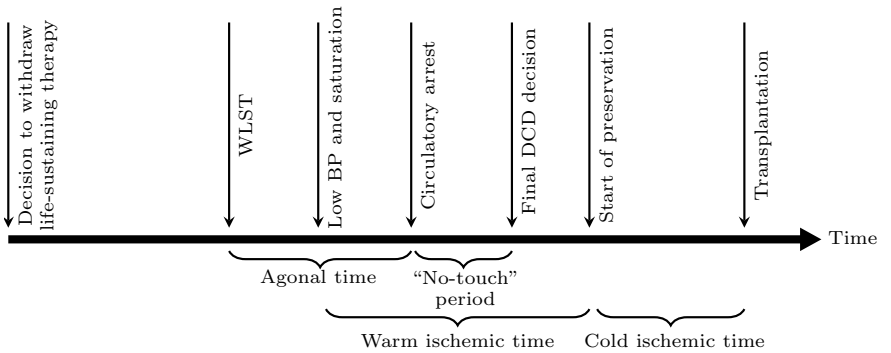

Figure 2.6 Timeline for the DCD process. WLST: Withdrawal of life-sustaining therapies, BP: blood pressure.

possible DCD donor should not spontaneously breathe and should have the potential to obtain circulatory arrest within a given time frame [Vävnadsrådet, 2022].

The withdrawal of life-sustaining treatments (WLST) is the first step in the cDCD process. WLST is performed in a planned setting in the hospital, and the patient is usually on ventilator support. Following WLST, several time events are observed. Figure 2.6 shows a timeline of the WLST process. These events are [EDQM, 2022]:

1. WLST; withdrawal of life-sustaining therapies. Life support is turned off (commonly mechanical ventilation and ECMO[1]).

2. Onset of sustained significant hypoperfusion; low blood pressure (BP) and low oxygen saturation.

3. Cardio-respiratory (circulatory) arrest; no breathing observed and absence of pulsatile flow on an arterial line or absence of blood flow through the aortic valve on echocardiography (ECG) (if used). Asystole is not necessary to determine death [EDQM, 2022].

4. "No-touch" period; the time from circulatory arrest to the final DCD decision, where interruptions are not allowed. This time varies between 5 and 30 min in Europe [Lomero et al., 2020].

5. Final DCD decision; Based on the patient's irreversible state without the possibility of spontaneous recovery, the final decision to proceed with organ retrieval is made. The patient is legally declared dead at this point.

[1] Extracorporeal membrane oxygenation (ECMO) is a life support technique that provides cardiac and respiratory support to patients with severe heart and lung failure.

After the final DCD decision, the main goal is to minimize the warm ischemic[2] time. The length of the warm ischemic time affects the outcome of the transplantation, and acceptable periods for ischemia have been defined [Vävnadsrådet, 2022]:

- Agonal time (sometimes called withdrawal time); the time from WLST to circulatory arrest. This time varies, in general, from a few minutes to a few hours.
- Functional warm ischemic time (FWIT); the time from significant hypoperfusion to the start of preservation (usually in-situ perfusion).
- Cold ischemic time; the time from preservation to transplantation.

cDCD can only take place if cardio-respiratory arrest follows within 2–4 hours after WLST. Up to 90 % of the cDCD donors will have circulatory arrest within two hours after WLST [Leiden et al., 2016]. Acceptable times for FWIT vary from 30 min for livers and hearts to 90 min for the pancreas and lungs and up to 180 min for kidneys [Smith et al., 2019; Vävnadsrådet, 2022].

In recent years, DCD has been implemented more and more frequently in Europe. As of 2021, 12 European countries included cDCD and 14 countries included uDCD in their transplantation programs, of which eight countries have implemented both. The fact that countries have focused on different types of DCD relates to different legislations, ethical concerns, end-of-life practices, and organizational approaches to the treatment of out-of-hospital circulatory arrest. In countries that have implemented DCD, these donors have become an important source of organs for transplantation. For example, in the Netherlands, DCD donors represent 59 % of all deceased donors [NHS Blood and Transplant, 2019]. DCD is used mainly in kidney, lung, and liver transplantation [EDQM, 2022], all showing results comparable to those of DBD donation.

In [Jawitz et al., 2022], the authors estimated that DCD heart transplantation has the potential to increase the donor pool by 30 %. However, the annual number of DCD heart donors still counts less than 1000 worldwide [EDQM, 2022]. As of 2022, cDCD heart transplantations were successfully carried out in the United Kingdom, Australia, and Belgium [EDQM, 2022]. So far, DCD heart transplantation has shown results comparable to DBD. The timeline from WLST to organ retrieval is critical for the outcome of heart transplantation because the heart is more sensitive to ischemic damage than, for example, the kidneys and lungs.

Current status of organ donation in Sweden There is a strong will to donate in Sweden. However, only a fraction of the population dies in circumstances that allow organ donation. In Sweden in 2023, 258 deceased donors were used, of which 190 were DBD donors and 68 were cDCD donors [Scandiatransplant, 2023]. A total of

[2] Ischemia occurs when blood flow (and thus oxygen) is reduced to a part of the body

Hearts transplanted in 2023	On the waiting list for a heart (Oct 1, 2024)
68 hearts	27 patients
Average waiting time for a heart (2023)	Transplanted within a year on the waiting list
4 months	74 %

Figure 2.7 Heart transplantation and waiting list figures for Sweden in 2023/2024. Data from [Scandiatransplant, 2023].

906 organs were transplanted [Socialstyrelsen, 2023a], and a majority were kidney transplants.

The first donation of cDCD took place in 2020 [Socialstyrelsen, 2023b]. cDCD is currently allowed for kidney, liver, lungs, and pancreas. There is no current plan to introduce uDCD for transplantation in Sweden. Sweden's current DCD protocol is described in [Vävnadsrådet, 2022]. The protocol follows the steps described previously, with the following additions and specifications:

- At WLST, all treatments should be withdrawn except for the palliative treatment. Palliative treatment includes opioids, sedatives, pain/ anxiety treatment, and anticholinergics[3].
- After WLST, the donor is monitored with invasive arterial pressure and pulse oximetry. ECG should not be used as it can give a false impression of life for the attendant next of kin.
- Circulatory arrest is determined when the following is fulfilled: no palpable pulse, no audible heart sounds at auscultation[4], no spontaneous breathing, and fixed, usually dilated pupils.
- The "no-touch period" for cDCD is 5 minutes.

In 2023, 68 hearts were transplanted in Sweden. In Figure 2.7, we illustrate the current status of the waiting list for hearts in Sweden. As shown in Figure 2.7, most patients on the waiting list are transplanted within one year. However, the need is expected to grow in the future, which is consistent with the rest of the world [EDQM, 2022]. The potential of DCD for heart transplantation in Sweden is yet to be investigated. As DCD for heart transplantation becomes more and more common in the world with promising results, there is potential for future implementation in Sweden.

[3] Anticholinergics blocks acetylcholine and is used for treating example dizziness and hallucinations.
[4] Ausculation means listening to the internal sounds of the body, usually using a stethoscope.

(a) Heart without ischemic myocardial contracture.

(b) Heart with ischemic myocardial contracture.

Figure 2.8 Example of a heart with (lower) and without (upper) ischemic myocardial contracture (IMC). Note that the left ventricular lumen is almost invisible in the contracted heart. Both photos are in the same scale, indicated in (b). From [Wahlquist et al., 2021b].

2.3.2 Ischemic Myocardial Contracture (IMC)

When the myocardium[5] performs mechanical work under warm ischemic conditions, the heart muscle becomes stiff and loses its contractility. This is known as ischemic myocardial contracture (IMC) or "stone heart" [Cooley et al., 1972b]. IMC is a severe condition that can occur in DCD hearts and prevents the heart from being transplanted. Figure 2.8 shows an example of a heart with and without IMC. The prevention and delay of IMC have been investigated in several works [Cooley et al., 1972a; Hearse et al., 1977]. For example, cooling, administration of β-blockers and calcium channel blockers have been suggested to reduce the risk of IMC [Cooley et al., 1972a; Zumbro et al., 1978]. However, these studies were performed in the 1970s and 1980s to prevent IMC in open-heart surgeries using cardiopulmonary bypass. The effect of these interventions on DCD hearts is yet to be investigated.

Only a few works have studied IMC in DCD hearts in the last few years, such as [Li et al., 2023], where the focus has been on understanding the mechanisms behind IMC rather than prevention.

[5] Myocardium – the cardiac muscle

2.3.3 Stabilization of cDCD Heart Donors

There are many legal, ethical, and logistical challenges associated with cDCD. The donation process must follow the "dead-donor rule", which means that organ donation cannot take place until the patient is legally declared dead. For DCD donors, this occurs when the patient has suffered a circulatory arrest [EDQM, 2022]. As DCD hearts are susceptible to ischemic damage, it is crucial to be careful at every step of the donation process. For example, minimizing the time from circulatory arrest to the start of preservation is essential to reduce the warm ischemic time and, therefore, reduce the ischemic damage. However, this is commonly regulated by law, which gives little or no room for modification.

An option to prevent ischemic damage in DCD hearts is to start organ-preserving treatment, via for example "ante-mortem" interventions. These are interventions after WLST that facilitate the cDCD process. Justification of ante-mortem interventions can be made on ethical and legal grounds if the intervention is in the patient's best interest and is not harmful to the patient. The following three conditions must be met for organ-preserving treatment in Sweden [Socialstyrelsen, 2023a]:

- It cannot be postponed until after death.
- It does not cause more than minor pain or harm.
- It does not prevent efforts for the patient's own sake.

Organ-preserving treatment is in general the same treatment that most patients receive for life-saving purposes, but is given to preserve the function of the organs so that they can be transplanted. Primarily, it is about maintaining the oxygenation of the organs, but can also include blood pressure support and other medications [MOD, 2024]. These interventions might prevent or reverse ischemic damage to improve the quality of donated organs. Ante-mortem interventions are allowed to a different extent in countries practicing cDCD. For example, the use of heparin is only allowed in some countries [EDQM, 2022].

Precision dosing can be used to maintain normal physiological variables (such as blood pressure and heart rate) in the donor while making sure that the interventions are in the patient's best interest. Both accurate drug models and robust control systems can be useful in this setting. With accurate models, we can predict the drug effect and with a control system, we can rapidly change the dose to account for changes in the patient's condition, which will change after WLST. Together, they can be used to prevent ischemic damage and improve the quality of donated organs. The ethical, legal, and logistic challenges of these interventions are further discussed in Section 4.2. In Paper I, we study how the precise administration of drugs can prevent IMC in cDCD hearts.

2.4 Application: Control of Anesthesia

Adequate anesthesia is essential for patient safety during surgery, but reaching and maintaining the desired level of anesthesia is challenging due to the inter-patient variability in the drug response. Therefore, accurate drug modeling is crucial for each patient to find the appropriate dose. Furthermore, automatic control systems, such as TCI and closed-loop control systems, can assist the anesthesiologist and compensate for disturbances. This section presents the components of anesthesia (Section 2.4.1), the most popular PKPD models for propofol (Section 2.4.2), TCI in anesthesia (Section 2.4.3), and closed-loop control of anesthesia (Section 2.4.4).

2.4.1 Anesthesia

General anesthesia is the induction of a state with temporary memory, consciousness, and sensation loss. Anesthesia can be divided into three components, each associated with a specific class of drugs. The three components are:

- **Hypnosis**: The main component of anesthesia, where hypnotic drugs induce unconsciousness. Some examples of purely hypnotic drugs are propofol, etomidate, and midazolam.
- **Analgesia**: The component that manages pain. Commonly used analgesic drugs are opioids, such as remifentanil, fentanyl, and morphine.
- **Immobilization**: The component that induces muscle relaxation. Neuromuscular blockers such as rocuronium and atracurium reduce patient movement and breathing during surgery. Since neuromuscular blocking drugs can cause breathing difficulties, they are commonly used together with a mechanical ventilator.

The anesthetic state is a combination of the three states presented above. A measure of the hypnotic state, the depth of hypnosis (*DoH*), represents the unconsciousness of the patient and is related to drug concentration in the brain. *DoH* can be estimated from the electroencephalogram (EEG), for example using the Bispectral Index (BIS) monitor or the WAV_{CNS} monitor [Vuyk and Mertens, 2003; Bibian et al., 2011]. Wavelet analysis is performed on the EEG signal to create an estimate of the *DoH*, as detailed in [Sigl and Chamoun, 1994]. The BIS and WAV_{CNS} indices are unitless numbers between 100 and 0, where 100 represents the fully awake state, and 0 represents an isoelectric EEG (no activity). A reference span for hypnosis during surgery is a BIS value of $60-40$ [Vuyk and Mertens, 2003]. Figure 2.9 shows how values of the BIS/WAV_{CNS} indices correspond to the hypnotic level.

The depth of analgesia (*DoA*), i.e., the pain level, is more difficult to measure. The difficulty comes from that the perception of pain is subjective and there is no direct measure of pain. Several clinically available pain monitors claim to measure analgesia, and an overview of the available monitors is given in [Ledowski, 2019].

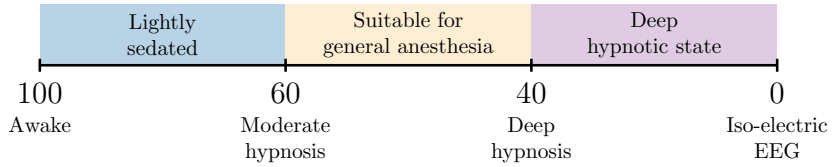

Figure 2.9 The BIS/WAV$_{\text{CNS}}$ index and the corresponding hypnotic level.

These monitors are based on different physiological signals, such as heart rate variability, skin conductance, and pupillary reflexes. However, the precision and reliability of these monitors are debated [Ledowski, 2019]. The most common method to determine the analgesic drug dose is to set it to a fixed ratio to the hypnotic drug dose [Schiavo et al., 2021]. There is also a strong synergistic effect between opioids and hypnotic drugs, which must be taken into account [Miller et al., 2009].

There are several available monitors for estimating neuromuscular blockade (NMB). A commonly used method is electromyography (EMG), which is used to estimate the muscle response to nerve stimulation. An extended overview of NMBs is provided in [Motamed, 2023].

General anesthesia is widely used during surgery, where the patient is in a state of unconsciousness and analgesia. If needed, muscle relaxation is also induced. Anesthesia can be divided into three main phases:

1. **Induction**: The phase in which the patient receives anesthetic drugs to induce anesthesia. The aim is to reach the desired level of anesthesia as quickly as possible without overdosing.

2. **Maintenance**: The phase in which the patient should remain at the desired level of anesthesia, commonly under continuous infusion of anesthetic drugs. During this phase, surgery is performed. These interventions can affect the level of consciousness and pain.

3. **Emergence**: The phase in which the patient awakens. Typically, this is the easiest phase to control, as the drug infusion is stopped and the patient will wake up.

A simulated example to illustrate the three phases of anesthesia is shown in Figure 2.10, illustrating an example of how the measured BIS signal can look during the three phases of anesthesia. During the induction phase, the *DoH* drops rapidly to the desired range. During the maintenance phase, the *DoH* is kept between a BIS value of 60 and 40, while during the emergence phase, the patient is returned to the awake state. The *DoH* estimate is commonly affected by noise, and several attempts have been made to identify the noise profile, for example, in [Pawlowski et al., 2022]. The noise profile of [Pawlowski et al., 2022] was used to create a realistic BIS signal in Figure 2.10.

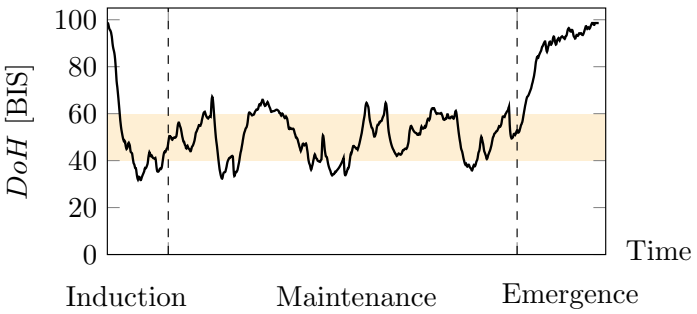

Figure 2.10 Simulated scenario of the BIS signal during the three phases of anesthesia: induction, maintenance, and emergence. The range for suitable *DoH* levels during maintenance is marked in orange. A noise profile, identified in [Pawlowski et al., 2022], was used to create a representative clinical scenario.

The main challenge of anesthesia is the inter-patient variability in the drug response. The drug infusion must be titrated (continuously measured and adjusted), as the patient's response to the drug is unknown beforehand. Overdosing can cause adverse effects such as hypotension and bradycardia, while underdosing can cause awareness during surgery. Nausea and vomiting were reported in 9.8 % of the anesthesia cases in 2009 [Miller et al., 2009], and vary between different types of surgery. In rare cases, even death can occur if the patient is overly sedated, but the risk is very low. Long-term effects of anesthesia are very rare.

This thesis focuses on the control of the hypnotic drug propofol. Propofol is widely used in surgery due to its rapid and smooth induction of anesthesia with a low risk of postoperative nausea and vomiting. Adverse effects of propofol are rare, where the most common are pain at the injection site, bradycardia (low heart rate), and hypotension (low blood pressure) [Sahinovic et al., 2018]. Propofol is administered intravenously and is commonly used for total intravenous anesthesia (TIVA). Propofol is commonly co-administered with the analgesic drug remifentanil, which is a fast-acting opioid [Sahinovic et al., 2018]. They have a synergistic effect, which means that both the dose of propofol and remifentanil can be reduced when they are administered together.

2.4.2 Pharmacological Models for Propofol

To deal with the inter-patient variability, population PKPD models are used to estimate drug concentration in the patient's body (see Section 2.1.3). In TCI and closed-loop control of anesthesia, population PKPD models are used in the underlying software to estimate drug concentrations and for control design.

For propofol, a three-compartment mammillary model, see Figure 2.1c, captures the main pharmacokinetic properties, as motivated by [Sahinovic et al., 2018]. The three-compartment PK model is commonly extended with an effect-site com-

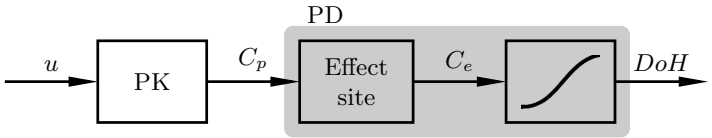

Figure 2.11 PKPD model for propofol from drug dose u to hypnotic depth DoH. The output from the PK model is the plasma concentration C_p, and the output from the effect-site compartment is the effect-site concentration C_e. The sigmoidal Emax model (Hill model) describes the relationship between C_e and DoH.

partment, modeling the delay it takes for the drug to travel from the blood plasma to the effect-site. Most propofol PD models use the sigmoidal Emax model (also called the Hill model) to characterize the relationship between effect-site concentration and clinical drug effect in the brain. The sigmoidal Emax model is detailed in Section 2.1.2. The full PKPD model from drug dose u to hypnotic depth DoH is shown in Figure 2.11.

Reduced-order models have been used for anesthesia control to deal with identifiability issues of the three- or four-compartment model [da Silva et al., 2014; Wahlquist et al., 2021a] An example of a reduced-order model is the first-order plus time delay (FOPTD) model, where the linear PKPD part is approximated by a first-order system, and the delay accounts for the time it takes for the drug to reach the effect site [Hahn et al., 2012]. The transfer function of the FOPTD model, from drug dose u to hypothetical effect-site concentration C_e, is given by

$$G_{u,C_e}(s) = \frac{k}{s+k} e^{-Ls}, \tag{2.12}$$

where k is the model parameter and L is the time delay. In [van Heusden et al., 2013], it was demonstrated that the performance of the FOPTD model was comparable to a more complex model for closed-loop anesthesia in a clinical study. In [da Silva et al., 2010], the authors suggested a fixed-pole model in which the poles of the linear PKPD model of Equation (2.3) and Equation (2.7) were fixed with a given ratio, also to deal with identifiability problems. The transfer function of the fixed-pole model from drug dose u to hypothetical effect-site concentration C_e is given by

$$G_{u,C_e}(s) = \frac{k_1 k_2 \alpha^3}{(s+\alpha)(s+k_1\alpha)(s+k_2\alpha)}, \tag{2.13}$$

where the three poles are given by α, $k_1\alpha$, and $k_2\alpha$, and where k_1 and k_2 are fixed constants. Note that both the FOPTD and the fixed-pole model have a static gain of one. The system gain is modeled by the parameters of the PD model. The fixed-pole model showed satisfactory performance in closed-loop control of anesthesia in simulation. However, the four-compartment linear PKPD model is still the most widely used compartmental model for propofol in clinical practice.

There are several published and clinically evaluated adult population PKPD models for propofol, where the most famous population PK models are the Marsh and Schnider models [Marsh et al., 1991; Schnider et al., 1998]. Both are used successfully and routinely in TCI systems [Masui et al., 2010; Coetzee, 2012]. The Marsh model has been used in the clinic for more than 30 years and is incorporated into the Diprifusor TCI system. Both models have also been used in closed-loop control of anesthesia, which is the topic of the next section Section 2.4.4. The Marsh and Schnider models for adults are detailed in the boxes below. The units of covariates age, weight, and height are years, kg, and cm, respectively. The Marsh model has, for easier comparison, been rewritten in terms of volumes and clearances rather than rate constants, which is how it was presented in the original publication [Marsh et al., 1991]. The Marsh model is a simple model with only weight (WGT) as a covariate, whereas the Schnider model is a more complex model with age (AGE), weight (WGT), height (HGT), and sex (men/women) as covariates. The Lean Body Mass (LBM) is calculated from weight and height and is used in the Schnider model. The LBM is calculated differently for men and women. In the Marsh and Schnider models, no random effects are included in the original formulation.

Marsh propofol PK model [Marsh et al., 1991]

$$
\begin{aligned}
V_1 &= 0.228 \cdot \mathrm{WGT}\ [\mathrm{L}] \\
V_2 &= 0.464 \cdot \mathrm{WGT}\ [\mathrm{L}] \\
V_3 &= 2.895 \cdot \mathrm{WGT}\ [\mathrm{L}] \\
CL &= 0.0271 \cdot \mathrm{WGT}\ [\mathrm{L\,min^{-1}}] \\
Q_2 &= 0.0255 \cdot \mathrm{WGT}\ [\mathrm{L\,min^{-1}}] \\
Q_3 &= 0.00955 \cdot \mathrm{WGT}\ [\mathrm{L\,min^{-1}}]
\end{aligned}
$$

Schnider propofol PK model [Schnider et al., 1998]

$$
\begin{aligned}
V_1 &= 4.27\ [\mathrm{L}] \\
V_2 &= 18.9 - 0.391\,(\mathrm{AGE} - 53)\ [\mathrm{L}] \\
V_3 &= 238\ [\mathrm{L}] \\
CL &= 1.89 + 0.0456\,(\mathrm{WGT} - 77) - 0.0681\,(\mathrm{LBM} - 59) + \\
&\quad 0.0264\,(\mathrm{HGT} - 177)\ [\mathrm{L\,min^{-1}}] \\
Q_2 &= 1.29 - 0.024\,(\mathrm{AGE} - 53)\ [\mathrm{L\,min^{-1}}] \\
Q_3 &= 0.836\ [\mathrm{L\,min^{-1}}]
\end{aligned}
$$

where

$$
\mathrm{LBM}_{\mathrm{men}} = 1.1 \cdot \mathrm{WGT} - 128 \cdot \left(\frac{\mathrm{WGT}}{\mathrm{HGT}}\right)^2
$$

$$
\mathrm{LBM}_{\mathrm{women}} = 1.07 \cdot \mathrm{WGT} - 148 \cdot \left(\frac{\mathrm{WGT}}{\mathrm{HGT}}\right)^2
$$

Deriving PKPD population models for children is challenging, since their size and body composition vary as they grow, making it difficult to identify an accurate model [Sahinovic et al., 2018]. Two examples of pediatric (children) population PK models for propofol that are available for TCI are the Paedfusor model and the Kataria model [Absalom et al., 2003; Kataria et al., 1994]. Also, modeling obese and elderly patients is challenging, as obese patients tend to be overdosed if the dose scales with weight, and elderly patients tend to have long delays in drug response [van Heusden et al., 2013; Eleveld et al., 2018].

A more recently published population PKPD model is the Eleveld model [Eleveld et al., 2018]. It is a complete model for children and adults (all ages, including obese and elderly), developed from a large data set with data from 30 previously published studies. Using a large data set allows for finding hidden relationships in the data, which is not possible with a smaller data set. The model has shown promising results in all patient groups. However, the Eleveld model is still under evaluation and is being compared with the more established models of Marsh and Schnider; see, for example, [Hosseinirad et al., 2023; Paolino et al., 2023b]. The Eleveld model differs from the traditional models as it is more complex, with complicated relationships between covariates and PKPD model parameters. It also includes more covariates than the Marsh and Schnider models, and these are: age, weight, height, sex, absence/presence of opiates, and site of blood sampling (arterial or venous). The Eleveld model is detailed in the box below.

Eleveld propofol PK model [Eleveld et al., 2018]

$$f_{\text{aging}}(x) = \exp\left(x(\text{AGE} - \text{AGE}_{\text{ref}})\right)$$

$$f_{\text{sigmoid}}(x, C_{e50}, \lambda) = \frac{x^{\lambda}}{x^{\lambda} + C_{e50}^{\lambda}}$$

$$f_{\text{central}}(x) = f_{\text{sigmoid}}(x, \theta_{12}, 1)$$

$$f_{\text{CLmat}} = f_{\text{sigmoid}}(\text{PMA}, \theta_8, \theta_9)$$

$$f_{\text{Q3mat}} = f_{\text{sigmoid}}(\text{AGE} + 40\text{weeks}, \theta_{14}, 1)$$

$$f_{\text{opi}}(x) = \begin{cases} 1, & \text{absence of opiates} \\ \exp\left(x \cdot \text{AGE}\right), & \text{presence of opiates} \end{cases}$$

$$f_{\text{Al-Sallami}} = \begin{cases} \left(0.88 + \frac{0.12}{1+(\text{AGE}/13.4)^{-12.7}}\right)\left(\frac{9270 \cdot \text{WGT}}{6680+216 \cdot \text{BMI}}\right), & \text{male} \\ \left(1.11 + \frac{-0.89}{1+(\text{AGE}/7.1)^{-1.1}}\right)\left(\frac{9270 \cdot \text{WGT}}{8780+244 \cdot \text{BMI}}\right), & \text{female} \end{cases}$$

$$V_{1,\text{arterial}}\ [\text{L}] = \theta_1 \frac{f_{\text{central}}(\text{WGT})}{f_{\text{central}}(\text{WGT}_{\text{ref}})} \cdot \exp\left(\eta_1\right)$$

$$V_{1,\text{venous}}\ [\text{L}] = V_{1,\text{arterial}}\left(1 + \theta_{17}(1 - f_{\text{central}}(\text{WGT}))\right)$$

$$V_2\ [\text{L}] = \theta_2 \frac{\text{WGT}}{\text{WGT}_{\text{ref}}} f_{\text{ageing}}(\theta_{10}) \cdot \exp\left(\eta_2\right)$$

$$V_3\ [\text{L}] = \theta_3 \frac{f_{\text{Al-Sallami}}}{f_{\text{Al-Sallami, ref}}} f_{\text{opi}}(\theta_{13}) \cdot \exp\left(\eta_3\right)$$

$$CL\ [\text{L/min}] = \left\{ \begin{matrix} \theta_4, & \text{male} \\ \theta_{15}, & \text{female} \end{matrix} \right\} \left(\frac{\text{WGT}}{\text{WGT}_{\text{ref}}}\right)^{0.75} \frac{f_{\text{CLmat}}}{f_{\text{CLmat, ref}}} f_{\text{opi}}(\theta_{11}) \cdot \exp\left(\eta_4\right)$$

$$Q_{2,\text{arterial}}\ [\text{L/min}] = \theta_5 \left(V_2/V_{2,\text{ref}}\right)^{0.75} \left(1 + \theta_{16}(1 - f_{\text{Q3mat}})\right) \cdot \exp\left(\eta_5\right)$$

$$Q_{2,\text{venous}}\ [\text{L/min}] = Q_{2,\text{arterial}} \cdot \theta_{18}$$

$$Q_3\ [\text{L/min}] = \theta_6 \left(V_3/V_{3,\text{ref}}\right)^{0.75} \frac{f_{\text{Q3mat}}}{f_{\text{Q3mat, ref}}} \cdot \exp\left(\eta_6\right)$$

For the Eleveld model, the θ-parameters as well as the η-parameters are available in the original publication [Eleveld et al., 2018] and were left out for readability.

The Marsh model does not incorporate an effect-site compartment in the original formulation. In the Diprifusor TCI system, the rate of the effect-site compartment k_{e0} is set to $k_{e0} = 0.26\ \text{min}^{-1}$, and this value varies between different TCI systems. The Schnider model uses $k_{e0} = 0.459\ \text{min}^{-1}$. The Eleveld model suggests a covariate-based PD model with random effects, which is not very common in pharmacometric models. It should be noted that there were only three individuals older

than 70 years in the PD data set in which the model was developed, which means that the PD model in [Eleveld et al., 2018] is not extensively validated for elderly patients. The Eleveld PD population model is detailed in the box below.

Eleveld PD model for propofol [Eleveld et al., 2018]

$$C_{e50}\ [\mu g L^{-1}] = \theta_{PD1} \cdot f_{\text{aging}}(\theta_{PD7}) \cdot \exp(\eta_{PD1})$$

$$k_{e0}\ [\text{min}^{-1}] = \left\{ \begin{matrix} \theta_{PD2}, & \text{arterial PK} \\ \theta_{PD8}, & \text{venous PK} \end{matrix} \right\} \cdot \left(\frac{\text{WGT}}{\text{WGT}_{\text{ref}}} \right)^{-0.25} \cdot \exp(\eta_{PD2})$$

$$\text{BIS}_{\text{baseline}} = \theta_{PD3}$$

$$\gamma = \begin{cases} \theta_{PD4}, & \text{for } C_e \leq C_{e50} \\ \theta_{PD9}, & \text{for } C_e > C_{e50} \end{cases}$$

$$\text{BIS} = \text{BIS}_{\text{baseline}} \frac{C_{e50}^{\gamma}}{C_{e50}^{\gamma} + C_e^{\gamma}} + \theta_{PD5} \cdot \varepsilon \cdot \exp(\eta_{PD3})$$

Note: ε denotes the residual observation error.

Common for these population PKPD models is that they tend to underestimate the plasma concentration of propofol [Sahinovic et al., 2018], leading to overdosing. They have, however, been shown to work well in practice.

2.4.3 TCI in Anesthesia

Automatic control of anesthesia has been introduced to improve patient safety, reduce the risk of over- and underdosing, and reduce the workload of the anesthesiologist. Using TCI in anesthesia simplifies the drug administration process compared to manual control and is today widely used for propofol. TCI has been successfully evaluated in several clinical studies, for example in [Mehta et al., 2008].

The TCI system implements one or several PKPD models, such as the Marsh model for adults and the Paedfusor model for children [Marsh et al., 1991; Absalom et al., 2003]. The anesthesiologist enters the patient's covariates, such as age, weight, and height, into the TCI system. Then, the anesthesiologist sets a reference effect-site concentration (in some cases a plasma concentration), and the TCI system calculates the infusion rate needed to reach and maintain the desired concentration. Studies have shown that anesthesiologists find it more intuitive to set a reference effect-site concentration rather than a desired *DoH*, as this is how inhaled anesthetics are administered [Struys et al., 2016]. If the anesthesiologist suspects a change in the patient's state, for example, due to surgical stimuli, the reference effect-site concentration can be adjusted to counteract the change. In addition, if the patient is not sufficiently, or too deeply, sedated, the target effect-site concentration can be adjusted to reach the desired *DoH*.

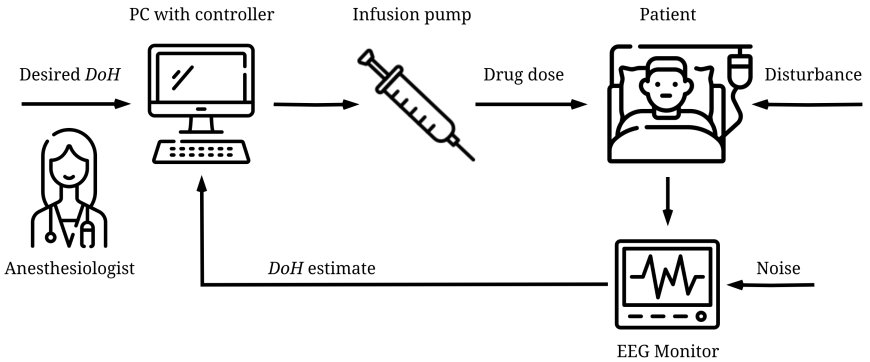

Figure 2.12 Closed-loop anesthesia. The anesthesiologist sets the desired anesthetic level, and the control system adjusts the drug dose to maintain the desired level. A monitor continuously measures the patient's hypnotic depth (*DoH*) and sends this information to the control system. Noise and disturbances affect the patient's response and the *DoH* estimate. Icons from `https://www.flaticon.com/free-icons/`

As mentioned in Section 2.2.2, TCI systems are heavily dependent on the precision of the underlying PKPD model. If model errors or disturbances are present, the TCI system cannot accurately predict the drug concentration in the body. This is illustrated in a simulation of TCI with propofol and the Schnider PK model in Figure 2.4. This discrepancy can lead to under- or overdosing, which can have severe consequences for the patient, as demonstrated in [Wahlquist et al., 2024]. Using a closed-loop control system can deal with these issues, as it can adjust the drug dose based on the patient's response, which is measured in real-time. This is discussed in the next section.

2.4.4 Closed-Loop Anesthesia

Closed-loop control of anesthesia has several advantages over TCI, as it can account for inter- and intra-patient variability and disturbances. Disturbances may affect the patient's hypnotic level. For example, surgical stimuli tend to increase the patient's awareness, which must be accounted for rapidly to avoid pain and awareness during surgery. This has motivated the introduction of closed-loop anesthesia to improve patient safety. It can also reduce the workload of the anesthesiologist, which can be heavy during long surgeries. Several studies have shown that closed-loop anesthesia also reduces the drug usage, see for example [Luginbuhl et al., 2003].

The concept of closed-loop anesthesia was introduced in the 1950s by [Bickford, 1950] and has been researched since. Clinical use of closed-loop anesthesia is largely limited to clinical trials. An example of an automatic control system for anesthesia is shown in Figure 2.12. The anesthesiologist sets a desired level of anesthesia, typically a *DoH* value of 50. In the induction phase, the goal is to reach the target value as quickly as possible without overshooting. During the maintenance

phase, the goal is to maintain stable hypnosis and to reject disturbances, originating, for example, from surgical stimuli. The patient's EEG is continuously measured and an estimated *DoH* is computed from the BIS or WAV_{CNS} monitor. This estimate is then used in the controller to compute a suitable dose to be delivered by the TIVA system with an infusion pump. The anesthesiologist supervises the control system and can switch to manual control if necessary.

Several closed-loop control strategies have been evaluated in simulation and clinical studies. Model-free and model-based control strategies have been proposed, the most common being PID control and model predictive control (MPC), respectively [van Heusden et al., 2014; Schiavo et al., 2021; Pawlowski et al., 2023; Paolino et al., 2023a]. Model-based control strategies rely on the PKPD model to predict drug concentration in the body and are therefore sensitive to model errors. Model-free control strategies only use the PKPD models for controller design and are often easier to implement. Therefore, model-free control strategies are more robust to model errors, which are almost always present in practice. However, model-based control strategies usually allow for constraint handling in the control design, which is useful for limiting over- and undershoots. In control design for anesthesia, the goal is to design a controller that can handle disturbances and model errors and works for a wide range of patients. Figure 2.13 shows an example of where a PID controller successfully rejects a disturbance during the maintenance phase. Typically, a set of performance measures are used to evaluate controller performance. Some examples of these are: time in the target range, time to reach the target range, and the overshoot from the reference value [Varvel et al., 1992].

Although closed-loop control has the potential to improve anesthesia care, several challenges need to be addressed. Poor electrode placement and electric interference can affect measurements and introduce measurement noise [Chan et al., 2012]. Incorporating the inter- and intra-patient variability in the control design is challenging but necessary for robust performance. This also assumes that the PKPD model is accurate, which is not always the case. This may lead to conservative control strategies to ensure patient safety. This would not be optimal, as it would lead to slow response times and poor performance. Another challenge is that complex control systems can be difficult for the anesthesiologist to understand, which is important for clinical acceptance. Therefore, the control system must be intuitive and easy to use and understand for the anesthesiologist. Although the controller is automatic, the anesthesiologist is responsible for patient safety and must be able to take over the control if needed. A more detailed overview of trends and challenges in closed-loop anesthesia control is provided in [Ghita et al., 2020].

In conclusion, automatic control of anesthesia has the potential to improve patient safety and reduce the workload of the anesthesiologist. Before these systems can be routinely implemented in clinical practice, the challenges of patient variability, disturbances, and measurement noise must be addressed. For successful implementation, the controller must be robust, easy to understand, and integrated into the existing clinical workflow.

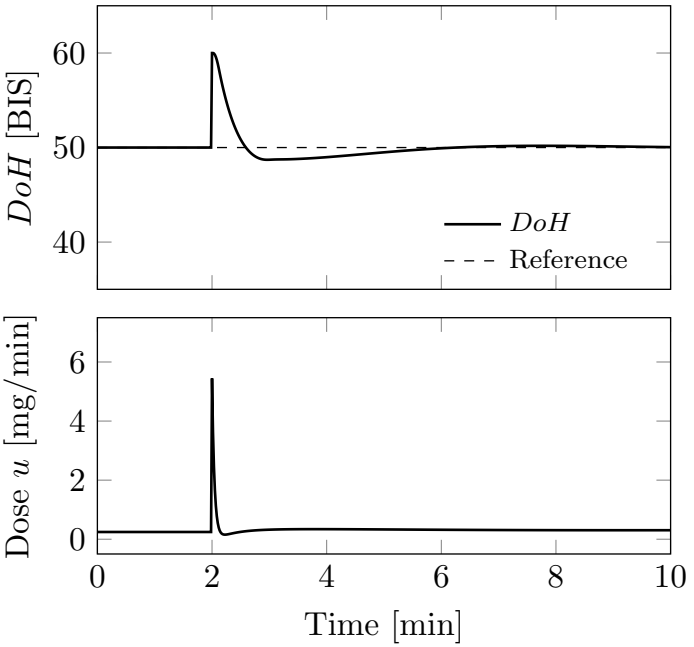

Figure 2.13 Example of disturbance rejection with a PID controller in closed-loop anesthesia. The disturbance is a positive step change of size 10 in the patient's *DoH* level and is introduced at $t = 2$ min.

3

Contribution

This chapter presents the main contribution of the thesis, which consists of six papers addressing the research questions outlined in Section 1.1. These papers and the author's contribution to each paper are summarized in Section 3.1. The key findings of the papers are then summarized in Section 3.2. The CRediT Contributor Roles Taxonomy is used to describe the author's contributions (in black in tables in Section 3.1) and the taxonomy is described in Section 3.3. The author has also contributed to several other peer-reviewed publications, which are listed in Section 3.4. These were omitted in the thesis to improve the coherence of the thesis and maintain focus on the main research questions.

3.1 Included Papers

Paper I

> Y. Wahlquist, K. Soltesz, Q. Liao, X. Liu, H. Pigot, T. Sjöberg, and S. Steen (2021b). "Prevention of ischemic myocardial contracture through hemodynamically controlled DCD". *Cardiovascular Engineering and Technology*. DOI: 10.1007/s13239-021-00537-8

Scientific Summary In Paper I, we developed an automatic control system to maintain normal blood pressure and heart rate in controlled donation after circulatory death (cDCD) donors. In a preclinical porcine study, the control system was able to maintain stable hemodynamics after withdrawal of life-sustaining treatment (WLST). None of the six individuals in the test group developed ischemic myocardial contracture (IMC) within 1 hour after WLST, compared to all six in the control group. This shows that the onset of IMC can be delayed up to 1 hour and potentially improve donor heart quality for transplantation, allowing more hearts to be available for transplantation. The study also highlights the potential for automatic control systems to facilitate controlled DCD in a calm and dignified manner.

During this work, we realized that the controller performance was limited by the quality of the drug model on which the controller was tuned. Therefore, for the following works, we decided to further investigate how these models are derived in the first place and how they can be improved to achieve better controller performance.

Writing - original draft	Writing - review & editing	Conceptualization
Data curation	Formal analysis	Investigation
Methodology	Resources	Software
Supervision	Validation	Visualization

Paper II

Y. Wahlquist, F. Bagge Carlson, and K. Soltesz (2023a). "Fast simulation of pharmacokinetics". *IFAC Proceedings Volumes (IFAC-PapersOnline) Presented at 22nd IFAC World Congress* **56**:2, pp. 2995–3000. DOI: 10.1016/j.ifacol.2023.10.1425

Scientific Summary In Paper II, we developed a fast simulator for pharmacokinetic (PK) compartmental models to handle irregular sampling times for infusion rates and drug concentration measurements. Existing simulators were not fast enough to be used in the machine learning methods that were developed, in which the PK model needs to be simulated millions of times. The simulator was successfully demonstrated on a three-compartment mammillary model and applied to a large dataset for propofol of more than 1000 simulated concentration curves. The simulator is available as an open-source package and can be used for fast simulation of low-order pharmacokinetic models in machine learning applications, see [Wahlquist, 2022].

Writing - original draft	Writing - review & editing	Conceptualization
Data curation	Formal analysis	Investigation
Methodology	Resources	Software
Supervision	Validation	Visualization

Paper III

Y. Wahlquist, J. Sundell, and K. Soltesz (2023b). "Learning pharmacometric covariate model structures with symbolic regression networks". *Journal of Pharmacokinetics and Pharmacodynamics*. DOI: 10.1007/s10928-023-09887-3

Scientific Summary In Paper III, we proposed a new method for developing covariate models that relate covariates, such as age or weight, to PKPD model parameters using a special neural network, called a symbolic regression network. For fast simulations of the PK model, we utilized the simulator developed in Paper II. The proposed methodology is a data-driven approach that can identify readable and interpretable covariate models, which are both crucial for clinical applicability. With this methodology, we can efficiently identify simple covariate relationships while exploring a large model search space and maintaining high predictive performance. Compared to traditional modeling methods, this method also allows automatic search for covariate relationships, which can significantly speed up the modeling process. The method's feasibility was demonstrated on a large data set of 1031 individuals for the anesthetic drug propofol. The resulting covariate model has comparable performance and accuracy to the current state-of-the-art model while being lower in complexity.

Writing - original draft	Writing - review & editing	Conceptualization
Data curation	Formal analysis	Investigation
Methodology	Resources	Software
Supervision	Validation	Visualization

Paper IV

Y. Wahlquist and K. Soltesz (2024). "Automated covariate modeling using efficient simulation of pharmacokinetics". *IFAC Journal of Systems and Control* **27**, p. 100252. DOI: 10.1016/j.ifacsc.2024.100252

Scientific Summary In Paper IV, we replaced the symbolic regression network from Paper III with a regular neural network to investigate if a more flexible function approximator could improve the predictive performance compared to a symbolic regression network. The results showed only a small improvement, suggesting that symbolic regression networks are able to capture the covariate relationships efficiently. Furthermore, the study revealed that it might not be the covariate model structure itself that limits performance, but rather the structure of the compartmental model and the quality of training data.

Writing - original draft	Writing - review & editing	Conceptualization
Data curation	Formal analysis	Investigation
Methodology	Resources	Software
Supervision	Validation	Visualization

Paper V

Y. Wahlquist, N. Paolino, M. Schiavo, A. Visioli, and K. Soltesz (2025). "Kalman filter soft sensor to handle signal quality loss in closed-loop controlled anesthesia". *Biomedical Signal Processing and Control*. DOI: 10.1016/j.bspc.2025.107506

Scientific Summary In Paper V, we used a Kalman filter to smoothly transition between open- and closed-loop control, based on measurement signal quality. If the signal quality is good, the system runs in closed loop based on the measurement, and if the signal quality is poor, the system runs in open loop. In addition, combinations of open- and closed-loop control are possible if signal quality is in between perfect and poor. This enables robust control of closed-loop anesthesia where, if both measurement and model predictions are poor, a combination of them provides a more reliable estimate of the patient's state. This is particularly useful in situations when disturbances and measurement noise are present. We demonstrated the method's effectiveness in a realistic simulated example with a PID controller on a representative data set of adults. The results showed that the proposed method significantly improved the controller performance compared to using only measurements (closed-loop) or model predictions (open-loop).

Writing - original draft	Writing - review & editing	Conceptualization
Data curation	Formal analysis	Investigation
Methodology	Resources	Software
Supervision	Validation	Visualization

Paper VI

Y. Wahlquist and K. Soltesz (2025). "Seamless integration of target-controlled infusion and closed-loop anesthesia". *Accepted to American Control Conference 2025*

Scientific Summary In Paper VI, we continued the work of combining open- and closed-loop control for robust anesthesia, focusing on how different types of disturbances and noise affect control performance. We introduced a method to seamlessly move between target-controlled infusion (TCI) and model predictive control (MPC) based on the measurement signal quality. The results showed that moving between TCI and MPC can effectively reduce the impact of disturbances and noise, which is particularly useful in surgery when surgical disturbances and electrical inference are present.

Writing - original draft	Writing - review & editing	Conceptualization
Data curation	Formal analysis	Investigation
Methodology	Resources	Software
Supervision	Validation	Visualization

3.2 Summary of Key Findings

The research aims of this thesis were presented in the introduction (Section 1.1) and the overarching aim was: to improve the modeling and control of pharmacological systems, with a particular focus on addressing patient variability and precision dosing. To connect the research to the aims, we summarize the key findings of the papers in this thesis in the following list:

- **Paper I**: We used precise drug control to stabilize blood pressure in DCD heart donors, which significantly delayed the onset of ischemic myocardial contracture (IMC), thus improving organ quality for transplantation.
- **Paper II**: We introduced a fast simulator for low-order compartmental pharmacokinetic models, called "FastPKSim.jl", to speed up model evaluation, which is crucial in machine learning applications. The simulator was used in Papers III and IV.
- **Paper III**: We introduced a machine learning method to identify simple and readable covariate models from clinical data, enabling faster and broader evaluation of model candidates.
- **Paper IV**: We compared neural networks to simpler covariate models for drug concentration prediction. The neural networks predicted marginally better than the simple, readable covariate model developed in Paper III, indicating that data quality and compartmental model structure probably limit predictive performance.
- **Paper V**: We proposed a method to move seamlessly between open- and closed-loop anesthesia depending on the quality of the measurement signal. This enabled a more robust control system, improving patient safety during surgical procedures.
- **Paper VI**: Building on the control system in Paper V, we further studied how disturbances and measurement noise affected the control system and how their effects could be minimized.

To further demonstrate how the papers are related to each other and the topics of modeling and control, a schematic overview of this is presented in Figure 3.1. The illustration shows how a method or result from one paper followed to the next, for example, how the simulator developed in Paper II was used in Papers III and IV.

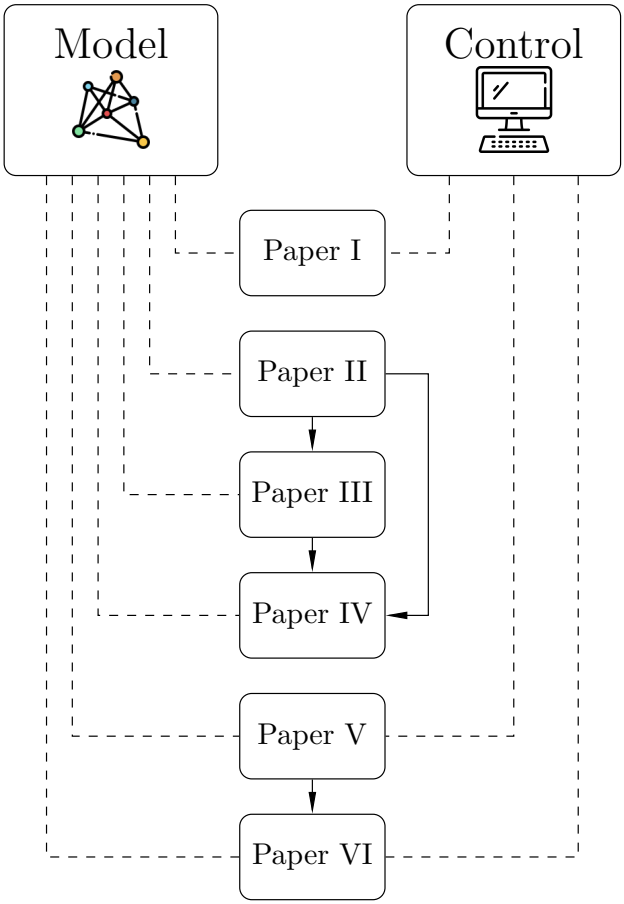

Figure 3.1 Connection of the papers to the topics of modeling and control (dashed) and to each other (arrows, solid). An arrow from Paper A to Paper B indicates that a method or result from Paper A was used in Paper B.

3.3 CRediT Contributor Roles Taxonomy

In Table 3.1, the CRediT Contributor Roles Taxonomy is described, taken from [NISO, 2024]. The CRediT taxonomy was introduced as a standardized system to clarify contributor roles in research and academic publications. The author's contributions to the included papers were categorized according to this taxonomy in Section 3.1.

Table 3.1 CRediT Contributor Roles Taxonomy

Role	Definition
Writing - original draft	Preparation, creation, and/or presentation of the published-work, specifically writing the initial draft (including substansive translation).
Writing - review - & editing	Preparation, creation, and/or presentation of the published work by those from the original research group, specifically critical review, commentary, or revision – including pre- or post-publication stages.
Conceptualization	Ideas; formulation or evolution of overarching research goals and aims.
Data curation	Management activities to annotate (produce metadata), scrub data, and maintain research data (including software code, where it is necessary for interpreting the data itself) for initial use and later re-use.
Formal analysis	Application of statistical, mathematical, computational, or other formal techniques to analyze or synthesize study data.
Investigation	Conducting a research and investigation process, specifically performing the experiments, or data/evidence collection.
Methodology	Development or design of methodology; creation of models.
Resources	Provision of study materials, reagents, materials, patients, laboratory samples, animals, instrumentation, computing resources, or other analysis tools.
Software	Programming, software development; designing computer programs; implementation of the computer code and supporting algorithms; testing of existing code components.
Supervision	Oversight and leadership responsibility for the research activity planning and execution, including mentorship external to the core team.
Validation	Verification, whether as a part of the activity or separate, of the overall replication/reproducibility of results/experiments and other research outputs.
Visualization	Preparation, creation and/ or presentation of the published work, specifically visualization/data presentation.

3.4 Additional Publications

The author of this thesis has also co-authored the following peer-reviewed publications.

J. Sundell, Y. Wahlquist, and K. Soltesz (2024). "Symbolic neural networks for automated covariate modeling in a mixed-effects framework". *IFAC-PapersOnLine* **58**:24. 12th IFAC Symposium on Biological and Medical Systems (BMS 2024), pp. 472–477. DOI: https://doi.org/10.1016/j.ifacol.2024.11.083

Y. Wahlquist, A. Gustafson, and K. Soltesz (2024). "Exploring the influence of patient variability on propofol target-controlled infusion performance". In: *2024 European Control Conference (ECC)*, pp. 3027–3032. DOI: 10.23919/ECC64448.2024.10590791

A. R. Ynineb, H. Farbakhsh, G. B. Othman, Y. Wahlquist, I. R. Birs, E. Yumuk, C. I. Muresan, D. K. R., D. Copot, C. M. Ionescu, and M. Neckebroek (2024). "Comparative analysis of pharmacokinetic-pharmacodynamic models for propofol and remifentanil using model predictive control". In: *2024 European Control Conference (ECC)*, pp. 3045–3050. DOI: 10.23919/ECC64448.2024.10590766

H. Pigot, Y. Wahlquist, and K. Soltesz (2023). "Actively controlled cardiac afterload". *IFAC-PapersOnLine* **56**:2, pp. 6484–6489. DOI: 10.1016/j.ifacol.2023.10.863

Y. Wahlquist, M. Morin, and K. Soltesz (2022). "Pharmacometric covariate modeling using symbolic regression networks". In: *2022 IEEE Conference on Control Technology and Applications (CCTA)*, pp. 1099–1104. DOI: 10.1109/CCTA49430.2022.9966112

Y. Wahlquist, A. Gojak, and K. Soltesz (2021a). "Identifiability of pharmacological models for online individualization". *IFAC-PapersOnLine* **54**:15, pp. 25–30. DOI: 10.1016/j.ifacol.2021.10.226

Y. Wahlquist, K. van Heusden, G. A. Dumont, and K. Soltesz (2020). "Individualized closed-loop anesthesia through patient model partitioning". *42nd Annual International Conference of the IEEE Engineering in Medicine and Biology Society (EMBC'20)*. DOI: 10.1109/EMBC44109.2020.9176452

4

Discussion

The work presented in this thesis contributes to the ongoing research of modeling and control of pharmacological systems. Two applications are addressed: optimizing organ quality in controlled DCD and improving control systems for anesthesia. With a combination of modeling, control technology, clinical data, and machine learning, this research advances both methodology and practical aspects of these fields.

The discussion covers the implications and significance for the field in Section 4.1, ethical considerations in Section 4.2 and possible future research directions are outlined in Section 4.3. Finally, the conclusions of the thesis are presented in Section 4.4.

4.1 Implications and Relevance to the Field

The work in this thesis has several implications for the field of pharmacological control systems and personalized medicine. The main focus of this thesis was to investigate how we can reduce the effects of inter- and intra-patient variability. This variability is a major challenge from several different points of view, for example, economically, logistically, and ethically. Giving the same dose to all patients may, for example, result in under- or overdosing, which can have severe consequences and, in the long run, lead to increased costs and workload for the healthcare system. Therefore, finding a way to adapt the treatment to each individual is important. This thesis has shown that there are several ways to deal with these challenges.

In controlled DCD, we have shown that by stabilizing the donor's hemodynamics with measurement feedback, the onset of IMC can be delayed. There are several benefits of this. First, stabilizing the donor's hemodynamics is beneficial not only for the heart but also for the donor, as normal blood pressure reduces the stress on the other organs at the end stage of life. Second, the quality of the heart is improved, which can expand the donor pool. This results in more organs available for transplantation and shorter waiting times for patients on the waiting list. Third, extending the time window for transplantation makes the transplantation process less

time-critical. This allows longer transports of the organ and reduces the logistical challenge related to heart transplantation. Fourth, using feedback control in controlled DCD allows for drug delivery to be performed in the background of the final moments of the donor's life. Sometimes, the family is present during the WLST process and automatic control running in the background can reduce the need for repeated manual interventions in front of the family. This allows the family to focus on saying goodbye rather than worrying about interruptions from medical personnel. This can help to provide a more calm and dignified process for all involved. However, transplantation and hemodynamic stabilization of DCD donors are not yet implemented in Sweden. Although current legislation does not allow for this, it is important to investigate the possibilities and implications of this technology for future use.

For anesthesia (or other drug dosing applications), more accurate dosing (with or without a controller) is safer for the patient. It reduces the risk of under- or overdosing, where the risk of pain or waking up during surgery is reduced and the recovery time is shortened. In the long run, this can reduce the costs of the healthcare system, as less resources are needed for the patient's recovery, as well as the reduced risk of complications. This is particularly important for elderly and obese patients, who can be difficult to sedate due to the longer time from drug infusion to clinical effect.

Feedback systems can reduce the workload of the anesthesiologist, which can be beneficial in long surgeries. The drug dose must be continuously adjusted during surgery, and with a control system, the anesthesiologist can focus on other tasks, such as monitoring breathing or other changes in the patient's physical state. However, the anesthesiologist is still responsible for patient safety and can intervene if necessary.

Using data-driven methods allows for automatic model development and processing of large datasets. This allows for finding better and more precise models and the possibility of identifying new physiological relationships. Data-driven methods have a large potential in healthcare and there are rapid developments in this field, every day new methods are entering the clinic.

4.2 Ethical Considerations

Ethics in pharmacology and control systems is of great importance, as this directly impacts patient safety. In the works enclosed in this thesis, we have used a combination of clinical data, animal models, and simulations to try to reach the research aims posed in the introduction. The clinical data used in the works are anonymized, and consent is declared in the original publications.

For the animal models used, pigs were chosen because of their similarity to humans in terms of anatomy and physiology (Paper I). Replacement of animal models with simulation models is generally not an alternative in the context of heart trans-

plantation, since there are no realistic simulation models for human hearts available. Therefore, using animal models is more ethically defensible than using human models in this context. The 3R methodology (Replace-Reduce-Refine) [Jordbruksverket, 2024] has been taken into consideration. Simulation studies have been used when possible to replace animal experiments. For example, the developed controllers were first evaluated in simulation before being tested in animal experiments. The number of animals used in the animal study was kept to a minimum, and in several cases, the same animals were also used for other research studies involving other organs. The animals received the best possible care to minimize discomfort and pain and received appropriate anesthesia, ensuring their well-being throughout the study. All personnel were trained in handling laboratory animals. Institutional and national guidelines were followed for the care and use of laboratory animals. The animals were treated according to the EU directive [European Parliament, 2010]. The large-animal study in Paper I was carried out with ethics permission M174-15, issued by "Malmö/Lunds Djurförsöksetiska Nämnd" (local REB).

In the DCD context, there are several ethical considerations to take into account. If the goal was to optimize the organ outcome, blood pressure should be lowered as quickly as possible. However, this is not ethical from the donor's point of view. Interventions must be made with the donor's best interest in mind and must not harm the donor. In the work of Paper I, we consider hemodynamic stabilization of the heart donor, which is beneficial for the donor, as well as for the donated heart. This motivates well-selected "ante-mortem" interventions in the DCD process, which can improve both the end-stage care of the donor and the quality of the donated organ, as explained in Section 2.3.3.

For closed-loop control of anesthesia, the anesthesiologist is always responsible for the patient's safety. They should be able to intervene if possible and have a basic understanding of how the control system works. Therefore, the control system must be transparent and understandable to clinical personnel, and preferably also intuitive. The control system should be seen as an aid, not a replacement, for the anesthesiologist. If the control system is adequately designed, it can be safer for the patient than manual dosing. An automated drug delivery system also reduces the likelihood of errors as they are more consistent and precise than a human. For example, in stressful and critical situations, human performance may be affected.

4.3 Future Work

The works presented in this thesis open up several future research directions. This section outlines future work that can build on the findings of this thesis.

Future research could further investigate how to develop robust control systems that work for all individuals, including children, the elderly, and obese patients. The control system should not be too conservative, as a slow control system will not be able to rapidly counteract changes in the patient's state. A slow controller

also has low clinical applicability, as "time is money" in the healthcare system. However, designing a robust controller is impossible if the patient models are not accurate. The population models that are used for controller synthesis today are mainly developed for other purposes, such as for drug development, and might not be suitable for control. Therefore, patient models that describe the variability in the population should be developed specifically for control design.

Another important aspect is that the control system should be understandable and transparent to the clinical personnel, as they are responsible for the patient's safety. The clinicians are unlikely to adopt a complex control system. Therefore, future research should focus on developing interpretable and understandable controllers. Interpretability is also highly relevant for model development with data-driven methods, which are commonly black-box models such as intricate neural networks. In Paper III, we demonstrated an example of how machine learning can be used to develop simple and interpretable models. This methodology should be further developed and tested on other datasets and models, to investigate its potential in other applications. In addition, more research should be done on how to include prior knowledge in model development, such as physiological relationships.

A few clinical trials are ongoing with automated control systems in anesthesia around the world. However, these systems have been suggested for decades and have not yet been implemented routinely in the clinic. This is likely due to ethical and safety concerns and the uncertainty about the reliability of the control system. Future research should focus on how to overcome these challenges and make this technology more accessible for clinical use.

In recent years, controlled DCD for heart transplantation has gained attention globally. Due to the promising results of already practicing countries, more countries are likely to implement this soon. However, ischemic damage will continue to be a challenge, and more research is needed to understand how ischemic myocardial contracture arises and how it can be prevented. This would open up more hearts available for transplantation.

Automatic control of blood pressure and heart rate can improve patient safety in many different areas, not only in DCD. For example, in the intensive care unit, where the patient's state is continuously changing, automatic control of blood pressure and heart rate can be useful. Future research should investigate how feedback systems can be used to control blood pressure and heart rate in these settings.

To summarize, the research presented in this thesis opens up several future research directions. The presented works demonstrate that patient safety can be improved with individualized and automated drug dosing, as long as certain challenges are addressed.

4.4 Conclusions

Every individual reacts differently to a drug, making it challenging to determine the right dose for each patient. In this thesis, we have explored how accurate models and robust control strategies can tackle the challenge of patient variability in the drug response. With a focus on two applications, controlled DCD and anesthesia, we have demonstrated that individualized and automated drug dosing improves patient safety through accurate dosing.

Using machine learning methods, we have developed a method to identify simple and interpretable models from data that capture patient variability well. The methodology presented here does not only automate and streamline the modeling process but also allows for exploring a wider range of model candidates. This approach can be applied to other drugs to find new covariate relationships.

In controlled DCD, we showed that precise drug dosing can delay the onset of ischemic myocardial contracture and therefore improve the quality of the heart for transplantation. This can potentially expand the donor pool and reduce the waiting time for patients on the waiting list. For anesthesia, we showed that combining model predictions with measurement feedback can improve controller performance in the presence of disturbances and measurement noise. This leads to safer anesthesia and reduces the risk of under- or overdosing.

In conclusion, the works in this thesis contribute to individualized drug dosing through accurate modeling and robust control systems. Future research should continue the development of these, ensuring that they are reliable, understandable, and applicable across a wide population. Specifically, collaboration between clinicians and engineers is crucial to reach a broader clinical use. The findings in this thesis are a step towards safer and more efficient healthcare.

Bibliography

Absalom, A., D. Amutike, A. Lal, M. White, and G. N. C. Kenny (2003). "Accuracy of the 'Paedfusor' in children undergoing cardiac surgery or catheterization". *British Journal of Anaesthesia* **91**:4, pp. 507–513. DOI: 10.1093/bja/aeg220.

Beijers, A. J. R., A. N. Roos, and A. J. G. H. Bindels (2014). "Fully automated closed-loop ventilation is safe and effective in post-cardiac surgery patients". *Intensive Care Medicine* **40**:5, pp. 752–753. DOI: 10.1007/s00134-014-3234-7.

Bezanson, J., A. Edelman, S. Karpinski, and V. B. Shah (2017). "Julia: A fresh approach to numerical computing". *SIAM Review* **59**:1, pp. 65–98. DOI: 10.1137/141000671.

Bibian, S., G. A. Dumont, M. Huzmezan, and C. R. Ries (2006). "Patient variability and uncertainty quantification in anesthesia: Part I – PKPD modeling and identification". *IFAC Proceedings Volumes*. 6th IFAC Symposium on Modeling and Control in Biomedical Systems **39**:18, pp. 549–554. DOI: 10.3182/20060920-3-FR-2912.00097.

Bibian, S., G. A. Dumont, and T. Zikov (2011). "Dynamic behavior of BIS, M-entropy and neuroSENSE brain function monitors". *Journal of Clinical Monitoring and Computing* **25**:1, pp. 81–87. DOI: 10.1007/s10877-010-9266-9.

Bickford, R. G. (1950). "Automatic electroencephalographic control of general anesthesia". *Electroencephalography and Clinical Neurophysiology* **2**:1, pp. 93–96. DOI: 10.1016/0013-4694(50)90014-9.

Brier, M. E., J. M. Zurada, and G. R. Aronoff (1995). "Neural network predicted peak and trough gentamicin concentrations". *Pharmaceutical Research* **12**:3, pp. 406–412. DOI: 10.1023/a:1016260720218.

Brown Sue A., Kovatchev Boris P., Raghinaru Dan, Lum John W., Buckingham Bruce A., Kudva Yogish C., Laffel Lori M., Levy Carol J., Pinsker Jordan E., Wadwa R. Paul, Dassau Eyal, Doyle Francis J., Anderson Stacey M., Church Mei Mei, Dadlani Vikash, Ekhlaspour Laya, Forlenza Gregory P., Isganaitis Elvira, Lam David W., Kollman Craig, and Beck Roy W. (2019). "Six-

month randomized, multicenter trial of closed-loop control in type 1 diabetes". *New England Journal of Medicine* **381**:18, pp. 1707–1717. DOI: 10.1056/NEJMoa1907863.

Chan, M., S. S. Ho, and T. Gin (2012). "Performance of the bispectral index during electrocautery". *J Neurosurg Anesthesiol* **24(1)**, pp. 9–13. DOI: 10.1097/ANA.0b013e31823058bf.

Chow, H.-H., K. M. Tolle, D. J. Roe, V. Elsberry, and H. Chen (1997). "Application of neural networks to population pharmacokinetic data analysis".

Coetzee, J. F. (2012). "Allometric or lean body mass scaling of propofol pharmacokinetics: towards simplifying parameter sets for target-controlled infusions". *Clinical Pharmacokinetics* **51**:3, pp. 137–145. DOI: 10.2165/11596980-000000000-00000.

Cooley, A., J. Reul, and C. Wukasch (1972a). "Ischemic contracture of the heart: "stone heart"." *Am J Cardiol* **29**, pp. 575–577.

Cooley, D. A., G. J. Reul, and D. C. Wukasch (1972b). "Ischemic contracture of the heart: "stone heart"". *The American Journal of Cardiology*. Symposium on Electrophysiologic Correlates of Clinical Arrhythmias **29**:4, pp. 575–577. DOI: 10.1016/0002-9149(72)90454-7.

Curry, S. and R. Whelpton (2017). *Introduction to Drug Disposition and Pharmacokinetics*. ISBN: 978-1-119-26104-9.

da Silva, M. M., J. M. Lemos, A. Coito, B. A. Costa, T. Wigren, and T. Mendonça (2014). "Local identifiability and sensitivity analysis of neuromuscular blockade and depth of hypnosis models". *Computer Methods and Programs in Biomedicine* **113**:1, pp. 23–36. DOI: 10.1016/j.cmpb.2013.07.020.

da Silva, M. M., T. Mendonça, and T. Wigren (2010). "Online nonlinear identification of the effect of drugs in anaesthesia using a minimal parameterization and BIS measurements". In: *Proceedings of the 2010 American Control Conference*, pp. 4379–4384. DOI: 10.1109/ACC.2010.5530791.

Domínguez-Gil, B. (2021). "International figures on donation and transplantation 2021". *Newsletter Transplant*.

Dumont, G. A., A. Martinez, and J. M. Ansermino (2009). "Robust control of depth of anesthesia". *International Journal of Adaptive Control and Signal Processing* **23**:5, pp. 435–454. DOI: 10.1002/acs.1087.

EDQM (2022). *Guide to the quality and safety of organs for transplantation, 8th Edition*. European Directorate for the Quality of Medicines & HealthCare, Council of Europe. ISBN: 978-92-871-9240-0.

Eleveld, D. J., P. Colin, A. R. Absalom, and M. M. R. F. Struys (2018). "Pharmacokinetic-pharmacodynamic model for propofol for broad application in anaesthesia and sedation". *British Journal of Anaesthesia* **120**:5, pp. 942–959. ISSN: 0007-0912, 1471-6771. DOI: 10.1016/j.bja.2018.01.018.

European Parliament (2010). *On the protection of animals used for scientific purpose*. Tech. rep. Directive 2010/63/EU. Council of Europe.

Ghita, M., M. Neckebroek, C. Muresan, and D. Copot (2020). "Closed-loop control of anesthesia: survey on actual trends, challenges and perspectives". *IEEE Access* **8**, pp. 206264–206279. DOI: 10.1109/ACCESS.2020.3037725.

Greer, D. M., S. D. Shemie, A. Lewis, S. Torrance, P. Varelas, F. D. Goldenberg, J. L. Bernat, M. Souter, M. A. Topcuoglu, A. W. Alexandrov, M. Baldisseri, T. Bleck, G. Citerio, R. Dawson, A. Hoppe, S. Jacobe, A. Manara, T. A. Nakagawa, T. M. Pope, W. Silvester, D. Thomson, H. Al Rahma, R. Badenes, A. J. Baker, V. Cerny, C. Chang, T. R. Chang, E. Gnedovskaya, M.-K. Han, S. Honeybul, E. Jimenez, Y. Kuroda, G. Liu, U. K. Mallick, V. Marquevich, J. Mejia-Mantilla, M. Piradov, S. Quayyum, G. S. Shrestha, Y.-y. Su, S. D. Timmons, J. Teitelbaum, W. Videtta, K. Zirpe, and G. Sung (2020). "Determination of brain death/death by neurologic criteria: the world brain death project". *JAMA* **324**:11, pp. 1078–1097. DOI: 10.1001/jama.2020.11586.

Hahn, J.-O., G. A. Dumont, and J. M. Ansermino (2012). "A direct dynamic dose-response model of propofol for individualized anesthesia care". *IEEE Transactions on Biomedical Engineering* **59**:2, pp. 571–578. DOI: 10.1109/TBME.2011.2177497.

Hearse, D. J., P. B. Garlick, and S. M. Humphrey (1977). "Ischemic contracture of the myocardium: mechanisms and prevention". *The American Journal of Cardiology* **39**:7, pp. 986–993. DOI: 10.1016/S0002-9149(77)80212-9.

Hosseinirad, S., K. van Heusden, and G. A. Dumont (2023). "Evaluating inter-individual variability captured by the Eleveld pharmacokinetics model". *Journal of Clinical Monitoring and Computing*. DOI: 10.1007/s10877-023-01083-5.

Hovorka, R., V. Canonico, L. J. Chassin, U. Haueter, M. Massi-Benedetti, M. O. Federici, T. R. Pieber, H. C. Schaller, L. Schaupp, T. Vering, and M. E. Wilinska (2004). "Nonlinear model predictive control of glucose concentration in subjects with type 1 diabetes". *Physiological Measurement* **25**:4, p. 905. DOI: 10.1088/0967-3334/25/4/010.

Janssen, A., F. C. Bennis, and R. A. A. Mathôt (2022a). "Adoption of machine learning in pharmacometrics: an overview of recent implementations and their considerations". *Pharmaceutics* **14**:9, p. 1814. DOI: 10.3390/pharmaceutics14091814.

Janssen, A., M. Hoogendoorn, M. H. Cnossen, and R. A. A. Mathôt (2022b). "Application of SHAP values for inferring the optimal functional form of covariates in pharmacokinetic modeling". *CPT: Pharmacometrics & Systems Pharmacology* **11**:8, pp. 1100–1110. DOI: 10.1002/psp4.12828.

Janssen, A., F. W. G. Leebeek, M. H. Cnossen, and R. A. A. Mathôt (2022c). "Deep compartment models: a deep learning approach for the reliable prediction of time-series data in pharmacokinetic modeling". *CPT: Pharmacometrics & Systems Pharmacology* **11**:7, pp. 934–945. DOI: 10.1002/psp4.12808.

Jawitz, O. K., B. S. Bryner, J. N. Schroder, and A. D. DeVore (2022). "Donation after circulatory death heart transplantation in the United States: An early report of donor characteristics". *JTCVS Techniques* **12**, pp. 104–107. DOI: 10.1016/j.xjtc.2021.12.014.

Jones, H. and K. Rowland-Yeo (2013). "Basic concepts in physiologically based pharmacokinetic modeling in drug discovery and development". *CPT: Pharmacometrics & Systems Pharmacology* **2**:8, p. 63. DOI: https://doi.org/10.1038/psp.2013.41.

Jordbruksverket (2024). *Det här är 3R*. https://jordbruksverket.se/djur/ovriga-djur/forsoksdjur-och-djurforsok/sveriges-3r-center/det-har-ar-3r. Accessed: 2024-08-16.

Kataria, B. K., S. A. Ved, H. F. Nicodemus, G. R. Hoy, D. Lea, M. Y. Dubois, J. W. Mandema, and S. L. Shafer (1994). "The pharmacokinetics of propofol in children using three different data analysis approaches". *Anesthesiology* **80**:1, pp. 104–122. DOI: 10.1097/00000542-199401000-00018.

Ledowski, T. (2019). "Objective monitoring of nociception: a review of current commercial solutions". *British Journal of Anaesthesia* **123**:2, e312–e321. DOI: 10.1016/j.bja.2019.03.024.

Leiden, H., B. Haase-Kromwijk, A. Hoitsma, and N. Jansen (2016). "Controlled donation after circulatory death in the Netherlands: more organs, more efforts". *The Netherlands Journal of Medicine* **74**:7.

Li, M., Z. Qin, E. Steen, A. Terry, B. Wang, B. Wohlfart, S. Steen, and A. Arner (2023). "Development and prevention of ischemic contracture ("stone heart") in the pig heart". *Frontiers in Cardiovascular Medicine* **10**. DOI: 10.3389/fcvm.2023.1105257.

Liu, R., X. Li, W. Zhang, and H.-H. Zhou (2015). "Comparison of nine statistical model based warfarin pharmacogenetic dosing algorithms using the racially diverse international warfarin pharmacogenetic consortium cohort database". *PLOS ONE* **10**:8, e0135784. DOI: 10.1371/journal.pone.0135784.

Lomero, M., D. Gardiner, E. Coll, B. Haase-Kromwijk, F. Procaccio, F. Immer, L. Gabbasova, C. Antoine, J. Jushinskis, N. Lynch, S. Foss, C. Bolotinha, T. Ashkenazi, L. Colenbie, A. Zuckermann, M. Adamec, J. Czerwinski, S. Karciauskaite, H. Ström, M. Lopez-Fraga, B. Dominguez-Gil, and the European Committee on Organ Transplantation of the Council of Europe (CD-P-TO) (2020). "Donation after circulatory death today: an updated overview of the european landscape". *Transplant International* **33**:1, pp. 76–88. DOI: https://doi.org/10.1111/tri.13506.

Luginbuhl, M., S. Wuthrich, S. Petersen-Felix, A. M. Zbinden, and T. W. Schnider (2003). "Different benefit of bispectal index (BIS) in desflurane and propofol anesthesia". *Acta Anaesthesiologica Scandinavica* **47**:2, pp. 165–173. DOI: 10.1034/j.1399-6576.2003.00041.x.

Marsh, B., M. White, N. Morton, and G. Kenny (1991). "Pharmacokinetic model driven infusion of propofol in children". *British Journal of Anaesthesia* **67**:1, pp. 41–48. DOI: 10.1093/bja/67.1.41.

Masui, K., R. Upton, A. Doufas, J. Coetzee, T. Kazama, E. Mortier, and M. Struys (2009). "The performance of compartmental and physiologically based recirculatory pharmacokinetic models for propofol: a comparison using bolus, continuous, and target-controlled infusion data". *Anesthesia and analgesia* **111**, pp. 368–79. DOI: 10.1213/ANE.0b013e3181bdcf5b.

Masui, K., R. N. Upton, A. G. Doufas, J. F. Coetzee, T. Kazama, E. P. Mortier, and M. M. R. F. Struys (2010). "The performance of compartmental and physiologically based recirculatory pharmacokinetic models for propofol: a comparison using bolus, continuous, and target-controlled infusion data". *Anesthesia and Analgesia* **111**:2, pp. 368–379. DOI: 10.1213/ANE.0b013e3181bdcf5b.

MathWorks (2023). *Matlab version: 23.2.0 (r2023b)*. Natick, Massachusetts, United States. URL: https://www.mathworks.com.

Mehta, D., J. McCormack, P. Fung, G. Dumont, and J. M. Ansermino (2008). "Target controlled infusion for kids: trials and simulations". In: *2008 30th Annual International Conference of the IEEE Engineering in Medicine and Biology Society*. Vancouver, BC, pp. 5818–5821. ISBN: 978-1-4244-1814-5. DOI: 10.1109/IEMBS.2008.4650537.

Messer, S., R. Axell, S. Colah, P. White, M. Ryan, A. Page, B. Parizkova, K. Valchanov, C. White, D. Freed, E. Ashley, J. Dunning, M. Goddard, J. Parameshwar, C. Watson, T. Krieg, A. Ali, S. Tsui, and S. Large (2016). "Functional assessment and transplantation of the donor heart after circulatory death." *J Heart Lung Transpl* **35**, pp. 1443–1452. DOI: 10.1016/j.healun.2016.07.004.

Miller, R., L. Eriksson, L. Fleisher, J. Wiener-Kronish, and W. Young (2009). *Miller's Anesthesia*. Elsevier Health Sciences. ISBN: 9781437720617.

MOD (2024). *Statistik och rapporter*. Accessed: 2024-10-29. URL: https://merorgandonation.se/statistik-och-rapporter.

Motamed, C. (2023). "Intraoperative monitoring of neuromuscular blockade". *Life* **13**:5, p. 1184. DOI: 10.3390/life13051184.

Mould, D. and R. Upton (2012). "Basic concepts in population modeling, simulation, and model-based drug development". *CPT: Pharmacometrics & Systems Pharmacology* **1**:9, pp. 1–14. DOI: 10.1038/psp.2012.4.

NHS Blood and Transplant (2019). *Annual report on the potential donor audit 2018-2019*. NHS Blood and Transplant. URL: https://nhsbtdbe.blob.core.windows.net/umbraco-assets-corp/16878/annual-pda-report-2018-19.pdf.

NISO (2024). *Contributor Role Taxonomy (CRediT)*. URL: credit.niso.org/ (visited on 2024-10-25).

Paolino, N., M. Schiavo, N. Latronico, F. Padula, M. Paltenghi, and A. Visioli (2023a). "On the use of FOPID controllers for maintenance phase of general anesthesia". *Applied Sciences* **13**:13, p. 7381. DOI: 10.3390/app13137381.

Paolino, N., M. Schiavo, N. Latronico, M. Paltenghi, and A. Visioli (2023b). "On the use of the Eleveld PK/PD model for the design of PID control of anesthesia". *IFAC-PapersOnLine*. 22nd IFAC World Congress **56**:2, pp. 3015–3020. DOI: 10.1016/j.ifacol.2023.10.1428.

Pawlowski, A., M. Schiavo, N. Latronico, M. Paltenghi, and A. Visioli (2022). "MPC for propofol anesthesia: the noise issue". In: *2022 IEEE Conference on Control Technology and Applications (CCTA)*, pp. 1087–1092. DOI: 10.1109/CCTA49430.2022.9966102.

Pawlowski, A., M. Schiavo, N. Latronico, M. Paltenghi, and A. Visioli (2023). "Event-based MPC for propofol administration in anesthesia". *Computer Methods and Programs in Biomedicine* **229**, p. 107289. DOI: 10.1016/j.cmpb.2022.107289.

Pigot, H., Y. Wahlquist, and K. Soltesz (2023). "Actively controlled cardiac afterload". *IFAC-PapersOnLine* **56**:2, pp. 6484–6489. DOI: 10.1016/j.ifacol.2023.10.863.

Rackauckas, C., Y. Ma, A. Noack, V. Dixit, P. K. Mogensen, S. Byrne, S. Maddhashiya, J. B. S. Calderón, J. Nyberg, J. V. Gobburu, and V. Ivaturi (2020). "Accelerated predictive healthcare analytics with Pumas, a high performance pharmaceutical modeling and simulation platform". *bioRxiv*. DOI: 10.1101/2020.11.28.402297. eprint: https://www.biorxiv.org/content/early/2020/11/30/2020.11.28.402297.full.pdf.

Rossetti, A. O., M. Oddo, G. Logroscino, and P. W. Kaplan (2010). "Prognostication after cardiac arrest and hypothermia: A prospective study". *Annals of Neurology* **67**:3, pp. 301–307. DOI: 10.1002/ana.21984.

Russell, D., M. P. Wilkes, S. C. Hunter, J. B. Glen, P. Hutton, and G. N. Kenny (1995). "Manual compared with target-controlled infusion of propofol". *British Journal of Anaesthesia* **75**:5, pp. 562–566. DOI: 10.1093/bja/75.5.562.

Sahinovic, M. M., M. M. R. F. Struys, and A. R. Absalom (2018). "Clinical pharmacokinetics and pharmacodynamics of propofol". *Clinical Pharmacokinetics* **57**:12, pp. 1539–1558. DOI: 10.1007/s40262-018-0672-3.

Scandiatransplant (2023). *Scandiatransplant Annual report 2023*. Annual data reports. Scandiatransplant office.

Schäublin, J., M. Derighetti, P. Feigenwinter, S. Petersen-Felix, and A. M. Zbinden (1996). "Fuzzy logic control of mechanical ventilation during anaesthesia". *British Journal of Anaesthesia* **77**:5, pp. 636–641. DOI: 10.1093/bja/77.5.636.

Schiavo, M., F. Padula, N. Latronico, L. Merigo, M. Paltenghi, and A. Visioli (2021). "Performance evaluation of an optimized PID controller for propofol and remifentanil coadministration in general anesthesia". *IFAC Journal of Systems and Control* **15**, p. 100121. DOI: 10.1016/j.ifacsc.2020.100121.

Schnider, T. W., C. F. Minto, P. L. Gambus, C. Andresen, D. B. Goodale, S. L. Shafer, and E. J. Youngs (1998). "The influence of method of administration and covariates on the pharmacokinetics of propofol in adult volunteers". *Anesthesiology* **88**:5, pp. 1170–1182. DOI: 10.1097/00000542-199805000-00006.

Servin, F. S. (1998). "TCI compared with manually controlled infusion of propofol: a multicentre study". *Anaesthesia* **53 Suppl 1**, pp. 82–86. DOI: 10.1111/j.1365-2044.1998.53s107.x.

Shafer, S. L. and K. M. Gregg (1992). "Algorithms to rapidly achieve and maintain stable drug concentrations at the site of drug effect with a computer-controlled infusion pump". *Journal of Pharmacokinetics and Biopharmaceutics* **20**:2, pp. 147–169. DOI: 10.1007/BF01070999.

Sheiner, L. B. and S. L. Beal (1980). "Evaluation of methods for estimating population pharmacokinetics parameters. I. Michaelis-Menten model: routine clinical pharmacokinetic data". *Journal of Pharmacokinetics and Biopharmaceutics* **8**:6, pp. 553–571. DOI: 10.1007/BF01060053.

Sheiner, L. B., B. Rosenberg, and K. L. Melmon (1972). "Modelling of individual pharmacokinetics for computer-aided drug dosage". *Computers and Biomedical Research* **5**:5, pp. 441–459. DOI: 10.1016/0010-4809(72)90051-1.

Sheiner, L. B., D. R. Stanski, S. Vozeh, R. D. Miller, and J. Ham (1979). "Simultaneous modeling of pharmacokinetics and pharmacodynamics: Application to d-tubocurarine". *Clinical Pharmacology & Therapeutics* **25**:3, pp. 358–371. DOI: 10.1002/cpt1979253358.

Sibieude, E., A. Khandelwal, P. Girard, J. S. Hesthaven, and N. Terranova (2022). "Population pharmacokinetic model selection assisted by machine learning". *Journal of Pharmacokinetics and Pharmacodynamics* **49**:2, pp. 257–270. DOI: 10.1007/s10928-021-09793-6.

Sibieude, E., A. Khandelwal, J. S. Hesthaven, P. Girard, and N. Terranova (2021). "Fast screening of covariates in population models empowered by machine learning". *Journal of Pharmacokinetics and Pharmacodynamics* **48**:4, pp. 597–609. DOI: 10.1007/s10928-021-09757-w.

Sigl, J. C. and N. G. Chamoun (1994). "An introduction to bispectral analysis for the electroencephalogram". *Journal of Clinical Monitoring* **10**:6, pp. 392–404. DOI: 10.1007/BF01618421.

Smith, M., B. Dominguez-Gil, D. M. Greer, A. R. Manara, and M. J. Souter (2019). "Organ donation after circulatory death: current status and future potential". *Intensive Care Medicine* **45**:3, pp. 310–321. DOI: 10.1007/s00134-019-05533-0.

Socialstyrelsen (2023a). *Donationsprocessen*. Date: 2023-10-01. URL: https://www.socialstyrelsen.se/kunskapsstod-och-regler/omraden/organ-och-vavnadsdonation/donationsprocessen/.

Socialstyrelsen (2023b). "Organdonation och transplantation i Sverige 2022". 2023-6-8576.

Soltesz, K., K. van Heusden, G. A. Dumont, T. Hägglund, C. L. Petersen, N. West, and J. M. Ansermino (2012). "Closed-loop anesthesia in children using a PID controller: a pilot study". *IFAC Proceedings Volumes*. 2nd IFAC Conference on Advances in PID Control **45**:3, pp. 317–322. DOI: 10.3182/20120328-3-IT-3014.00054.

Spataru, A., P. Eiben, and A. Pluddemann (2024). "Performance of closed-loop systems for intravenous drug administration: a systematic review and meta-analysis of randomised controlled trials". *Journal of Clinical Monitoring and Computing* **38**:1, pp. 5–18. DOI: 10.1007/s10877-023-01069-3.

Stanski, D. R. and P. O. Maitre (1990). "Population pharmacokinetics and pharmacodynamics of thiopental: the effect of age revisited". *Anesthesiology* **72**:3, pp. 412–422. DOI: 10.1097/00000542-199003000-00003.

Struys, M. M. R. F., T. De Smet, J. B. Glen, H. E. M. Vereecke, A. R. Absalom, and T. W. Schnider (2016). "The history of target-controlled infusion". *Anesthesia & Analgesia* **122**:1, pp. 56–69. DOI: 10.1213/ANE.0000000000001008.

Sundell, J., Y. Wahlquist, and K. Soltesz (2024). "Symbolic neural networks for automated covariate modeling in a mixed-effects framework". *IFAC-PapersOnLine* **58**:24. 12th IFAC Symposium on Biological and Medical Systems (BMS 2024), pp. 472–477. DOI: https://doi.org/10.1016/j.ifacol.2024.11.083.

van Heusden, K., J. M. Ansermino, K. Soltesz, S. Khosravi, N. West, and G. A. Dumont (2013). "Quantification of the variability in response to propofol administration in children". *IEEE Transactions on Biomedical Engineering* **60**:9, pp. 2521–2529. DOI: 10.1109/TBME.2013.2259592.

van Heusden, K., G. A. Dumont, K. Soltesz, C. L. Petersen, A. Umedaly, N. West, and J. M. Ansermino (2014). "Design and clinical evaluation of robust PID control of propofol anesthesia in children". *IEEE Transactions on Control Systems Technology* **22**:2, pp. 491–501. DOI: 10.1109/TCST.2013.2260543.

van Poucke, G., L. Bravo, and S. Shafer (2004). "Target controlled infusions: targeting the effect site while limiting peak plasma concentration". *IEEE Transactions on Biomedical Engineering* **51**:11, pp. 1869–1875. DOI: 10.1109/TBME.2004.827935.

Varvel, J. R., D. L. Donoho, and S. L. Shafer (1992). "Measuring the predictive performance of computer-controlled infusion pumps". *J Pharmacokinet Biopharm* **20**:1, pp. 63–94. DOI: 10.1007/BF01143186.

Vävnadsrådet (2022). *Protokoll för donation efter cirkulationsstillestånd, DCD. Version 2.0*.

Vuyk, J. and M. Mertens (2003). "Bispectral index scale (BIS) monitoring and intravenous anaesthesia". *Advances in Experimental Medicine and Biology* **523**, pp. 95–104. DOI: 10.1007/978-1-4419-9192-8_9.

Wahlquist, Y. (2022). *FastPKSim.jl*. commit: cd4a493. URL: https://github.com/wahlquisty/FastPKSim.jl (visited on 2024-10-09).

Wahlquist, Y., F. Bagge Carlson, and K. Soltesz (2023a). "Fast simulation of pharmacokinetics". *IFAC Proceedings Volumes (IFAC-PapersOnline) Presented at 22nd IFAC World Congress* **56**:2, pp. 2995–3000. DOI: 10.1016/j.ifacol.2023.10.1425.

Wahlquist, Y., A. Gojak, and K. Soltesz (2021a). "Identifiability of pharmacological models for online individualization". *IFAC-PapersOnLine* **54**:15, pp. 25–30. DOI: 10.1016/j.ifacol.2021.10.226.

Wahlquist, Y., A. Gustafson, and K. Soltesz (2024). "Exploring the influence of patient variability on propofol target-controlled infusion performance". In: *2024 European Control Conference (ECC)*, pp. 3027–3032. DOI: 10.23919/ECC64448.2024.10590791.

Wahlquist, Y., K. van Heusden, G. A. Dumont, and K. Soltesz (2020). "Individualized closed-loop anesthesia through patient model partitioning". *42nd Annual International Conference of the IEEE Engineering in Medicine and Biology Society (EMBC'20)*. DOI: 10.1109/EMBC44109.2020.9176452.

Wahlquist, Y., M. Morin, and K. Soltesz (2022). "Pharmacometric covariate modeling using symbolic regression networks". In: *2022 IEEE Conference on Control Technology and Applications (CCTA)*, pp. 1099–1104. DOI: 10.1109/CCTA49430.2022.9966112.

Wahlquist, Y., N. Paolino, M. Schiavo, A. Visioli, and K. Soltesz (2025). "Kalman filter soft sensor to handle signal quality loss in closed-loop controlled anesthesia". *Biomedical Signal Processing and Control*. DOI: 10.1016/j.bspc.2025.107506.

Wahlquist, Y. and K. Soltesz (2024). "Automated covariate modeling using efficient simulation of pharmacokinetics". *IFAC Journal of Systems and Control* **27**, p. 100252. DOI: 10.1016/j.ifacsc.2024.100252.

Wahlquist, Y. and K. Soltesz (2025). "Seamless integration of target-controlled infusion and closed-loop anesthesia". *Accepted to American Control Conference 2025*.

Wahlquist, Y., K. Soltesz, Q. Liao, X. Liu, H. Pigot, T. Sjöberg, and S. Steen (2021b). "Prevention of ischemic myocardial contracture through hemodynamically controlled DCD". *Cardiovascular Engineering and Technology*. DOI: 10.1007/s13239-021-00537-8.

Wahlquist, Y., J. Sundell, and K. Soltesz (2023b). "Learning pharmacometric covariate model structures with symbolic regression networks". *Journal of Pharmacokinetics and Pharmacodynamics*. DOI: 10.1007/s10928-023-09887-3.

Ynineb, A. R., H. Farbakhsh, G. B. Othman, Y. Wahlquist, I. R. Birs, E. Yumuk, C. I. Muresan, D. K. R., D. Copot, C. M. Ionescu, and M. Neckebroek (2024). "Comparative analysis of pharmacokinetic-pharmacodynamic models for propofol and remifentanil using model predictive control". In: *2024 European Control Conference (ECC)*, pp. 3045–3050. DOI: 10.23919/ECC64448.2024.10590766.

Zumbro, G. L., L. Tillman, A. O. Bailey, and R. L. Treasure (1978). "A comparison between propranolol and hypothermia in preventing ischemic contracture of the left ventricle (stone heart)". *The Annals of Thoracic Surgery* **25**:6, pp. 541–550. DOI: 10.1016/S0003-4975(10)63606-5.

Paper I

Prevention of Ischemic Myocardial Contracture Through Hemodynamically Controlled DCD

Ylva Wahlquist Kristian Soltesz Qiuming Liao Xiaofei Liu
Henry Pigot Trygve Sjöberg Stig Steen

Abstract

Purpose– Ischemic myocardial contracture (IMC) or "stone heart" is a condition with rapid onset following circulatory death. It inhibits transplantability of hearts donated upon circulatory death (DCD). We investigate the effectiveness of hemodynamic normalization upon withdrawal of life-sustaining therapy (WLST) in a large-animal controlled DCD model, with the hypothesis that reduction in cardiac work delays the onset of IMC.

Methods– A large-animal study was conducted comprising of a control group ($n = 6$) receiving no therapy upon WLST, and a test group ($n = 6$) subjected to a protocol for fully automated computer-controlled hemodynamic drug administration. Onset of IMC within 1 h following circulatory death defined the primary end-point. Cardiac work estimates based on pressure-volume loop concepts were developed and used to provide insight into the effectiveness of the proposed computer-controlled therapy.

Results– No test group individual developed IMC within 1 h, whereas all control group individuals did ($4/6$ within 30 min).

Conclusion– Automatic dosing of hemodynamic drugs in the controlled DCD context has the potential to prevent onset of IMC up to 1 h, enabling ethical and medically safe organ procurement. This has the potential to increase the use of DCD heart transplantation, which has been widely recognized as a means of meeting the growing demand for donor hearts.

Keywords– DCD, Organ preservation, Ischemic damage, Hemodynamic control, Closed-loop drug administration

Originally published in Cardiovascular Engineering and Technology (2021). The original version is available at `https://doi.org/10.1007/s13239-021-00537-8`.

(a) Heart without ischemic myocardial contracture.

(b) Heart with ischemic myocardial contracture.

Figure 1. Transverse sections of two hearts from 35 kg pigs. Heart (a) was procured 1 h after circulatory death, from one of the test group animals; (b) was procured 30 min after circulatory death, from one of the control group animals. Notice that the left-ventricular lumen is almost gone in the contracted heart. Both photos are in the same scale, indicated in (b).

1. Introduction

1.1 Ischemic Myocardial Contracture

Ischemic myocardial contracture (IMC), commonly referred to as *stone heart*, develops when the myocardium is exerting mechanical work under warm ischemic conditions [Cooley et al., 1972; Hearse et al., 1977]. The contracture commences at the apex of the heart, and subsequently extends throughout the left heart, before also affecting the right heart. Figure 1 shows cross sections of (a) one heart without, and (b) one with IMC. The contracture prevents the affected myocardium from performing mechanical work.

During the early era of open-heart surgery using cardiopulmonary bypass, IMC was identified as a rare, but fatal condition [Cooley et al., 1972]. Since it is associated with a loss of perfusion of the affected myocardium, the condition can typically not be reversed, as it prevents transport of required pharmacological substances to the affected site. Several works [Zumbro et al., 1978; Garcia-Dorado et al., 1997]

have investigated preventive measures. Administration of β-blockers, calcium antagonists and regional hypothermia, have all been shown to significantly reduce the risk of IMC [Cooley et al., 1972; Hearse et al., 1977].

The advent of modern cardioplegia and general methodology development within cardiopulmonary bypass surgery have resulted in fewer instances of IMC. Consequently, the research interest in prevention of ischemic myocardial contracture has also decreased over the last three decades.

1.2 Controlled Donation Upon Circulatory Death (DCD)

The inability to meet the demand of transplantable solid organs through donation upon brain death (DBD) from heart-beating brain-dead donors, has led to the reintroduction of donation upon circulatory death (DCD) in several legislations [Manara et al., 2012; Morrissey and Monaco, 2013]. Ischemic damage, resulting in graft failure, is the main medical concern associated with DCD transplantation [Messer et al., 2016; Dhital et al., 2020]. Procurement of DCD hearts is therefore performed under tight temporal constraints, and with maximal effort spent to prevent ischemic myocardial damage [Dhital et al., 2020; MacDonald and Dhital, 2019]. This has limited its clinical application to Maastricht category III donors [Koostra et al., 1995]. This category constitutes in-hospital patients, where a decision to end life-sustaining ventilator support is based on the best interest of the patient.

As opposed to the determination of brain death, there exist no universally accepted criteria for the determination of circulatory death. Instead, its definition relies on the concepts of cessation and irreversibility of cardiopulmonary function [European Parliament, 2010]. This has resulted in substantial DCD protocol variations between centra [Manara et al., 2012].

The course of events following withdrawal of life-sustaining therapy (WLST), that all clinical protocols have to relate to, is illustrated in Figure 2. The time between WLST and death is referred to as the agonal phase. The possibility of (short-term) survival [Suntharalingam et al., 2009], illustrated by the right cycle in Figure 2 imposes legal and ethical restrictions on admissible treatments during, and leading up to, the agonal phase. Particularly, ante-mortem interventions should be motivated by the best interest of the patient and must not interfere with the possibility of (short-term) survival.

Measures for organ optimization mainly translate into reducing warm ischemic time. For heart organs, a distinction is made between warm ischemia in asystole and functional warm ischemia [Manara et al., 2012], where the greater metabolic needs of the latter make it more problematic in the DCD context.

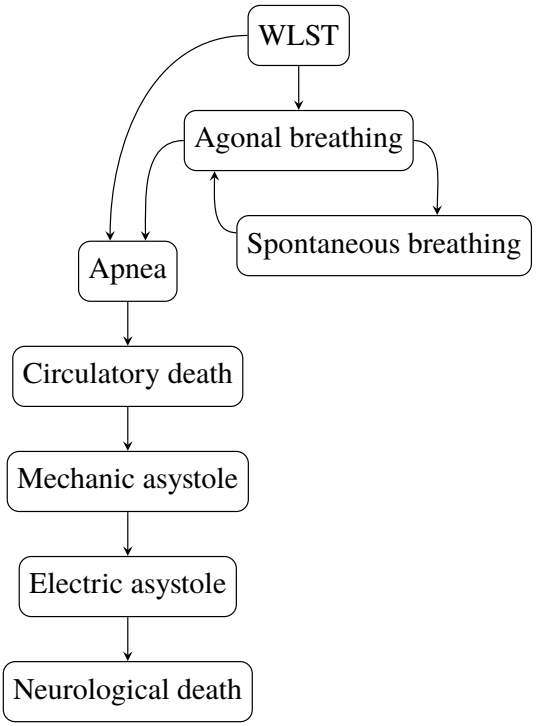

Figure 2. The course of events following withdrawal of life-sustaining therapy (WLST). Contemporary protocols prevent DCD donation where prolonged episodes (hours to days) are spent in the right cycle. However, such cases are rare, with circulatory death occurring within 2 h in over 70 % of cases [Suntharalingam et al., 2009]

1.3 Hemodynamic Control in DCD

The onset of the agonal phase is typically associated with a cathecolamine "storm", resulting in increased systemic resistance, and leading up to relative hypertension, possible tachycardia, and thus an increase in myocardial metabolism [Novitzky et al., 2006]. Control of hemodynamic parameters is a potentially viable means of postponing the onset of IMC, and warm ischemic damage in general. Hemodynamic parameters available for pharmacological control include:

- vascular resistance (through arterial and venous tone);
- heart rate;
- myocardial contractility.

Cardiac output and tissue perfusion are directly dependent on the above three parameters. In this study we control these parameters with the goal of facilitating cardiac output after WLST, while limiting the associated cardiac work to

avoid episodes of relative hypertension, tachycardia, and ischemia-induced ventricular fibrillation (VF). In this nominal work, we investigate whether the proposed methodology can serve to postpone the onset of ischemic myocardial contracture in a DCD large animal model.

Treatment associated with WLST needs to be delivered with dignity. To meet this need and the critical timing requirements imposed by the scenario, we have developed and demonstrated a fully automated feedback control system, in which a computer administers the delivery of intravenous drugs. The system adjusts the individual dosage of drugs in real-time based on the patient's hemodynamic response, thus avoiding over- or under-dosing.

2. Methods

2.1 Cardiac Work Estimation

The hypothesis underlying the study is that the time between WLST and incidence of IMC is correlated with the ischemic work of the heart following WLST. To investigate this hypothesis, one under-estimating approximation

$$\underline{W} \propto \int_0^T P_{sys}(t) HR(t) \mathrm{d}t \tag{1}$$

and one over-estimating approximation

$$\bar{W} \propto \int_0^T P_{sys}^2(t) HR(t) \mathrm{d}t \tag{2}$$

of cardiac work were used where $t = 0$ and $t = T$ denote the instances of WLST, and asystole or VF instance, respectively. P_{sys} is the instantaneous systolic aortic pressure and HR is the instantaneous heart rate, defined at the instances of systolic peaks as $1/\Delta t$, where Δt is the time passed since the preceding systolic peak. See Supplementary Section A for further details.

2.2 Hemodynamic Control

We have developed and evaluated a feedback control system based on a computer-controlled infusion pump array; real-time invasive arterial pressure acquisition system; and a PC running software for measurement, control, actuation, logging, and associated graphical user interface. The base hardware has been described in previous works [Soltesz et al., 2018; Soltesz et al., 2017b].

The overall objective of the control system was to normalize vascular resistance between the instance of WLST and the incidence of circulatory collapse, defined in Section 2.3, in order to facilitate cardiac output while limiting the amount of associated cardiac work. Individualized administration of the drugs is necessary to safely account for the variation in hemodynamic response between individuals after

WLST. This motivates computer-controlled real-time adjustment of the timing and number of doses administered according to systolic aortic pressure measurements as opposed to using a fixed bolus protocol. From prior research [Soltesz et al., 2018], we have established the feasibility of normalizing systolic pressure using closed-loop computer control of noradrenaline and nitroglycerine. Nitroglycerine dosing was used as the control signal to decrease vascular resistance. Both bolus and continuous infusion dosing were considered in pilot experiments. It was concluded that bolus dosing was necessary to achieve sufficiently fast responses in P_{sys}. Based on pilot experiments described in Supplementary Section E, the bolus size was set to 1.5 mg.

Pilot experiments indicated tachycardia and tolerance effects when exceeding three nitroglycerine boluses following WLST. If these were not sufficient to establish normotension, subsequent boluses of a synergistic calcium antagonist (nimodipine) and β-blocker (esmolol) mixture, comprising of nimodipine and esmolol, were administered. While counteracting both hypertension and tachycardia, the response time is slower, and the peak effect lower, compared to the nitroglycerine boluses.

Ventricular fibrillation was identified as the main contributor to IMC in our pilot experiments. To prevent this, a lidocaine bolus was given at the time of circulatory death, defined in Section 2.3. A bolus dose of the calcium antagonist and β-blocker mixture were administered together with the lidocaine to prevent a prolonged episode of low-intensity myocardical work following circulatory death. The timing and doses of all drugs used in hemodynamic control are given in Supplementary Table C.1 and Table C.3.

A noradrenaline "safety" feedback controller was implemented for automatic drug infusion to counteract potential overdosing of nitroglycerine, otherwise resulting in hypotension. Systolic aortic pressure responses to constant noradrenaline infusions were recorded in three pilot experiments, and are shown in Supplementary Figure E.4.

Time-delayed first-order linear differential equation models were identified from the noradrenaline infusion responses shown in Supplementary Figure E.4, by minimizing the output error $\mathcal{L}_2$ norm. A proportional-integral-derivative (PID) controller was optimized for robust performance across these models. The optimization objective was to minimize the time from hypotension due to overdosing of nitroglycerine until acceptable systolic aortic blood pressure values were reached. A step disturbance was used to model the effect of nitroglycerine on the systolic aortic pressure. In the controller optimization, constraints were imposed to enforce robustness over the model set. More details of the controller design can be found in Supplementary Section E.

To attenuate high-frequency measurement noise, a second-order low-pass filter was connected in series with the controller, resulting in the Laplace domain repre-

sentation

$$\begin{aligned} K &= CF \\ C(s) &= k_p + k_i \frac{1}{s} + k_d s \\ F(s) &= \frac{1}{\left(sT_f + 1\right)^2} \end{aligned} \tag{3}$$

where C is the PID controller, F is the low-pass filter and s is the Laplace variable. The PID parameters were $k_p = 9.63 \times 10^{-4}$ mg/h/mmHg, $k_i = 2.96 \times 10^{-5}$ mg/h/mmHg/s, $k_d = 8.14 \times 10^{-3}$ mg/h/mmHg s and $T_f = 2$ s. The controller was implemented with clamping anti-windup on the PC used in data acquisition and drug delivery actuation.

The set-point of this noradrenaline "safety" controller was set to 70 mmHg for P_{sys}, and the for during the first 3 min following WLST, whereafter the controller was automatically deactivated.

2.3 Experimental Study

The primary end-point was to study IMC occurrence 60 min after circulatory death. The secondary end-point was the time between circulatory death and observed IMC.

Equal control and test group sizes of $n = 6$ each were determined, based on 70 % anticipated 60 min IMC incidence in the control group, and 0 % in the test group, at a false positive rate $\alpha = 0.05$, and false negative rate $\beta = 0.2$ (i.e., 80 % power). Inclusion criteria for both groups were defined to facilitate comparability of outcomes: stable hemodynamics at the time of WLST, with $P_{sys} \leq 110$ mmHg and $HR \leq 110$ min; absence of agonal breathing following WLST; adherence to drug dosing protocol of the study; absence of anomalies at dissection. Details about animals excluded from the study and conducted pilot cases can be found in Supplementary Section B.

Anesthesia was induced through intravenous injection of atropine, xylazin, and ketamine. Subsequently, midazolam and rocuronium were intravenously administered before placement of an endotracheal tube through tracheostomy. The animals were then mechanically ventilated using volume-controlled and pressure-regulated ventilation.

Upon introduction of intravenous propofol anesthesia, and intubation, the animals were instrumented with transducers to measure arterial and venous blood pressure and a 5-lead ECG. Arterial blood gas samples were collected and analyzed at baseline, and $1, 2, ..., 5$ min following WLST. The animals were given heparin to prevent coagulation. Doses and further details on the drugs are provided in Supplementary Section C.

A neuromuscular blockade was established to prevent agonal breathing, whereupon WLST was performed. If the heart rate exceeded 110 bpm between WLST and circulatory collapse, a bolus of esmolol and nimodipine was given. Circulatory collapse was defined to occur at the first incidence of $P_{sys} < 40$ mmHg. Circula-

tory death (cessation and irreversibility of cardiopulmonary function [Tibballs and Bhatia, 2015]) was defined as persistent circulatory collapse combined with arterial saturation remaining below $s_aO_2 = 30$ %. Previous studies [Cooley et al., 1972; Iyer et al., 2016] have associated a systolic pressure fall beneath 50 mmHg with severe ischemia, motivating the choice of the lower systolic pressure limit. By this time, the animals was hypoxic with an arterial oxygen saturation well below 30 % [Iyer et al., 2016]. Following a hands-off time of 30 min, sternotomy was performed, and the heart was inspected and palpated for IMC every 5 min until 60 min had passed since circulatory death. If there were palpable and visible signs of contracture in the left ventricular wall, IMC was confirmed. When IMC was verified or when 60 min had passed since circulatory death, the heart was excised and transversely cut into slices as shown in Figure 1. The heart was then dissected to inspect for anomalies that could have affected the outcome. To complement the qualitative diagnostic assessment with a quantitatively comparable measure, the left ventricular wall thickness was measured as the average thickness within a transverse plane halfway between the atrial-ventricular plane and the apex.

The test and control group protocols were identical with the exception of the test group being subjected to the hemodynamic control protocol described in Section 2.2. The test group protocol is illustrated through the flowchart in Figure 3. Drugs used in the test group protocol were nitroglycerine, noradrenaline, lidocaine, esmolol and nimodipine, see Figure 3 and Supplementary Table C.1 and Table C.3 for details about bolus dosing and timing. Noradrenaline was administered by the aforementioned "safety" feedback control system using an Alaris TIVA infusion pump. Bolus doses of the other drugs were manually administered, due to a lack of remote-controlled bolus capability of the Alaris TIVA pumps. This was later implemented, and two additional fully automated cases, one illustrated in Figure 4, were successfully completed.

3. Results

The investigated method for normalization of hemodynamics upon WLST with the aim to facilitate DCD procurement of hearts resulted in none of the six test group individuals developing IMC within 60 min of warm ischemia following circulatory death. All six control group individuals developed IMC within 60 min, with four having developed IMC by the time of sternotomy, 30 min following circulatory death.

Figure 1 shows representative cross sections of two hearts from the study: (a) was procured from a test group animal 60 min following circulatory death; (b) from a control group animal 30 min following circulatory death. The heart in (a) shows no signs of IMC, while IMC is fully developed in (b), as seen by the severely restricted left-ventricular lumen. The average left ventricular wall thickness, measured halfway between the atrial-ventricular plane and the apex at the time of dissection, was

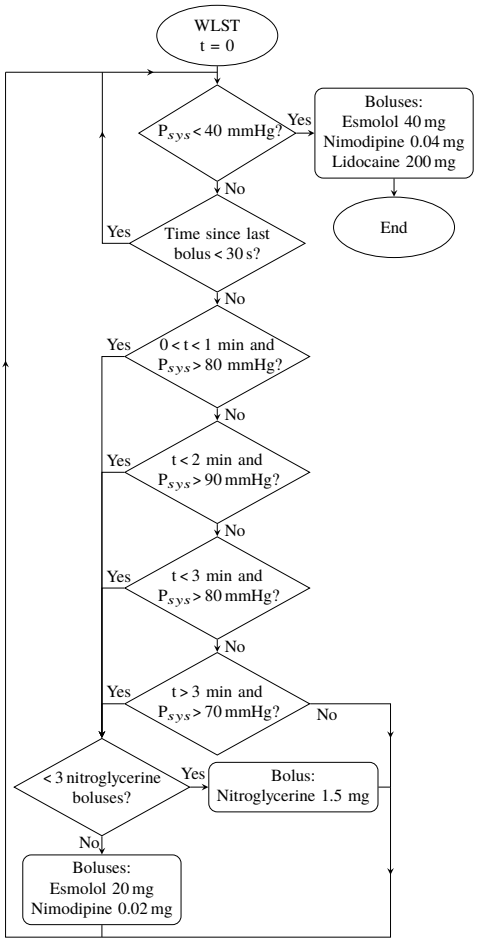

Figure 3. Flow chart illustrating the test group protocol. Time $t = 0$ starts at the instance of WLST. The noradrenaline "safety" controller is activated during the first 3 min following WLST, in order to avoid hypotension in case of low nitroglycerine tolerance. If the heart rate exceeded 110 bpm between WLST and circulatory collapse, an additional bolus of esmolol and nimodipine was given.

10 mm (range $8-16$) within the test group and 20 mm (range $16-22$) within the control group.

Figure 5 shows the hemodynamic responses for all test and control subjects, following withdrawal of life-sustaining therapy at $t = 0$ min. The markers in Figure 5a show oxygen saturation (s_aO_2) of arterial blood gas samples. The dotted horizontal line corresponds to $s_aO_2 = 30$ %. All individuals reached an arterial saturation below 30 % within 3 min following WLST. The mean $\pm$ standard deviation durations

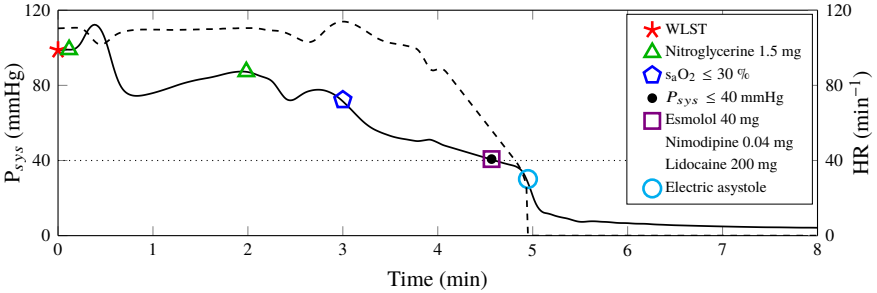

Figure 4. Representative test group experiment with fully automated drug dosing according to the protocol illustrated in Figure 3. Systolic pressure, P_{sys} is shown solid and heart rate, HR, in dashed. Markers indicate events according to the figure legend. The dotted black line indicates the systolic pressure associated with circulatory collapse.

between WLST and occurrence of $s_aO_2 = 30$ %, linearly interpolated between samples, were 133 ± 38 s in the test group and 143 ± 27 s in the control group. Mean $\pm$ standard deviation desaturation rates were -29 ± 4 %min^{-1} in the test group and -33 ± 12 %min^{-1} in the control group. This indicates similar metabolic rates between the groups. Systolic aortic pressures (P_{sys}) are shown in Figure 5b. The dotted horizontal line corresponds to $P_{sys} = 40$ mmHg, indicating the systolic pressure associated with circulatory collapse. Heart rates (HR), computed from ECG RR-intervals until loss of QRS-complex, or onset of VF, are shown in Figure 5c. Per-individual events are shown in the top part of Figure 6, in which time zero corresponds to circulatory death. The bottom part visualizes the temporal distribution of events.

There was no notable overdosing of nitroglycerine in any of the cases. Consequently, the noradrenaline controller administered only very small drug doses in two cases: 1.1 µg, beginning 149 s in T4 after WLST; 6.5 µg in T6, beginning 113 s after WLST.

Work indices $\underline{W}$ and $\bar{W}$ for all individuals are shown in Figure 7. The distributions of their final values are shown to the right in the same figure. The median decrease in work indices between control and test group was 59 % for $\underline{W}$ and 68 % for $\bar{W}$.

The single-sided Mann-Whitney test reveals a significant ($p < 0.002$) difference in IMC incidence 60 min after withdrawal of life-sustaining therapy between the groups.

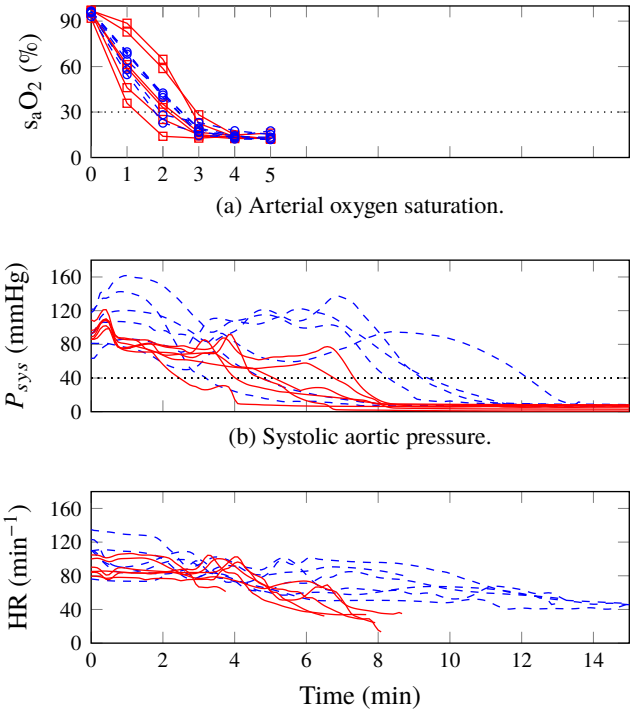

(a) Arterial oxygen saturation.

(b) Systolic aortic pressure.

(c) Heart rate.

Figure 5. Test (solid red, squares) and control (dashed blue, circles) group hemodynamic responses following withdrawal of life-sustaining therapy (WLST) at time 0 min. The dotted horizontal line in (a) indicates oxygen saturation $s_aO_2 = 30\,\%$. The dotted horizontal line in (b) indicates the systolic aortic pressure, $P_{sys} = 40$ mmHg, associated with circulatory collapse. Circulatory death was defined to occur when both $s_aO_2 < 30\,\%$ and $P_{sys} < 40$ mmHg were fulfilled.

4. Discussion

This study demonstrated that it is feasible to postpone ischemic myocardial contraction up to 1 h following circulatory death, through automatic control of hemodynamic drug delivery.

However, further investigation needs to be undertaken to see if the asystolic non-contracted heart may be reconditioned to partial or full function after 30 min or 60 min of circulatory arrest *in situ* at normothermia. Histological comparison, *ex vivo* functional evaluation, and ultimately transplantation are markers suggested for further evaluation to determine feasibility for transplantation. A method to recondition and preserve porcine hearts has been developed in-house [Qin et al., 2020; Steen et al., 2016]. Safe orthotopic transplantation was done with hearts extracted

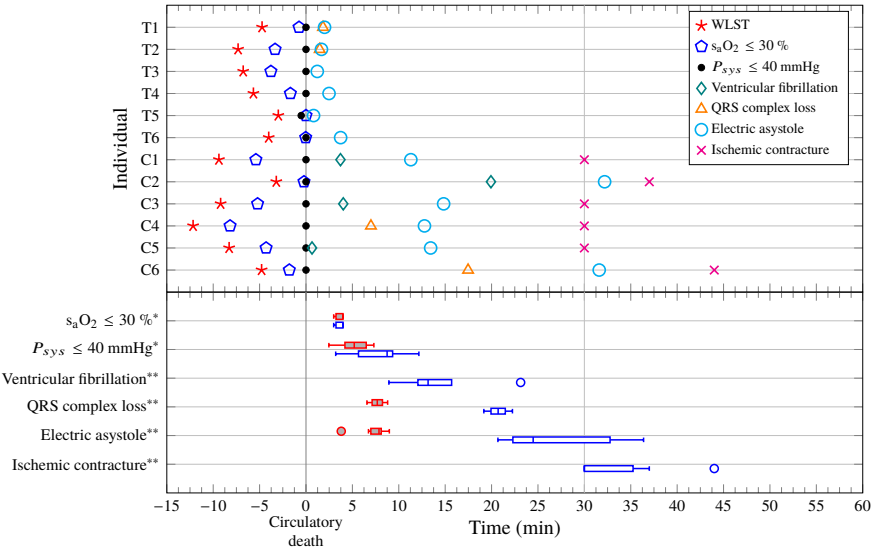

Figure 6. Distribution of events. The top part shows events for test (T) and control (C) group individuals. QRS complex loss markers have been omitted for individuals where QRS complex loss coincided with ventricular fibrillation or electric asystole. IMC incidence has been reported as 30 min if IMC was observed at the instance of sternotomy, which was performed 30 min after circulatory death. The bottom part shows the distribution of events within the study groups. Filled red boxes are used for the test group; empty blue ones for the control group. In absence of incidence, IMC and ventricular fibrillation statistics are not presented for the test group. Note that the distributions of arterial saturation $s_aO_2 < 30$ %, and systolic pressure $P_{sys} < 40$ mmHg, are reported with the withdrawal of life-sustaining therapy (WLST) time instance as zero reference, while all other events are reported with the time instance of circulatory death as zero reference.

24 h after brain death and kept vital by non-ischemic-heart-perfusion (NIHP) for 24 h [Steen et al., 2016]. To validate non-contracted hearts up to 1 h after circulatory death, we plan to do NIHP, followed by orthotopic transplantation. If the function of such hearts is good, this method may support broader clinical implementation of heart transplantation following withdrawal of life-sustaining therapy (controlled DCD).

While it is possible to implement the protocol manually in a controlled lab environment with well-rehersed personnel, its clinical feasibility is low, taking into account the narrow timing requirements and the requirement of calm and dignity in the presence of next of kin. The use of a feedback control system solves both these problems. Clinical implementation relies only on standard ICU monitoring and intravenous access, both of which can be expected in the considered patient category.

The controlled DCD model used in this work is similar to the clinical scenario

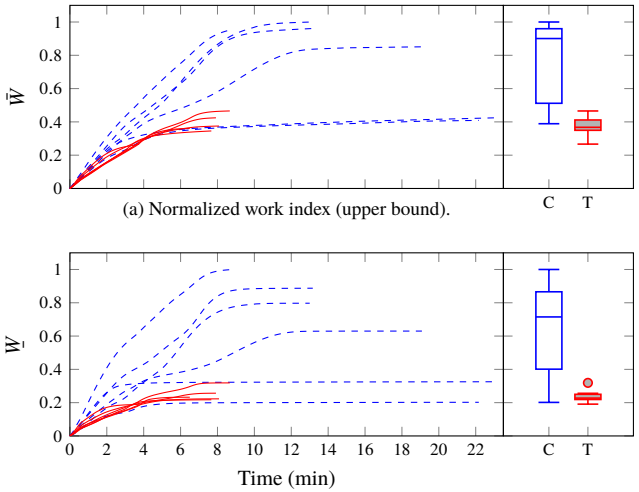

(a) Normalized work index (upper bound).

(b) Normalized work index (lower bound).

Figure 7. Normalized work indices between withdrawal of life-sustaining therapy (WLST) at time 0 min and the incidence of either asystole or ventricular fibrillation are shown to the left. Test group estimates are shown in solid red; control group estimates in dashed blue. The two lowermost curves in the control group correspond to individuals C2 and C6 in Figure 6, which showed circulatory collapse less than five minutes after WLST. Data computed using Equation (1) is shown in (a) and using Equation (2) is shown in (b). The normalized work index final value distributions of the control group (C, empty blue boxes) and test group (T, filled red boxes) are shown to the right.

[Wind et al., 2012]. However, unlike the clinical scenario, the animals had not suffered neurological damage. Measures were therefore taken to establish a standardization of the agonal phase, further explained in Supplementary Section C, manifested in the small variability in desaturation profiles shown in Figure 5a. While the test group protocol was designed to include only drugs broadly accepted in the considered context, local protocols can affect admissibility of certain drugs. We have found no reason to believe that the test group results could not have been obtained by means of another set of drugs with similar hemodynamic effects, as long as timing and dosing are appropriately chosen.

There is no internationally recognized definition of circulatory death. It is therefore debatable whether the definition used in this work ($s_aO_2 \leq 30$ % and $P_{sys} < 40$ mmHg) would gain broad acceptance. However, the conclusion of the study would be the same with slightly differing definition of circulatory death (based on the same parameters), as can be verified by studying the profiles of Figure 5.

As seen in Figure 5, and reported in other preclinical studies [Iyer et al., 2016; Niederberger et al., 2019], the time between WLST and circulatory collapse is generally shorter than in clinic, where it is usually around $15-20$ min, in absence of

agonal breathing [Messer et al., 2016]. Furthermore, the circulatory collapse process progressed somewhat more rapidly in the test group. This was observed during the study, once the test and control group protocols had been fixed. In subsequent experiments we made the automated drug delivery less aggressive, and increased the systolic pressure setpoint for the noradrenaline "safety" controller during the initial phase following WLST. With these changes to the test group protocol, we were able to postpone IMC beyond h with hemodynamic trajectories like those of the study controls.

The final values of the work indices in Figure 7 and corresponding IMC onset times in Figure 6 indicate that the work indices constitute useful predictors of IMC onset. Circulatory collapse occurred after less than five minutes in two of the control group individuals: C2 and C6 in Figure 6. This resulted in work indices similar to those representative for the test group and a later occurrence of stone heart (37 min and 44 min). Relatedly, the distinct difference in final work indices between the control and test group shown in Figure 7 indicates that the investigated protocol for pharmacological normalization of hemodynamics is effective in postponing the onset of IMC following WLST in the considered large animal model.

5. Conclusion

A pharmacological method, intended to postpone the onset of ischemic myocardial contracture (IMC), with the aim to facilitate controlled DCD procurement of hearts, was developed and evaluated. None of the six test group animals developed IMC within 60 min of warm ischemia, following circulatory death caused by withdrawal of life-sustaining therapy. All six control group animals developed ischemic myocardial contracture within 60 min following circulatory death, with four having developed IMC by the time of sternotomy, 30 min following circulatory death. This demonstrates pre-clinical feasibility of the proposed method, and motivates further research aimed at adapting it for the clinical setting. Further studies are needed to investigate whether the function of the heart can be fully restored.

Supplementary Information

The online version contains supplementary material available at `https://doi.org/10.1007/s13239-021-00537-8`.

Acknowledgements

The authors would like to acknowledge Zhi Qin with Zhengzhou University, China, for assisting with the study.

Author Contributions

Study conceptualization: KS, SS, YW; Experimental surgery: QL, XL, SS; Engineering: KS, YW; Data analysis and manuscript: HP, TS, KS, SS, YW.

Funding

Open access funding provided by Lund University. The work was funded by the Swedish government through the Swedish Research Council (grant 2017-04989) and the Hans-Gabriel and Alice Trolle Wachtmeister Foundation for Medical Research. Wahlquist and Soltesz are members of the Excellence Center at Linköping-Lund in Information Technology (ELLIIT).

Data Availability

No data outside that presented in enclosed plots and tabulations have been used.

Code Availability

Code for computing the statistics presented in the manuscript is available from the corresponding author upon request.

Conflict of Interest

The authors have no conflicts of interest to disclose.

Ethical Approval

The study ran under ethics permission M174-15, issued by "Malmö/Lunds Djurförsöksetiska Nämnd" (local REB).

Research involving Animal Rights

Twelve Swedish pigs (sus scrofa domesticus) with a median body weight of 35 kg (range $30-40$ kg) were included in the study with equal control and test group sizes of $n=6$. Large-animal experiments were motivated by the lack of adequate dynamic models describing the impact of pharmacological treatments on the duration to onset of IMC, or data on which such models could be based. All institutional and national guidelines for the care and use of laboratory animals were followed and approved by the appropriate institutional committees. The animals were treated in compliance with EU directive [European Parliament, 2010].

Informed Consent

No human studies were carried out by the authors for this article.

References

Cooley, A., J. Reul, and C. Wukasch (1972). "Ischemic contracture of the heart: "stone heart"." *Am J Cardiol* **29**, pp. 575–577.

Dhital, K., P. Ludhani, S. Scheuer, M. Connellan, and P. Macdonald (2020). "DCD donations and outcomes of heart transplantation: the Australian experience." *Indian J Thorac Cardiovasc Surg*. DOI: 10.1007/s12055-020-00998-x.

European Parliament (2010). *On the protection of animals used for scientific purpose*. Tech. rep. Directive 2010/63/EU. Council of Europe.

Garcia-Dorado, D., M. Gonzalez, J. Barrabes, M. Ruiz-Meana, J. Solares, R. Lidon, J. Blanco, Y. Puigfel, H. Piper, and J. Soler-Soler (1997). "Prevention of ischemic rigor contracture during coronary occlusion by inhibition of Na^+-H^+ exchange." *Cardiovasc Res* **35**, pp. 80–89.

Hearse, D., P. Garlick, and S. Humphrey (1977). "Ischemic contracture of the myocardium: mechanisms and prevention." *Am J Cardiol* **39**:7, pp. 986–993. DOI: 10.1016/S0002-9149(77)80212-9.

Iyer, A., H. Chew, L. Gao, J. Villanueva, M. Hicks, A. Doyle, G. Kumarasinghe, A. Jabbour, P. Jansz, M. Feneley, R. Harvey, R. Graham, K. Dhital, and P. Macdonald (2016). "Pathophysiological trends during withdrawal of life support: implications for organ donation after circulatory death." *Transplantation* **100**:12, pp. 2621–2629. DOI: 10.1097/TP.0000000000001396.

Koostra, G., J. Daemen, and A. Oomen (1995). "Categories of non-heart-beating donors." *Transplant Proc* **27**:5, pp. 2893–2894.

MacDonald, P. and K. Dhital (2019). "Heart transplantation from donation-after-circulatory-death (DCD) donors: back to the future–evolving trends in heart transplantation from DCD donors." *J Heart Lung Transpl* **38**:6, pp. 599–600. DOI: 10.1016/j.healun.2019.03.010.

Manara, A., P. Murphy, and G. O'Callaghan (2012). "Donation after circulatory death." *Brit J Anaesth* **108**, pp. i108–i121. DOI: 10.1093/bja/aer357.

Messer, S., R. Axell, S. Colah, P. White, M. Ryan, A. Page, B. Parizkova, K. Valchanov, C. White, D. Freed, E. Ashley, J. Dunning, M. Goddard, J. Parameshwar, C. Watson, T. Krieg, A. Ali, S. Tsui, and S. Large (2016). "Functional assessment and transplantation of the donor heart after circulatory death." *J Heart Lung Transpl* **35**, pp. 1443–1452. DOI: 10.1016/j.healun.2016.07.004.

Morrissey, P. and A. P. Monaco (2013). "Donation after circulatory death: current practices, ongoing challenges, and potential improvements." *Transplantation* **97**:3, pp. 258–264. DOI: 10.1097/01.TP.0000437178.48174.db.

Niederberger, P., E. Farine, M. Raillard, M. Dornbierer, D. Freed, S. Large, H. Chew, P. MacDonald, S. Messer, C. White, T. Carrel, H. Tevaearai Stahel, and S. Longnus (2019). "Heart transplantation with donation after circulatory death: what have we learned from preclinical studies?" *Circ-Heart Fail* **12**:4. DOI: 10.1161/CIRCHEARTFAILURE.118.005517.

Novitzky, D., D. Cooper, J. Rosendale, and H. Kauffman (2006). "Hormonal therapy of the brain-dead organ donor: experimental and clinical studies." *Transplantation* **82**, pp. 1396–1401. DOI: 10.1097/01.tp.0000237195.12342.f1.

Qin, G., B. Wohlfart, L. Zuo, J. Hu, T. Sjöberg, and S. Steen (2020). "Intact coronary and myocardial functions after 24 hours of non-ischemic heart preservation." *Scand Cardiovasc J* **54**, pp. 59–65. DOI: 10.1080/14017431.2019.1684553.

Soltesz, K., C. Grimholt, and S. Skogestad (2017a). "Simultaneous design of PID controller and measurement filter by optimization". *IET Control Theory A* **11**:3, pp. 348–348. DOI: 10.1049/iet-cta.2016.0297.

Soltesz, K., T. Sjöberg, T. Jansson, R. Johansson, A. Robertsson, A. Paskevicius, Q. Liao, G. Qin, and S. Steen (2018). "Closed-loop regulation of arterial pressure after acute brain death." *J Clin Monit Comput* **32**, pp. 429–437. DOI: 10.1007/s10877-017-0033-z.

Soltesz, K., C. Sturk, A. Paskevicius, L. Qiuming, Q. Guangqi, T. Sjöberg, and S. Steen (2017b). "Closed-loop prevention of hypotension in the heartbeating brain-dead porcine model." *IEEE T Bio-med Eng* **64**:6, pp. 1310–1317. DOI: 10.1109/TBME.2016.2602228.

Steen, S., A. Paskevicius, Q. Liao, and T. Sjöberg (2016). "Safe orthotopic transplantation of hearts harvested 24 hours after brain death and preserved for 24 hours." *Scand Cardiovasc J* **50**, pp. 193–200. DOI: 10.3109/14017431.2016.1154598.

Suntharalingam, C., L. Sharples, C. Dudley, J. Bradley, and C. Watson (2009). "Time to cardiac death after withdrawal of life-sustaining treatment in potential organ donors." *Am J Transplant* **9**, pp. 2157–2165. DOI: 10.1111/j.1600-6143.2009.02758.x.

Tibballs, J. and N. Bhatia (2015). "Transplantation of the heart after circulatory death of the donor: time for a change in law?" *Med J Australia* **203**:6, pp. 268–270. DOI: 10.5694/mja15.00295.

Wind, J., M. Snoeijs, C. Brugman, J. Vervelde, J. Zwaveling, W. van Mook, and E. van Heurn (2012). "Prediction of time of death after withdrawal of life-sustaining treatment in potential donors after cardiac death." *Crit Care Med* **40**:3, pp. 766–769. DOI: 10.1097/CCM.0b013e318232e2e7.

Zumbro, G., L. Tillman, A. Bailey, and R. Treasure (1978). "A comparison between propranolol and hypothermia in preventing ischemic contracture of the left ventricle (stone heart)." *Ann Thorac Surg* **25**:6, pp. 541–550. DOI: 10.1016/S0003-4975(10)63606-5.

Supplementary Information

A. Cardiac work estimation

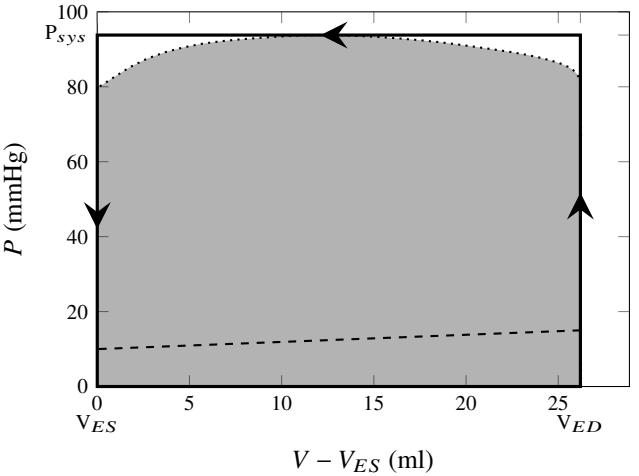

Figure A.1. Systolic pressure-volume (PV) path (dotted) between end-diastole, (*ED*, mitral valve closure), and end-systole, (*ES*, aortic valve closure), was recorded in a 30 kg pig during one pilot experiment, represented Figure A.2. The left-ventricular diastolic PV path, from *ES* to *ED*, of the cardiac cycle (dashed) is only qualitatively illustrated, and not used when considering the entire heart, rather than the isolated left ventricle. The net work performed by the left-ventricle during the cardiac cycle is the area between the dotted and dashed lines; corresponding net work performed by the heart is quantified by the grey area. The area enclosed by the solid line is the proposed cardiac cycle work estimate, $\hat{W}_c$, defined through Equation (7).

Left ventricular pressure-volume (PV) loops are frequently used in clinical and research cardiology. The PV loop shows ventricular pressure plotted against ventricular volume over one or several cardiac cycles, providing a contour similar to the one enclosing the grey area of Figure A.1. Integrating pressure over volume in the PV loop over one cardiac cycle yields the work exerted *on* the system. The work exerted *by* the system is hence

$$W(V_1, V_2) = -\int_{V_1}^{V_2} P(V)\, dV, \tag{4}$$

when transitioning from a volume V_1 to another volume V_2 along the PV contour. To be accurate, Equation (4) provides an upper bound for this work, and that bound is tight for lossless systems. This assumption is tacitly made in cardiac PV loop analysis, where the area enclosed by the PV contour is defined to be the stroke work.

It is, however, not valid during ventricular fibrillation (VF), in which considerable energy is consumed without resulting in net blood transport, and hence no work is done according to Equation (4).

Letting t_1 be the time at which the volume is V_1, i.e., $V(t_1) = V_1$, and similarly defining t_2 through $V(t_2) = V_2$, the work of Equation (4) can be expressed as

$$W(t_1,t_2) = -\int_{t_1}^{t_2} P(t)\frac{dV}{dt}dt = -\int_{t_1}^{t_2} \varphi(t)P(t)\,dt, \tag{5}$$

where $\varphi(t) = \dot{V}(t)$ is the volumetric flow rate entering the left ventricle. When $W > 0$, the left ventricle exerts work *on* the blood; when $W < 0$, the blood exerts work on the left ventricle. Since $P > 0$ throughout the cardiac cycle, $W > 0$ holds whenever left ventricular volume decreases ($\dot{V}(t) < 0$, characterized by the dotted line in Figure A.1), and work is exerted by the blood whenever left ventricular volume increases: $\dot{V}(t) > 0$, characterized by the dashed line in Figure A.1. The relatively small fraction of work exerted *by* the blood, quantified by the area under the dashed line in Figure A.1, can be viewed as a free contribution when the left ventricle is considered as an isolated system, which is commonly the case in PV loop analysis. However, when considering the entire heart, this contribution is not free: it is the combined contribution of the atria and the right ventricle.

Under the valid assumption that central venous pressure is low compared to aortic pressure, the work W_c, exerted by the heart during one cardiac cycle can thus be expressed

$$W_c = \int_{t_{ED}}^{t^{ES}} P(t)\,CO(t)\,dt, \tag{6}$$

where P is the (instantaneous) aortic pressure, t_{ED} the end-diastolic time instance, t_{ES} the end-systolic time instance, and $CO(t) = -\varphi$ the (instantaneous) cardiac output.

A fair approximation of W_c, $\hat{W}_c$, is obtained by replacing the contour segment between V_{ED} and V_{ES} with the systolic isobar in Figure A.1, P_{sys}. Then Equation (6) is approximated by

$$\hat{W}_c = P_{sys}\,SV, \tag{7}$$

where $SV = V_{ES} - V_{ED}$ is the stroke volume. The estimate $\hat{W}_c$ corresponds to the area enclosed by the solid line in Figure A.1. The total energy consumption between WLST and the incidence of either asystole or VF is the sum of the individual W_c contributions.

A reasonable assumption is that SV is positively correlated with P_{sys}. This will be expressed as $SV(P_{sys})$, where $SV : \mathbb{R}^+ \mapsto \mathbb{R}^+$ is some bounded monotonously non-decreasing function. The resulting relative difference in estimated work Equation (7) between cardiac cycles with systolic pressures P_a and $P_b < P_a$ is

$$\frac{P_a SV(P_a) - P_b SV(P_b)}{P_a SV(P_a)} = 1 - \frac{P_b}{P_a}\frac{SV(P_b)}{SV(P_a)}. \tag{8}$$

The properties of $SV(P_{sys})$, combined with $P_b < P_a$, yield $SV(P_b) \leq SV(P_a)$, with equality when $SV(P_{sys}) \propto 1$, i.e., when SV is not increasing with P_{sys}.

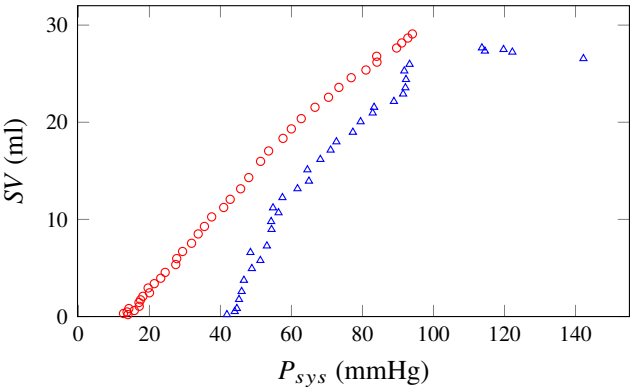

Figure A.2. Relationship between systolic aortic pressure, P_{sys}, and stroke volume, SV, measured in 30 kg animals during two pilot experiments: one illustrated by red circles; the other by blue triangles.

To justify this assumption, the nature of $SV(P_{sys})$ was investigated through two pilot experiments, where a transit-time flow meter, connected to the LabChart system detailed in Section C, was secured across the aorta upon sternotomy, and otherwise adhering to the control group protocol. This enabled computing SV as the time integral of flow over each cardiac cycle. The outcome is shown in Figure A.2, confirming that the monotonicity assumption on $SV(P_{sys})$ is sound. Furthermore, it suggests that while the conservative estimate $\underline{W}$ is accurate for the saturated region (almost horizontal segment of blue triangles), the non-saturated region (the remainder of plotted data) is better approximated by $SV(P_{sys}) \propto P_{sys}$.

A lower bound of the estimate is therefore obtained by assuming that SV is independent of P_{sys}, resulting in the total work estimate

$$\underline{W} \propto \int_0^T P_{sys}(t)\, HR(t)\, dt, \tag{9}$$

where $t = 0$ and $t = T$ denote the instances of WLST, and asystole or VF instance, respectively. HR is the instantaneous heart rate, defined at the instances of systolic peaks as $1/\Delta t$, where Δt is the time passed since the preceding systolic peak.

The pilot experiments also suggest an upper bound on the total work estimate

$$\bar{W} \propto \int_0^T P_{sys}^2(t)\, HR(t)\, dt, \tag{10}$$

based on SV being proportional to P_{sys}.

Since $\underline{W}$ and $\bar{W}$ are defined only up to proportionally, they will be denoted work *indices* rather than *estimates*, and their utility is limited to comparison between individuals or groups, within which cardiovascular physiology is similar. The central hypothesis, investigated in the study, is that the time integrals of these indices following WLST provides useful predictions of IMC incidence, and thus suggest how pharmacological normalization of hemodynamics can serve to prevent IMC.

Evaluation of the estimation of the work over one cardiac cycle Equation (7) of the main manuscript relies on SV, or equivalently CO, being measured. However, pilot experiments revealed that manipulation of the ischemic heart easily triggers the onset of IMC. Placement of a PV loop catheter was consequently ruled out as an option for the controlled study. Similarly, the pleural access required to place an ultra-sonic flow probe over the aorta was found to result in (partial) collapse of the lungs, suspected to affect the desaturation process. Consequently, WLST was performed with intact thorax during the study.

B. Excluded animals and pilot cases

Three animals were excluded, all from the test group, for the following reasons: insufficient curarization resulting in agonal breathing; systolic pressure rise prior to WLST (the experiment was concluded and IMC was absent 60 min after circulatory death); nitroglycerine administration exceeding protocol limit.

In addition to the 12 included plus 3 excluded study cases, 11 pilot cases were conducted: 6 to obtain modeling data for controller design, 3 to determine adequate doses of the drugs that were not computer-controlled, and 2 to investigate the $SV(P_{sys})$ relationship explained in Supplementary Section A. Pilot experiment and excluded animals fell within the same weight range as those included in the study.

C. Study details

The animals were mechanically ventilated using volume-controlled (4 L minute volume at 18 breaths/min) and pressure-regulated ventilation (5 cm_2O PEEP). Inspired oxygen fraction was 21 %, and end tidal CO_2 was kept between 4.5 kPa and 5.5 kPa. Details of drugs and equipment used in the experiments can be found in Table C.1 and Table C.2.

Three venous catheters were secured into the superior vena cava with their tips at the level of the right atrium. These catheters were used for anesthesia maintenance, continuous venous pressure monitoring and manual drug administration. Two catheters of the same type were secured into the ascending aorta for online arterial pressure monitoring and blood gas sampling. Arterial blood gas samples were collected and analyzed at baseline, and $1, 2, \ldots, 5$ min following WLST.

Blood pressure transducers were connected to the arterial and venous catheters, and intermittently flushed with saline solution. Separate transducer pairs were used

for the feedback control system and visualization. Both systems logged to file, results presented herein are from the LabChart logs. A 5-lead ECG was also connected to LabChart, running on a Windows 7 PC.

Rocoronium was infused at 60 mg/h, with an additional 50 mg bolus just before WLST, to prevent agonal breathing. Without complete neuromuscular blockade, one would expect a much larger spread between desaturation profiles, prompting increased study group sizes in order to draw valid comparative conclusions. Rocuronium was therefore administered to establish a neuromuscular blockade, and the endotracheal tube was clamped at the instance of WLST. Both these measures should be viewed as parts of the large-animal model, and not the proposed DCD protocol. They guarantee a total absence of gas exchange.

Bolus dose timing for the test group individuals are shown in Table C.3.

D. Nitroglycerine bolus dose

Aortic systolic pressure responses to nitroglycerine, collected during two pilot experiments, are shown in Figure D.3. The experiments indicated that a bolus dose of $1-2$ mg results in a sufficient response, and that there is an apparent saturation in the vasodilative effect beyond this dose. Dose size was therefore fixed to 1.5 mg throughout the main study.

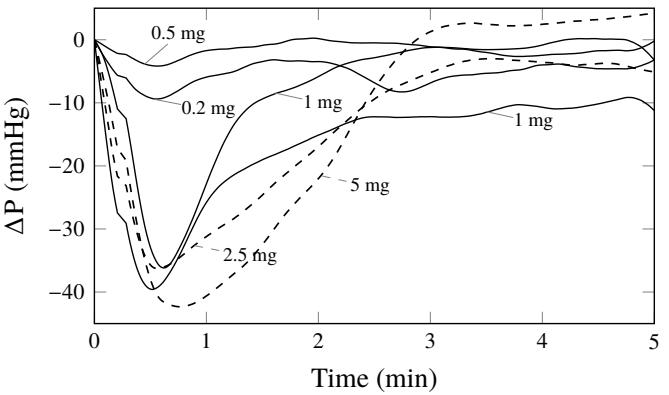

Figure D.3. Systolic pressure deviations, $\Delta P_{sys} = P_{sys} - P_0$, resulting from a nitroglycerine bolus at time zero, where P_0 denotes the baseline value of the systolic pressure P_{sys}. The responses were obtained through two pilot experiments on one 30 kg pig (dashed) and one 35 kg pig (solid).

Table C.1. Complete list of drugs used in the main study, together with corresponding dose and manufacturer specifications. Saline solution was administered to compensate for dehydration losses.

Drug	Dose	Full drug name and manufacturer
atropine	0.5 mg	Atropin, Mylan AB, Stockholm, Sweden
esmolol	20 mg/bolus	Brevibloc, Baxter Medical AB, Kista, Sweden
heparin	25000 IU	Heparin, LEO Pharma AB, Malmö, Sweden
ketamine	750 mg	Ketaminol vet, Intervet, Boxmeer, Netherlands
lidocaine	200 mg	Xylocard, Aspen Nordic, Dublin, Ireland
midazolam	25 mg	Midazolam, Panpharma S.A, Trittau, Germany
nimodipine	0.02 mg/bolus	Nimotop, Bayer Healthcare AG, Leverkusen, Germany
nitroglycerine	1.5 mg/bolus	Nitroglycerin, BioPhausia AB, Stockholm, Sweden
noradrenaline	computer controlled	Noradrenalin, Pfizer AB, Sollentuna, Sweden
propofol	4 mg/kg/h	Propofol-Lipuro, B. Braun Medical AB, Melsungen, Germany
rocuronium	20 mg, 60 mg/h	Rocuronium, Fresenius Kabi, Graz, Austria
xylazin	100 mg	Rompun vet, Bayer AB, Solna, Sweden

Table C.2. Instrumentation for measurement and drug delivery

Equipment	Name	Manufacturer
Flow meter	Flowmeter CM4000	CardioMed, Lindsay, Canada
Ventilator	Servo Ventilator 300	Siemens AB, Solna, Sweden
Venous catheter	Secalon-T	Merit Medical, Singapore
Blood gas analyzer	ABL 700	Radiometer, Copenhagen, Denmark
Blood pressure transducer	Meritrans DTXPlus	Merit Medical, Singapore
DAQ	PowerLab 16/35	AD Instruments, Colorado Springs, CO
Infusion pump	Alaris TIVA	BD, Franklin Lakes, NJ
LabChart 8	AD Instruments	Colorado Springs, CO

Table C.3. Bolus dose timing for test group individuals T1-T6, in seconds measured from WLST.

	Nitroglycerine			Esmolol and Nimodipine			Lidocaine, Esmolol and Nimodipine ($P_{sys} = 40$ mmHg)
	#1	#2	#3	#1	#2	#3	#1
T1	5	83	212	233			292
T2	3	81	194	216	260	292	296
T3	6			347			409
T4	177			207			350
T5	11	73					165
T6	12	126	169	192			233

E. Noradrenaline controller

A noradrenaline "safety" controller was implemented for automatic drug infusion to counteract potential overdosing of nitroglycerine, otherwise resulting in hypotension. Systolic aortic pressure responses to constant noradrenaline infusions were recorded in three pilot experiments, and are shown in Figure E.4. These step responses for noradrenaline were used for identification of low-order models for the dynamics. A first-order model with time delay

$$P(s) = \frac{b}{s+a} e^{-sL} \tag{11}$$

is sufficient to describe the drug response dynamics. The model parameters a, b, L were identified by minimizing the output error $\mathcal{L}_2$ norm, with the error being the difference signal between measured response and corresponding model output. The resulting model parameters can be found in Table E.4. A discrete time version (zero-order hold with 1 s sampling period) of the filtered PID controller was then synthesized based on a modification of the methodology in [Soltesz et al., 2017a]. A second-order filter F was chosen to guarantee high frequency roll-off, and the filter

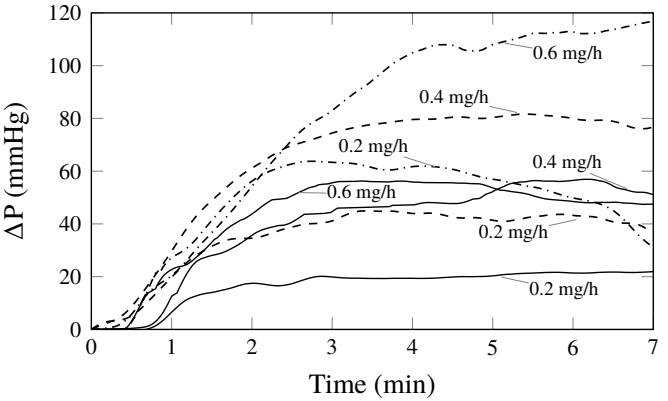

Figure E.4. Systolic pressure deviations, $\Delta P_{sys} = P_{sys} - P_0$, resulting from a noradrenaline infusion at time zero, where P_0 denotes the baseline value of the systolic pressure P_{sys}. The responses were obtained through pilot experiments using three pigs, two weighing 30 kg (solid and dashed) and one weighing 35 kg (dot-dashed).

time constant was fixed to $T_f = 2$ s, upon inspection of measurement noise characteristics in the systolic pressure signal.

The PID parameters k_p, k_i, k_d of Equation (3) were optimized by minimizing settling time following a step output disturbance, modeling a sudden change in systolic pressure. The minimization was performed such that the maximum closed-loop 2 % settling time across the identified models was minimized. The minimization was subject to a constraint, limiting the response overshoot to 50 % of the amplitude of the disturbance step amplitude, across all identified models. This constraint was introduced to limit hypertension peaks and introduce additional robustness to the closed-loop system. The resulting optimized PID parameters were $k_p = 9.63 \cdot 10^{-4}$ mg/h/mmHg, $k_i = 2.96 \cdot 10^{-5}$ mg/h/mmHg/s, and $k_d = 8.14 \cdot 10^{-3}$ mg/h/mmHg·s.

Table E.4. First order model parameters with time delay Equation (11), identified from noradrenaline infusion responses in Figure E.4

a	*b*	*L*
0.013	1.49	22.00
0.014	1.92	42.25
0.023	1.94	33.11
0.020	4.28	26.99
0.015	3.04	26.60
0.061	12.47	34.87
0.014	2.48	54.68

Paper II

Fast Simulation of Pharmacokinetics

Ylva Wahlquist Fredrik Bagge Carlson Kristian Soltesz

Abstract

Fast simulation of linear time-invariant (LTI) pharmacokinetic (PK) models is crucial to mixed-effect modeling techniques, used extensively in pharmacological research and development. The by far most common LTI PK models are particularly structured compartmental systems with one, two or three compartments. Here we develop and demonstrate very efficient, and down to machine precision exact, simulators for those structures. Our proposed method is benchmarked against state-of-the art software for simulation of linear systems, using a clinically relevant data set.

Keywords: Pharmacokinetics and drug delivery, physiological modeling, biomedical system simulation

Originally published in IFAC-PapersOnLine and presented at the 22nd IFAC World Congress in Yokohama, Japan (IFAC WC 2023). The original version is available at `https://doi.org/10.1016/j.ifacol.2023.10.1425`.

1. Introduction

Simulation of linear pharmacological (PK) models lies at the core of modern pharmacometric methods, widely used in pharmacological research and response prediction. In particular, pharmacometric mixed-effect modeling relies on a large number (thousands or more) of such simulations, to approximate integrals through sampling from patient-individual parameter distributions. These simulations are normally conducted within custom software.

In concurrent work, we are developing neural-network-based symbolic regression for modeling the relation between known patient covariates such as age or gender, and parameters of the PK model, as outlined in [Wahlquist et al., 2022]. Training these networks requires a several-fold increase in PK model simulations. Even with modern computing power at hand, the large number of simulations constitutes a bottle neck.

The most widely known tool/software that provides simulation of such systems is NONMEM introduced by [Sheiner and Beal, 1980] in the 1980s. Lately, the software Pumas AI has received attention as a faster alternative to NONMEM, as described in [Rackauckas et al., 2020]. Much of the speedup is attributed to Pumas AI being implemented in the the Julia language, with native support for differential programming, see [Bezanson et al., 2017].

There are also numerous softwares that can simulate linear PK models through numeric integration of ODEs. Such methods are accessible through for example the *lsim* function in Matlab and DifferentialEquations.jl ([Rackauckas and Nie, 2017]) in Julia. Such numeric ODE integration methods approximate the solution using either fixed or adaptive time step lengths. They do not exploit the fact that the dynamics are LTI, and they do not exploit the fact that the considered input is a sequence of steady infusion levels (steps) and boluses (impulses), administered at known, but typically unevenly spaced, time instances.

Since the dynamics are LTI, a faster alternative is to compute the exact solution of the ODE only at the dose change instances, and observation instances (that may differ from them). Doing so naively involved the evaluation of an exponential matrix.

We tailor a method for exactly solving the ODE at instances of interest. By exploiting the structure of one, two, and three compartment LTI PK models, we avoid the need of evaluating exponential matrices, without introducing the need of solving a linear equation system in each time step, otherwise associated with diagonalizing the system matrix.

The efficiency of the proposed method is demonstrated through benchmarking it against commonly used solvers, using a large model set for the anesthetic drug propofol.

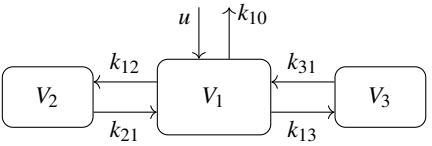

Figure 1. Mammillary three-compartment PK model. The drug is administered to the central compartment at infusion rate u, from where the drug is also eliminated with elimination rate k_{10}. Two peripheral compartments are connected to the central compartment where transfer rates constants k_{ij} governs the drug transfer from compartment i to j. The compartmental volumes are V_1, V_2 and V_3, respectively.

2. Pharmacokinetic modeling

Pharmacokinetics describe the absorption and distribution of a drug within the body. To be able to simulate pharmacokinetics and predict physiological parameters, such as the compartment volumes, it is common to use a compartment model. The idea of the compartment model is to collect organs or tissue of similar properties together in compartments and model the drug transfer between them.

Commonly used compartment models are structures of one, two, and three compartments. A one-compartment model approximates the body as a single compartment where the drug concentration is assumed to be uniformly distributed and eliminated through a first-order process. Extending this model results in the two- and three-compartment models, where the different compartments relate to different types of tissue.

The compartment models can have different topologies, due to how the compartments are arranged, and where sources and sinks enters and exits the system. For example, a mammillary model consists of a central compartment with peripheral compartments connected to it, with no interconnections among other compartments. In the context of intravenously administered drugs, the central compartment models the blood plasma.

Figure 1 provides a schematic illustration of the three-compartment mammillary model, used, for example, to model the PK of the anesthetic drug propofol, as explained in [Sahinovic et al., 2018]. We can also note from the figure that as long as addition and elimination are associated with the central compartment, as is the case for most intravenously administered drugs, the two models of two or one compartment are special cases of the three compartment model.

Diffusion processes transferring drug between communicating compartments are governed by non-negative transfer rate constants k_{ij}, as shown in Figure 1.

A state-space representation of the one-compartment model relating drug infusion rate $u(t)$ to drug concentration $x(t)$ is given by the first-order LTI model

$$\dot{x} = -k_{10}x + \frac{1}{V_1}u, \tag{1}$$

where k_{10} is the elimination-rate constant (1/time), and V_1 is the volume of distribution of the single compartment. We have left out the time dependence on the state variables $x(t)$ and input $u(t)$ for readability.

Similarly, the second-order compartment model is given by

$$\dot{x}_1 = -(k_{10}+k_{12})x_1 + k_{21}x_2 + \frac{1}{V_1}u, \tag{2a}$$

$$\dot{x}_2 = k_{12}x_1 - k_{21}x_2, \tag{2b}$$

where x_1 denotes drug concentration within the central compartment, while x_2 is the peripheral compartment concentration.

The third-order mammillary compartment model, shown in Figure 1, corresponds to

$$\dot{x}_1 = -(k_{10}+k_{12}+k_{13})x_1 + k_{21}x_2 + k_{31}x_3 + \frac{1}{V_1}u, \tag{3a}$$

$$\dot{x}_2 = k_{12}x_1 - k_{21}x_2 \tag{3b}$$

$$\dot{x}_3 = k_{13}x_1 - k_{31}x_3, \tag{3c}$$

where $x_k \,\forall k \in \{1,2,3\}$, is the drug concentration within compartment k.

3. Simulation of LTI systems

For a pharmacological relevant scenario, the input u changes only at discrete time instances during a treatment. At these instances, there is either a step change in the infusion rate, a drug bolus (modeled by an impulse), or both.

The peripheral compartment concentrations are most commonly not directly measurable, as the peripheral compartments are modeling constructs, rather than actual tissues. However, the central compartment concentration can be measured by drawing blood samples at discrete time instances.

Motivated by the circumstances detailed above, we consider methods for simulation of LTI systems when the input is a linear combination of time-shifted impulses and steps. This means that we are dealing with events from the list below, occurring in a sequence of known time instances:

- An impulse of fixed magnitude added to the central compartment;
- Addition of drug mass at a constant rate to the central compartment;
- Observation of the central compartment concentration.

3.1 General solution of LTI systems

Let $\boldsymbol{x}$ be a state vector where x_k represents the drug concentration of compartment $k = 1, ..., n$. The state dynamics of a scalar-input LTI system can be written as

$$\dot{\boldsymbol{x}}(t) = A\boldsymbol{x}(t) + Bu(t) \tag{4}$$

where A is an $n \times n$ matrix, B is an $n \times 1$ column vector and u is the input. For the PK models introduced in Section 2, A and B are uniquely determined by transfer-rate constants and the central compartment volume V_1.

The exact solution of Equation (4), derived in for example [Åström and Wittenmark, 2011], is

$$\boldsymbol{x}(t) = e^{At}\boldsymbol{x}(0) + \int_0^t e^{A(t-\tau)}Bu(\tau)d\tau, \tag{5}$$

We assign $t = 0$ to the instance where drug is first administered, corresponding to an initial drug concentration $\boldsymbol{x}(0) = \mathbf{0}$. If that is not the case, the zero time can be shifted so that $\boldsymbol{x}(0) = 0$ holds.

The solution Equation (5) can be evaluated through numerical approximation of the integral, and there exist numerous numerical integration methods to this end. Examples include *ode45* and other related methods accessible from the *lsim* wrapper in Matlab or DifferentialEquations.jl in Julia.

If the input changes only at discrete time instances t_k, a more efficient alternative to fixed (or adaptively variable) step-length numeric integration is to perform a exact zero-order-hold (ZOH) discretization of Equation (5):

$$\boldsymbol{x}(t_{k+1}) = e^{A(t_{k+1}-t_k)}\boldsymbol{x}(t_k) + \int_{t_k}^{t_{k+1}} e^{A(t_{k+1}-\tau)}d\tau Bu(t_k), \tag{6}$$

which can be rewritten on the compact form

$$\boldsymbol{x}_{k+1} = \Phi_k\boldsymbol{x}_k + \Gamma_k u_k, \tag{7a}$$

so that

$$\begin{aligned} \Phi_k &= e^{Ah_k}, \\ \Gamma_k &= \int_0^{h_k} e^{A\tau}d\tau B, \end{aligned} \tag{7b}$$

where the sampling period is

$$h_k = t_{k+1} - t_k, \tag{7c}$$

and subscript k denotes time dependence so that for example $\boldsymbol{x}_k = \boldsymbol{x}(t_k)$.

3.2 Simulation with impulses and piece-wise constant inputs

If we consider the input being an impulse (bolus) of magnitude v_k, administered at time t_k, we have

$$u_k = \delta_k v_k, \tag{8}$$

where $\delta_k = \delta(t_k)$ is the Dirac distribution (unit impulse) centered at $t = t_k$. For this case the state update of Equation (7a) becomes

$$\begin{aligned} \boldsymbol{x}_{k+1} &= e^{Ah_k}\boldsymbol{x}_k + \int_0^{h_k} e^{A\tau} B v_k \delta_0(\tau) d\tau \\ &= e^{Ah_k}\boldsymbol{x}_k + e^{Ah_k} B v_k = \Phi_k(\boldsymbol{x}_k + B v_k). \end{aligned} \tag{9}$$

If we instead consider a piece-wise constant input $u_k = w_k$, then Equation (5) takes on the form

$$\begin{aligned} \boldsymbol{x}_{k+1} &= e^{Ah_k}\boldsymbol{x}_k + \int_0^{h_k} e^{A\tau} d\tau B w_k \\ &= \Phi_k \boldsymbol{x}_k + \Gamma_k w_k. \end{aligned} \tag{10}$$

Combining Equation (9) and Equation (10), we get the updated state vector under both an impulse and a piece-wise constant input

$$\boldsymbol{x}_{k+1} = \Phi_k (\boldsymbol{x}_k + B v_k) + \Gamma_k w_k. \tag{11}$$

As a consequence of the identity

$$\underbrace{\begin{bmatrix} \Phi_k & \Gamma_k \\ 0 & I \end{bmatrix}}_{M} = \exp\left(\underbrace{\begin{bmatrix} A & B \\ 0 & 0 \end{bmatrix}}_{E} h_k \right), \tag{12}$$

which can be easily verified through $dM/dh_k = ME$, it is possible to evaluate Φ_k and Γ_K in Equation (7b) by computing an exponential matrix of dimension $n+1$. This makes the approach less computationally expensive than numeric integration schemes for small tolerances.

4. Fast simulation of PK models

Computing the matrix exponential needed to evaluate A_d at each dosing instance is the most time-consuming task associated with simulating the system using the exact solution for piece-wise constant inputs. We next show how we can get rid of this step.

Using the Laplace transform, the state dynamics Equation (4) can be written

$$X(s) = (sI - A)^{-1} B U(s). \tag{13}$$

For the considered PK models, this is equivalent to

$$\frac{X(s)}{U(s)} = \frac{\text{adj}(sI-A)B}{\det(sI-A)} = \frac{1}{V_1}\frac{\text{adj}(sI-A)\boldsymbol{e}_1}{\det(sI-A)}, \tag{14}$$

where the last equivalence comes from the fact that $B = (1/V_1)\boldsymbol{e}_1$, where $\boldsymbol{e}_1$ is the first unit vector in Euclidean $\mathbb{R}^n$. The numerator $\text{adj}(sI-A)$ is completely determined by the rate constants. For the i^{th} state in the state vector $X(s)$, with $i = 1,\ldots,n$, we can evaluate Equation (14) so that for each state $X_i(s)$

$$\frac{X_i(s)}{U(s)} = \frac{1}{V_1}\frac{\sum_{j=1}^{n} p_{ji}s^{n-j}}{(s-\lambda_1)\ldots(s-\lambda_n)}, \tag{15}$$

where p_{ij} are the numerator polynomial coefficients and λ_k is the k^{th} eigenvalue of the A-matrix. For the considered models, all eigenvalues are unique, real and strictly negative. Each of these eigenvalues can be explicitly expressed as a function of the rate constants of the system. We used a computer algebra system to solve the eigenvalue problem $A - \lambda I = 0$ for the three compartment case, to obtain the form

$$\lambda = \begin{bmatrix} -c_1 - c_7 \\ -c_9 - c_{10} \\ c_9 - c_{10} \end{bmatrix} \tag{16a}$$

where

$$\begin{aligned}
b_1 &= k_{10} + k_{12} + k_{13} + k_{21} + k_{31} \\
b_2 &= k_{21}(k_{10} + k_{13} + k_{31}) + k_{31}(k_{10} + k_{12}) \\
b_3 &= k_{10}k_{21}k_{31} \\
c_1 &= b_1/3 \\
c_2 &= c_1^3 \\
c_3 &= b_2/3 \\
c_4 &= c_3 - c_1^2 \\
c_5 &= (b_1c_3 - b_3)/2 \\
c_6 &= 2\left(c_5 + \sqrt{c_4^3 + (c_2 - c_5)^2} - c_2\right)^{1/3} \\
c_7 &= -\text{Re}(c_6) \\
c_8 &= \text{Im}(c_6) \\
c_9 &= c_8\sqrt{3}/2 \\
c_{10} &= c_1 - c_7/2.
\end{aligned} \tag{16b}$$

was obtained by manual substitutions within the corresponding expression tree.

Performing a partial-fraction decomposition of Equation (15), we obtain

$$\frac{X_i(s)}{U(s)} = \frac{1}{V_1}\sum_{j=1}^{n}\frac{r_{ji}}{s-\lambda_j}. \tag{17}$$

In the case of the three-compartment model and for state x_1—corresponding to the measurable central compartment concentration—the partial fraction decomposition is given by

$$\frac{p_{11}s^2+p_{21}s+p_{31}}{(s-\lambda_1)(s-\lambda_2)(s-\lambda_3)} = \frac{r_{11}}{s-\lambda_1}+\frac{r_{21}}{s-\lambda_2}+\frac{r_{31}}{s-\lambda_3}. \tag{18}$$

By multiplying both sides to get a common denominator, we obtain

$$\begin{aligned} p_{11}s^2+p_{21}s+p_{31} &= r_{31}(s-\lambda_2)(s-\lambda_3)+ \\ & r_{21}(s-\lambda_1)(s-\lambda_3)+r_{31}(s-\lambda_1)(s-\lambda_2). \end{aligned} \tag{19}$$

Matching powers of s results in the linear system

$$\underbrace{\begin{bmatrix} 1 & 1 & 1 \\ -(\lambda_2+\lambda_3) & -(\lambda_1+\lambda_3) & -(\lambda_1+\lambda_2) \\ \lambda_2\lambda_3 & \lambda_1\lambda_3 & \lambda_1\lambda_2 \end{bmatrix}}_{Q}\underbrace{\begin{bmatrix} r_{11} \\ r_{21} \\ r_{31} \end{bmatrix}}_{\boldsymbol{r}_1} = \underbrace{\begin{bmatrix} p_{11} \\ p_{21} \\ p_{31} \end{bmatrix}}_{\boldsymbol{p}_1}, \tag{20}$$

where the elements of P are completely determined by the transfer-rate constants.

Performing partial-fraction expansions of Equation (15) also for $k=1$ and $k=3$, we have that

$$QR = P, \tag{21a}$$

where

$$P = \begin{bmatrix} \boldsymbol{p}_1 & \boldsymbol{p}_2 & \boldsymbol{p}_3 \end{bmatrix} = \begin{bmatrix} 1 & 0 & 0 \\ k_{21}+k_{31} & k_{12} & k_{13} \\ k_{21}k_{31} & k_{12}k_{31} & k_{13}k_{21} \end{bmatrix}, \tag{21b}$$

$$R = \begin{bmatrix} \boldsymbol{r}_1 & \boldsymbol{r}_2 & \boldsymbol{r}_3 \end{bmatrix} = \begin{bmatrix} r_{11} & r_{12} & r_{13} \\ r_{21} & r_{22} & r_{23} \\ r_{31} & r_{32} & r_{33} \end{bmatrix}, \tag{21c}$$

where P is expressed in terms of the rate constants of the mammillary three compartment model Equation (3). (Note that despite the variable naming, Q and R are in general not the QR factors of P.)

Solving Equation (20) for $\boldsymbol{r}_1$, or more generally Equation (21a) for R, can be done by first explicitly computing the inverse of Q, since $R = Q^{-1}P$. For the three-compartment case, the inverse of Q can be expressed in terms of the eigenvalues as

$$Q^{-1} = \begin{bmatrix} \lambda_1^2/d_1 & \lambda_1/d_1 & 1/d_1 \\ \lambda_2^2/d_2 & \lambda_2/d_2 & 1/d_2 \\ \lambda_3^2/d_3 & \lambda_3/d_3 & 1/d_3 \end{bmatrix}, \tag{22a}$$

where

$$\begin{aligned} d_1 &= (\lambda_1 - \lambda_3)(\lambda_1 - \lambda_2), \\ d_2 &= (\lambda_2 - \lambda_3)(\lambda_2 - \lambda_1), \\ d_3 &= (\lambda_3 - \lambda_2)(\lambda_3 - \lambda_1). \end{aligned} \tag{22b}$$

The two-compartment model is a special case, obtained by removing the third row and column of the involved matrices, and equating any entry coefficient with subscript 3 to zero.

For a one-compartment model, there will be no need for a partial-fraction decomposition as the model is already of first order, resulting in $Q = 1$. Therefore, the one-compartment model can be simulated directly as explained below, with $R = 1$.

The same methodology can be used also for models of $n > 3$ compartments. However, for such models, the matrices P and Q do generally not have closed-form entries. However, they can still be numerically pre-computed. Doing so, and performing a LU factorization, enables replacement of the exponential matrix associated with each time step with one forward and one backward substitution needed to obtain R from P and the factors of Q.

Having computed R, we have access to the right-hand side of Equation (17). For each eigenvalue $j = 1, \ldots, n$, and state $i = 1, \ldots, n$, the right-hand side comprises of a parallel interconnection of n first-order systems, as a result of the partial-fraction expansion Equation (17). Each of these are on the form

$$\frac{r_{ij}}{V_1} \frac{1}{s - \lambda_j}. \tag{23}$$

A possible state-space realization of Equation (23) is

$$\begin{aligned} \dot{z}_j &= \lambda_j z_j + u, \\ x_j &= \frac{r_{ij}}{V_1} z_j. \end{aligned} \tag{24}$$

Zero-order-hold sampling of Equation (24) with sampling period h_k results in

$$\begin{aligned} z_{k+1} &= \varphi_j z_k + \gamma_j u_k, \\ x_k &= \frac{r_{ij}}{V_1} z_k, \end{aligned} \tag{25a}$$

where

$$\begin{aligned} \varphi_j &= e^{\lambda_j h_k}, \\ \gamma_j &= \frac{1}{\lambda_j} (\varphi_j - 1). \end{aligned} \tag{25b}$$

We will now return to study the full system. For all eigenvalues $j = 1, \ldots, n$, we put the corresponding φ_j, γ_j and z_j from Equation (25) into arrays of length j.

This allows us to perform parallel computations of each subsystem and therefore speeding up the simulation of the full system. The resulting updating scheme is

$$z_{k+1} = \boldsymbol{\varphi}_k \odot z_k \oplus \boldsymbol{\gamma}_k u_k, \tag{26a}$$

$$\boldsymbol{x}_k = \frac{1}{V_1} R^\top z_k, \tag{26b}$$

where

$$z = \begin{bmatrix} z_1 & \dots & z_n \end{bmatrix}^\top, \tag{27a}$$

$$\boldsymbol{\varphi} = \begin{bmatrix} \varphi_1 & \dots & \varphi_n \end{bmatrix}^\top, \tag{27b}$$

$$\boldsymbol{\gamma} = \begin{bmatrix} \gamma_1 & \dots & \gamma_n \end{bmatrix}^\top, \tag{27c}$$

and $\odot$ denotes the element-wise product (sometimes also called the Hadamard or Schur product) and $\oplus$ denotes the vector addition so that $. \oplus u = . + \mathbf{1}u$.

We have now demonstrated how an n-compartment model can be simulated as a system of n first-order systems, which increases the computational efficiency compared to traditional methods. Specifically, for the case of $n \leq 3$ compartment models with unique eigenvalues, the approximation-free simulation of the state evolution between consecutive (bolus or infusion change) dosing events comes down to computing R of Equation (17). The inverse Q^{-1} is pre-computed using the closed-form expression Equation (22), relying on the also pre-computed eigenvalues of the system matrix A. Due to the structure of the system, the eigenvalues can be evaluated using the algorithm presented in Equation (16), that is computationally much cheaper than solving a general eigenvalue problem of dimension $n = 3$. Finally, the simulation only results in the computation of three *scalar* exponentials and simple arithmetic operations.

4.1 Simulation algorithm

Instead of simulating the system with $\boldsymbol{x}$ as a state, we can simulate the system in Equation (26) with z as a state and convert back to $\boldsymbol{x}$ once we are interested in the physiological state. The simulation can now be divided into two parts, pre-processing and simulation between events. The pre-processing part includes a computation of R and the n eigenvalues of A. Once this has been done, cheap simulation between events can be performed in parallel.

If we use the state update for impulses and piece-wise constant inputs in Section 3 and Equation (11) together with the state update in Equation (27), we get

$$z_{k+1} = \boldsymbol{\varphi}_k \odot (z_k \oplus v_k) \oplus \boldsymbol{\gamma}_k w_k, \tag{28}$$

where z_0 is some initial state.

The simulation between events now only has two vector-vector additions and two element-wise product evaluations, each involving n elements.

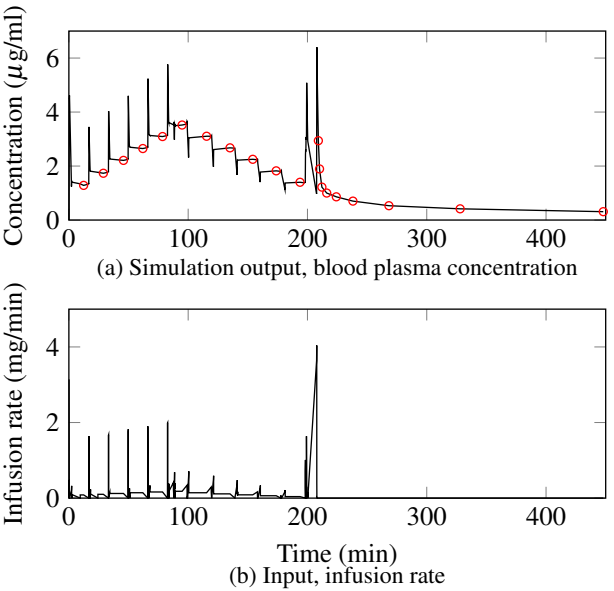

Figure 2. Simulation of one patient in the model set published in [Eleveld et al., 2018]. The upper figure shows the simulation output, the blood plasma concentration of the central compartment. Red circles shows times for observation. The lower figure shows the infusion rate, administered to the central compartment.

At those time instances when we are interested in the physiological state x_i, the output can be computed from Equation (26b), with the state update given in Equation (28).

5. Simulation example

In this paper, we consider simulation of a model set for the anesthetic drug propofol. It has been published in full in in a supplement to [Eleveld et al., 2018] and is a data collection from 30 previously published studies. The model set includes identified individual model parameters of the three-compartment model, input infusion data and blood plasma concentrations of 1033 patients as well as observation times.

One simulated example is shown in Figure 2 where the upper figure shows the simulated blood plasma concentration in black, and where the observation instances are marked in red. Note that we are typically only interested in the state at these instances. The lower part of Figure 2 illustrates the infusion rate.

The simulations algorithms compared in this paper are implemented in either Matlab or Julia. In Matlab, *lsim* has been used for simulation. Due to the fact that the time between events is not constant, *lsim* has to be called at each time instance.

Table 1. Wall-clock time for simulation of the model set (1033 patients) published in [Eleveld et al., 2018]. The simulations has been performed in Matlab and Julia, using the simulation methods described in Section 5. Memory allocation count is not accessible for the Matlab simulation.

Software	Method	Time (ms)	Allocations
Matlab	*lsim*	64585	-
Julia	$x_{k+1} = \Phi_k x_k + \Gamma_k u_k$	548	$2.03 \cdot 10^6$
Julia	DifferentialEquations.jl	230	$2.79 \cdot 10^7$
Julia	FastPKSim.jl	1.58	0

In Julia, the proposed simulation algorithm in Section 4.1, available through the package FastPKsim.jl [Wahlquist, 2022b] is compared to direct computation of the exact solution in Equation (11) and simulation using DifferentialEquations.jl with callbacks. For the direct method in Equation (11), computation of the exponential matrix is performed using Padé approximation.

6. Results

Table 1 shows the wall-clock time for simulation of the full model set (1033 patients) published in [Eleveld et al., 2018], with the simulations in Matlab and Julia, as explained in Section 5. Even though all simulations in Table 1 are on the millisecond scale, faster simulations are of outmost importance if thousands (or more) simulations needs to be performed. All simulations were performed single-threaded. For each simulation method, we performed 10 simulations and in the table, we present the median simulation time of these simulations. Simulations in Julia also includes the total memory allocation, which is not available for the Matlab simulation.

The proposed simulator can be found in the Julia package FastPKSim.jl, see [Wahlquist, 2022b]. Code and data used to generate the results in Table 1 are available in a GitHub repo, see [Wahlquist, 2022a]. All computations were performed on a standard Linux PC (Intel i5-8265U, 8-core processor) in Julia 1.8.2 and Matlab 2022b.

7. Discussion

In this paper, we have demonstrated a fast simulator for LTI PK compartment models of $n = 1$, 2 or 3 compartments. Instead of simulating an n-compartment model, we simulate n first-order models, resulting in a significant speedup compared to traditional methods. By exploiting model structure, we circumvent the need to solve a linear equation system at each time step to obtain a diagonalizing transform needed to achieve this. For models with $n > 3$ compartments (being far less common in

pharmacological applications), we would additionally rely on one forward and one backward substitution using pre-computed LU factors of Q to solve the equation system associated with diagonalization. Taking care to avoid dynamic memory allocation further contributes to high efficiency of our implementation in FastPKSim.jl. In comparison to existing ODE-solvers where the solution is approximate to some degree, the proposed simulator is exact down to the precision of the scalar exponential function evaluation.

When using the simulator as part of an inference engine or to train a symbolic regression network as in [Wahlquist et al., 2022], differentiation through the simulator (with respect to model parameters) is necessary. Since Julia has native support for automatic differentiation, this can be performed very cheaply with $\mathcal{O}(1)$ complexity, and with exactness limited only by machine precision. In contrast, ODE solvers called through the *lsim* wrapper in Matlab would need to rely on finite-difference approximations to compute gradients.

In near-future work, we aim to setup FastPKSim.jl to run fully parallelized on a cloud architecture, and use automatic differentiation to train symbolic regression networks, to demonstrate viability of the methodology introduced in [Wahlquist et al., 2022] in realistic data-driven modeling scenarios—something that would require far too long computational times using conventional ODE solvers.

Funding

This work was partially funded by the Swedish government through the Swedish Research Council (grant 2017-04989), The Royal Physiographic Society in Lund, the Hans-Gabriel and Alice Trolle-Wachtmeister foundation and by the Swedish foundation for Strategic Research. The authors are members of the Excellence Center at Linköping-Lund in Information Technology (ELLIIT).

References

Åström, K. and B. Wittenmark (2011). *Computer-Controlled Systems: Theory and Design, Third Edition*. Dover Books on Electrical Engineering. Dover Publications. ISBN: 9780486486130.

Bezanson, J., A. Edelman, S. Karpinski, and V. B. Shah (2017). "Julia: A fresh approach to numerical computing". *SIAM Review* **59**:1, pp. 65–98. DOI: 10.1137/141000671.

Eleveld, D. J., P. Colin, A. R. Absalom, and M. M. R. F. Struys (2018). "Pharmacokinetic-pharmacodynamic model for propofol for broad application in anaesthesia and sedation". *British Journal of Anaesthesia* **120**:5, pp. 942–959. ISSN: 0007-0912, 1471-6771. DOI: 10.1016/j.bja.2018.01.018.

Rackauckas, C., Y. Ma, A. Noack, V. Dixit, P. K. Mogensen, S. Byrne, S. Maddhashiya, J. B. Santiago Calderón, J. Nyberg, J. V. Gobburu, et al. (2020). "Accelerated predictive healthcare analytics with pumas, a high performance pharmaceutical modeling and simulation platform". *bioRxiv*. DOI: 10.1101/2020.11.28.402297.

Rackauckas, C. and Q. Nie (2017). "DifferentialEquations.jl – a performant and feature-rich ecosystem for solving differential equations in Julia". *Journal of Open Research Software* **5**:1.

Sahinovic, M. M., M. M. R. F. Struys, and A. R. Absalom (2018). "Clinical pharmacokinetics and pharmacodynamics of propofol". *Clinical Pharmacokinetics* **57**:12, pp. 1539–1558. DOI: 10.1007/s40262-018-0672-3.

Sheiner, L. B. and S. L. Beal (1980). "Evaluation of methods for estimating population pharmacokinetics parameters. I. Michaelis-Menten model: routine clinical pharmacokinetic data". *Journal of Pharmacokinetics and Pharmacodynamics* **8**, pp. 553–571. DOI: 10.1007/BF01060053.

Wahlquist, Y. (2022a). *Fast simulation of pharmacokinetics*. commit: 5246112. URL: https://github.com/wahlquisty/fast-simulation-of-pharmacokinetics (visited on 2022-09-29).

Wahlquist, Y. (2022b). *FastPKSim.jl*. commit: 55e878d. URL: https://github.com/wahlquisty/FastPKSim.jl (visited on 2022-09-30).

Wahlquist, Y., M. Morin, and K. Soltesz (2022). "Pharmacometric covariate modeling using symbolic regression networks". In: *2022 IEEE Conference on Control Technology and Applications (CCTA)*, pp. 1099–1104. DOI: 10.1109/CCTA49430.2022.9966112.

Paper III

Learning Pharmacometric Covariate Model Structures with Symbolic Regression Networks

Ylva Wahlquist Jesper Sundell Kristian Soltesz

Abstract

Efficiently finding covariate model structures that minimize the need for random effects to describe pharmacological data is challenging. The standard approach focuses on identification of relevant covariates, and present methodology lacks tools for automatic identification of covariate model structures. Although neural networks could potentially be used to approximate covariate-parameter relationships, such approximations are not human-readable and come at the risk of poor generalizability due to high model complexity.

In the present study, a novel methodology for the simultaneous selection of covariate model structure and optimization of its parameters is proposed. It is based on symbolic regression, posed as an optimization problem with a smooth loss function. This enables training of the model through back-propagation using efficient gradient computations.

Feasibility and effectiveness are demonstrated by application to a clinical pharmacokinetic data set for propofol, containing infusion and blood sample time series from 1031 individuals. The resulting model is compared to a published state-of-the-art model for the same data set. Our methodology finds a covariate model structure and corresponding parameter values with a slightly better fit, while relying on notably fewer covariates than the state-of-the-art model. Unlike contemporary practice, finding the covariate model structure is achieved without an iterative procedure involving manual interactions.

Keywords: Pharmacometrics, Covariate modeling, Pharmacokinetics, Symbolic regression, Neural networks

Originally published in Journal of Pharmacokinetics and Pharmacodynamics (2023). The original version is available at `https://doi.org/10.1007/s10928-023-09887-3`.

1. Introduction

Pharmacokinetics (PK) are the dynamics governing drug uptake, distribution and elimination from the body. For many drugs, it is common to assert a low-order linear and time-invariant (LTI) compartment model for PK modeling. Such low-order models typically capture the uptake, distribution, and elimination dynamics adequately. Increasing model complexity through, for example, additional compartments results in models where the parameters are not practically identifiable from data collected during clinical trials or clinical practice.

While suitable PK model structures (e.g. number of compartments and topology) for common drugs can be established from data, a notable challenge exists in that the parameter values that explain the PK for one individual, are often not suitable for another. Such inter-individual variability is partly explainable by individual-specific features that are referred to as covariates, and partly attributed to random effects.

The purpose of pharmacometric covariate modeling is to identify covariates (i.e., fixed effects) responsible for inter-individual variability, thus minimizing random effects. The gold standard is to approach this problem in a Bayesian setting using mixed-effect modeling, for which there exists both mature [Sheiner and Beal, 1980] and novel [Rackauckas et al., 2020] tools. However, to apply mixed-effect modeling, one needs to decide which of possibly many covariates (e.g. age, body mass, gender, or genetic factors) to include. One also needs to decide on a parametric function that maps included covariates to parameters of the PK model. There is a tradition of using functions that are of sufficiently low complexity to be human-readable, and some function classes are more popular than others [Marsh et al., 1991; Eleveld et al., 2018]. However, for data sets including numerous covariates, selection of covariates and functions to consider is a combinatorial problem, where the search space may become limiting. Furthermore, due to step-wise approaches typically used for covariate identification, functions including multiple covariates are typically only considered if supported by prior knowledge [Jonsson and Karlsson, 1998].

Recently, the interest in combining machine learning (ML) and pharmacometrics [McComb et al., 2022] has increased. For example, ML has shown promising results in concentration predictions [Bräm et al., 2022], identification of influential covariates [Janssen et al., 2022; Sibieude et al., 2021], as well as parameter regression and model selection with the use of genetic algorithms and neural networks (NNs) [Sibieude et al., 2022]. The ML methods have been able to match, and even beat, classic NLME modeling at a much higher computational speed. However, using ML to select influential covariates and identify the structural model simultaneously has, to our knowledge, not yet been studied.

In the present paper, we provide an automatic method for simultaneous covariate selection and identification of covariate functions using an adaptation of ML. Similarly to the current standard approach, we maintain simple human-readable ex-

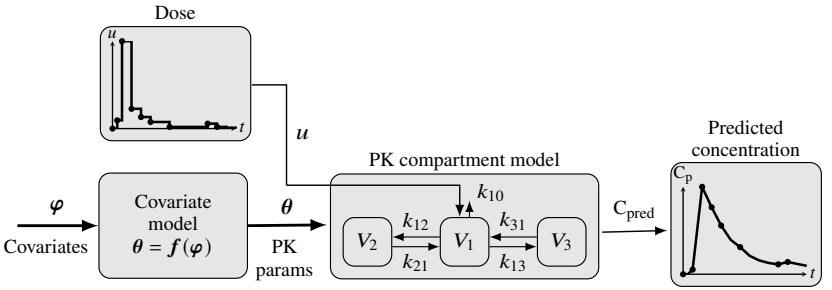

Figure 1. Mammillary three-compartment model example illustrating our novel method. The objective is to automatically learn the covariate model $\boldsymbol{f}$ that maps a known covariate vector $\boldsymbol{\varphi}$ (comprising e.g., age, gender, or genetic factors) to the parameter vector $\boldsymbol{\theta}$ (e.g. rate constant $k_{\cdot\cdot}$ and volumes $V_{\cdot}$) of a fixed-structure pharmacometric (PK) model. The method is data-driven in that it uses drug administration profiles (time series data) u, and model-based in that it assumes a PK model of known structure. In this example, $\boldsymbol{f}$ is learned to minimize some error measure between observed (i.e. measured from samples) blood plasma concentrations and corresponding predictions C_{pred} by the model. Dots in the graphs show instances of dose changes and blood samples, respectively.

pressions. The method is based on symbolic regression [Davidson et al., 2003], that approximates the underlying combinatorial problem with a smooth continuous one, thus enabling the use of efficient gradient-based optimization methods.

To illustrate utility, we apply our methodology to a large data set for the drug propofol and compare the resulting covariate model with the current state-of-the-art model [Eleveld et al., 2018]. Our method produces a model with increased predictive performance, using fewer covariates. Furthermore, the covariate model is optimized autonomously in contrast to the prevalent iterative and manual procedure.

2. Methods

The method described in this paper aims to automatically learn closed-form pharmacometric parameter–covariate relationships from data. We will consider learning expressions for PK model parameters from drug administration and resulting blood plasma concentration data, both of which are time series, but not necessarily synchronous or equidistant samples. The overarching setup for this is shown in Figure 1 and we will focus on a concrete example based on a large multi-study data set published in [Eleveld et al., 2018] for the anesthetic drug propofol, commonly modeled with a mammillary three-compartment model [Schnider et al., 1998].

Table 1. Covariate candidates considered in the PK model of [Eleveld et al., 2018] as well as in our modeling. Individuals of the data set fall within the reported ranges.

Covariate	Interpretation	Unit	Range
φ_1	Age	Years	0–88
φ_2	Weight	kg	0.68–160
φ_3	BMI	$\mathrm{kg\,m^{-2}}$	6.2–52.8
φ_4	Gender	Male/female	670 M/ 361 F
φ_5	Blood sampling site	Arterial/venous	727 A/ 306 V

2.1 Data set

We demonstrate our method on a data set composed of propofol plasma concentration observations from 1,031 individuals[1] from 30 clinical studies aggregated by Eleveld et al. [Eleveld et al., 2018], from here on referred to as the *data set*. Ethical approvals of the underlying studies are declared in the original publications, referenced by [Eleveld et al., 2018]. The data set contains 15,433 observations, of which 11,530 were arterial and 3903 venous. Of the 1031 individuals, there were 670 males and 361 females with ages ranging from 27 weeks to 88 years, and weights ranging from 0.68 to 160 kg, see Table 1.

The main reason for choosing this data set as a demonstrator is that propofol is a drug with well-studied pharmacokinetics. Evidence of this, which also constitutes a benchmark for our demonstrator, is the model presented in [Eleveld et al., 2018]. Furthermore, the data set is that it has been openly disclosed by Eleveld et al., enabling transparent third-party analysis of our work.

In our model development, we consider age, weight, BMI, gender, and blood sampling site (arterial or venous) as potential covariates of our PK model. These are the same candidates as considered in [Eleveld et al., 2018], where individual demographics were disclosed as part of the data set.

The data was pre-processed the same way as in [Eleveld et al., 2018]: data points corresponding to subsequent infusion changes spaced closer than 1 s apart in the time dimension, or 0.5 $\mu\mathrm{g\,s^{-1}}$ in the dose dimension were merged.

[1] The original data set in [Eleveld et al., 2018] comprises of 1033 individuals but two of them were excluded due to lack of observation data.

2.2 Pharmacokinetic model

We consider a three-compartment mammillary model to describe the pharmacokinetics of propofol. The drug concentration x_i [$\mu g\,L^{-1}$] in compartment $i \in \{1,2,3\}$ is

$$\dot{x}_1 = -(k_{10}+k_{12}+k_{13})x_1 + k_{21}x_2 + k_{31}x_3 + \frac{1}{V_1}u, \tag{1a}$$

$$\dot{x}_2 = k_{12}x_1 - k_{21}x_2, \tag{1b}$$

$$\dot{x}_3 = k_{13}x_1 - k_{31}x_3, \tag{1c}$$

where k_{ij} describes the drug transfer rate $[1/s]$ from compartment j to i. The drug is administered at rate u [$\mu g\,s^{-1}$] to the central compartment ($i = 1$), which is also where the propofol plasma concentration is measured. The volume of the central compartment is V_1 [L].

In the literature, the equivalent parameterization of volumes (V_1, V_2, V_3) and clearances (CL, Q_2, Q_3) constitutes a common alternative to Equation (1). The conversion between these parameterizations is

$$CL = k_{10}V_1, \qquad [L\,s^{-1}] \tag{2a}$$

$$Q_2 = k_{12}V_1, \qquad [L\,s^{-1}] \tag{2b}$$

$$Q_3 = k_{13}V_1, \qquad [L\,s^{-1}] \tag{2c}$$

$$V_2 = \frac{k_{12}}{k_{21}}V_1, \qquad [L] \tag{2d}$$

$$V_3 = \frac{k_{13}}{k_{31}}V_1. \qquad [L] \tag{2e}$$

We have chosen to implement our method using the parameterization Equation (1) due to numeric benefits. These are further explained in [Wahlquist et al., 2023], where we developed a fast and natively differentiable simulator for the three-order mammillary model.

2.3 Covariate model

The covariate model, shown in Figure 1, is expressed as a function $\boldsymbol{f}$ that maps the covariate vector $\boldsymbol{\varphi} = [\varphi_1, \ldots, \varphi_{n_\varphi}]^\top$ to the vector $\boldsymbol{\theta} = [\theta_1, \ldots, \theta_{n_\theta}]^\top$ of PK model parameters. Thus $\boldsymbol{f}$ has components $f_1, \ldots, f_{n_\theta}$, each mapping the covariate vector $\boldsymbol{\varphi}$ to one of the n_θ PK model parameters.

In our example with the three-compartment model for propofol, there are $n_\varphi = 5$ covariates and $n_\theta = 6$ PK model parameters according to Table 1.To not favor covariates based on their scale, all input covariates were normalized during model development. Continuous inputs (age, weight and BMI) were scaled from 0 to 1, and categorical inputs (gender and blood sampling site) were scaled to ± 0.5.

2.4 Predictive performance

To assess the quality of a particular covariate model candidate $\boldsymbol{f}$, we need a performance measure that captures how well $\boldsymbol{f}$ reflects the training data. Most optimization methods, including the ones used in this paper, relies on this measure being scalar.

For comparability, we employ the same scalar performance measures as those used in [Eleveld et al., 2018]: We train our model to minimize an ensemble average of absolute logarithmic error (ALE). Subsequently, we evaluate predictive performance in terms of ALE, and three additional error measures: logarithmic error (LE), prediction error (PE), and absolute prediction error (APE).

For each individual in the data set, there is a vector of observation–prediction errors, where each entry corresponds to the difference between a blood sample observation and the value predicted by the model. Observation-prediction errors could thus be computed for each sample, over a time series for one individual, or the entire data set. This prompts a consistent notation and we index by ij the error over a sample j for individual i, whereas a total error over a time series for an individual is indexed by i.

The per-sample (absolute) logarithmic error (A)LE [Masui et al., 2010] is thus

$$\mathrm{LE}_{ij} = \ln(C_{\mathrm{obs}_{ij}}/C_{\mathrm{pred}_{ij}}), \tag{3a}$$

$$\mathrm{ALE}_{ij} = |\mathrm{LE}_{ij}|, \tag{3b}$$

where $C_{\mathrm{obs}_{ij}}$ are observed (measured) plasma concentrations and $C_{\mathrm{pred}_{ij}}$ are corresponding predictions produced by the model.

Similarly, the per-sample (absolute) prediction error (A)PE [Varvel et al., 1992] is

$$\mathrm{PE}_{ij} = \left(\frac{C_{\mathrm{obs}_{ij}} - C_{\mathrm{pred}_{ij}}}{C_{\mathrm{pred}_{ij}}}\right) \cdot 100\% \tag{4a}$$

$$\mathrm{APE}_{ij} = |\mathrm{PE}_{ij}|. \tag{4b}$$

To avoid divisions by zero if $C_{\mathrm{pred}_{ij}} = 0$, a special casing is needed where the error is set to zero for such samples.

Using Equation (3) and Equation (4), corresponding per-individual errors were computed by taking the median, resulting in the median absolute logarithmic error (MdALE):

$$\mathrm{MdALE}_i = \mathrm{median}\left(\mathrm{ALE}_{ij}\right), \quad j = 1, \ldots, n_i, \tag{5}$$

where n_i is the number of entries of the time series from individual i.

To train the model of [Eleveld et al., 2018] and the ones considered here, a single scalar loss function representing model fit is required. This is obtained by averaging across the individuals. Training the covariate model to minimize ALE

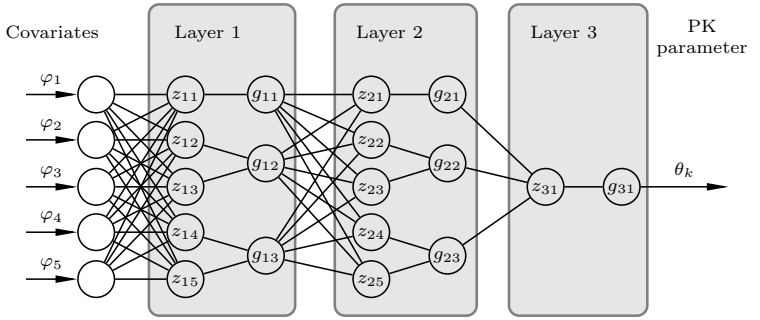

Figure 2. Symbolic regression network with three layers, each marked by a gray box. The output of node z_{li} at layer l is the i^{th} component of $\boldsymbol{z}_l = W_l \boldsymbol{x}_l + \boldsymbol{b}_l$, where $\boldsymbol{x}_l$, W_l and $\boldsymbol{b}_l$ are the input vector, weight matrix, and bias vector of that layer. The base expressions g_{li} acting on z_{li} take on the role of activation functions used in ordinary ANNs. For example is the output of the first layer (and therefore input to the second layer) $\boldsymbol{x}_2 = \boldsymbol{g}_1(W_1 \boldsymbol{x}_1 + b_1)$. Input and output of the network is the covariate vector $\boldsymbol{\varphi} = \boldsymbol{x}_1$ and the PK parameter $\theta_k = \boldsymbol{x}_4$, respectively.

thus translates into minimizing

$$J_{\text{ALE}} = \frac{1}{n} \sum_{i=1}^{n} \text{MdALE}_i, \tag{6}$$

where n is the number of individuals in the data set.

Similarly to the analysis performed in [Eleveld et al., 2018], ALE and APE were used as indicators of model accuracy and LE and PE were used as indicators of bias. Values closer to zero for ALE and APE reflect better accuracy and values closer to zero for LE and PE indicate less bias.

Clinically acceptable ranges for MdPE_i and MdAPE_i are $10-20\%$ and $20-40\%$, respectively [Schüttler et al., 1988; Eleveld et al., 2018; Varvel et al., 1992]. This translates to acceptable clinical ranges for bias measure $\text{MdLE}_i < 0.18$ and accuracy measure $\text{MdALE}_i < 0.34$.

Of note, the choice of loss function will affect how outliers are penalized, where using an average loss across individuals would for example penalize outliers more than a median loss over individuals.

2.5 Symbolic regression networks

At the core of our methodology lies a small artificial neural network (ANN) with a specific structure, that of a *symbolic regression network* [Martius and Lampert, 2017], representing a simple closed-form expression. In our case, the purpose is to learn human-readable closed-form expressions describing the covariate model $\boldsymbol{f}$. A schematic illustration of such network is shown in Figure 2.

In general, ANNs can be viewed as flexible function approximators that can be trained to represent input-output mappings that fit available data. An ANN consists of n_l layers, where the output vector $\boldsymbol{x}_{l+1}$ of layer l is obtained by applying a vector of nonlinear *activation functions* $\boldsymbol{g}_l$ to an affine transformation $\boldsymbol{z}_l$ to the layer input $\boldsymbol{x}_l$:

$$\boldsymbol{z}_l = W_l \boldsymbol{x}_l + \boldsymbol{b}_l, \tag{7a}$$

$$\boldsymbol{x}_{l+1} = \boldsymbol{g}_l(\boldsymbol{z}_l). \tag{7b}$$

The linear weight matrices W_l and bias vectors $\boldsymbol{b}_l$ constitute the free parameters used to train the network. In the conventional case, the components of the activation functions $\boldsymbol{g}_l$ are monotonously increasing functions, such as sigmoids [Dubey et al., 2022]. In contrast, a symbolic regression network can be understood as an ANN with the additional constraint that the resulting approximator $\boldsymbol{f}$ should be a human-readable closed-form expression of a mathematical function [Orzechowski et al., 2018; Martius and Lampert, 2017; Sahoo et al., 2018; Kim et al., 2021]. Training of symbolic regression networks is therefore often referred to as equation learning [Martius and Lampert, 2017]. The methodology has gained broad attention for its ability to produce impressive results in discovering (known) physical laws from data [Udrescu et al., 2020].

The activation functions $\boldsymbol{g}$ of a symbolic regression network represent mathematical functions that we refer to as *base expressions*. In standard symbolic regression, a sequence of topologies with different base expressions and scalar parameters–of which the weight matrices and bias vectors in Equation (7) would constitute a special case–are evaluated in search of one that fits the available data well [Koza, 1992]. Conventional equation learning is thus a combinatorial problem, with poor (exponential) time complexity, and therefore often approached using genetic algorithms [Koza, 1992].

Instead of relying on random perturbations as in genetic algorithms, we use gradient-based optimization methods common to conventional ANN training. To ensure human-readability, we enforce sparsity of the ANN by alternating training epochs with pruning epochs, in which the least important parameters are removed from the network. We next rely on a concrete example based on the Eleveld data set, to describe and illustrate this approach.

We set out with a nominal (unpruned) network of Figure 2. It constitutes our nominal representation of f_k, where the inputs are the covariates according to Table 1. Thus, the output of the network represents one of the PK parameters θ_k, such as k_{10} or V_1 of Equation (1). For a model with n_θ PK parameters, we use a parallel interconnection of n_θ symbolic regression networks, each modeling one component f_k of $\boldsymbol{f}$, mapping the covariate vector $\boldsymbol{\varphi}$ to each PK parameter θ_k, $k = 1, \ldots, n_\theta$.

In our example, the base expressions of each layer $l \in \{1,2,3\}$, with input vector $\boldsymbol{z}_l = \begin{bmatrix} z_{l1}, & z_{l2}, & \ldots \end{bmatrix}^\top$, were chosen to cover previously published PK models for propofol, such as [Eleveld et al., 2018] and [Schnider et al., 1998]:

$$\boldsymbol{g}_1(\boldsymbol{z}_1) = \begin{bmatrix} z_{11} \\ z_{12} \cdot z_{13} \\ |z_{14}|^{z_{15}}, \end{bmatrix}$$

$$\boldsymbol{g}_2(\boldsymbol{z}_2) = \begin{bmatrix} z_{21} \\ z_{22} \cdot z_{23} \\ \frac{z_{24}}{z_{25}+1}, \end{bmatrix}$$

$$g_3(z_3) = |z_3|,$$

where the g_3 assures positive output of the final layer. The division in $\boldsymbol{g}_2$ has the term one in the denominator to assure that the output does not blow if $z_{25} \geq 0$ approaches zero.

Training Minimizing the *loss function* Equation (6) across trainable parameters of the covariate model $\boldsymbol{f}$ is referred to as training. In our case, these parameters are stacked into a vector $\boldsymbol{\gamma}$, made up by the elements of all weight matrices and bias vectors. Since the data set is static, we can view training as minimization of the scalar-valued function $J_{\text{ALE}}(\boldsymbol{\gamma})$. In order to do so, we need to evaluate $J_{\text{ALE}}(\boldsymbol{\gamma})$. Doing so requires simulation of one PK model for each data set individual, to obtain the predicted plasma concentration at each observation time instance. This can be efficiently done using the method introduced in [Wahlquist et al., 2023].

In addition to the supporting fast simulation, the method of [Wahlquist et al., 2023] enables exact and efficient evaluation of derivatives of individual prediction errors with respect to the trainable model parameters. This allows us to train the covariate model $\boldsymbol{f}$ using conventional ANN back-propagation, using the stochastic gradient-based optimization algorithm ADAM [Kingma and Ba, 2017]. As with artificial neural networks in general, establishing formal convergence guarantees is challenging. However, in practice both standard deep learning networks and our symbolic regression do converge to models that fit data adequately well. Similarly to the deep learning case, convergence rate will also vary with data, choice of activation functions, learning rate, and initialization of the training. Our implementation, using the neural network package Flux [Innes, 2018b], relies on the differential programming capabilities of the Julia language [Bezanson et al., 2017]. A full disclosure of our implementation is found in the GitHub repository [Wahlquist, 2023].

Pruning To obtain simple human-readable expressions from an initially dense symbolic regression network, such as the one in Figure 2, we alternate between parameter training of the fixed network structure and pruning of the network.
The goal of this pruning is to obtain a sparse network structure, which translates into a readable expression of the corresponding covariate model. In the pruning process, we remove covariates and network parameters that have relatively little influence on the network output. This process is visually exemplified in in Figure 3.

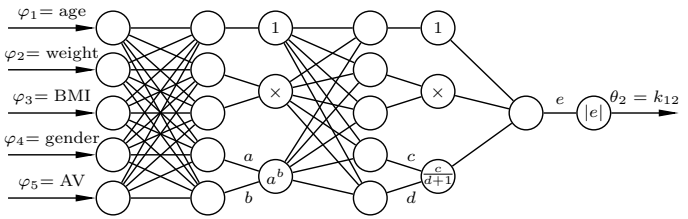

(a) Nominal (dense) symbolic regression network

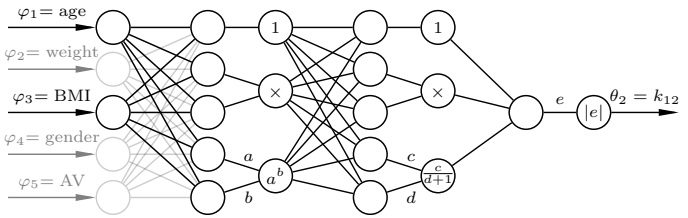

(b) Symbolic regression network after covariate pruning

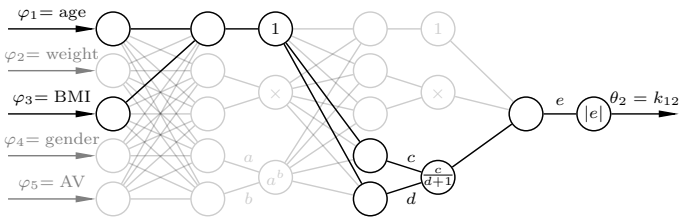

(c) Final symbolic regression network after covariate and parameter pruning

Figure 3. Pruning sequence of a symbolic regression network with output pharmacokinetic parameter $\theta_2 = k_{12}$. Input covariates are age, weight, gender, and arterial or venous sampling (AV). The nominal network has three dense layers, each followed by base expressions such as 1 (feedforward), multiplication, power function, division and absolute value. A black line represents a connection between two nodes, and a gray line represents a pruned (removed) connection. The final network represents the covariate expression of Equation (10b)

It is desirable to only include as many covariates as needed to explain the data [Jonsson and Karlsson, 1998]. Therefore, we start by identifying and removing the least important covariates from the symbolic regression network to obtain expressions with fewer covariates. Next, we prune network parameters $\boldsymbol{\gamma}$ (linear weights and biases) to obtain simple covariate expressions. Pruning a network parameter is achieved by fixing its value to zero and removing it from the vector $\boldsymbol{\gamma}$ of trainable parameters.

Before each pruning iteration, we train the network until convergence. This

translates into finding a local minimum of the loss function in Equation (6). At such minima, the partial derivatives of the loss function with respect to the trainable parameters are zero. Therefore, the second derivatives define the first non-zero terms of the Taylor series expansion that describe local parameter sensitivities, as further explained in Supplementary Section A. The second-order derivatives make up the elements of the Hessian matrix. Specifically its diagonal elements represent sensitivities in the corresponding individual parameters.

In the Taylor series expansion, the second-order terms take on the form

$$S(\gamma_k) = \gamma_k^2 H_k, \tag{8}$$

where H_k is the k^{th} Hessian diagonal element of the loss function with respect to the network parameter γ_k. $S(\gamma_k)$ denotes *salience* of a parameter γ_k [LeCun et al., 1989].

For pruning of the network parameters $\boldsymbol{\gamma}$, Equation (8) may be used directly. However, computing the salience for a covariate is not as straightforward since the Hessian elements would differ between individuals. A solution to this is to sum the salience contribution of each individual,

$$S(\varphi_k) = \sum_{i=1}^{n} \varphi_{ik}^2 (H_i)_k, \tag{9}$$

where $(H_i)_k$ is the k^{th} diagonal element of the Hessian, H_i, determining the sensitivity of the covariate φ_{ik} for individual i, and n is the number of individuals.

We use the Zygote package [Innes, 2018a] in Julia to compute the Hessian diagonal elements. In Supplementary Section A, we give a more detailed description of the Hessian-based pruning method, providing mathematical insight into this methodology.

Recipe: Symbolic regression A compact summary of our training and pruning scheme is provided below. Initially, we start with a nominal symbolic regression network, like the one shown in Figure 3a. It is sequentially trained and pruned until we obtain a final expression of sufficient complexity and fit. Our training and pruning sequence of a symbolic regression network is as follows:

1. Choose a nominal symbolic regression network architecture, and corresponding base expressions.
2. Train the network until convergence.
3. Compute the salience of each (remaining) covariate, $S(\varphi_k)$ of Equation (9).
4. Sort the covariates by saliency and remove the covariate with the smallest salience.
5. If the desired final number of covariates is reached, continue to step 6, otherwise return to step 2.

6. Train the reduced network until convergence.
7. Compute the salience of each (remaining) trainable network parameter, $S(\gamma_k)$ of Equation (8).
8. Sort the network parameters by saliency and remove N parameters with the smallest salience.
9. If the desired final number of network parameters is reached, continue to step 10, otherwise return to step 6.
10. Train the reduced network until convergence.
11. Convert the resulting network to a readable functional expression.

The number of covariates and network parameters to keep in the final symbolic regression network is a trade-off between fit to data and complexity of the final expression. In our example, illustrated in Figure 3, we remove one covariate at each pruning iteration, until only two covariates are left. Next, we remove the $N = 10$ least sensitive parameters in the first parameter pruning iteration, and then one parameter per subsequent pruning iteration until only twelve network parameters are left. More details of the pruning and training can be found in [Wahlquist, 2023]. In [Wahlquist et al., 2022], we demonstrate that our methodology can identify functions of known shapes correctly.

Initialization of the parameter values associated with step 1 of the recipe affects the fit of the resulting final model. To mitigate the risk of poor model fit due to an unfortunate initialization, the recipe could be run several times, where the best fitting model is kept. In our example, we have executed the recipe eight times.

2.6 Limits of performance

Structural mismatch between the asserted PK model structure Equation (1) and the data, in combination with measurement errors, induce upper and lower limits on prediction errors of the trained covariate model. Here we explain how these limits can be characterized by training two additional models.

Even with a very complex covariate model, one cannot expect perfect fit to data (zero loss). This is because the fixed (three-compartment) PK model structure is only an approximation of the actual pharmacokinetics, combined with (blood sample) measurement errors. Part of the loss remaining after applying our covariate modeling scheme can thus be attributed to this mismatch. To indicate how much, we optimize one set of (three-compartment) PK parameters for each individual in the data set. This results in a completely covariate-free model. While it will fit data better than any covariate model, it does not generalize. This makes it practically useless for purposes other than providing an upper limit for performance.

Another natural question to ask is how much we gain (in terms of loss) by considering covariate dependencies. To do this, we optimize a constant, i.e. covariate-free, model — one where all individuals share the same (three-compartment) PK parameter values. This model does constitute a lower bound of the achievable predictive performance that any covariate-based model should beat.

For these two additional models, PK parameter optimization was done with the optimization package Optim.jl [Mogensen and Riseth, 2018], to minimize the same loss as for our covariate model based on symbolic regression. Implementation details can be found in [Wahlquist, 2023].

3. Results

Applying the proposed methodology to the Eleveld data set [Eleveld et al., 2018], resulted in the following covariate model, mapping covariates to rate constants and central compartment volume of the PK model Equation (1):

$$k_{10} = 0.00441\frac{\mathrm{WGT}}{\mathrm{WGT_{max}}} + 0.00342 \quad [\mathrm{s^{-1}}] \quad (10a)$$

$$k_{12} = \left|\frac{0.158\frac{\mathrm{AGE}}{\mathrm{AGE_{max}}} - 0.00431\frac{\mathrm{BMI}}{\mathrm{BMI_{max}}} - 0.188}{0.64\frac{\mathrm{AGE}}{\mathrm{AGE_{max}}} - 0.0174\frac{\mathrm{BMI}}{\mathrm{BMI_{max}}} - 0.743}\right| \quad [\mathrm{s^{-1}}] \quad (10b)$$

$$k_{13,\mathrm{male}} = \frac{0.0058\left(\frac{\mathrm{AGE}}{\mathrm{AGE_{max}}}\right)^2 + 0.00208\frac{\mathrm{AGE}}{\mathrm{AGE_{max}}} + 0.0026}{2.75\left(\frac{\mathrm{AGE}}{\mathrm{AGE_{max}}}\right)^2 + 0.985\frac{\mathrm{AGE}}{\mathrm{AGE_{max}}} + 0.601} \quad [\mathrm{s^{-1}}] \quad (10c)$$

$$k_{13,\mathrm{female}} = \frac{0.0058\left(\frac{\mathrm{AGE}}{\mathrm{AGE_{max}}}\right)^2 - 0.00208\frac{\mathrm{AGE}}{\mathrm{AGE_{max}}} + 0.0026}{2.75\left(\frac{\mathrm{AGE}}{\mathrm{AGE_{max}}}\right)^2 - 0.985\frac{\mathrm{AGE}}{\mathrm{AGE_{max}}} + 0.601} \quad [\mathrm{s^{-1}}] \quad (10d)$$

$$k_{21} = \left|0.00408\left(\frac{\mathrm{BMI}}{\mathrm{BMI_{max}}}\right)^2 - 8.16\cdot 10^{-4}\frac{\mathrm{BMI}}{\mathrm{BMI_{max}}} - 0.0057\frac{\mathrm{BMI}}{\mathrm{BMI_{max}}}\frac{\mathrm{WGT}}{\mathrm{WGT_{max}}} + 0.00218\right| \quad [\mathrm{s^{-1}}] \quad (10e)$$

$$k_{31,\mathrm{male}} = 4.52\cdot 10^{-5} + 1.92\cdot 10^{-5}\frac{\mathrm{AGE}}{\mathrm{AGE_{max}}} \quad [\mathrm{s^{-1}}] \quad (10f)$$

$$k_{31,\mathrm{female}} = 4.52\cdot 10^{-5} - 1.92\cdot 10^{-5}\frac{\mathrm{AGE}}{\mathrm{AGE_{max}}} \quad [\mathrm{s^{-1}}] \quad (10g)$$

$$V_1 = 0.0596\frac{\mathrm{AGE}}{\mathrm{AGE_{max}}} + 18.7\frac{\mathrm{WGT}}{\mathrm{WGT_{max}}} - 13.7\left(\frac{\mathrm{WGT}}{\mathrm{WGT_{max}}}\right)^2 - 3.5\frac{\mathrm{AGE}}{\mathrm{AGE_{max}}}\frac{\mathrm{WGT}}{\mathrm{WGT_{max}}} - 0.0557. \quad [\mathrm{L}] \quad (10h)$$

AGE, WGT, BMI represent age [years], weight [kg] and body mass index [$\mathrm{kg\,m^{-2}}$]. The subscript max represent the input normalization where $\mathrm{AGE_{max}} = 88$ years, $\mathrm{WGT_{max}} = 160$ kg and $\mathrm{BMI_{max}} = 52.8\ \mathrm{kg\,m^{-2}}$.

The subscript male or female indicates different PK parameter expressions depending on gender. The blood sampling site (arterial or venous) was available as a

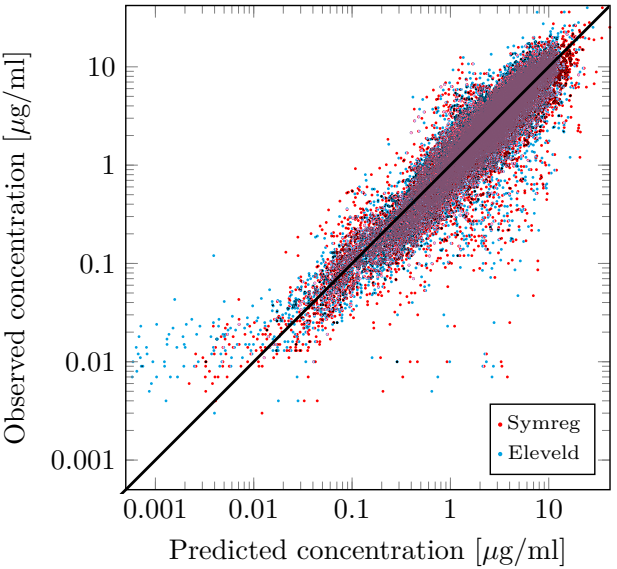

Figure 4. Predicted versus observed propofol concentrations of our covariate model (Symreg, red) compared to the Eleveld covariate model in [Eleveld et al., 2018] (Eleveld, blue) in logarithmic scale. The identity function, representing a perfect model fit, is shown in black.

modeling covariate, but was automatically pruned by the symbolic regression algorithm.

The obtained model of Equation (10) is less complex than the Eleveld model in [Eleveld et al., 2018], provided in Supplementary Section B for reference, and comparable to simpler covariate models for propofol, such as [Marsh et al., 1991; Schüttler et al., 1988].

The predicted concentrations of the final covariate model on the Eleveld data set are shown in Figure 4 together with the corresponding Eleveld model predictions. The distribution of errors between predicted and observed predictions is shown in the boxplot in Figure 5, indicating comparable predictive capability of the models, despite our model being less complex, and involving fewer of the available covariates. For ease of comparison, we present the corresponding average prediction errors in Table 2. We compare our model to the Eleveld model, to a covariate-free PK model where all individuals share the same parameters values, and to a covariate-free individual models with unique parameter sets. As expected, adding covariates explains some, but not all, variability between patients. This can be seen by comparing our model to the constant PK model and the individual models. As seen in Table 2, all of the prediction errors: MdLE, MdALE, MdPE, and MdAPE fall within clinically acceptable ranges, as presented further above.

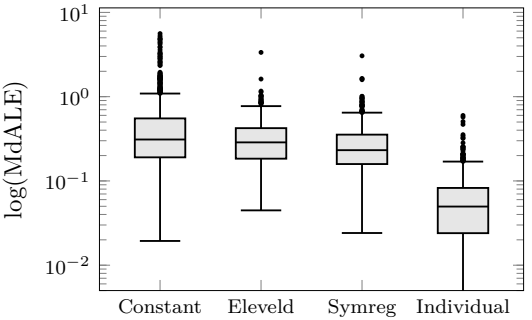

Figure 5. Comparison of prediction error MdALE Equation (5) between predicted and observed propofol concentrations for pharmacokinetic models. Our covariate model is denoted Symreg and the Eleveld covariate model is described in [Eleveld et al., 2018]. The constant model represents one parameter set over the population and individual represents individual set of model parameters. The lower whisker for the individual models goes to zero.

Table 2. Comparison of prediction errors for the propofol data set in [Eleveld et al., 2018] (1,031 individuals) for several pharmacokinetic models, all trained with MdALE Equation (5) as loss. Individual and constant PK model(s) are shown for comparison, representing best and worst case limits, respectively.

Method	Mean MdALE	Mean MdLE	Mean MdAPE	Mean MdPE
Constant model	0.501	0.140	211	181
Eleveld model	0.325	0.0791	34.8	14.4
Symbolic regression	0.279	-0.0489	27.4	-0.266
Individual models	0.0623	$1.65 \cdot 10^{-4}$	6.21	0.0178

4. Discussion

We have introduced a novel symbolic regression methodology for simultaneously automating the search for a suitable covariate model structure and optimization of its parameters. Similar to contemporary methodologies, it relies on a user-specified set of base expressions from which the covariant model can be composed. However, and in important contrast to contemporary methods, the need for a combinatorial search across combinations of these expressions is voided.

Throughout the paper, a propofol PK modeling example has been used as a demonstrator. Within this example, the proposed methodology manages to accomplish slightly better data fit than the result of state-of-the-art modeling [Eleveld et al., 2018] (see Figures 4 and 5, Table 2), while relying on fewer covariates, see Equation (10). The obtained values of individual volumes and clearances were comparable to those in [Eleveld et al., 2018].

The introduced methodology is broadly applicable to PK modeling from time series data, and likewise to pharmacodynamic (PD) modeling, and combined pharmacokinetic and pharmacodynamic (PK/PD) modeling. It's main benefit lies in that it poses the search for a suitable PK model as symbolic regression with a smooth loss function. This, in combination with efficient methods for simulation and gradient computations [Wahlquist et al., 2023] enables efficient model learning using back-propagation.

Another advantage is that the method can find covariate functions that are both simple and explain available data, while having a structure that would generally not be considered in a manual model structure search, unless explicitly supported by prior knowledge. However, the obtained covariate model is deterministic in the sense that we do not obtain a distribution over individual PK parameter values. It would be possible to integrate this methodology into the traditional mixed-effect modeling framework. Yet, this would be computationally much more demanding, which is why we propose first applying symbolic regression in a deterministic setting to arrive at a covariate model structure, and then (if desired) apply mixed-effect modeling to maximize parameter likelihood (with respect to some parameter priors and subject to the considered data) within the found structure.

In this paper, we have focused on models that are of sufficiently low complexity to be human-readable, which is achieved by enforcing sparsity of the neural network that constitutes the expression tree of the covariate model. If human readability is not necessary, an ordinary deep ANN could be employed instead. However, there is also a trade-off between fit to training data (expressiveness) and generalization to yet unseen data due to possible over-fitting. Enforcing human-readability naturally limits flexibility of the model, thus decreasing this risk of over-fitting. The ability to manually specify base expression also provides a means to integrate expert knowledge into the model. For example, a suspicion that a compartment volume should correlate to the square of patient age would motivate multiplication as a base expression.This enables incorporating expert knowledge into the model, for example a clearance to the power of 0.75 as in [West et al., 1997], or compartmental allometry as in [Anderson and Holford, 2008].

We assessed the model's out-of-sample prediction performance using a five-fold cross-validation. The data set was divided into five equal parts, and a covariate model was trained on four of the partitions, excluding one each time. The excluded partition, referred to as the validation set, was used to evaluate the model. This process was repeated for all five partitions to obtain an average predictive performance. The resulting mean (range) MdALE from cross-validation on the test sets was 0.303 (0.152–0.423), similar to the mean MdALE of 0.279 in Table 2. There was thus only a modest 10 % difference in mean error between the training and validation sets, which suggests no over-fitting issue. If such a problem had occurred, reducing the number of covariates and parameters (harder pruning) could have balanced the prediction errors on both sets.

The way we have employed the methodology here differs from how covari-

ate models are usually trained using mixed-effect modeling. Rather than asserting parameter priors and selecting the most likely parameters from the posterior distribution that the data infers, we have chosen to train a scalar loss function, resulting in a deterministic covariate model. It would in theory be possible to embed our methodology within an inference engine, but at the cost of high computational cost. If a Bayesian interpretation is desired, a likely better alternative is to first run our methodology to arrive at a covariate model structure–as we have done in our example–and then assert parameter priors to the parameters of the resulting model, to finally apply mixed-effect modeling to compute the corresponding posteriors.

5. Conclusion

We have presented a novel methodology for automatic and simultaneous covariate model structure discovery and parameter optimization. This model was demonstrated using an example on which it outperforms state-of-the-art modeling, in that it finds expressions that match data slightly better, while relying on notably fewer covariates. We conclude that the potential of automated model structure discovery is substantial; it could greatly optimize the process of pharmacometric covariate modeling. Additionally, it's likely to provide an improved balance between model complexity and data fit. This improved balance is something that could be challenging to achieve when simply assessing a series of pre-set model structure candidates in sequence.

Acknowledgments

We would like to thank Fredrik Bagge Carlson with JuliaHub for support in setting up the computational framework that we have used in the implementation of our proposed methodology. We would also like to thank Prof. Mats Karlsson's research group at the Division of Pharmacometrics, Department of Pharmacy, at Uppsala University, for rewarding discussions regarding the methodology.

Author contributions

All authors designed the study, Wahlquist performed the coding, Wahlquist and Soltesz analyzed the results. All authors authored, critically reviewed and approved the manuscript for submission.

Funding

This work was partially supported by the Wallenberg AI, Autonomous Systems and Software Program (WASP) funded by the Knut and Alice Wallenberg Foundation. All authors are members of the ELLIIT Strategic Research Area at Lund University.

Data availability

Code and data for reproducing the results is available in [Wahlquist, 2023].

Declarations

The authors declare no conflict of interest.

References

Anderson, B. J. and N. H. G. Holford (2008). "Mechanism-based concepts of size and maturity in pharmacokinetics". *Annual Review of Pharmacology and Toxicology* **48**, pp. 303–332. DOI: 10.1146/annurev.pharmtox.48.113006.094708.

Bezanson, J., A. Edelman, S. Karpinski, and V. B. Shah (2017). "Julia: a fresh approach to numerical computing". *SIAM Rev* **59**:1, pp. 65–98. DOI: 10.1137/141000671.

Bräm, D. S., N. Parrott, L. Hutchinson, and B. Steiert (2022). "Introduction of an artificial neural network-based method for concentration-time predictions". *CPT: Pharmacometrics & Systems Pharmacology* **11**:6, pp. 745–754. DOI: 10.1002/psp4.12786.

Davidson, J. W., D. A. Savic, and G. A. Walters (2003). "Symbolic and numerical regression: experiments and applications". *Inf Sci*. Recent Advances in Soft Computing **150**:1, pp. 95–117. DOI: 10.1016/S0020-0255(02)00371-7.

Dubey, S. R., S. K. Singh, and B. B. Chaudhuri (2022). "Activation functions in deep learning: a comprehensive survey and benchmark". *Neurocomputing* **503**, pp. 92–108. DOI: 10.1016/j.neucom.2022.06.111.

Eleveld, D. J., P. Colin, A. R. Absalom, and M. M. R. F. Struys (2018). "Pharmacokinetic-pharmacodynamic model for propofol for broad application in anaesthesia and sedation". *Brit J Anaesth* **120**:5, pp. 942–959. DOI: 10.1016/j.bja.2018.01.018.

Innes, M. (2018a). "Don't unroll adjoint: differentiating SSA-form programs". *CoRR*. URL: arXiv.1810.07951.

Innes, M. (2018b). "Flux: elegant machine learning with Julia". *J Open Source Softw*. DOI: 10.21105/joss.00602.

Janssen, A., M. Hoogendoorn, M. H. Cnossen, and R. A. Mathôt (2022). "Application of SHAP values for inferring the optimal functional form of covariates in pharmacokinetic modeling". *CPT: Pharmacometrics & Systems Pharmacology* **11**:8, pp. 1100–1110. DOI: 10.1002/psp4.12828.

Jonsson, E. N. and M. O. Karlsson (1998). "Automated covariate model building within NONMEM". *Pharm Res* **15**:9, pp. 1463–1468. DOI: 10.1023/a:1011970125687.

Kim, S., P. Y. Lu, S. Mukherjee, M. Gilbert, L. Jing, V. Ceperic, and M. Soljacic (2021). "Integration of neural network-based symbolic regression in deep learning for scientific discovery". *IEEE Trans Neural Networks Learn Syst* **32**:9, pp. 4166–4177. DOI: 10.1109/TNNLS.2020.3017010.

Kingma, D. P. and J. Ba (2017). "Adam: a method for stochastic optimization". In: *Proceedings of the 3rd International Conference on Learning Representations (ICLR)*. DOI: 10.48550/arXiv.1412.6980.

Koza, J. R. (1992). *Genetic Programming: On the Programming of Computers by Means of Natural Selection*. MIT Press, Cambridge, MA, USA. ISBN: 0-262-11170-5. DOI: 10.1007/BF00175355.

LeCun, Y., J. Denker, and S. Solla (1989). "Optimal brain damage". In: *Advances in neural information processing systems*. Vol. 2. Morgan-Kaufmann.

Marsh, B., M. White, N. Morton, and G. Kenny (1991). "Pharmacokinetic model driven infusion of propofol in children". *British Journal of Anaesthesia* **67**:1, pp. 41–48. DOI: 10.1093/bja/67.1.41.

Martius, G. and C. H. Lampert (2017). "Extrapolation and learning equations". In: *5th International Conference on Learning Representations, ICLR 2017, Toulon, France*. DOI: 10.48550/arXiv.1610.02995.

Masui, K., R. N. Upton, A. G. Doufas, J. F. Coetzee, T. Kazama, E. P. Mortier, and M. M. R. F. Struys (2010). "The performance of compartmental and physiologically based recirculatory pharmacokinetic models for propofol: a comparison using bolus, continuous, and target-controlled infusion data". *Anesthesia and Analgesia* **111**:2, pp. 368–379. DOI: 10.1213/ANE.0b013e3181bdcf5b.

McComb, M., R. Bies, and M. Ramanathan (2022). "Machine learning in pharmacometrics: Opportunities and challenges". *British Journal of Clinical Pharmacology* **88**:4, pp. 1482–1499. DOI: 10.1111/bcp.14801.

Mogensen, P. K. and A. N. Riseth (2018). "Optim: a mathematical optimization package for Julia". *J Open Source Softw* **3**:24, p. 615. DOI: 10.21105/joss.00615.

Orzechowski, P., W. La Cava, and J. H. Moore (2018). "Where are we now? A large benchmark study of recent symbolic regression methods". In: *Proceedings of the Genetic and Evolutionary Computation Conference*. Kyoto, Japan, pp. 1183–1190. DOI: 10.1145/3205455.3205539.

Rackauckas, C., Y. Ma, A. Noack, V. Dixit, P. K. Mogensen, C. Elrod, M. Tarek, S. Byrne, S. Maddhashiya, J. B. S. Calderón, M. Hatherly, J. Nyberg, J. V. Gobburu, and V. Ivaturi (2020). "Accelerated predictive healthcare analytics with pumas, a high performance pharmaceutical modeling and simulation platform". *bioRxiv*. DOI: 10.1101/2020.11.28.402297.

Sahoo, S. S., C. H. Lampert, and G. Martius (2018). "Learning equations for extrapolation and control". In: *Proceedings of the 35th International Conference on Machine Learning, ICML 2018, Stockholm, Sweden*. Vol. 80. Proceedings of Machine Learning Research. PMLR, pp. 4439–4447. DOI: 10.48550/arXiv.1806.07259.

Schnider, T. W., C. F. Minto, P. L. Gambus, C. Andresen, D. B. Goodale, S. L. Shafer, and E. J. Youngs (1998). "The influence of method of administration and covariates on the pharmacokinetics of propofol in adult volunteers". *Anesthesiology* **88**:5, pp. 1170–1182. DOI: 10.1097/00000542-199805000-00006.

Schüttler, J., S. Kloos, H. Schwilden, and H. Stoeckel (1988). "Total intravenous anaesthesia with propofol and alfentanil by computer-assisted infusion". *Anaesthesia* **43**:s1, pp. 2–7. DOI: 10.1111/j.1365-2044.1988.tb09059.x.

Sheiner, L. B. and S. L. Beal (1980). "Evaluation of methods for estimating population pharmacokinetics parameters. I. Michaelis-Menten model: routine clinical pharmacokinetic data". *J Pharmacokinet Biopharm* **8**:6, pp. 553–571. DOI: 10.1007/BF01060053.

Sibieude, E., A. Khandelwal, P. Girard, J. S. Hesthaven, and N. Terranova (2022). "Population pharmacokinetic model selection assisted by machine learning". *Journal of Pharmacokinetics and Pharmacodynamics* **49**:2, pp. 257–270. DOI: 10.1007/s10928-021-09793-6.

Sibieude, E., A. Khandelwal, J. S. Hesthaven, P. Girard, and N. Terranova (2021). "Fast screening of covariates in population models empowered by machine learning". *Journal of Pharmacokinetics and Pharmacodynamics* **48**:4, pp. 597–609. DOI: 10.1007/s10928-021-09757-w.

Udrescu, S.-M., A. Tan, J. Feng, O. Neto, T. Wu, and M. Tegmark (2020). "AI Feynman 2.0: Pareto-optimal symbolic regression exploiting graph modularity". In: *Proceedings of the 34th International Conference on Neural Information Processing Systems*. NIPS'20, pp. 4860–4871. DOI: 10.48550/arXiv.2006.10782.

Varvel, J. R., D. L. Donoho, and S. L. Shafer (1992). "Measuring the predictive performance of computer-controlled infusion pumps". *J Pharmacokinet Biopharm* **20**:1, pp. 63–94. DOI: 10.1007/BF01143186.

Wahlquist, Y. (2023). *Learning pharmacometric structures*. commit: dfafb1f. URL: https://github.com/wahlquisty/learning-pharmacometric-covariate-structures (visited on 2023-03-03).

Wahlquist, Y., F. Bagge Carlson, and K. Soltesz (2023). "Fast simulation of pharmacokinetics". English. *IFAC PapersOnline*. ISSN: 2405-8963.

Wahlquist, Y., M. Morin, and K. Soltesz (2022). "Pharmacometric covariate modeling using symbolic regression networks". In: *2022 IEEE Conference on Control Technology and Applications (CCTA)*, pp. 1–24. DOI: 10.1109/CCTA41146.2020.9206396.

West, G. B., J. H. Brown, and B. J. Enquist (1997). "A general model for the origin of allometric scaling laws in biology". *Science* **276**:5309, pp. 122–126. DOI: 10.1126/science.276.5309.122.

Supplementary Information

A. Hessian-based pruning

In this appendix we provide a mathematical interpretation of the roles played by the Hessian and parameter saliences in our pruning approach.

The effect of perturbing the parameter vector can be analyzed by approximating the loss function $J(\boldsymbol{\gamma})$ by a Taylor series. A perturbation $\partial\boldsymbol{\gamma}$ of the parameter vector $\boldsymbol{\gamma}$ will change the loss function by

$$\partial J(\boldsymbol{\gamma}) = \nabla J(\boldsymbol{\gamma})\partial\boldsymbol{\gamma} + \frac{1}{2}\sum_i H_{ii}\partial\gamma_i{}^2 + \frac{1}{2}\sum_{i\neq j} H_{ij}\partial\gamma_i\partial\gamma_j + \mathcal{O}(||\partial\boldsymbol{\gamma}||^3),$$

where $\partial\gamma_i$ are the components of $\partial\boldsymbol{\gamma}$, $\nabla J(\boldsymbol{\gamma})$ is the gradient of the loss function and H_{ij} are the elements of the Hessian matrix H of J with respect to $\boldsymbol{\gamma}$ so that

$$\nabla J(\boldsymbol{\gamma}) = \frac{\partial J(\boldsymbol{\gamma})}{\partial\boldsymbol{\gamma}} \qquad H_{ij} = \frac{\partial^2 J(\boldsymbol{\gamma})}{\partial\gamma_i\partial\gamma_j}.$$

The goal is to prune the parameters that are *least* sensitive, i.e. those that affect the loss J the least when perturbed. Even for our size of network, repeatedly computing the full Hessian H would notably slow down training of the symbolic regression model. Instead, we make a diagonal approximation of the Hessian, neglecting cross terms H_{ij} with $i \neq j$.

Allowing training to converge before each pruning iteration, ensures that $\nabla J(\boldsymbol{\gamma}) = 0$ (or in practice negligible), thus enabling approximation of $\partial J(\boldsymbol{\gamma})$ by

$$\partial J(\boldsymbol{\gamma}) \approx \frac{1}{2}\sum_i H_{ii}\partial\gamma_i^2.$$

This approximation is then used to form an importance measure (salience) of our network parameters, according to [LeCun et al., 1989], where the salience of parameter γ_i becomes

$$S(\gamma_i) = H_{ii}\gamma_i^2.$$

B. The Eleveld model

The Eleveld PK covariate model in [Eleveld et al., 2018] is defined by

$$
\begin{aligned}
f_{\text{ageing}}(x) &= \exp\left(x(\text{AGE} - \text{AGE}_{\text{ref}})\right) \\
f_{\text{sigmoid}}(x, E50, \lambda) &= \frac{x^{\lambda}}{x^{\lambda} + E50^{\lambda}} \\
f_{\text{central}}(x) &= f_{\text{sigmoid}}(x, \theta_{12}, 1) \\
f_{\text{CLmaturation}} &= f_{\text{sigmoid}}(\text{PMA}, \theta_8, \theta_9) \\
f_{\text{Q3maturation}} &= f_{\text{sigmoid}}(\text{AGE} + 40\text{weeks}, \theta_{14}, 1) \\
f_{\text{opioids}}(x) &= \begin{cases} 1, & \text{absence of opiates} \\ \exp\left(x \cdot \text{AGE}\right), & \text{presence of opiates} \end{cases} \\
f_{\text{Al-Sallami}} &= \begin{cases} \left(0.88 + \frac{0.12}{1+(\text{AGE}/13.4)^{-12.7}}\right)\left(\frac{9270 \cdot \text{WGT}}{6680+216\text{BMI}}\right), & \text{males} \\ \left(1.11 + \frac{-0.89}{1+(\text{AGE}/7.1)^{-1.1}}\right)\left(\frac{9270 \cdot \text{WGT}}{8780+244\text{BMI}}\right), & \text{females} \end{cases} \\
V_{1,\text{arterial}}(\text{L}) &= \theta_1 \frac{f_{\text{central}}(\text{WGT})}{f_{\text{central}}(\text{WGT}_{\text{ref}})} \\
V_{1,\text{venous}}(\text{L}) &= V_{1,\text{arterial}}\left(1 + \theta_{17}(1 - f_{\text{central}}(\text{WGT}))\right) \\
V_2(\text{L}) &= \theta_2 \frac{\text{WGT}}{\text{WGT}_{\text{ref}}} f_{\text{ageing}}(\theta_{10}) \\
V_3(\text{L}) &= \theta_3 \frac{f_{\text{Al-Sallami}}}{f_{\text{Al-Sallami, ref}}} f_{\text{opioids}}(\theta_{13}) \\
CL(\text{L/min}) &= \left\{ \begin{matrix} \theta_4, & \text{male} \\ \theta_{14}, & \text{female} \end{matrix} \right\} \left(\frac{\text{WGT}}{\text{WGT}_{\text{ref}}}\right)^{0.75} \frac{f_{\text{CLmaturation}}}{f_{\text{CLmaturation, ref}}} f_{\text{opioids}}(\theta_{11}) \\
Q_{2,\text{arterial}}(\text{L/min}) &= \theta_5 \left(V_2/V_{2,\text{ref}}\right)^{0.75} \left(1 + \theta_{16}(1 - f_{\text{Q3maturation}})\right) \\
Q_{2,\text{venous}}(\text{L/min}) &= Q_{2,\text{arterial}} \cdot \theta_{18} \\
Q_3(\text{L/min}) &= \theta_6 \left(V_3/V_{3,\text{ref}}\right)^{0.75} \frac{f_{\text{Q3maturation}}}{f_{\text{Q3maturation, ref}}}
\end{aligned}
$$

where the reference patient is male, 35 years old, 70 kg and 1.7 metres tall. All parameters values θ can be found in the original publication of [Eleveld et al., 2018].

Paper IV

Automated Covariate Modeling using Efficient Simulation of Pharmacokinetics

Ylva Wahlquist Kristian Soltesz

Abstract

Pharmacometric modeling plays an important role in drug development and personalized medicine. Pharmacometric covariate models can be used to describe the relationships between patient characteristics (such as age and weight) and pharmacokinetic (PK) parameters. Traditionally, the functional structure of these relationships are obtained manually. This is a time-consuming task, and consequently limits the search space of covariate relationships. The use of data-driven machine learning (ML) in pharmacometrics has the potential to automate the search for adequate model structures, which can speed up the modeling process and enable the evaluation of a wider range of model candidates. Even with moderately sized data sets, ML approaches require millions of simulations of pharmacokinetic (PK) models, which dictates the need for an efficient simulator. In this paper, we demonstrate how to automate covariate modeling using neural networks (NNs), that are trained using efficient PK simulation techniques. We apply the methodology to a propofol data set with 1031 individuals and compare the results to previously published covariate models for propofol. We use the NN as a function approximator that relates covariates to the parameters of a three-compartment PK model, and train it on dose and plasma concentration time series. Our study demonstrates that NN-based covariate modeling allows for automation of the otherwise time-consuming task of identifying which of available covariates to include in the model, and what functional mappings from these covariates to PK model parameters to consider in the model search. Additional to this saving in modeler effort, the NN-based model obtained in our clinical data set example has PK parameters within a clinically reasonable range, and slightly enhanced predictive precision than a previously published state-of-the-art covariate models for propofol model.

Keywords: Pharmacokinetics and drug delivery; Physiological modeling; Biomedical system simulation; Machine learning; Neural networks

Originally published in IFAC Journal of Systems and Control (2024). Reprinted with permission under CC BY-NC. The original version is available at `https://doi.org/10.1016/j.ifacsc.2024.100252`.

1. Introduction

1.1 Background and motivation

Pharmacokinetics (PK) is the study of how a drug affects the body and is commonly modeled by linear time-invariant (LTI) compartmental models. These models describe the uptake, distribution, and elimination dynamics of the drug and are used to predict drug concentrations and physiological parameters. A suitable PK model structure, such as the number of compartments and topology, can be readily determined from data [Sahinovic et al., 2018]. However, PK parameters, such as the volume of distribution, vary between individuals and affects the drug response. This inter-individual variability can be partly explained by introducing covariates, such as age and weight, to the PK modeling.

Pharmacometric covariate modeling relies on determining the relationship between covariates and PK parameters. In covariate modeling, the goal is to identify covariates that explains the inter-individual variability. For example, letting a volume of distribution depend on patient weight can result in a PK model that better fits dose-response data. The inclusion of covariates explains some of the inter-individual variability, but not all. The remaining variability is commonly modeled by statistical components, so-called random effects. An example of a covariate model is shown in Figure 1.

Traditionally, covariate models are derived with non-linear mixed-effect modeling (NLME), where the most widely used software is NONMEM [Sheiner and Beal, 1980], and a more modern alternative is Pumas AI [Rackauckas et al., 2020]. Commonly, NLME modeling includes one or several manual steps, where the modeler successively adds covariates and covariate relationships. This is done partially based on physiological knowledge and partially on how the inclusion of a covariate relationship improves the fit to dose-response data. These manual steps constitute a time-consuming task. For an expert they can take all from hours to weeks, in effect limiting the admissible search space for covariate relationships.

In this paper, we study covariate modeling of the pharmacokinetics of the anesthetic drug propofol. There exist several covariate models for propofol derived with NONMEM [Eleveld et al., 2018; Schüttler and Ihmsen, 2000] where the structural covariate model was derived manually.

In [Wahlquist et al., 2023b], we demonstrated how to obtain readable and interpretable covariate models with symbolic regression networks, further explained in Section 1.2. Then, it is natural to ask how much better fit we can get with a more complex function approximator, an neural network (NN) with regular activation functions, such as the ReLU or a sigmoid. In this paper, we study this problem by training an NN that relates covariates to PK parameters of the compartment model. Naturally, a more complex function approximating the covariate model will be able to fit the data better. In this paper, we study how much better this fit is and if it is worth the trade-off of readability.

We demonstrate the method on a data set for propofol and compare the final covariate model to the covariate models in [Eleveld et al., 2018] and [Wahlquist et al., 2023b]. The drug administration data is a mix of boluses and infusions, which makes it a suitable data set for demonstrating the use of the simulator FastPKSim.jl in this setting [Wahlquist et al., 2023a]. More details of the data set can be found in Section 3.

1.2 Machine learning in pharmacometrics

Machine learning (ML) is a potential tool for automating pharmacometric modeling tasks [Janssen et al., 2022c; Sibieude et al., 2022; Wahlquist et al., 2023b]. More specifically, NNs are general function approximators that enable the capture of intricate relationships. ML also allows for automation and speed-up of modeling tasks that are normally done manually. For example, ML can automate the process of evaluating many covariate relationships of the structural covariate model. An overview of the current use and possibilities of ML in pharmacometrics can be found in [Janssen et al., 2022a].

In several papers, it was suggested to use NNs to predict drug concentrations directly from dosing data [Brier et al., 1995; Chow et al., 1997; Liu et al., 2015]. As pointed out in [Janssen et al., 2022c], these models tend to lack the ability to extrapolate outside of these predicted time points and instead suggest that ML should be used to predict latent parameters of another function, such as the model parameters of a compartment model. An example of this is shown in Figure 1 and is the approach in this paper, where we use NNs to predict the model parameters of a PK compartment model.

A few examples of where NNs have been used to estimate PK parameters are given in [Janssen et al., 2022c] and [Sibieude et al., 2021]. In [Janssen et al., 2022c], the authors demonstrate how to use an NN to learn PK parameters of a two-compartment model for a standard half-life FVIII concentrate to treat hemophilia A for a given set of covariates. One single IV dose was simulated with a few observations for each patient in the training data set. The method was implemented in Julia with the differential equations solver in DifferentialEquations.jl [Rackauckas and Nie, 2017].

In [Wahlquist et al., 2023b], we present an automatic covariate modeling method that uses symbolic regression networks to derive a covariate model. The symbolic regression network was used to obtain a readable and interpretable covariate model. It is a type of neural network that can discover mathematical expressions by using sparse neural networks with a different set of activation functions compared to regular NNs. The symbolic regression network was trained on drug administration profiles (time series) and covariates in the Eleveld et al. data set [Eleveld et al., 2018]. The obtained covariate model showed a comparable and slightly better fit than the covariate model derived with NONMEM in [Eleveld et al., 2018].

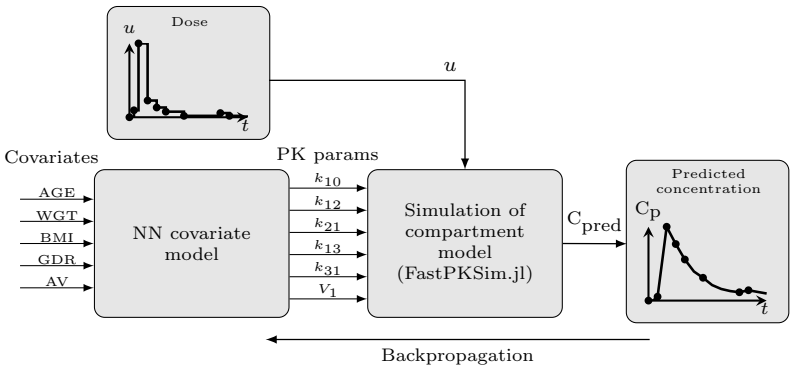

Figure 1. Covariate modeling with a neural network (NN) and simulator of pharmacokinetics (PK). The NN takes five covariates as input (age, weight, BMI, gender and blood sampling site, arterial or venous) and outputs six PK parameters of the three-compartment model in Equation (1). The predicted PK parameters are input to the FastPKSim.jl simulator to compute the predicted plasma concentrations C_{pred} with given drug administration profiles u (time series data). A training loss is computed from predicted plasma concentrations and observed (measured) concentrations, and the NN parameters are updated with backpropagation.

Another example of where ML has been used for pharmacometrics is the problem of covariate selection [Janssen et al., 2022b; Ogami et al., 2021]. In [Janssen et al., 2022b] and [Ogami et al., 2021] the authors use SHapley Additive exPlanations (SHAP) to study the relationship between covariates and PK parameters estimated from ML models. SHAP can be used as an importance measure of each covariate so that less important covariates can be eliminated in the model building.

However, ML models have the disadvantage of lacking interpretability. Also, ML does not guarantee extrapolation and interpolation between training points. Still, ML has the potential to be a powerful tool in pharmacometrics if these limitations are addressed. Even if ML has the potential to speed up modeling tasks, it is still limited by the computational cost of the simulation, which has to be carried out thousands of times in network training. Therefore, a fast simulator of pharmacokinetics (or pharmacodynamics) has to be used together with the NN to handle large data sets efficiently.

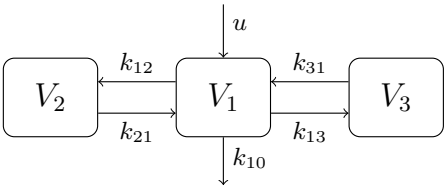

Figure 2. Mammillary three-compartment PK model. The mass rate flow $u(t)$ is administered into the central compartment of volume V_1 via infusion, and eliminated from it at a rate $k_{10}x_1$. Two peripheral compartments of volumes V_2 and V_3 are connected to the central one, and the drug transfer between these and the central compartment are described by the rate constants k_{ij}, from compartment i to j.

2. Methods

2.1 Pharmacokinetic modeling

Pharmacokinetics are commonly modeled by low-order compartmental models due to the ease of interpretation and estimation of the model parameters. The most common compartment models are one-, two- and three-compartment models. The one-compartment model is the simplest representation and is often used to model the central compartment of the body. The two-compartment model is used to model the central and peripheral compartments of the body. The three-compartment model is used to model the central, peripheral, and deep peripheral compartments of the body.

An example of a compartment model for an intravenously administered drug is a mammillary three-compartment model, illustrated in Figure 2. The central compartment models the blood plasma, and the two peripheral compartment models slow-perfused (such as fat) and fast-perfused (such as muscle) tissue. The addition and elimination of the drug is associated with the central compartment, and drug diffuses between the central and peripheral compartments. The diffusion from compartment i to j is modeled through a non-negative transfer rate constant k_{ij}.

If drug elimination is assumed to follow a first-order process, the mammillary three-compartment model is a linear time-invariant (LTI) system. It can be described by the following state-space representation:

$$\dot{x}_1 = -(k_{10}+k_{12}+k_{13})x_1 + k_{21}x_2 + k_{31}x_3 + \frac{1}{V_1}u, \tag{1a}$$

$$\dot{x}_2 = k_{12}x_1 - k_{21}x_2, \tag{1b}$$

$$\dot{x}_3 = k_{13}x_1 - k_{31}x_3, \tag{1c}$$

relating drug infusion rate $u(t)$ [$\mu g\, s^{-1}$] to drug concentration $x_i(t)$ [$\mu g\, L^{-1}$] of compartment i, where k_{10} is the elimination-rate constant [s^{-1}], and V_1 [L] is the volume of distribution of the central compartment.

2.2 Simulation of pharmacokinetics

Simulation of a PK model is the process of computing the drug concentrations $x_i(t)$ of the compartments $i = 1, \ldots, n$ at time t given the drug input $u(t)$ and the PK model parameters V_i and k_{ij} in Equation (1). Simulation of PK models is a crucial part of pharmacometric covariate modeling where it is used to evaluate possible covariate model structures [Schnider et al., 1998].

There exist several methods for simulating PK models (or more general differential equations), such as the DifferentialEquations.jl [Rackauckas and Nie, 2017] package in Julia and the *lsim* function in Matlab. However, these methods do not use the fact that the dynamics of compartmental systems are LTI. Taking this into account can reduce computational demands notably when the input $u(t)$ is a sequence of step changes and impulses. Instead, these softwares sample the dynamics at a sufficiently high rate to resolve both the dynamics Equation (1) and input events (changes in $u(t)$).

In [Wahlquist, 2022], we introduced FastPKSim.jl, a fast and exact (down to numeric precision) simulator for compartmental LTI systems. It is tailored for the simulation of one- two- and three-compartment models with boluses and constant infusion changes issued at possibly irregular time instances. The simulator is implemented in Julia and is available as an open-source package [Wahlquist, 2022]. The efficiency of the simulator was demonstrated in [Wahlquist et al., 2023a] by benchmarking it against commonly used solvers. The benchmark showed a speed-up of approximately 40 000 times compared to the standard simulator in MATLAB, *lsim*, and around 150 times compared to DifferentialEquations.jl, being the most widely used ODE solver in Julia.

The concentrations of the peripheral compartments are in general not measurable, whereas the the central compartment concentration can be measured at discrete time points by sampling the blood plasma. Data sets for modeling purposes therefore comprises time series that consist of the following discrete-time events:

- Drug infusion at a constant rate (step input) to the central compartment;
- Drug bolus (impulse) to the central compartment;
- Observation (measurement) of the central compartment concentration.

In the following section, we will describe the simulation algorithm in FastPKSim.jl [Wahlquist, 2022; Wahlquist et al., 2023a], which is tailored for simulation of the above events.

2.3 Fast simulation of pharmacokinetics - FastPKSim.jl

In this paper, we use the efficient simulator FastPKSim.jl [Wahlquist, 2022] to simulate PK compartment models. FastPKSim.jl is a Julia package for fast and exact simulation of compartmental systems with boluses and infusion inputs at irregular time instances. The simulator is available as an open-source package [Wahlquist, 2022]. Below, we will describe the simulator, and refer to [Wahlquist et al., 2023a] for further details.

The dynamics of any LTI system with scalar input $u(t)$ can be written

$$\dot{\boldsymbol{x}}(t) = A\boldsymbol{x}(t) + Bu(t), \tag{2}$$

where $\boldsymbol{x}$ is the state vector and $x_i(t)$ is the drug concentration in compartment $i = 1,\ldots,n$. A and B are the system and input matrices, and for a system with scalar input B is a column vector. The exact solution of Equation (2), as derived in for example [Åström and Wittenmark, 2011], is

$$\boldsymbol{x}(t) = e^{At}\boldsymbol{x}(0) + \int_0^t e^{A(t-\tau)}Bu(\tau)d\tau. \tag{3}$$

We assume the initial concentration at $t = 0$ to be zero so that $\boldsymbol{x}(0) = \mathbf{0}$. This corresponds to the therapy being initiated at a point in time where no drug has previously been administered, making it a reasonable assumption.

In contrast to common ODE solvers like *ode45* in Matlab, which use numeric integration to approximate Equation (3) directly, we use the fact that the input changes only at discrete points in time to perform an exact zero-order-hold (ZOH) discretization of Equation (3). If these events are indexed by k, the discrete state update of Equation (3) becomes

$$\boldsymbol{x}_{k+1} = \Phi_k\boldsymbol{x}_k + \Gamma_k u_k, \tag{4a}$$

so that

$$\begin{aligned} \Phi_k &= e^{Ah_k}, \\ \Gamma_k &= \int_0^{h_k} e^{A\tau}d\tau B, \end{aligned} \tag{4b}$$

and the sampling period

$$h_k = t_{k+1} - t_k, \tag{4c}$$

is the time between event k and $k+1$, so that $\boldsymbol{x}_k = \boldsymbol{x}(t_k)$ and $u_k = u(t_k)$.

Now, we consider the input to be either a piece-wise constant infusion $u_k = w_k$ or an impulse (bolus) $u_j = \delta_k v_k$, administered at time t_k, where δ_k denotes the Dirac distribution (unit impulse) centered at t_k. For our inputs of piece-wise constant infusions and impulses, we can rewrite Equation (4a) to

$$\boldsymbol{x}_{k+1} = \Phi_k(\boldsymbol{x}_k + Bv_k) + \Gamma_k w_k, \tag{5}$$

where v_k is the magnitude of the impulse at time t_k, and w_k is the magnitude of the constant infusion at time t_k.

The matrices Φ_k and Γ_k can be computed using matrix exponentials. Computing these can be computationally expensive since they have to be evaluated at each dosing instance t_k. Instead of computing Φ_k and Γ_k at each dosing instance, we can use the fact that our PK compartment models are of low order to get a simpler form for the state update Equation (5).

The state dynamics Equation (2) can be written in the Laplace domain as

$$X(s) = (sI - A)^{-1} BU(s) = \frac{\text{adj}(sI - A)B}{\det(sI - A)} U(s), \tag{6}$$

where $X(s)$ and $U(s)$ are the Laplace transforms of $x(t)$ and $u(t)$, respectively. For the considered PK models, we have $B = V^{-1}\boldsymbol{e}_1$, where $\boldsymbol{e}_1$ is the first unit vector in Euclidean $\mathbb{R}^n$, while A is uniquely determined by the rate constants.

From now on, we will only consider the three-compartment model of Figure 2, which is the compartmental structure used in this paper. For the i^{th} state $X_i(s)$, with $i = 1,2,3$, we can evaluate Equation (3), so that

$$\frac{X_i(s)}{U(s)} = \frac{p_{1i}s^2 + p_{2i}s + p_{3i}}{(s-\lambda_1)(s-\lambda_2)(s-\lambda_3)}, \tag{7}$$

where p_{ji} are the polynomial coefficients of $\text{adj}(sI - A)\boldsymbol{e}_1$. The eigenvalues of the A-matrix are denoted λ_i, $i = 1,2,3$ and are all unique real and strictly negative for the considered PK models. The eigenvalues can be determined in closed form from the rate constants, and are given by Equation (20) in Supplementary Section A.

The idea is now to use the partial fraction expansion of Equation (7) to get a state update equation for each state $X_i(s)$ at each dosing instance t_k. Then, all states can be computed in parallel and we can combine the results to compute the state update Equation (5).

A partial fraction decomposition of Equation (7) results in

$$\frac{X_i(s)}{U(s)} = \frac{p_{1i}s^2 + p_{2i}s + p_{3i}}{(s-\lambda_1)(s-\lambda_2)(s-\lambda_3)} = \frac{r_{1i}}{s-\lambda_1} + \frac{r_{2i}}{s-\lambda_2} + \frac{r_{3i}}{s-\lambda_3}. \tag{8}$$

By matching powers of s in Equation (8), we get the relationship between the coefficients p_{ji} and r_{ji}, expressed in terms of the eigenvalues. This can be expressed as a linear equation system

$$QR = P, \tag{9a}$$

where

$$Q = \begin{bmatrix} 1 & 1 & 1 \\ -(\lambda_2+\lambda_3) & -(\lambda_1+\lambda_3) & -(\lambda_1+\lambda_2) \\ \lambda_2\lambda_3 & \lambda_1\lambda_3 & \lambda_1\lambda_2 \end{bmatrix}, \tag{9b}$$

$$P = \begin{bmatrix} 1 & 0 & 0 \\ k_{21}+k_{31} & k_{12} & k_{13} \\ k_{21}k_{31} & k_{12}k_{31} & k_{13}k_{21} \end{bmatrix}, \tag{9c}$$

$$R = \begin{bmatrix} r_{11} & r_{12} & r_{13} \\ r_{21} & r_{22} & r_{23} \\ r_{31} & r_{32} & r_{33} \end{bmatrix}. \tag{9d}$$

P is expressed in terms of the rate constants of the three-compartment model and Q is determined by the eigenvalues of the system matrix A.

Solving Equation (9) for R can be done by explicitly computing the inverse of Q, since $R = Q^{-1}P$, where the inverse of Q is given by

$$Q^{-1} = \begin{bmatrix} \lambda_1^2/d_1 & \lambda_1/d_1 & 1/d_1 \\ \lambda_2^2/d_2 & \lambda_2/d_2 & 1/d_2 \\ \lambda_3^2/d_3 & \lambda_3/d_3 & 1/d_3 \end{bmatrix}, \tag{10a}$$

and

$$\begin{aligned} d_1 &= (\lambda_1-\lambda_3)(\lambda_1-\lambda_2), \\ d_2 &= (\lambda_2-\lambda_3)(\lambda_2-\lambda_1), \\ d_3 &= (\lambda_3-\lambda_2)(\lambda_3-\lambda_1). \end{aligned} \tag{10b}$$

Both Q^{-1} and R can be precomputed using the closed-form expressions Equation (10) and Equation (9), respectively, relying on the pre-computed eigenvalues of the system matrix A. Computing Q, Q^{-1} and P for the one- and two-compartment model can be done similarly, with each constituting a special case of the three-compartment model.

Now, all parts of the partial fraction expansion of Equation (8) are known, and our system can be seen as a parallel interconnection of three first-order systems. Each part of the partial fraction decomposition is given by

$$\frac{r_{ji}}{V_1}\frac{1}{s-\lambda_j}, \tag{11}$$

where λ_j is the j^{th} eigenvalue of the system matrix A and i denotes the i^{th} state.

To simulate Equation (11), we discretize a state-space realization of Equation (11) with zero-order-hold (ZOH) sampling and sampling time h_k to get

$$\begin{aligned} z_{k+1} &= \varphi_j z_k + \gamma_j u_k, \\ x_k &= \frac{r_{ij}}{V_1} z_k, \end{aligned} \tag{12a}$$

where

$$\begin{aligned} \varphi_j &= e^{\lambda_j h_k}, \\ \gamma_j &= \frac{1}{\lambda_j}(\varphi_j - 1), \end{aligned} \tag{12b}$$

and z is the state variable of the subsystem.

We can now perform parallel simulations of the three subsystems Equation (11) to speed up the simulation of the full system Equation (2), where each subsystem corresponds to one of the three states x_i.

For all of the eigenvalues $j = 1, \ldots 3$, we create the corresponding column vectors for φ_j, γ_j and z_j, so that

$$\boldsymbol{z} = \begin{bmatrix} z_1 & z_2 & z_3 \end{bmatrix}^\top, \tag{13a}$$

$$\boldsymbol{\varphi} = \begin{bmatrix} \varphi_1 & \varphi_2 & \varphi_3 \end{bmatrix}^\top, \tag{13b}$$

$$\boldsymbol{\gamma} = \begin{bmatrix} \gamma_1 & \gamma_2 & \gamma_3 \end{bmatrix}^\top. \tag{13c}$$

For our system inputs u_k of piece-wise constants infusions of magnitude w_k and impulses of magnitude v_k, we can use the state update in Equation (5) together with the state update of each first-order system to get the final state update

$$\boldsymbol{z}_{k+1} = \boldsymbol{\varphi}_k \odot (\boldsymbol{z}_k \oplus v_k) \oplus \boldsymbol{\gamma}_k w_k, \tag{14a}$$

$$\boldsymbol{x}_k = \frac{1}{V_1} R^\top \boldsymbol{z}_k, \tag{14b}$$

where $\odot$ denotes the element-wise product and $\oplus$ denotes the vector addition so that $. \oplus u = . + \mathbf{1}u$. The initial state is assumed to be zero, so that $\boldsymbol{z}_0 = \mathbf{0}$.

We can now simulate our three-compartment model as a system of first-order models, which allows for parallel computations and a significant simulation speed-up compared to traditional simulators, as demonstrated in [Wahlquist et al., 2023a]. By precomputing R, only being based on eigenvalues and rate constants, we only need to compute $\boldsymbol{\varphi}$ at every dosing instance t_k. This makes the simulator suitable for the simulation of boluses and infusions at irregularly spaced time instances as there is no need to compute expensive matrix exponentials at each dosing instance. Also, at the time instances when we are only interested in changing the dose and not observing the central compartment concentration x_1, we only need to compute $\boldsymbol{z}$ with Equation (14a).

To tightly integrate this simulator with the training of neural networks, we also need fast computation of gradients of the simulation output with respect to trainable parameters. In [Wahlquist et al., 2023a], we demonstrated the ability of FastPKSim.jl to differentiate through the simulator and thus obtain the desired gradients. However, we have not put in an extensive effort to optimize the associated numeric computations, as has been done in for example the development of DifferentialEquations.jl.

3. Automated covariate modeling with neural networks

The covariates are input to our NN, which acts as a function approximator of the covariate model. The NN outputs the parameters of the three-compartment PK model that are the rate constants and the central compartment volume. To be able to find a suitable covariate model structure, we need to perform thousands of simulations of the PK compartment model. Therefore, we use the FastPKSim.jl simulator to compute the plasma concentrations at each observation time instance for a given set of PK parameters.

Then, the plasma concentrations are compared to the observed concentrations, and the NN parameters are updated using backpropagation with gradient-based optimization. An overview of how the inputs and outputs of the NN and simulator are connected is shown in Figure 1.

3.1 Data set

We demonstrate our method on the multi-study data set for the anesthetic drug propofol collected by Eleveld et al. [Eleveld et al., 2018]. The data set originates from 30 studies of $8-120$ individuals each, taking place between 1987 and 2018. The data set will from now on be referred to as the "Eleveld data set". Ethical approvals for the studies behind this data set are found in the original publications.

The data set includes observational data from 1031 individuals, of which 670 are male and 361 are female, with ages ranging from 27 weeks to 88 years, and weights ranging from 0.68 to 160 kg. For these individuals, there are 15 433 blood plasma concentration observations, of which 11 530 are arterial and 3903 are venous measurements. Data pre-processing was done in the same manner as performed in [Eleveld et al., 2018; Wahlquist et al., 2023b], where subsequent infusion changes smaller than 0.5 $\mu g\,s^{-1}$ in the dose dimension and less than 1 s in the time dimension, were merged. This resulted in 61 940 drug infusions, constant infusions and boluses, administered to the individuals. The considered covariates for the PK modeling are age, weight, BMI, gender, and blood sampling site (arterial or venous). During model development, the continuous covariates (age, weight and BMI) were normalized between 0 and 1, and the categorical covariates (gender and blood sampling site) were set to ± 0.5.

3.2 Predictive performance

To assess the accuracy of the covariate model, we need a set of metrics. Some common metrics are given in [Varvel et al., 1992], which all have their advantages and disadvantages [Soltesz et al., 2013]. In this paper, we use the absolute logarithmic error (ALE) as our main metric during model development, since this metric was used to evaluate the model proposed in the original publication of the Eleveld covariate model [Eleveld et al., 2018].

For sample j of an individual i, the (absolute) logarithmic error (A)LE is defined as

$$\mathrm{LE}_{ij} = \ln\left(\frac{C_{\mathrm{obs}_{ij}}}{C_{\mathrm{pred}_{ij}}}\right), \tag{15a}$$

$$\mathrm{ALE}_{ij} = \left|\mathrm{LE}_{ij}\right|, \tag{15b}$$

where $C_{\mathrm{obs}_{ij}}$ are observed (measured) plasma concentrations and $C_{\mathrm{pred}_{ij}}$ are the predictions.

Similarly, we can define the prediction errors

$$\mathrm{PE}_{ij} = \left(\frac{C_{\mathrm{obs}_{ij}} - C_{\mathrm{pred}_{ij}}}{C_{\mathrm{pred}_{ij}}}\right) \cdot 100\%, \tag{16a}$$

$$\mathrm{APE}_{ij} = \left|\mathrm{PE}_{ij}\right|. \tag{16b}$$

To avoid division by zero when $C_{\mathrm{pred}_{ij}} = 0$, we set the error to zero for those samples.

We compute a median prediction error over all samples and define this as our per-individual prediction error. Then, the median absolute logarithmic error (MdALE) becomes

$$\mathrm{MdALE}_i = \mathrm{median}\left(\mathrm{ALE}_{ij}\right). \tag{17}$$

Similar measures can be computed for the median logarithmic error (MdLE), median absolute prediction error (MdAPE), and median prediction error (MdPE).

To get a measure of a model's performance over the entire population (N individuals), we compute the mean of the per-individual prediction errors, so that

$$\mathrm{mean(MdALE)} = \frac{1}{N}\sum_{i=1}^{N}\mathrm{MdALE}_i. \tag{18}$$

During model development, we use the measure mean(MdALE) Equation (18) as our measure of model fit, similarly to [Eleveld et al., 2018; Wahlquist et al., 2023b]. After training the NN, we compare the final model fit with the Eleveld model and the symbolic regression model from [Wahlquist et al., 2023b] using the per-population prediction errors mean(MdALE), mean(MdLE), mean(MdAPE), and mean(MdPE).

The prediction errors ALE and APE are used as indicators of model accuracy, while LE and PE are used as indicators of bias. Clinically acceptable values for the per-individual prediction errors are $10-20$ % for MdPE_i, $20-40$ % for MdAPE_i, < 0.18 for MdLE_i, and < 0.34 for MdALE_i [Schüttler et al., 1988; Varvel et al., 1992; Eleveld et al., 2018; Wahlquist et al., 2023b].

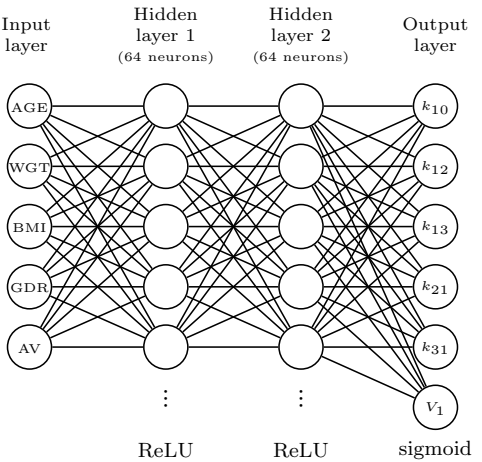

Figure 3. Neural network (NN) architecture with five covariates as inputs (age, weight, BMI, gender and blood sampling site, arterial or venous) and six pharmacokinetic (PK) parameters of the three-compartment model in Equation (1) as outputs. The NN has two hidden layers with 64 neurons each, with ReLU activation functions. The output layer has a sigmoid activation function to ensure positive outputs.

3.3 Neural network training and architecture

We represent our covariate model by an NN that maps covariates to PK parameters. The inputs to the NN are the five covariates: age, weight, BMI, gender, and sampling site (arterial or venous). The outputs are the six PK parameters of the three-compartment model: rate constants k_{10}, k_{12}, k_{21}, k_{13}, k_{31}, and central compartment volume V_1.

The NN architecture is similar to the one in [Janssen et al., 2022c], with two hidden layers, each with 64 neurons and ReLU activation functions. Nonlinear activation functions enable capturing more complex relationships of the covariate model. A sigmoid activation function is applied to the output layer to ensure positive PK parameters. The NN architecture used for covariate modeling is shown in Figure 3, We implement the neural network in the Julia programming language with the ML package Flux.jl [Innes, 2018].

The training of the NN was performed with the loss function J, which is mean(MdALE) Equation (17) and $\mathcal{L}_2$-regularization that reduces the risk of overfitting, so that

$$J(\theta) = \text{mean(MdALE)} + \frac{\lambda}{2N}\sum_{i=1}^{n_\theta}\theta_i^2, \tag{19}$$

where θ are the trainable parameters of the NN, n_θ is the number of trainable parameters, and λ is the regularization parameter. We set $\lambda = 0.1$. N is the number

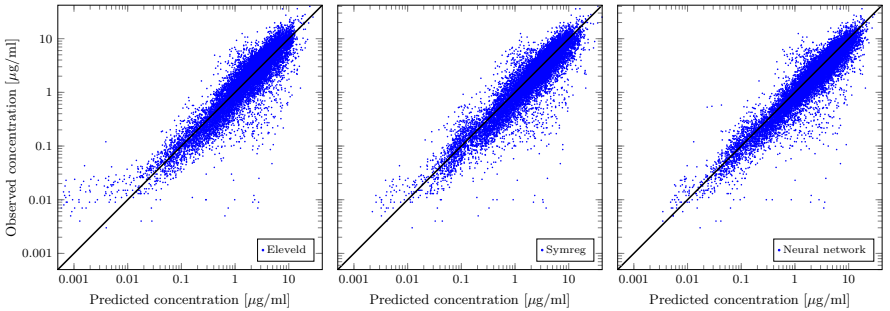

Figure 4. Predicted versus observed propofol concentrations in log-log scale of three covariate models for the Eleveld data set [Eleveld et al., 2018]. The Eleveld model [Eleveld et al., 2018] predictions are shown to the left, the symbolic regression model [Wahlquist et al., 2023b] predictions are shown in the middle, and the neural-network based covariate model derived in this is shown to the right. The identity function, representing a perfect model fit, is shown in black.

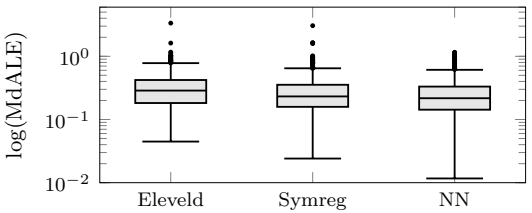

Figure 5. Box plots showing the distribution of prediction errors MdALE Equation (17) for the three covariate models: the Eleveld model [Eleveld et al., 2018], the symbolic regression model [Wahlquist et al., 2023b], and the neural network model derived in this paper.

of individuals in the data set. To further reduce the impact of overfitting, we use five-fold cross-validation in the hyper parameter tuning process. We use backpropagation with stochastic gradient-based optimization with the ADAM optimizer with a learning rate of $5 \cdot 10^{-4}$ to update the trainable parameters of the NN (weights and biases). The NN was trained for 5000 epochs. We refer the interested reader to the code repository [Wahlquist, 2024] for further implementation details, including hyper parameter values (see Figure 3).

4. Results

Figure 4 shows the final covariate model predictions together with the predictions of the Eleveld model in [Eleveld et al., 2018] and the symbolic regression model in [Wahlquist et al., 2023b]. The difference between the predictions from the compared models is small, but the covariate model derived in this paper has a slightly better fit than the other models. To illustrate the prediction error distribution of the compared

Table 1. Average of per-individual prediction errors for three covariate models: the Eleveld model [Eleveld et al., 2018], the symbolic regression model [Wahlquist et al., 2023b], and the neural network model derived in this paper.

Method	Mean MdALE	Mean MdLE	Mean MdAPE	Mean MdPE
Eleveld model	0.325	0.0791	34.8	14.4
Symbolic regression	0.279	-0.0489	27.4	-0.266
Neural network	0.263	-0.102	24.8	-6.34

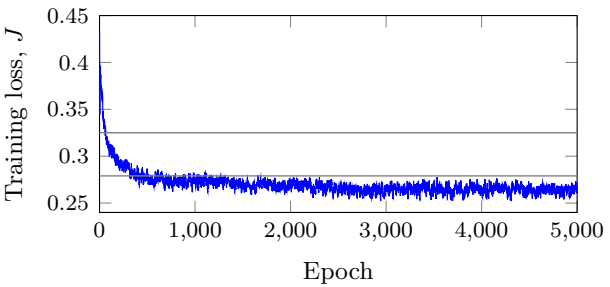

Figure 6. Training loss J Equation (19) of the neural network training process on the Eleveld data set [Eleveld et al., 2018]. Mean(MdALE) loss Equation (18) of the Eleveld model [Eleveld et al., 2018] is shown in the upper gray line, and the corresponding loss for the symbolic regression model [Wahlquist et al., 2023b] is shown in the lower gray line for comparison.

models between observed and predicted concentrations, Figure 5 shows a box plot of the per-individual prediction errors MdALE in Equation (17). In particular, we notice fewer outliers for the covariate model derived in this paper.

The model performance over the population is computed as the mean of the per-individual prediction errors, as explained in Section 3.2, and these are shown in Table 1. There, we notice that the metrics that indicate precision, mean(MdALE) and mean(MdAPE), are lower for the NN covariate model in this paper compared to the two other models. However, the metrics indicating bias, mean(MdLE) and mean(MdPE), are higher for the NN covariate compared to the symbolic regression network model. All prediction errors are within clinically accepted limits, which was introduced in Section 3.2.

The PK parameters predicted by the NN covariate model are shown in Figure 7. The predicted PK parameters are within the same range as those predicted by the Eleveld model in [Eleveld et al., 2018] and the symbolic regression model in [Wahlquist et al., 2023b], which illustrates that the NN generates sound predictions.

The training loss in Equation (18) of each training epoch is shown in Figure 6,

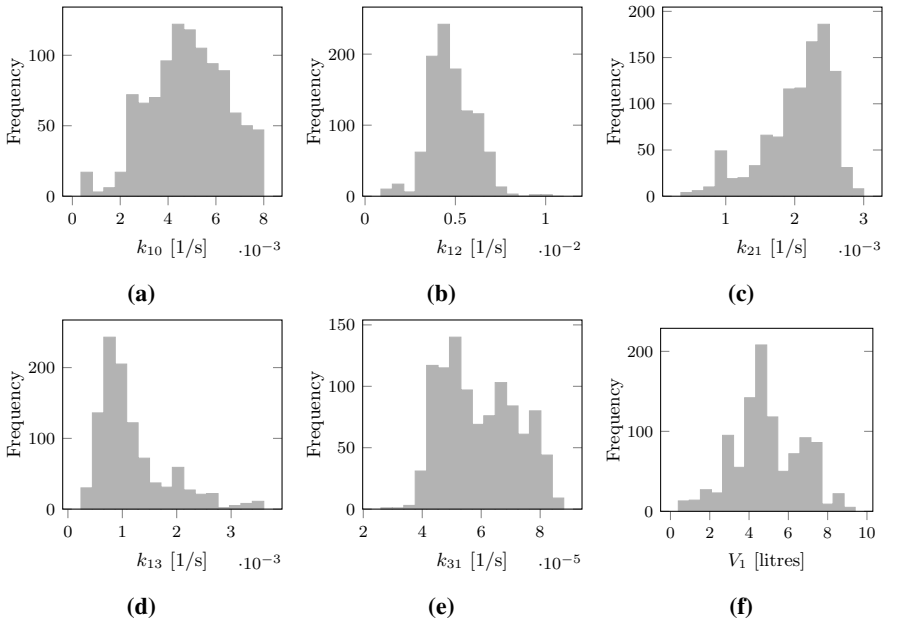

Figure 7. Distribution of predicted PK parameters of the three-compartment model Equation (1) from our covariate model on the propofol data set [Eleveld et al., 2018].

confirming that the NN has been trained until sufficient convergence.

For our training process of 5000 epochs on the Eleveld data set with 1031 individuals, we have to perform more than five million individual simulations, corresponding to more than 300 million dosing events. This illustrates the need for a fast simulator. In total, the training process took 14 400 seconds (four hours) on a computer with an Intel Core i5-8265U CPU and 16 GB RAM, which means that the average training time per individual and epoch was 2.8ms.

To minimize the risk of overfitting, we used regularization and five-fold cross-validation in the training and hyper parameter tuning process. Over five folds, the ratio between the average loss J in Equation (19) in the validation and training sets was 1.16, which indicates that the model is slightly overfitted (see Table 1).

5. Discussion

In this paper, we demonstrate how to automatically learn covariate relationships for pharmacometric covariate modeling. The covariate model is represented by an NN, that is trained using an efficient simulator of pharmacokinetics, FastPKSim.jl.

We show that the predicted plasma concentrations from the NN covariate model are slightly better than predictions from the Eleveld model in [Eleveld et al., 2018]

and comparable to those from the symbolic regression model in [Wahlquist et al., 2023b]. As shown in Figure 7, the NN covariate model produces predictions of the PK model parameters within the same range as the compared models [Eleveld et al., 2018; Wahlquist et al., 2023b], reinforcing the model's validity and soundness. These ranges of the final PK parameters are commonly recognized as a sign of model validity. For example, in [Eleveld et al., 2018], PK parameter values were tightly constrained during model development, to ensure that the final parameters were within a specified range.

As shown in Table 1, our final covariate model shows better precision but worse bias than the symbolic regression model in [Wahlquist et al., 2023b]. However, the differences are small, and all prediction errors are within clinically accepted limits. The choice of NN structure and hyper parameters affects the final model fit. In this paper, we have used a simple NN structure similar to the one in [Janssen et al., 2022c] without further exploration of activation functions and neurons in each layer. The hyper parameters for network training were heuristically based on the ones used in [Janssen et al., 2022c] and [Wahlquist et al., 2023b]. A grid search for determining hyper parameters could result in more accurate predictions.

We use the mean of the per-individual prediction errors mean (MdALE) Equation (18) as our measure of model fit, similarly to what were done in [Eleveld et al., 2018] and [Wahlquist et al., 2023b]. However, this measure is good for optimizing median performance, but not for the average or the worst cases. Using this measure may result in predictions being far off for some individuals. To improve the model fit, we could use a different loss function, for example, the mean squared error (MSE), which penalizes outliers more, ensuring safety for more individuals.

The covariate model derived in this paper is a black-box model, which means that the relationship between covariates and PK parameters can be difficult to interpret. This is a general problem with NNs. There are several methods to improve the explainability of NNs, where one example is symbolic regression networks [Wahlquist et al., 2023b]. However, in several cases, for example [*DermaSensor* 2024] and [*AI-Rad Companion Chest X-ray, Siemens Healthineers* 2024], regulatory agencies have deemed that clinical usefulness outweighs lacking explainability. When using diagnostic tools as the two cited examples, it is typically hard to independently validate their output. In contrast, our methodology generates a PK model that can undergo standard model validity tests, such as cross-validation on data that was not used in the training of the model.

To avoid overfitting, we use regularization and five-fold cross-validation in the training and hyper parameter tuning process. Even after taking these measures, the final model is slightly overfitted. This means that the NN might not inter- and extrapolate so well on unseen data, so the model might not be valid for predictions outside the range of the training data. However, the Eleveld data set is a rather large data set, covering a wide range of covariates, which means that the covariate model should perform well on unseen data. To further ensure good inter- and extrapolation, the NN covariate model should be validated on a different data set. Other options to

reduce overfitting could be to use a different regularization, or dropout (more suitable for large networks) [Srivastava et al., 2014]. Also, developing a readable and interpretable covariate model, like the one in [Eleveld et al., 2018; Schnider et al., 1998; Wahlquist et al., 2023b], could be an option to reduce overfitting.

We demonstrate how to use an efficient simulator of pharmacokinetics to speed up the pharmacometric model development process. By further optimizing automatic differentiation through the simulator, we could speed up the training process even more. Another way to further speed up the training process could be to use starting values for the predicted PK parameters for the NN as was done in [Janssen et al., 2022c].

ML has the potential to improve pharmacometric modeling by automating the model-building process. This allows for a faster model development where more covariate relationships are explored, better explaining the inter-patient variability in the drug response.

There is more work to be done within ML for pharmacometric modeling. Some examples of problems to tackle are: how to identify relevant covariates and how to add known knowledge to the model-building process. In this work, we address the identification of relevant covariates implicitly during training, since unimportant covariates will have small impact on the prediction. It would be possible to use a more refined method for covariate selection, such as a Hessian-based sensitivity analysis, as was done in [Wahlquist et al., 2023b]. Incorporating further expert knowledge could be accomplished for example by using symbolic regression networks [Wahlquist et al., 2023b], where an expert can influence the type of functional expressions to be considered. Here, we have decided to not impose any constraints on the model search, but rather allow the NN to adapt freely. While this comes at a cost of explainability, it increases the chances of approximating the best possible fit to the available data. As such, the models yielded by our methodology can serve as an approximation of what predictive capability one can expect for a given data set. In this context, it is assuring that the model we obtain in this study does not outperform the one obtained by state-of-the-art methodology by much. This indicates that the predictive performance of the traditionally obtained model is limited by its training data. While predictive performance are comparable, the main advantage we offer is thus to cut away manually labor-intense and tedious modeling task associated with the traditional approach of manual covariate model structure selection.

6. Conclusion

We have presented a methodology for automating covariate modeling where covariate relationships are learned from data using neural networks. To be able to simulate dose-response data efficiently during model development, we use an efficient simulator of pharmacokinetics, FastPKSim.jl. This methodology was demonstrated on a propofol data set, where the final covariate model predictions were compared to

previously published models. We conclude that the potential of automatic covariate modeling is significant, as it allows for a faster model development process where a wider search space of covariate relationships is explored.

CRediT authorship contribution statement

Ylva Wahlquist: Conceptualization, Formal analysis, Methodology, Software, Validation, Visualization, Writing – original draft, Writing – review & editing.
Kristian Soltesz: Conceptualization, Formal analysis, Methodology, Supervision, Writing – original draft, Writing – review & editing.

Declaration of competing interest

The authors declare that they have no known competing financial interests or personal relationships that could have appeared to influence the work reported in this paper.

Acknowledgements

This work was partially supported by the Wallenberg AI, Autonomous Systems and Software Program (WASP) funded by the Knut and Alice Wallenberg Foundation. The authors are members of the Excellence Center at Linköping-Lund in Information Technology (ELLIIT).

Data Availability

I have shared the data on GitHub (`https://github.com/wahlquisty/automated-covariate-modeling-with-fastpksim`).

References

AI-Rad Companion Chest X-ray, Siemens Healthineers (2024). //www.healthairegister.com/. Accessed: 2024-02-28.

Åström, K. and B. Wittenmark (2011). *Computer-Controlled Systems: Theory and Design, Third Edition*. Dover Books on Electrical Engineering. Dover Publications. ISBN: 9780486486130.

Brier, M. E., J. M. Zurada, and G. R. Aronoff (1995). "Neural network predicted peak and trough gentamicin concentrations". *Pharmaceutical Research* **12**:3, pp. 406–412. DOI: 10.1023/a:1016260720218.

Chow, H.-H., K. M. Tolle, D. J. Roe, V. Elsberry, and H. Chen (1997). "Application of neural networks to population pharmacokinetic data analysis".

DermaSensor (2024). https://www.dermasensor.com/. Accessed: 2024-02-28.

Eleveld, D. J., P. Colin, A. R. Absalom, and M. M. R. F. Struys (2018). "Pharmacokinetic-pharmacodynamic model for propofol for broad application in anaesthesia and sedation". *British Journal of Anaesthesia* **120**:5, pp. 942–959. ISSN: 0007-0912, 1471-6771. DOI: 10.1016/j.bja.2018.01.018.

Innes, M. (2018). "Flux: elegant machine learning with julia". *Journal of Open Source Software*. DOI: 10.21105/joss.00602.

Janssen, A., F. C. Bennis, and R. A. A. Mathôt (2022a). "Adoption of machine learning in pharmacometrics: an overview of recent implementations and their considerations". *Pharmaceutics* **14**:9, p. 1814. DOI: 10 . 3390 / pharmaceutics14091814.

Janssen, A., M. Hoogendoorn, M. H. Cnossen, and R. A. A. Mathôt (2022b). "Application of SHAP values for inferring the optimal functional form of covariates in pharmacokinetic modeling". *CPT: Pharmacometrics & Systems Pharmacology* **11**:8, pp. 1100–1110. DOI: 10.1002/psp4.12828.

Janssen, A., F. W. G. Leebeek, M. H. Cnossen, and R. A. A. Mathôt (2022c). "Deep compartment models: a deep learning approach for the reliable prediction of time-series data in pharmacokinetic modeling". *CPT: Pharmacometrics & Systems Pharmacology* **11**:7, pp. 934–945. DOI: 10.1002/psp4.12808.

Liu, R., X. Li, W. Zhang, and H.-H. Zhou (2015). "Comparison of nine statistical model based warfarin pharmacogenetic dosing algorithms using the racially diverse international warfarin pharmacogenetic consortium cohort database". *PLOS ONE* **10**:8, e0135784. DOI: 10.1371/journal.pone.0135784.

Ogami, C., Y. Tsuji, H. Seki, H. Kawano, H. To, Y. Matsumoto, and H. Hosono (2021). "An artificial neural network-pharmacokinetic model and its interpretation using Shapley additive explanations". *CPT: Pharmacometrics & Systems Pharmacology* **10**:7, pp. 760–768. DOI: 10.1002/psp4.12643.

Rackauckas, C., Y. Ma, A. Noack, V. Dixit, P. K. Mogensen, S. Byrne, S. Maddhashiya, J. B. Santiago Calderón, J. Nyberg, J. V. Gobburu, et al. (2020). "Accelerated predictive healthcare analytics with pumas, a high performance pharmaceutical modeling and simulation platform". *bioRxiv*. DOI: 10.1101/2020.11.28.402297.

Rackauckas, C. and Q. Nie (2017). "DifferentialEquations.jl – a performant and feature-rich ecosystem for solving differential equations in Julia". *Journal of Open Research Software* **5**:1.

Sahinovic, M. M., M. M. R. F. Struys, and A. R. Absalom (2018). "Clinical pharmacokinetics and pharmacodynamics of propofol". *Clinical Pharmacokinetics* **57**:12, pp. 1539–1558. DOI: 10.1007/s40262-018-0672-3.

Schnider, T. W., C. F. Minto, P. L. Gambus, C. Andresen, D. B. Goodale, S. L. Shafer, and E. J. Youngs (1998). "The influence of method of administration and covariates on the pharmacokinetics of propofol in adult volunteers". *Anesthesiology* **88**:5, pp. 1170–1182. DOI: 10.1097/00000542-199805000-00006.

Schüttler, J., S. Kloos, H. Schwilden, and H. Stoeckel (1988). "Total intravenous anaesthesia with propofol and alfentanil by computer-assisted infusion". *Anaesthesia* **43**:s1, pp. 2–7. DOI: 10.1111/j.1365-2044.1988.tb09059.x.

Schüttler, J. and H. Ihmsen (2000). "Population pharmacokinetics of propofol:A multicenter study". *Anesthesiology* **92**:3, pp. 727–738. DOI: 10.1097/00000542-200003000-00017.

Sheiner, L. B. and S. L. Beal (1980). "Evaluation of methods for estimating population pharmacokinetics parameters. I. Michaelis-Menten model: routine clinical pharmacokinetic data". *Journal of Pharmacokinetics and Pharmacodynamics* **8**, pp. 553–571. DOI: 10.1007/BF01060053.

Sibieude, E., A. Khandelwal, P. Girard, J. S. Hesthaven, and N. Terranova (2022). "Population pharmacokinetic model selection assisted by machine learning". *Journal of Pharmacokinetics and Pharmacodynamics* **49**:2, pp. 257–270. DOI: 10.1007/s10928-021-09793-6.

Sibieude, E., A. Khandelwal, J. S. Hesthaven, P. Girard, and N. Terranova (2021). "Fast screening of covariates in population models empowered by machine learning". *Journal of Pharmacokinetics and Pharmacodynamics* **48**:4, pp. 597–609. DOI: 10.1007/s10928-021-09757-w.

Soltesz, K., G. A. Dumont, and J. M. Ansermino (2013). "Assessing control performance in closed-loop anesthesia". In: *21st Mediterranean Conference on Control and Automation*, pp. 191–196. DOI: 10.1109/MED.2013.6608720.

Srivastava, N., G. Hinton, A. Krizhevsky, I. Sutskever, and R. Salakhutdinov (2014). "Dropout: a simple way to prevent neural networks from overfitting". *The Journal of Machine Learning Research* **15**:1, pp. 1929–1958.

Varvel, J. R., D. L. Donoho, and S. L. Shafer (1992). "Measuring the predictive performance of computer-controlled infusion pumps". *J Pharmacokinet Biopharm* **20**:1, pp. 63–94. DOI: 10.1007/BF01143186.

Wahlquist, Y. (2022). *FastPKSim.jl*. URL: https://github.com/wahlquisty/FastPKSim.jl.

Wahlquist, Y. (2024). *Automated covariate modeling using efficient simulation of pharmacokinetics*. Commit: 0cdd6c0. URL: https://github.com/wahlquisty/automated-covariate-modeling-with-fastpksim.

Wahlquist, Y., F. Bagge Carlson, and K. Soltesz (2023a). "Fast simulation of pharmacokinetics". *IFAC Proceedings Volumes (IFAC-PapersOnline), 22nd IFAC World Congress*.

Wahlquist, Y., J. Sundell, and K. Soltesz (2023b). "Learning pharmacometric covariate model structures with symbolic regression networks". *Journal of Pharmacokinetics and Pharmacodynamics*. Accepted. DOI: 10.21203/rs.3.rs-3062691/v1.

Supplementary Information

A. Eigenvalues of the three-compartment model

In the following section, we show the eigenvalues of the three-compartment model in Equation (1). We used a computer algebra system to solve the eigenvalue problem $A - \lambda I = 0$ for the three compartment model, to obtain the form

$$\lambda = \begin{bmatrix} -c_1 - c_7 \\ -c_9 - c_{10} \\ c_9 - c_{10} \end{bmatrix} \tag{20a}$$

where

$$\begin{aligned}
b_1 &= k_{10} + k_{12} + k_{13} + k_{21} + k_{31} \\
b_2 &= k_{21}(k_{10} + k_{13} + k_{31}) + k_{31}(k_{10} + k_{12}) \\
b_3 &= k_{10} k_{21} k_{31} \\
c_1 &= b_1/3 \\
c_2 &= c_1^3 \\
c_3 &= b_2/3 \\
c_4 &= c_3 - c_1^2 \\
c_5 &= (b_1 c_3 - b_3)/2 \\
c_6 &= 2\left(c_5 + \sqrt{c_4^3 + (c_2 - c_5)^2} - c_2\right)^{1/3} \\
c_7 &= -\mathrm{Re}(c_6) \\
c_8 &= \mathrm{Im}(c_6) \\
c_9 &= c_8\sqrt{3}/2 \\
c_{10} &= c_1 - c_7/2.
\end{aligned} \tag{20b}$$

was obtained by manual substitutions within the corresponding expression tree.

Paper V

Kalman Filter Soft Sensor to Handle Signal Quality Loss in Closed-Loop Controlled Anesthesia

Ylva Wahlquist Nicola Paolino Michele Schiavo
Antonio Visioli Kristian Soltesz

Abstract

Background and objective: This study aims to enhance the performance of a closed-loop anesthetic depth control system by fusing noise-corrupted clinical measurements with a non-perfect pharmacological model.

Methods: We implement a Kalman filter to constitute a trade-off between model prediction and measurement signal dependence for depth of hypnosis (*DoH*) control using a previously evaluated PID controller. This trade-off is adjusted online, based on signal quality index (*SQI*) feedback, provided by the clinical *DoH* monitor, in this case assumed to be the bispectral index (BIS) monitor.

Results: Our simulations show that the proposed solution leads to fundamental performance improvements over the traditional monitor feedback case, which fails to provide the required clinical performance when the *SQI* drops due to signal inference. In particular, the soft sensor approach increases the time of *DoH* within the recommended clinical range of 40–60 BIS from 71% to 99%, compared to simple feedback of the noisy monitor output.

Conclusion: Our Kalman filter soft-sensor approach succeeds in importantly increasing system robustness to measurement signal disturbances by combining sensor measurements and model predictions.

Keywords: Closed-loop anesthesia, Kalman filter, PID control

Originally published in Biomedical Signal Processing and Control (2025). The original version is available at `https://doi.org/10.1016/j.bspc.2025.107506`.

1. Introduction

A key challenge in general anesthesia is to adequately control the depth of hypnosis (*DoH*) in the patient [Blayney, 2012]. In this paper, we consider *DoH* control using the intravenously infused drug propofol. The control is challenging, since *DoH* cannot be measured directly, but is only observed indirectly through correlated signals and patient signs. In addition to manual titration, two computer-controlled dosing regimens have gained ground.

Of these, target-controlled infusion (TCI) [Absalom et al., 2016] has received the broadest clinical acceptance to date. TCI is a model-based feed-forward strategy, that optimizes an infusion trajectory offline, based on a user-provided reference. As such, it is vulnerable both to model errors and external disturbances, since the infusion is not based on actual measurements of the patient state. However, if the anesthesiologist suspects model errors or disturbances based on patient observations, they can update the setpoint concentration.

The other computer-controlled dosing strategy that has to date been employed in several research studies is closed-loop control. It relies on feedback from a *DoH* estimate, provided by a non-invasive processed electroencephalogram (pEEG) monitor [Rampil, 1998]. Such monitors report *DoH* on the bispectral index (BIS) scale, where 100 is the maximum achievable cortical activity (being awake corresponds to a value near 100), and 0 represents an iso-electric EEG (corresponding to the maximally achievable *DoH*) [Vuyk and Mertens, 2003].

Closed-loop systems are well known to outperform open-loop ones when suitably designed and tuned. That is why several research efforts have been made to design closed-loop architectures, as demonstrated by [Ghita et al., 2020; Hosseinzadeh et al., 2020; Agarwal et al., 2009]. The closed-loop control algorithm could be a simple proportional-integrative-derivative (PID) [Visioli, 2006] controller as in [Dumont et al., 2009; Gonzalez-Cava et al., 2021; Padula et al., 2017; Puri et al., 2007; Soltesz et al., 2013], or some more advanced one as in e.g., [Merigo et al., 2017; Merigo et al., 2020; Pawlowski et al., 2022a; Copot et al., 2017; Paolino et al., 2023; Mendez et al., 2016; Mendez et al., 2018]. We have previously shown that the control performance of these systems is mainly limited by the modeling uncertainties such as those coming from inter- and intra-patient variability, rather than by the choice of control algorithm [Gonzalez-Cava et al., 2021; Soltesz et al., 2019]. Hence, we base our example on a PID-controlled system, although the methodology we introduce is equally applicable to other types of controllers. While closed-loop systems provide some means to attenuate external disturbances and cope with model errors, they are vulnerable to corruption of the measurement that constitutes the feedback signal.

Alongside a *DoH* estimate, clinical *DoH* monitors provide a signal quality index (*SQI*) ranging from 0–100 (low–high signal quality). This index, which is updated and displayed on the monitor, provides the anesthesiologist with an estimate of the current BIS measurement reliability. In clinical practice, a *DoH* measure associ-

ated with an $SQI \leq 50$ is considered unreliable [*BIS™ Complete Monitoring System* 2013]. Signal quality loss directly affects the anesthesiologist's working procedure since they cannot rely on the *DoH* monitor while adjusting the drug infusion rate. Low *SQI* values are common during general surgery [Dahaba, 2005; Chan et al., 2012]. This can, for example, be due to forehead motion, improper sensor placement, or electrical inference from the use of an electro-scalpel [Gjika et al., 2016].

We consider a scenario where the monitor *DoH* estimate is corrupted by inference. By introducing a novel soft-sensor approach to closed-loop controlled anesthesia, we can maintain patient safety despite loss of signal quality. This is achieved by a Kalman filter, a classic methodology that has been only recently exploited in biomedical and biomechanical engineering [Oikonomou et al., 2009; Misgeld et al., 2017]. In particular, the usage of a Kalman filter in the anesthesia field has been proposed in, for example, [Aubouin-Pairault et al., 2024] to estimate both the state and parameters of the system to predict the future trajectory. Here, a linear Kalman filter is used to shift the balance from measurement to model reliance (i.e., from ordinary closed-loop towards TCI), when *SQI* is decreased. When signal quality is good (*SQI* closer to 100), feedback will essentially be based on the monitor output, as in conventional closed-loop controlled anesthesia. In contrast, when signal quality is poor (*SQI* closer to 0), the feedback will be based mainly on the model prediction, and effectively behave like TCI.

In this work, we introduce a novel Kalman-filter-based soft-sensor concept for anesthesia control. To demonstrate this methodology, we use a patient simulator that explicitly models both patient variability (model uncertainty), measurement disturbances that our model-based soft-sensor is purposed to attenuate, and measurement noise.

The novelty of our approach thus lies in using the Kalman filter as a tuning knob to shift between model and measurement reliance, rather than as the minimum-variance estimator where its tuning parameters are optimized to minimize estimation error, assuming some Gaussian state and measurement noise processes.

2. System architecture

Our proposed closed-loop control architecture is shown in Figure 1. It consists of four main components: the patient dynamics (Section 2.1), the Kalman-filter-based soft sensor (Section 2.2), the clinical *DoH* monitor (Section 2.3), and the drug-dosing closed-loop controller (Section 2.4).

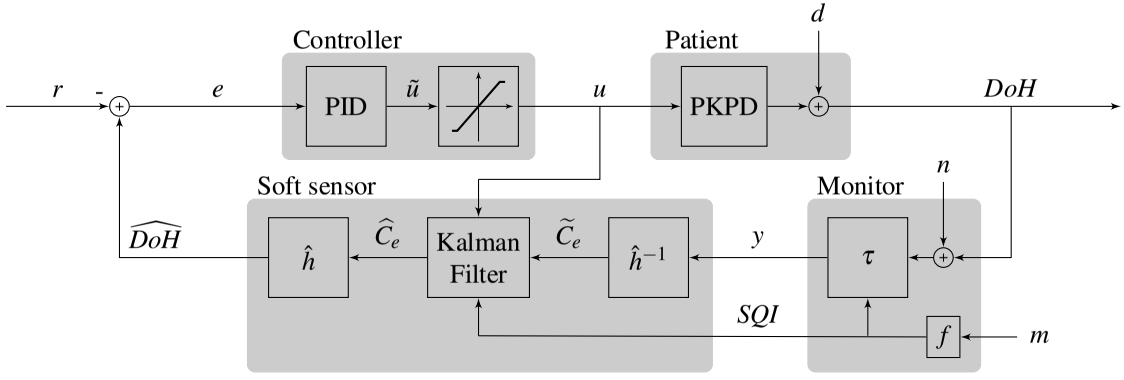

Figure 1. Control scheme featuring the proposed Kalman-filter-based soft sensor (bottom left shaded box). The components are described one by one in Sections 2.1 to 2.4. The objective is to follow the *DoH* reference r, by adequately titrating the infusion rate u, in presence of surgical disturbance d, measurement noise n, electric monitor inference m, and imperfection of the patient model.

2.1 Patient

Kalman filtering is a model-based approach, and in our case, patient dynamics are modeled by a conventional four-compartment linear pharmacological model [Soltesz et al., 2019; Schnider et al., 1998; Åström and Murray, 2008]. These linear models are the gold standard to represent propofol pharmacokinetics and they have been employed in commercial devices, such as in TCI [Struys et al., 2000]. Precisely, the model is defined as

$$\dot{\boldsymbol{x}}(t) = A\boldsymbol{x}(t) + Bu(t), \tag{1a}$$
$$C_e(t) = C\boldsymbol{x}(t), \tag{1b}$$

where

$$A = \begin{bmatrix} -(k_{10}+k_{12}+k_{13}) & k_{21} & k_{31} & 0 \\ k_{12} & -k_{21} & 0 & 0 \\ k_{13} & 0 & -k_{31} & 0 \\ \dfrac{k_{e0}}{V_1} & 0 & 0 & -k_{e0} \end{bmatrix}, \tag{2a}$$
$$B = \begin{bmatrix} 1 & 0 & 0 & 0 \end{bmatrix}^\top, \tag{2b}$$
$$C = \begin{bmatrix} 0 & 0 & 0 & 1 \end{bmatrix}. \tag{2c}$$

The system in Equation (1) represents a linear system since the right-hand sides of Equation (1a) and Equation (1b) are both linear functions of the state $\boldsymbol{x}$ and input u.

Propofol infusion is modeled by the input signal u [mg s^{-1}]. The first state component, x_1 [mg], represents the mass of propofol in the blood plasma, while the last, $x_4 = C_e$ [mg L^{-1}], models the effect-site concentration, being the drug concentration in the cortex of the brain. The other state components, x_2 [mg] and x_3 [mg], model the mass distribution in fast and slow tissue, respectively. The parameters k_{10}, k_{12}, k_{13}, k_{21}, k_{31}, and k_{e0}, in units of s^{-1}, are rate constants, and V_1 [L] models the blood plasma volume. Note that the effect-site concentration, or any of the other states, is not directly measurable.

Saturation effects at low and high effect-site drug concentrations are modeled using a Hill sigmoid output nonlinearity [Goutelle et al., 2008]

$$DoH(t) = h(C_e(t); \gamma, C_{e50}, E_0, E_{\max}) = E_0 - E_{\max}\frac{C_e(t)^\gamma}{C_e(t)^\gamma + C_{e50}^\gamma}. \tag{3}$$

The DoH level in the absence of a drug is $E_0 \lessapprox 100$ BIS, and the maximum deviation from this level is $E_{\max} \lessapprox 100$ BIS. The effect-site concentration C_{e50} [mg L^{-1}] is the concentration at which the hypnotic depth is halfway between the limits defined through E_0 and $E_{\max}$, $DoH = E_0 - E_{\max}/2$. The third parameter of Equation (3), γ, is a unitless shape parameter that defines the steepness of the sigmoid, such that the limit $\gamma \to \infty$ defines a DoH step between E_0 and $E_0 - E_{\max}$ at $C_e = C_{e50}$. Together,

Equations (2) and (3) constitutes a so-called pharmacokinetic–pharmacodynamic (PKPD) model, as thoroughly introduced and explained in [Soltesz et al., 2019].

Since we will use our model in a closed-loop interconnection with a periodically sampled controller, we will use the approximation-error-free zero-order-hold discretization of Equation (2). Denoting the sampling period $T_s = 1$ s, we index the samples so that if $\boldsymbol{x}(t) = \boldsymbol{x}_k$, then $\boldsymbol{x}(t+T_s) = \boldsymbol{x}_{k+1}$. This results in the discrete state space representation

$$\boldsymbol{x}_{k+1} = F\boldsymbol{x}_k + Gu_k, \tag{4a}$$

$$(C_e)_k = H\boldsymbol{x}_k, \tag{4b}$$

with constant matrices $F = \exp(AT_s)$, $G = \int_0^{T_s} \exp(As)\, ds\, B$, and $H = C$, as derived and explained in [Åström and Wittenmark, 1984]. The input at sample k is denoted u_k.

The drug response dynamics vary between patients and are commonly modeled with fixed and random effects. The fixed effects model the variability that can be explained by covariates such as age, height, and weight. The random effects model the remaining variability that is not explained by covariates [Soltesz et al., 2019]. This is a well-established methodology for modeling dynamic uncertainty in the drug response.

For a particular model parameter θ with fixed effect (nominal) value θ_0, the parameter is assumed to be drawn from the log-normal distribution

$$\theta = \theta_0 \exp(\eta_p), \tag{5}$$

where the random effect η_p is a normal stochastic variable with zero mean and variance σ_p^2 [Vanluchene et al., 2004].

To reflect this, we use the Schnider population model [Schnider et al., 1998], which expresses the model parameters mentioned in the individual patient covariates age, height, weight, and gender. The Schnider model incorporates intra-patient variability (i.e., random effects) through coefficients of variation (CV). The variances σ_θ^2 of the PK parameter θ relates to the corresponding CV_θ through [Canchola et al., 2017]

$$\sigma_\theta^2 = \log\left(\left(\frac{CV_\theta}{100}\right)^2 + 1\right). \tag{6}$$

Surgical stimulation typically increases the level of awareness in the patient, thus affecting *DoH*. It is customary [Melia et al., 2017; Soltesz et al., 2019] to model the effect of such stimulation as an additive disturbance d, acting on *DoH*, as shown in Figure 1.

2.2 Soft sensor

The Kalman filter is an optimal state estimator, in the sense that it provides the state estimate that minimizes error variance, given that the system dynamics are linear and the noise is Gaussian [Welch and Bishop, 1995].

While the Hill function Equation (3) is non-linear, it is invertible. Particularly, if we equate the right-hand-side of Equation (3) its inverse is

$$C_e(t) = h^{-1}(DoH(t); \gamma, C_{e50}, E_0, E_{\max}) = C_{e50} \left(\frac{E_{\max}}{E_0 - DoH(t)} - 1 \right)^{-1/\gamma}. \quad (7)$$

Since the parameters are not known with certainty, we will use estimates $\hat{\gamma}$, $\widehat{C}_{e50}$, $\widehat{E}_0$, $\widehat{E}_{\max}$, as explained further in Section 3.2. The blocks $\hat{h}$ and $\hat{h}^{-1}$ in Figure 1 are thus obtained analogs of Equation (3) and Equation (7). In particular, $\hat{h}^{-1}$ constitutes a linearizing transform, providing a purely measurement-based plasma concentration estimate $\widetilde{C}_e$, used to drive the Kalman filter.

The Kalman filter utilizes the model Equation (2) together with a sequence of sampled input–output data $u, \widetilde{C}_e$ to provide an online estimate $\hat{\boldsymbol{x}}$ of the system state $\boldsymbol{x}$.

Internally, the filter stores its estimate, alongside an error covariance matrix estimate P, which it updates dynamically and uses to compute a gain vector L that is used to drive the estimated state towards the actual one based on model input–output data.

In the following, we present the equations defining the standard Kalman filter. We use $\hat{\boldsymbol{x}}_{k,k-1}$ to denote the estimate of $\boldsymbol{x}_k$, based on data up to and including $k-1$; $\hat{\boldsymbol{x}}_{k,k}$ is the updated estimate incorporating the data sample k. The same double-index notation is used for the covariance estimate P. The update equations for the gain L, covariance P and state estimate $\hat{\boldsymbol{x}}$ are given by

$$L_k = P_{k,k-1} H^\top (H P_{k,k-1} H^\top + R_k)^{-1}, \quad (8a)$$

$$P_{k,k} = (I - L_k H) P_{k,k-1} (I - L_k H)^\top + L_k R_k L_k^\top, \quad (8b)$$

$$\hat{\boldsymbol{x}}_{k,k} = \hat{\boldsymbol{x}}_{k,k-1} + L_k ((\widetilde{C}_e)_k - H \hat{\boldsymbol{x}}_{k,k-1}), \quad (8c)$$

$$(\widehat{C}_e)_k = H \hat{\boldsymbol{x}}_{k,k}, \quad (8d)$$

while the prediction step is defined by

$$\hat{\boldsymbol{x}}_{k+1,k} = F \hat{\boldsymbol{x}}_{k,k} + G u_k, \quad (9a)$$

$$P_{k+1,k} = F P_{k,k} F^\top + Q_k, \quad (9b)$$

where F, G, H define the model dynamics according to Equation (4). The measurement equation is given by Equation (8d). The matrices Q and R are the assumed covariances of the additive Gaussian noise, which corrupts the true state $\boldsymbol{x}$ and the output C_e, respectively. Since we only have one measurement signal, R is scalar in our case. Further details, including a derivation of Equations (8) to (9) being optimal in the minimum-variance sense, can be found in [Becker, 2023].

In essence, the Kalman filter combines its prior state estimate with the current measurement to reduce the uncertainty associated with its current state estimate.

When the measurement covariance R is large, the Kalman gain is low. Then, the Kalman filter therefore relies more on the model than the measurement for its state estimate update.

The main novelty of our approach is to relate the measurement covariance R to the *SQI*, to establish a trade-off between measurement and model reliance. We do this by asserting the simple affine relationship

$$R(SQI) = R_{\min} + (R_{\max} - R_{\min}) \left(1 - \frac{SQI}{100}\right), \tag{10}$$

where the tuning parameters $R_{\min}$ and $R_{\max}$ define the values of R attained at $SQI = 100$ and $SQI = 0$, respectively. This means that if $SQI = 100$ and the signal quality is perfect, a small value of R, $R_{\min}$, is used. Adversely, if the signal quality is poor with $SQI = 0$, R becomes $R_{\max}$. As the algorithms used to calculate the *SQI* are proprietary, it is not straightforward to tailor the mapping model from *SQI* to R. As a first approach, we have opted for a simple linear model to constitute the mapping between *SQI* and R.

Since our setting lacks process noise as modeled by Kalman covariance Q, we use Q as a constant parameter. For simplicity, we assert a diagonal structure of Q, corresponding to the independent noise added to individual states being mutually independent Gaussians. We therefore consider the four diagonal elements of Q, together with $R_{\min}$ and $R_{\max}$ to be parameters of our filter, where R varies with *SQI* according to Equation (10).

In our application, we do not have support for the assumption that the process noise is Gaussian. Instead, we consider R and Q as free design parameters of the filter, that are tuned using a population-based approach (that is, using the same values for all the patients) to enable shifting between model and measurement reliance. Therefore, the Kalman filter will not be optimal even though the performance may still be satisfactory. If the noise characteristics at some point will be known to be better described by some other (spectral) noise model, this can be incorporated into the observer design.

The parameters values were optimized offline to minimize the mean square error (MSE) between the simulated patient *DoH* and the corresponding Kalman filter estimate $\widehat{DoH}$, which is the norm $\mathcal{L}_2$ of $\widehat{DoH} - DoH$. MSE values for each patient were summed, which means that they all contributed equally. The choice of patient population and simulation scenario used in this optimization are those described below in Section 3.2 and Section 3.1, respectively. In summary, our design choices are to:

- Optimize $R_{\min}$, $R_{\max}$ and diagonal fixed (time-independent) Q offline to minimize estimation error across a set of simulations (see Section 4);
- Update R online, based on the current *SQI*, according to Equation (10).

2.3 Monitor

The *DoH* estimate y, emerging from a clinical monitor, is noisy, even when $SQI = 100$. To reflect this, we use an additive noise model n, as shown in Figure 1. We will consider both an idealized noise-free case, $n = 0$, and a clinically realistic case, where n is a random cycled noise sequence, recorded by a BIS monitor under stable anesthetic conditions, as explained in [Pawlowski et al., 2022b].

As schematically illustrated in Figure 1, the (not directly measurable) electro-scalpel inference signal m enters the monitor, where its effect (through an uncharacterized function f) is mapped to SQI. Here, we model this inference with a delay τ that is computed starting from the SQI as

$$\tau = \tau_{\max} \left(1 - \frac{SQI}{100}\right). \tag{11}$$

That is, the inference m affects the SQI and results in the monitor output being delayed from $y(t)$ to $y(t-\tau)$, whenever $SQI < 100$. The delay ranges linearly between $\tau = 0$ s and $\tau = \tau_{\max} = 120$ s, based on SQI. This delay model is consistent with observations of our clinical collaborators and is supported by behavior observed in previous studies, e.g., [Chan et al., 2012].

In this formulation, the delay of the BIS monitor is not taken into account. We have focused on providing a delay model that describes the degradation of the SQI. Modeling the monitor delay poses a challenge, as the manufacturer has not disclosed the exact response and filtering dynamics of the BIS monitor. Neglecting modeling of the BIS delay has been shown to work in practice, as several clinical studies have been successfully carried out without considering the BIS delay [Liu et al., 2006; Struys et al., 2001].

A simulated example of the monitor model is shown in Figure 2, to illustrate how inference by the electro-scalpel is assumed to affect the monitor and the true *DoH*, respectively. The blue and red curves in Figure 2 show the actual *DoH*, and monitor output y, respectively. The discrepancy is due to the delay model Equation (11) and constitutes the measurement corruption that our soft-sensor approach aims to mitigate the effect. For visual clarity, Figure 2 shows a scenario with $n = 0$, i.e., in the absence of measurement noise.

2.4 Controller

We use a filtered PID controller [Visioli, 2006], which has previously been evaluated in [Schiavo et al., 2021a]. Its underlying continuous-time transfer function from error e to unsaturated infusion rate $\tilde{u}$ is

$$\frac{\tilde{U}(s)}{E(s)} = K_p \left(1 + \frac{1}{sT_i} + \frac{sT_d}{1 + sT_d/N}\right), \tag{12}$$

with proportional gain $K_p = 0.2$ mg/BIS/s, integral time $T_i = 386$ s, derivative time $T_d = 13.8$ s, and filtering factor $N = 5$. The PID controller values have been

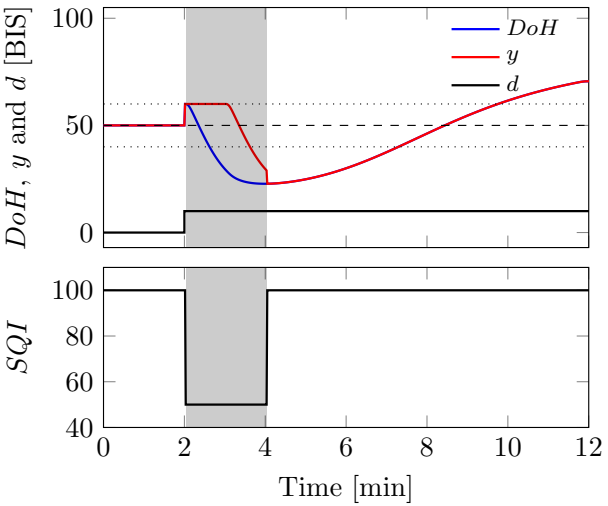

Figure 2. *DoH* (top, blue) and monitor output y (top, red). An *SQI* (bottom, black) drop from 100 to 50 is introduced at $t = 2$ min, and after that, an additive step disturbance $d = 10$ BIS (top, black) occurs. The signal degradation remains during 2 min (shaded area). The associated inference-induced corruption of the monitor output (top, discrepancy between blue and red) is defined in Section 2.3. The dashed black line indicates the *DoH* reference, and the dotted lines delimit the range between $DoH = 40$ BIS and $DoH = 60$ BIS.

obtained by minimizing the integral absolute error (IAE) over a simulation example with additive disturbances, see [Schiavo et al., 2021a] for details.

The actual infusion rate u is then saturated to within the range 0–1200 $\mathrm{mL\,h^{-1}}$, representative of several clinical infusion pumps. For the concentration of standard propofol solutions of 20 $\mathrm{mg\,mL^{-1}}$, this corresponds to u within the range 0–6.67 $\mathrm{mg\,s^{-1}}$.

3. Comparative simulation study

This section defines the details of our comparative study.

3.1 Surgical scenario

The performance of the proposed control structure was evaluated by repeated simulation of a maintenance phase of fifty minutes of anesthesia. We compare a nominal case, “monitor feedback”, with our novel architecture, “soft-sensor feedback”. In the monitor feedback case, the soft-sensor block of Figure 1 was replaced with the moving average filter that was clinically evaluated in connection with the controller of Section 2.4, as described in [Schiavo et al., 2021c]. This filter averages the eight most recent samples and was used to smooth out the signal.

We study a disturbance scenario to evaluate and compare performance: electro-scalpel activity causes a drop in *SQI* from 100 to 50, immediately followed by a step disturbance $d = 10$ BIS to reflect a lowered hypnotic depth in the patient resulting from the stimulation. After 2 min, surgical stimulation stops and *SQI* returns to 100. However, the disturbance $d = 10$ BIS remains, reflecting a lasting nociceptive response. As the actual *SQI* dynamics are unknown, we have modeled the *SQI* drop with a double-step since it represents the "worst-case" nature in being abrupt. Moreover, steps are arguably the most common disturbance models considered in the context of closed-loop control systems.

Both the 2 min duration of electro-scalpel stimulation and the associated drop to $SQI = 50$ were derived from data collected during several surgeries. To also investigate the effect of a negative output disturbance step, a second inference episode is initiated with the return from $d = 10$ BIS to $d = 0$ BIS.

The Kalman filter was initialized in the state that corresponds to a *DoH* of 50 in stationarity, i.e., $x_0 = -F^{-1}Bu_{\text{ref}}$, where u_{ref} is the control signal corresponding to a *DoH* of 50 in stationarity.

The transients that arise during the initial convergence of the moving average and the Kalman filter, respectively, were truncated from the comparative evaluation. This is realistic, as in clinical use, the filter would typically be activated and allowed to converge before the system is switched from manual to closed-loop drug delivery.

3.2 Patient model population

We have taken both inter- and intra-patient variability into account. This has been achieved by simulating the procedure, detailed in Section 3.1, for 13 distinct individuals with covariates (age, height, weight, sex) and parameter values (E_0, $E_{\max}$, C_{e50}, γ) disclosed in [Padula et al., 2017], who have already proven to be representative of a broad population. The covariate values were used to obtain a nominal patient model Equation (2) using the Schnider model [Schnider et al., 1998].

For each nominal model, 10 perturbations were obtained by drawing from the associated random effect distributions Equation (5) to reflect model uncertainty caused by variability. Here, it can be noted that different draws were used in the optimization of the Kalman filter, as described in Section 2.2, and the subsequent evaluation simulations.

The Kalman filter incorporates the fixed-effects model only, which introduces a model error between the true patient and the Kalman filter model. The soft-sensor design was also performed without knowledge of E_0, $E_{\max}$, C_{e50}, and γ for each patient in the data set of [Padula et al., 2017]. Instead, the $\hat{h}^{-1}$ and $\hat{h}$ blocks of the soft sensor (see Figure 1) were designed on previously published assumed typical values $E_0 = 95.9$ BIS, $E_{\max} = 87.5$ BIS, $C_{e50} = 4.92\ \text{mg}\,\text{L}^{-1}$, and $\gamma = 2.69$ according to [Vanluchene et al., 2004].

3.3 Performance evaluation

To evaluate the performance of the proposed control structure, we compared the *DoH* resulting from a closed loop between the soft-sensor and monitor feedback cases, with and without measurement noise. This comparison was conducted across a population of simulated patients, detailed in Section 3.2.

To evaluate disturbance rejection from the proposed control structure, we used two performance indices, introduced in [Ionescu et al., 2008]:

- NADIR: the lowest or highest *DoH* reached after a positive or negative step disturbance, respectively (indicated by NADIR pos and NADIR neg).
- Time-to-target (TT): the time from step disturbance to first entering the range of 45–55 BIS.

From a clinical point of view, it is interesting to see how well the controller manages to maintain *DoH* within the 40–60 BIS range, as mentioned, e.g., [Soltész, 2013], which was also investigated.

4. Results

Figure 3 shows *DoH* resulting from simulating the scenario of Section 3.1 for each of the 130 perturbed patient models according to Section 3.2. The figure corresponds to the noise-free case $n = 0$. Figure 3(a) shows the results using the conventional monitor feedback approach; Figure 3(b) shows the results resulting from our novel soft-sensor architecture. The median patient, in terms of *DoH* reference deviation MSE, is highlighted in red. The Kalman filter parameters used for the simulations in Figure 3(b) from the optimization described in Section 2.2 are

$$R_{\min} = 5.07 \cdot 10^{-6}, \tag{13a}$$
$$R_{\max} = 0.250, \tag{13b}$$
$$Q = \operatorname{diag}\left(4.79 \cdot 10^{-3}, 0, 1.52 \cdot 10^{-1}, 2.77 \cdot 10^{-4}\right). \tag{13c}$$

Results shown in Figure 4 are related to simulations performed with the introduction of measurement noise n according to Section 2.3. The Kalman filter parameters, obtained with noise present during the offline optimization phase, were

$$R_{\min} = 0.771, \tag{14a}$$
$$R_{\max} = 1.79, \tag{14b}$$
$$Q = \operatorname{diag}\left(5.79 \cdot 10^{-2}, 1.83 \cdot 10^{-2}, 2.70 \cdot 10^{-2}, 2.12 \cdot 10^{-4}\right). \tag{14c}$$

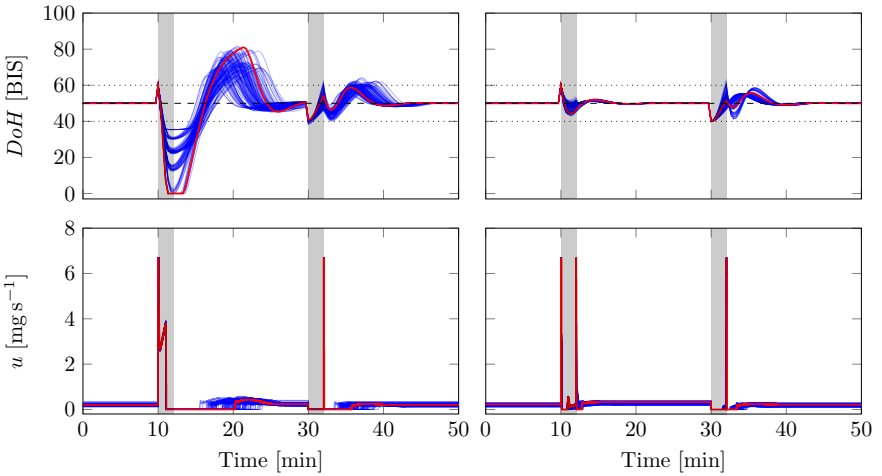

(a) Monitor feedback (b) Soft-sensor feedback

Figure 3. Blue solid lines represent *DoH* (upper) and propofol infusion rates (lower) for 10 perturbations of each of 13 nominal patient PKPD model, as explained in Section 3.2. The red solid line represents the mean response obtained for the entire set. According to Section 3.1, a positive step disturbance enters at $t = 10$ min, followed by a negative one at $t = 30$ min. The *SQI* drops to 50 immediately following each disturbance, before it returns to 100 after 2 min, as indicated by the shaded areas. The dashed black line indicates the *DoH* reference $r = 50$ BIS, and the dotted lines illustrate the limits of the clinically recommended range between $DoH = 40$ BIS and $DoH = 60$ BIS. Figure 3(a) corresponds to the nominal case, where feedback is established directly from the monitor measurement; Figure 3(b) employs feedback from the proposed soft sensor. A representative patient simulation is shown in red for each case.

Figure 5 shows histograms of the *DoH* values in Figure 3 and Figure 4. The percentage of *DoH* values within the clinically desired 40–60 BIS range in Figure 5 is 76% for monitor feedback and 100% for soft-sensor feedback without noise. The corresponding values are 71% and 99%, respectively, for the case with noise. Performance measures introduced in Section 3.3 are reported in Table 1.

To evaluate the proposed soft sensor on a wider range of individuals and to show that the tuning of the parameters is effective in general, we study the same simulation scenario as in Figure 3 over a larger data set of 500 individuals, introduced in [Schiavo et al., 2021b]. This is shown in Figure 6.

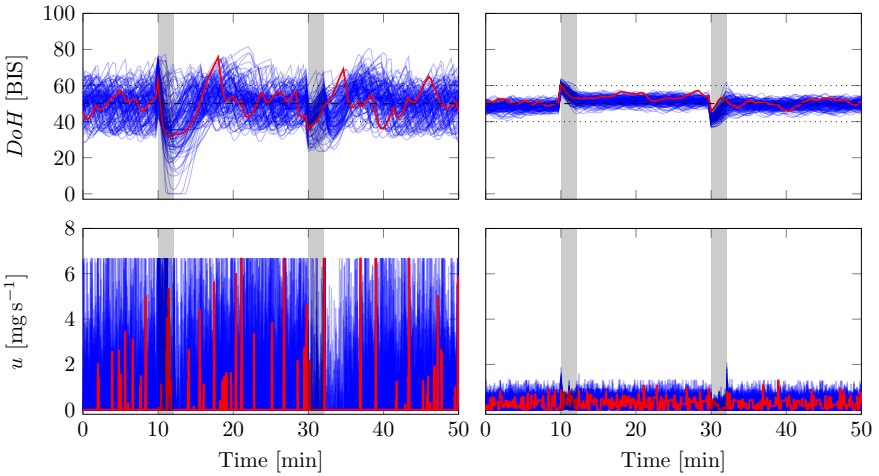

(a) Monitor feedback (b) Soft-sensor feedback

Figure 4. Simulated *DoH* (upper) and propofol infusion rate (lower) for 130 perturbed patient PKPD models, in the presence of measurement noise. Figure and color content correspond to that of Figure 3.

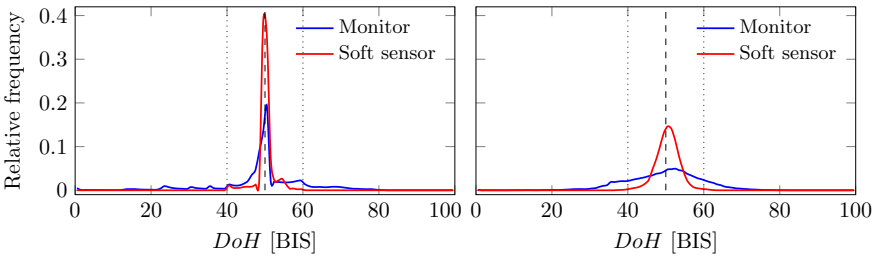

(a) Without noise (b) With noise

Figure 5. Distribution of *DoH* values from Figures 3 to 4, without and with Kalman filter soft sensor in the control loop.

Table 1. Spread of performance measures presented as min–max (median) for the simulations in Figures 3 to 4.

Feedback	Noise	NADIR pos [BIS]	NADIR neg [BIS]	TT pos [s]	TT neg [s]
Monitor	No	0–35 (23)	57–64 (60)	9–15 (12)	50–106 (65)
Soft sensor	No	43–50 (48)	54–63 (55)	10–21 (14)	49–104 (66)
Monitor	Yes	0–45 (34)	57–81 (65)	0–269 (15)	0–350 (55)
Soft sensor	Yes	44–52 (48)	50–62 (53)	0–264 (70)	0–313 (59)

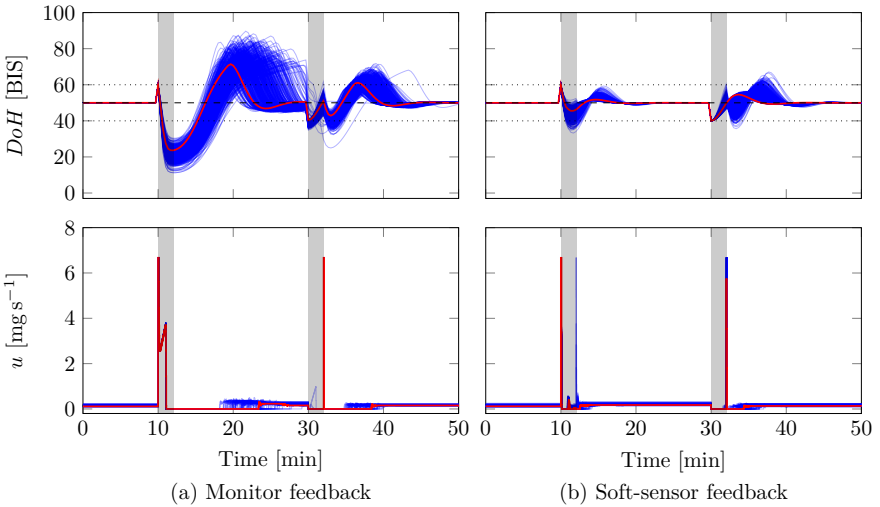

(a) Monitor feedback (b) Soft-sensor feedback

Figure 6. Simulated *DoH* (upper) and propofol infusion rate (lower) for 500 patient PKPD models to evaluate how the soft sensor handles inter-patient variability on a larger data set from [Schiavo et al., 2021b]. Figure and color content correspond to that of Figure 3.

5. Discussion

We have conducted a comparison between closed-loop *DoH* control using conventional low-pass filtered monitor output as a feedback signal and a novel soft-sensor architecture that integrates the patient model and the knowledge of signal quality.

The performance improvement of our novel architecture over that of the conventional one is perhaps best visualized in the histograms of Figure 5. They show that the distribution of *DoH* values is more closely centered around the *DoH* maintenance reference $r = 50$ BIS. This is also reflected in the performance indices reported of Table 1. While the difference in time-to-target (TT) between the compared architectures is marginal, the under- and overshoots associated with reaching the target, as well as *DoH* oscillations, differ substantially, as seen in Figures 3 to 6.

An in-depth effort has been made to ensure realistic simulation circumstances. Instead of assuming perfect model knowledge, which is common in simulation works studying closed-loop control anesthesia, we have adopted a stochastic uncertainty in model parameters, grounded in clinical data [Schnider et al., 1998]. Specifically, we have repeatedly sampled (10 perturbations) from this uncertainty for each of 13 nominal patients defined through population covariate values from a published dataset [Padula et al., 2017], with the pharmacodynamic parameters of Equation (3). The design of the soft sensor is based solely on assumed knowledge of the nominal model, as described in Section 3.2. Along the same lines, we have used previously published models of surgical disturbance d [Soltesz et al., 2019], and measurement noise n [Pawlowski et al., 2022b].

For relating electro-scalpel inference m to *SQI*, as well as corruption of monitor measurement y, we have formulated our own model Equation (11), as introduced in Section 2.3. This has been done based on communication with our senior anesthesiologist collaborator, who has observed a delay in monitoring reporting following such inference. We believe that the fidelity of this simple model could be improved upon. However, its sole purpose in the current context is to provide a substantial corruption of the monitor output y, which is reflected in *SQI*. The fact that the inference signal m in our simple model is directly mapped to $SQI = m$ is just a matter of convenience for notation. Neither this nor the knowledge about how *SQI* therefore relates to the delay τ through Equation (11) has been exploited in the soft-sensor design. Instead, the soft sensor assumes only that the measurement uncertainty—in terms of variance R of an additive Gaussian measurement noise—is an affine function of *SQI*, according to Equation (10), mapping the 100–0 *SQI* range to an $R_{\min}$–$R_{\max}$ range. Thus, the soft sensor is agnostic of the monitor dynamics mapping inference m to corruption on y, which is later reported by the *SQI*. Although the monitor dynamics are not taken into account in the proposed architecture, the performance is satisfactory. Doing so would be unrealistic, even if the performance could be slightly improved.

Another implication is that our methodology can be expected to work satisfactorily not only with the BIS monitor but also other clinical monitors, such as the WAV_{CNS} [Hahn et al., 2012] or CONOX [Jensen et al., 2014], that output both a *DoH* estimate y and associated *SQI*.

On a similar note, our Kalman filter assumes signal corruption by Gaussian noise added to the signal $\widetilde{C}_e$ in Figure 1. At least for the noise contribution of n to this signal, a more accurate model could be incorporated. Also, here, satisfactory performance in the absence of such a model is positive, since it demonstrates that a low-fidelity noise model is sufficient for our architecture to outperform the nominal one with simple monitor feedback. While more advanced sensor fusion methods like the extended or unscented Kalman filters could be considered in scenarios where the model is not linear like in Equation (1), the simple linear Kalman filter already provides significant performance improvements. Its simplicity and interpretability make it an attractive choice for real-world implementation unless there is a strong

motivation for more complex alternatives.

Some of the residual error arising from model mismatch is accounted for by the process noise model Q. Like with R, the underlying assumed noise structure does not match exactly that of the considered system. However, optimizing R and (an assumed diagonal) Q according to Section 2.2 yields satisfactory performance. To implement this soft-sensor in practice, $R_{\min}$, $R_{\max}$ and Q would be optimized offline, with R then adjusted online based on Equation (10).

6. Conclusions

A realistic closed-loop controlled anesthesia scenario is considered, in which model uncertainties and external disturbances are present. In this setting, our comparative simulation study clearly illustrates robust performance benefits from merging a model-based and data-driven approach through a Kalman filter soft sensor. In particular, it enables online balance between model and measurement reliance, based on an estimation of measurement quality.

Based on the results presented, we are confident to take the next steps toward the clinical evaluation of the proposed soft-sensor architecture within an existing clinical closed-loop anesthesia research platform, which to date has seen extensive clinical use [Schiavo et al., 2021c; Schiavo et al., 2022].

CRediT author statement

Ylva Wahlquist: Conceptualization, Methodology, Software, Visualization, Writing – Original Draft, Writing – Review & Editing.
Nicola Paolino: Conceptualization, Methodology, Software, Writing – Original Draft, Writing – Review & Editing.
Michele Schiavo: Conceptualization, Methodology, Validation, Writing – Review & Editing.
Antonio Visioli: Conceptualization, Validation, Supervision, Writing – Review & Editing.
Kristian Soltesz: Conceptualization, Validation, Supervision, Writing – Review & Editing.

Acknowledgments

The authors would like to acknowledge Massimiliano Paltenghi with the Department of Anesthesiology, Critical Care and Emergency, Spedali Civili di Brescia, Brescia, Italy for sharing his clinical expertise on the relationship between electric inference and monitor dynamics.

Wahlquist and Soltesz are members of the ELLIIT Strategic Research Area at Lund University. This work was partially supported by the European Union

NextGeneration EU (Piano Nazionale di Ripresa e Resilienza (PNRR) - Missione 4 componente 2, investimento 3.3 - Decreto del Ministero dell'Università e della Ricerca n.352 del 09/04/2022). Paolino has been partially funded by CSMT Innovative Contamination Hub.

Disclosure statement

The authors declare no conflict of interest.

References

Absalom, A. R., J. I. B. Glen, G. J. C. Zwart, T. W. Schnider, and M. M. R. F. Struys (2016). "Target-controlled infusion: a mature technology". *Anesthesia & Analgesia* **122**:1, pp. 70–78. DOI: 10.1213/ANE.0000000000001009.

Agarwal, J., G. D. Puri, and P. J. Mathew (2009). "Comparison of closed loop vs. manual administration of propofol using the bispectral index in cardiac surgery". *Acta Anaesthesiologica Scandinavica* **53**:3, pp. 390–397. DOI: 10.1111/j.1399-6576.2008.01884.x.

Åström, K. J. and B. Wittenmark (1984). *Computer controlled Systems: Theory and design*. 3rd ed. Dover Publications, Mineola, NY. ISBN: 978-0-486-48613-0.

Åström, K. J. and R. M. Murray (2008). *Feedback Systems: An Introduction for Scientists and Engineers*. Princeton University Press, Princeton, NJ. ISBN: 978-0-691-13576-2.

Aubouin-Pairault, B., M. Fiacchini, and T. Dang (2024). "Comparison of multiple Kalman filter and moving horizon estimator for the anesthesia process". *Journal of Process Control* **136**, p. 103179. DOI: 10.1016/j.jprocont.2024.103179.

Becker, A. (2023). *Kalman Filter: From the Ground Up*. First edition. ISBN: 978-965-598-439-2.

BIS™ Complete Monitoring System (2013). Medtronic. Minneapolis, Minnesota, U.S. URL: https://asiapac.medtronic.com/content/dam/covidien/library/global/multi/product/brain-monitoring/BISCompleteMonitor_OperatorsManual_Multi_10103075A00.pdf.

Blayney, M. R. (2012). "Procedural sedation for adult patients: an overview". *Continuing Education in Anaesthesia, Critical Care & Pain* **12**:4, pp. 176–180. DOI: 10.1093/bjaceaccp/mks016.

Canchola, J. A., S. Tang, P. Hemyari, E. Paxinos, and E. Marins (2017). "Correct use of percent coefficient of variation (%CV) formula for log-transformed data". *MOJ Proteomics & Bioinformatics* **Volume 6**:Issue 4. DOI: 10.15406/mojpb.2017.06.00200.

Chan, M., S. S. Ho, and T. Gin (2012). "Performance of the bispectral index during electrocautery". *J Neurosurg Anesthesiol* **24(1)**, pp. 9–13. DOI: 10.1097/ANA.0b013e31823058bf.

Copot, D., C. Muresan, R. De Keyser, and C. Ionescu (2017). "Patient specific model based induction of hypnosis using fractional order control". *IFAC-PapersOnLine* **50**:1, pp. 15097–15102. DOI: 10.1016/j.ifacol.2017.08.2238.

Dahaba, A. (2005). "Different conditions that could result in the bispectral index indicating an incorrect hypnotic state". *Anesthesia & Analgesia* **101**:3, pp. 765–773. DOI: https://doi.org/10.1213/01.ane.0000167269.62966.af.

Dumont, G. A., A. Martinez, and J. M. Ansermino (2009). "Robust control of depth of anesthesia". *International Journal of Adaptive Control and Signal Processing* **23**:5, pp. 435–454. DOI: 10.1002/acs.1087.

Ghita, M., M. Neckebroek, C. Muresan, and D. Copot (2020). "Closed-loop control of anesthesia: survey on actual trends, challenges and perspectives". *IEEE Access* **8**, pp. 206264–206279. DOI: 10.1109/ACCESS.2020.3037725.

Gjika, E., M. Pekker, A. Shashurin, M. Shneider, T. Zhuang, J. Canady, and M. Keidar (2016). "The cutting mechanism of the electrosurgical scalpel". *Journal of Physics D: Applied Physics* **50**:2, p. 025401. DOI: 10.1088/1361-6463/50/2/025401.

Gonzalez-Cava, J. M., F. Bagge Carlson, O. Troeng, A. Cervin, K. van Heusden, G. A. Dumont, and K. Soltesz (2021). "Robust PID control of propofol anaesthesia: uncertainty limits performance, not PID structure". *Computer Methods and Programs in Biomedicine* **198**, p. 105783. DOI: 10.1016/j.cmpb.2020.105783.

Goutelle, S., M. Maurin, F. Rougier, X. Barbaut, L. Bourguignon, M. Ducher, and P. Maire (2008). "The Hill equation: a review of its capabilities in pharmacological modelling". *Fundamental & Clinical Pharmacology* **22**:6, pp. 633–648. DOI: 10.1111/j.1472-8206.2008.00633.x.

Hahn, J. O., G. A. Dumont, and J. M. Ansermino (2012). "Robust closed-loop control of hypnosis with propofol using WAV_{CNS} index as the controlled variable". *Biomedical Signal Processing and Control* **7**:5, pp. 517–524. DOI: 10.1016/j.bspc.2011.09.001.

Hosseinzadeh, M., K. van Heusden, M. Yousefi, G. A. Dumont, and E. Garone (2020). "Safety enforcement in closed-loop anesthesia. a comparison study". *Control Engineering Practice* **105**, p. 104653. DOI: 10.1016/j.conengprac.2020.104653.

Ionescu, C. M., R. De Keyser, B. C. Torrico, T. De Smet, M. Struys, and J. E. Normey-Rico (2008). "Robust predictive control strategy applied for propofol dosing using BIS as a controlled variable during anesthesia". *IEEE Transactions*

on Biomedical Engineering **55**:9, pp. 2161–2170. DOI: 10.1109/TBME.2008.923142.

Jensen, E. W., J. F. Valencia, A. Lopez, T. Anglada, M. Agusti, Y. Ramos, R. Serra, M. Jospin, P. Pineda, and P. Gambus (2014). "Monitoring hypnotic effect and nociception with two EEG-derived indices, qCON and qNOX, during general anaesthesia". *Acta Anaesthesiologica Scandinavica* **58**:8, pp. 933–941. DOI: 10.1111/aas.12359.

Liu, N., T. Chazot, A. Genty, A. Landais, A. Restoux, K. McGee, P. Laloe, B. Trillat, L. Barvais, and M. Fischler (2006). "Titration of propofol for anesthetic induction and maintenance guided by the bispectral index: closed-loop versus manual control: a prospective, randomized, multicenter study". *Anesthesiology* **104**:4, pp. 686–695. DOI: 10.1097/00000542-200604000-00012.

Melia, U., E. Gabarron, M. Agusti, N. Souto, P. Pineda, J. Fontanet, M. Vallverdu, E. W. Jensen, and P. Gambus (2017). "Comparison of the qCON and qNOX indices for the assessment of unconsciousness level and noxious stimulation response during surgery". *Journal of Clinical Monitoring and Computing* **31**, pp. 1273–1281. DOI: 10.1007/s10877-016-9948-z.

Mendez, J. A., A. Leon, A. Marrero, J. M. Gonzalez-Cava, J. A. Reboso, J. I. Estevez, and J. F. Gomez-Gonzalez (2018). "Improving the anesthetic process by a fuzzy rule based medical decision system". *Artificial Intelligence in Medicine* **84**, pp. 159–170. DOI: 10.1016/j.artmed.2017.12.005.

Mendez, J. A., A. Marrero, J. A. Reboso, and A. Leon (2016). "Adaptive fuzzy predictive controller for anesthesia delivery". *Control Engineering Practice* **46**, pp. 1–9. DOI: 10.1016/j.conengprac.2015.09.009.

Merigo, L., M. Beschi, F. Padula, N. Latronico, M. Paltenghi, and A. Visioli (2017). "Event-based control of depth of hypnosis in anesthesia". *Computer Methods and Programs in Biomedicine* **147**, pp. 63–83. DOI: 10.1016/j.cmpb.2017.06.007.

Merigo, L., F. Padula, N. Latronico, M. Paltenghi, and A. Visioli (2020). "Event-based control tuning of propofol and remifentanil coadministration for general anaesthesia". *IET Control Theory & Applications* **14**:19, pp. 2995–3008. DOI: 10.1049/iet-cta.2019.1067.

Misgeld, B. J. E., M. Luken, R. Riener, and S. Leonhardt (2017). "Observer-based human knee stiffness estimation". *IEEE Transactions on Biomedical Engineering* **64**:5, pp. 1033–1044. DOI: 10.1109/TBME.2016.2587841.

Oikonomou, V., A. Tzallas, S. Konitsiotis, D. Tsalikakis, and D. Fotiadis (2009). "The use of Kalman filter in biomedical signal processing". In: *Kalman Filter Recent Advances and Applications*. IntechOpen. DOI: 10.5772/6805.

Padula, F., C. Ionescu, N. Latronico, M. Paltenghi, A. Visioli, and G. Vivacqua (2017). "Optimized PID control of depth of hypnosis in anesthesia". *Computer Methods and Programs in Biomedicine* **144**, pp. 21–35. DOI: 10.1016/j.cmpb.2017.03.013.

Paolino, N., M. Schiavo, N. Latronico, F. Padula, M. Paltenghi, and A. Visioli (2023). "On the use of FOPID controllers for maintenance phase of general anesthesia". *Applied Sciences* **13**, p. 7381. DOI: 10.3390/app13137381.

Pawlowski, A., M. Schiavo, N. Latronico, M. Paltenghi, and A. Visioli (2022a). "Linear MPC for anesthesia process with external predictor". *Computers & Chemical Engineering* **161**, p. 107747. DOI: 10.1016/j.compchemeng.2022.107747.

Pawlowski, A., M. Schiavo, N. Latronico, M. Paltenghi, and A. Visioli (2022b). "MPC for propofol anesthesia: the noise issue". In: *2022 IEEE Conference on Control Technology and Applications (CCTA)*, pp. 1087–1092. DOI: 10.1109/CCTA49430.2022.9966102.

Puri, G. D., B. Kumar, and J. Aveek (2007). "Closed-loop anaesthesia delievery system (CLADS) using bispectral index; a performance assessment study". *Anaesthesia and Intensive Care* **35**, pp. 357–362. DOI: 10.1177/0310057X0703500306.

Rampil, I. J. (1998). "A primer for EEG signal processing in anesthesia". *Anesthesiology* **89**, pp. 980–1002. DOI: 10.1097/00000542-199810000-00023.

Schiavo, M., F. Padula, N. Latronico, M. Paltenghi, and A. Visioli (2021a). "Individualized pid tuning for maintenance of general anesthesia with propofol". *IFAC-PapersOnLine* **54**:3, pp. 679–684. DOI: 10.1016/j.ifacol.2021.08.320.

Schiavo, M., F. Padula, N. Latronico, M. Paltenghi, and A. Visioli (2022). "A modified PID-based control scheme for depth-of-hypnosis control: Design and experimental results". *Computer Methods and Programs in Biomedicine* **219**, p. 106763. DOI: 10.1016/j.cmpb.2022.106763.

Schiavo, M., L. Consolini, M. Laurini, N. Latronico, M. Paltenghi, and A. Visioli (2021b). "Optimized feedforward control of propofol for induction of hypnosis in general anesthesia". *Biomedical Signal Processing and Control* **66**, p. 102476. DOI: 10.1016/j.bspc.2021.102476.

Schiavo, M., F. Padula, N. Latronico, L. Merigo, M. Paltenghi, and A. Visioli (2021c). "Performance evaluation of an optimized PID controller for propofol and remifentanil coadministration in general anesthesia". *IFAC Journal of Systems and Control* **15**, p. 100121. DOI: 10.1016/j.ifacsc.2020.100121.

Schnider, T. W., C. F. Minto, P. L. Gambus, C. Andresen, D. B. Goodale, S. L. Shafer, and E. J. Youngs (1998). "The influence of method of administration and covariates on the pharmacokinetics of propofol in adult volunteers". *Anesthesiology* **88**:5, pp. 1170–1182. DOI: 10.1097/00000542-199805000-00006.

Soltesz, K., J. Hahn, T. Hägglund, G. A. Dumont, and J. M. Ansermino (2013). "Individualized closed-loop control of propofol anesthesia: a preliminary study". *Biomedical Signal Processing and Control* **8**:6, pp. 500–508. DOI: 10.1016/j.bspc.2013.04.005.

Soltesz, K., K. van Heusden, and G. Dumont (2019). *Models for control of intravenous anesthesia*. Ed. by D. Copot. Elsevier, Amsterdam, Netherlands. Chap. 5, pp. 119–156. ISBN: 9780128159750. DOI: 10.1016/B978-0-12-815975-0.00010-2.

Soltész, K. (2013). *On automation in anesthesia*. PhD thesis. Lund University, Lund, Sweden. ISBN: 978-91-7473-484-3.

Struys, M. M. R. F., T. De Smet, B. Depoorter, L. F. M. Versichelen, E. P. Mortier, F. J. E. Dumortier, S. L. Shafer, and G. Rolly (2000). "Comparison of plasma compartment versus two methods for effect compartment–controlled target-controlled infusion for propofol". *Anesthesiology* **92**:2, p. 339. DOI: 10.1097/00000542-200002000-00021.

Struys, M. M. R. F., T. De Smet, L. F. M. Versichelen, S. Van de Velde, R. Van den Broecke, and E. P. Mortier (2001). "Comparison of closed-loop controlled administration of propofol using bispectral index as the controlled variable versus standard practice controlled administration". *Anesthesiology* **95**:1, pp. 6–17. DOI: 10.1097/00000542-200107000-00007.

Vanluchene, A., H. Vereecke, O. Thas, E. Mortier, S. Shafer, and M. Struys (2004). "Spectral entropy as an electroencephalographic measure of anesthetic drug effect: a comparison with bispectral index and processed midlatency auditory evoked response". *Anesthesiology* **101**, pp. 34–42. DOI: 10.1097/00000542-200407000-00008.

Visioli, A. (2006). *Practical PID control*. Springer Science & Business Media. ISBN: 978-1-84628-585-1.

Vuyk, J. and M. Mertens (2003). "Bispectral index scale (BIS) monitoring and intravenous anaesthesia". *Advances in Modelling and Clinical Application of Intravenous Anaesthesia*, pp. 95–104. DOI: 10.1007/978-1-4419-9192-8_9.

Welch, G. and G. Bishop (1995). *An introduction to the Kalman filter*. Tech. rep. University of North Carolina. DOI: 10.5555/897831.

Paper VI

Seamless Integration of Target-Controlled Infusion and Closed-Loop Anesthesia

Ylva Wahlquist **Kristian Soltesz**

Abstract

The anesthetic drug propofol is commonly used to control hypnotic depth (suppression of awareness) in patients undergoing surgery or intensive care. In addition to manual titration, a model-based open-loop feed-forward strategy called target-controlled infusion (TCI) has attained some clinical popularity. Research on closed-loop control, with awareness estimates derived from an electroencephalogram (EEG), has proven feasible through several extensive clinical studies over the past decades. While TCI is vulnerable to model imperfections, closed-loop control is susceptible to corrupt measurements. By combining Kalman-filter-based state estimation with model predictive control (MPC), we introduce a novel anesthetic dosing regimen that can transition seamlessly between TCI and closed-loop control, thus constituting an adequate trade-off between model and measurement reliance. We introduce this regimen and provide a realistic simulation example that highlights its strengths compared to pure TCI or closed-loop control of propofol infusion.

Keywords: Biomedical systems, Model Predictive Control, Kalman filtering

Accepted for presentation at the American Control Conference (ACC) 2025 and for publication in the conference proceedings.

1. Introduction

Hypnosis is the pharmacologically induced anesthetic component utilized to temporarily repeal awareness, as mandated by certain surgical procedures. Intravenous drugs, such as propofol, are becoming increasingly popular and are commonly administered manually and titrated by an anesthesiologist based on monitor readings, patient signs, and experience.

Target-controlled infusion (TCI) is a model-based augmentation to manual titration. When TCI is used, the anesthesiologist enters a desired set point (reference) drug concentration in the blood plasma [Absalom and Mason, 2017]. Based on this reference and an underlying patient model of the assumed pharmacokinetics, the TCI system computes an optimized infusion trajectory that is then applied [Absalom and Mason, 2017]. The patient model is adapted to covariates such as age, weight, and sex. Several such pharmacokinetic covariate models have been used as the basis for TCI systems, e.g., [Absalom et al., 2003; Schnider et al., 1998]. TCI is a feed-forward open-loop control strategy, which means that it cannot account for model errors or disturbances that divert the true plasma concentration from that assumed by the TCI system model. However, the anesthesiologist can update the plasma concentration setpoint if observations make it plausible that the patient is subjected to inadequate anesthetic depth, possibly caused by external disturbances.

When TCI relies solely on a dynamic patient model, closed-loop controlled anesthesia constitutes a dosing regimen where the infusion rate is updated based on an online measurement [van Heusden et al., 2019; Schiavo et al., 2021]. This measurement is typically an estimate of the depth of hypnosis (*DoH*), calculated from a non-invasive electroencephalogram (EEG) signal. The anesthesiologist sets a desired reference anesthetic depth, usually given on the BIS scale, where a value close to the maximum of 100 BIS indicates that the patient is fully aware, and the range 40–60 BIS is adequate for many clinical use cases [Vuyk and Mertens, 2003]. Too deep anesthesia may result in adverse effects, such as post-operative nausea, while insufficient anesthesia can lead to awareness during surgery.

While the lack of clinical feedback in TCI makes it vulnerable to model error, the presence of clinical feedback makes closed-loop anesthesia vulnerable to measurement disturbances and sensor noise. This motivates a unified framework that combines TCI and closed-loop control to obtain a tunable trade-off between the two. This paper presents such a framework, based on a combination of Kalman filtering state estimation and model predictive control (MPC). We provide illustrative and motivating examples and conclude with a realistic simulated use case.

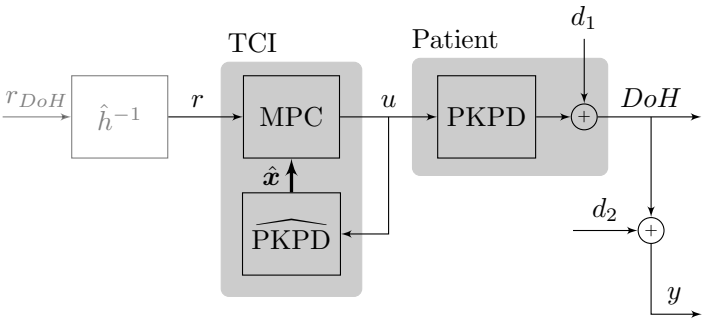

Figure 1. Schematic illustration of open-loop control with TCI. The *DoH* reference r_{DoH} is transformed by $\hat{h}^{-1}$ into a plasma concentration which is inverted through Equation (5) to create the reference r for the MPC, which computes a control signal u based on the state estimate $\hat{\boldsymbol{x}}$ from the underlying PKPD model. This transform is in gray, as it is typically conducted implicitly by the monitoring anesthesiologist, who sets r directly, in the case of TCI control. The disturbances d_1 and d_2 act on the *DoH* and its measurement y, respectively.

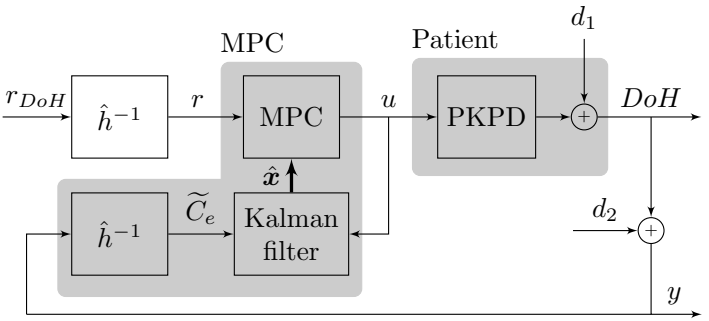

Figure 2. Schematic illustration of closed-loop control with MPC. The reference for *DoH*, r_{DoH}, is inverted through $\hat{h}^{-1}$ in Equation (5) to create the reference for the MPC, which computes a control signal u based on the state estimates from the Kalman filter. The disturbances d_1 and d_2 act on the *DoH* and the measurement y, respectively.

2. Modeling and control

Ordinary TCI is schematically illustrated in Figure 1, and our novel hybrid approach is illustrated in Figure 2. The patient is represented by a PKPD model, defined in Section 2.1. The measurement y and disturbances d_1, d_2 are explained in Section 2.2 and the Kalman filter state estimator in Section 2.3. Finally, the MPC that governs dosing in both the TCI and the closed-loop case is presented in Section 2.4.

2.1 Patient model

At the core of our approach lies a pharmacokinetic-pharmacodynamic (PKPD) model. The structure of this model is well established in the context of closed-loop controlled anesthesia [Sahinovic et al., 2018; Soltesz et al., 2020]. The PK part of the model is a mammillary three-compartment system, relating drug infusion rate u [mg s^{-1}] to the blood plasma drug concentration $x_3 = C_p$ [mg L^{-1}] [Sahinovic et al., 2018]. The PD model, connected in series to the output of the PK model, consists of a linear and a non-linear part. The linear part is a first-order lag filter relating the blood plasma concentration $x_3 = C_p$ to the effect-site (brain cortex) concentration $x_4 = C_e$. A zero-order-hold discretization, in our examples with sampling period $T_s = 10$ s (sufficient to resolve the dynamics) can thus be expressed

$$\boldsymbol{x}_{k+1} = A\boldsymbol{x}_k + Bu_k, \tag{1a}$$

$$(C_e)_k = C\boldsymbol{x}_k = (x_4)_k, \tag{1b}$$

where

$$\boldsymbol{x}_k = \left[(x_1)_k, (x_2)_k, (x_3)_k, (x_4)_k\right]^\top, \tag{2}$$

as detailed in for example [Wahlquist et al., 2021].

The non-linear part of the PD model relates effect-site concentration $C_e = x_4$ to *DoH* via the Hill sigmoid

$$DoH = h(C_e; E_0, C_{e50}, \gamma) = E_0\left(1 - \frac{C_e^\gamma}{C_e^\gamma + C_{e50}^\gamma}\right), \tag{3}$$

C_{e50} corresponds to a $DoH = 50$ BIS, and γ determines the steepness of the sigmoid.

The variability in the *DoH* response between individuals is accounted for using a pharmacometric covariate model. In this work, we use the Schnider population model [Schnider et al., 1998], which expresses the parameters of the continuous-time counterpart of Equation (1) as a function of the covariates age, weight, and sex. The remaining variability, not explained by these covariates, is modeled using a log-normal distribution, so that

$$\theta = \theta_0 \exp(\eta_\theta), \tag{4}$$

where θ_0 is the covariate-adjusted parameter value, and the random effect η_θ is a normal stochastic variable with zero mean and variance σ_θ^2. These random effects thus capture intra-individual variability and the part of the inter-individual variability not explained by the covariates.

2.2 Measurements and disturbances

Disturbances pose a central challenge for both TCI and closed-loop control. Surgical stimulation is commonly [Soltesz et al., 2020] modeled by an additive disturbance d_1, affecting the actual DoH, as shown in Figure 1.

It is not possible to measure the full patient state or the true DoH directly. Instead, the only available measurement is $y = DoH + d_2$, where d_2 corrupts measurement noise, as shown in Figure 1. That is, d_1 affects the actual DoH and consequently also the measurement y, while d_2 affects the measurement y, without influencing the true DoH in the case of TCI shown in Figure 1. However, in the case of closed-loop feedback shown in Figure 2, d_2 will influence the true DoH through the controller.

This work considers disturbances in double-steps of magnitude 20 BIS. Step disturbances are commonly used [Soltész, 2013], as they can be considered to be the worst case in the anesthesia control context.

2.3 Patient state estimation

Since the full state of Equation (1) is not directly measurable, we use the Kalman filter to obtain state estimates. It utilizes the system input u, together with the effect-site concentration estimate

$$\hat{C}_e = \hat{h}^{-1}(DoH; E_0, C_{e50}, \gamma) = C_{e50}\left(\frac{E_0 - DoH}{DoH}\right)^{1/\gamma}. \tag{5}$$

to produce a state estimate $\hat{\boldsymbol{x}}$.

To begin with, we will, somewhat optimistically, assume perfect knowledge of the PD dynamics, $\hat{h} = h$, resulting in $\hat{h}^{-1}$ constituting a perfectly linearizing transform. However, in our concluding realistic simulation scenario of Section 4, we use a previously published population average for the parameters in Equation (5) to obtain a corresponding, but non-perfectly linearizing $\hat{h}^{-1}$. This was also done in [Wahlquist et al., 2025], where the same population average resulted in satisfactory results.

The Kalman filter equations are presented below, with the following notation: $\hat{\boldsymbol{x}}_{k,k-1}$ denotes the estimate of the state vector $\boldsymbol{x}_k$, based on data up to and including sample $k-1$, and $\hat{\boldsymbol{x}}_{k,k}$ is the updated estimate at sample k. The same notation is used for the covariance estimate P. The state update is governed by

$$L_k = P_{k,k-1}C^\top \left(CP_{k,k-1}C^\top + R_k\right)^{-1}, \tag{6a}$$

$$P_{k,k} = (I - L_k C)P_{k,k-1}(I - L_k C)^\top + L_k R_k L_k^\top, \tag{6b}$$

$$\hat{\boldsymbol{x}}_{k,k} = \hat{\boldsymbol{x}}_{k,k-1} + L_k\left((\tilde{C}_e)_k - C\hat{\boldsymbol{x}}_{k,k-1}\right), \tag{6c}$$

and the prediction is given by

$$\boldsymbol{x}_{k,k+1} = A\boldsymbol{x}_{k,k} + Bu_k, \tag{7a}$$

$$P_{k+1,k} = AP_{k,k}A^\top + Q_k, \tag{7b}$$

where A, B, C are the system matrices of Equation (1). Kalman filtering is a well-understood and documented technique, and we refer to [Welch and Bishop, 1995] for further details and insights.

The scalar R_k and the matrix Q_k quantify measurement and state uncertainty in the sample k. While they can be viewed to represent covariances of Gaussian disturbances within the Kalman filtering framework, we instead consider them as free tuning parameters that enable a trade-off between measurement and model reliance.

The Kalman filter state estimate is a weighted sum of its most recent measurement and the previous state estimate, where the Kalman gain L is the proportionality constant. When the measurement uncertainty R is large, the Kalman gain L will decrease, shifting trust from measurement to model, and vice versa.

2.4 MPC formulation

The objective of our MPC– which is to be used both for TCI and closed-loop controlled infusion– is to produce an optimal drug infusion trajectory to follow an effect-site concentration reference. Its roles in each of these use cases are shown in Figure 1 and Figure 2, respectively.

In TCI, the MPC relies solely on a PKPD patient model, without utilizing the *DoH* measurement y. In closed-loop mode, the MPC instead utilizes Kalman-filter state estimates based on y, as explained in Section 2.3.

We denote the effect-site concentration profile across a horizon of N samples by $\boldsymbol{x}_4$ so that $\boldsymbol{x}_4 = \begin{bmatrix}(x_4)_1 \dots (x_4)_N\end{bmatrix}^\top$, and the reference trajectory $\boldsymbol{r} = \begin{bmatrix}r_1 \dots r_N\end{bmatrix}^\top$. The objective of our MPC is to find the infusion trajectory $\boldsymbol{u} = \begin{bmatrix}u_1 \dots u_N\end{bmatrix}^\top$ that minimizes the quadratic cost function

$$J'_e(\boldsymbol{x}_4) = \sum_{k=1}^{N} \left((x_4)_k - r_k\right)^2. \tag{8}$$

To enable minimization over $\boldsymbol{u}$, we rewrite Equation (8) in terms of $\boldsymbol{u}$. With the initial state $\boldsymbol{x}_0$ and the use of Equation (1), we get

$$J_e(\boldsymbol{u}) = \frac{1}{2}\boldsymbol{u}^\top F^\top F\boldsymbol{u} + (\boldsymbol{x}_0^\top E^\top F - \boldsymbol{r}^\top F)\boldsymbol{u}, \tag{9}$$

where

$$E = \begin{bmatrix} A_4^1 \\ \vdots \\ A_4^N \end{bmatrix}, F = \begin{bmatrix} A_4^0 B_4 & & & \\ A_4^1 B_4 & A_4^0 B_4 & & \\ \vdots & \vdots & \ddots & \\ A_4^{N-1} B_4 & A_4^{N-2} B_4 & \dots & A_4^0 B_4 \end{bmatrix}, \tag{10}$$

and where A_4 is the fourth row of A, and B_4 the fourth element of B. A complete derivation can be found in [Wahlquist et al., 2024].

Preventing ringing in u Figure 3 shows the solution that minimizes Equation (9), following a negative step disturbance $d_1 = -20$ BIS. It results in undesired ringing in the infusion rate u (red). To avoid this, we add a cost term that penalizes sample-to-sample differences in u:

$$J'_{\Delta u}(\boldsymbol{u}) = \alpha \sum_{k=2}^{N} (u_k - u_{k-1})^2 \tag{11}$$

where α is a tuning parameter for this penalty.

Rewriting Equation (11) as a quadratic form, and using that Equation (11) is scalar, results in

$$J_{\Delta u}(\boldsymbol{u}) = \frac{\alpha}{2} \boldsymbol{u}^\top G^\top G \boldsymbol{u}, \tag{12}$$

where

$$G = \begin{bmatrix} -1 & 1 & & & \\ & -1 & 1 & & \\ & & \ddots & \ddots & \\ & & & -1 & 1 \end{bmatrix}. \tag{13}$$

The blue lines in Figure 3 show the effect of introducing this penalty with $\alpha = 0.1$. As can be seen, the red ($\alpha = 0$) and blue ($\alpha = 0.1$) *DoH* are not distinguishable, while there is no ringing in the blue control signal.

Constraints We introduced constraints to keep the infusion rate nonnegative, $u_k \geq 0$ for $k = 1, \ldots, N$. That is, element-wise larger than zero, $\boldsymbol{u} \succcurlyeq \mathbf{0}_{N\times 1}$, where $\mathbf{0}_{N\times 1}$ is a zero vector of size $N \times 1$. Similarly, the infusion rate is bounded by the maximum possible infusion rate of the pump, $u_{\max} = 1200\ \mathrm{mL\,h^{-1}}$, representative of several clinical infusion pumps. This corresponds to $u_{\max} = 6.67\ \mathrm{mg\,s^{-1}}$ with a propofol concentration of 20 $\mathrm{mg\,mL^{-1}}$. The corresponding constraint can be written as $\boldsymbol{u} \preccurlyeq u_{\max} \mathbf{1}_{N\times 1}$. The combined infusion rate constraints are thus

$$\begin{bmatrix} -I_{N\times N} \\ I_{N\times N} \end{bmatrix} \boldsymbol{u} \preccurlyeq \begin{bmatrix} \mathbf{0}_{N\times 1} \\ u_{\max} \mathbf{1}_{N\times 1} \end{bmatrix}. \tag{14}$$

MPC as a quadratic program The MPC cost, combining Equation (9) and Equation (12), is

$$\begin{aligned} J(\boldsymbol{u}) &= J_e(\boldsymbol{u}) + J_{\Delta u}(\boldsymbol{u}) \\ &= \frac{1}{2} \boldsymbol{u}^\top (F^\top F + \alpha G^\top G) \boldsymbol{u} + (\boldsymbol{x}_0^\top E^\top F - \boldsymbol{r}^\top F) \boldsymbol{u}. \end{aligned} \tag{15}$$

Minimizing Equation (15) subject to Equation (14) corresponds to solving a quadratic program (QP), for which there exist solvers such as `quadprog` in MATLAB [MathWorks, 2024] that were used in our examples.

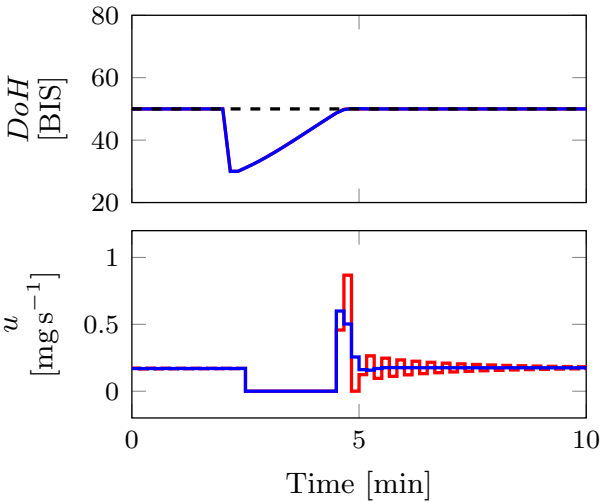

Figure 3. *DoH* and infusion rate u with (red, $\alpha = 0$) and without (blue, $\alpha = 0.1$) ringing following a negative step disturbance $d_1 = -20$ BIS in Figure 5. The red and blue *DoH* curves are not visually distinguishable.

In the closed-loop MPC case, one such QP is solved at each sample as a new measurement and the corresponding Kalman-filter state estimate arrive. In the TCI case, the optimization problem will only be solved once over a horizon, unless the anesthesiologist changes the reference and a new trajectory is computed. In this work, we use a practically sufficient prediction horizon of 10 min, corresponding to $N = 60$.

3. Disturbance rejection comparison

We evaluated the performance of TCI and closed-loop MPC subject to disturbances d_1 and d_2, as introduced in Section 2.2, and initially under the assumption of a perfect model, $\widehat{\text{PKPD}} = \text{PKPD}$ and $\hat{h}^{-1} = h^{-1}$ in Figure 1 and Figure 2.

The patient state is initialized to $DoH = 50$ BIS, i.e., $\boldsymbol{x}_0 = -A^{-1}Bu_{\text{ref}}$, where u_{ref} is the corresponding stationary control signal. At $t = 5$ min, a double step in d_1 or d_2 is introduced, with a duration of five minutes. The rejection of disturbances by TCI and closed-loop MPC is shown in Figure 4 and Figure 5, respectively.

Since we assume perfect model knowledge and no additional noise, the Kalman filter is tuned to behave like there is (almost) no state or measurement noise, i.e., R and Q are chosen to be (almost) zero (but not exactly zero for numerical reasons). The chosen values were $R = 10^{-6}$ mg^2/s^2 and $Q = 10^{-6} I_4$ mg^2/s^2, where I_4 is the identity matrix of size 4×4.

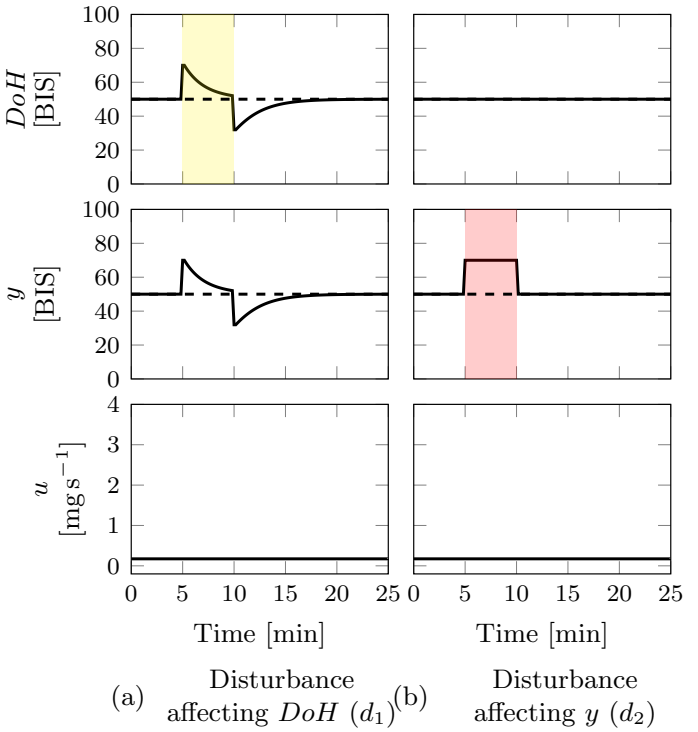

Figure 4. Disturbance rejection by TCI for two types of disturbances; d_1 affecting the *DoH* directly (a, in yellow) and d_2 affecting the measurement (b, in red), as introduced in Section 2.2. The reference is shown in dashed.

To compare disturbance rejection for open- and closed-loop control (TCI and closed-loop MPC), we calculate the mean square error (MSE) from the actual *DoH* and its reference $r_{DoH} = 50$ BIS. These are shown in Table 1 for the simulations in Figure 4 and Figure 5. The TCI is expected to perform well under measurement disturbances (d_2) but worse under disturbances that affect the *DoH* as it does not feedback on the measurement signal y. In contrast, the MPC was able to reduce the impact of disturbances acting on *DoH*, but overdoses when there is a measurement error, unable to differentiate between the two disturbances.

4. Simulation scenario

While the examples of Section 3 illustrate two extremes, we also include a more realistic scenario, where we study induction and maintenance for a representative example patient. The demographic data for this patient are the first patient in the data set presented in [Ionescu et al., 2008].

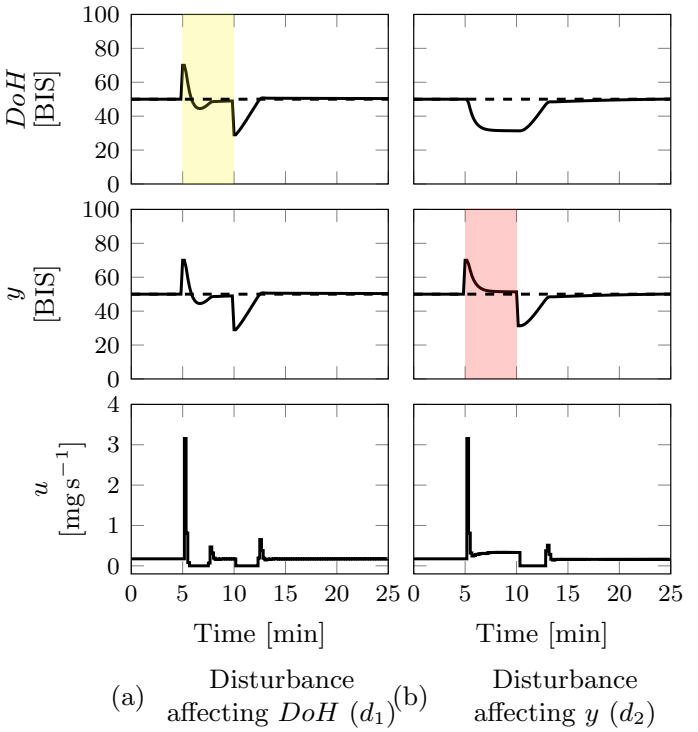

Figure 5. Disturbance rejection by MPC for two types of disturbances; d_1 affecting the *DoH* directly (a, in yellow) and d_2 affecting the measurement (b, in red), as introduced in Section 2.2. The reference is shown in dashed.

Table 1. Mean squared errors (MSE) between actual *DoH* and the reference value of $r_{DoH} = 50$ BIS for each of the disturbance scenarios in Figure 4 and Figure 5, respectively. The disturbances d_1 and d_2 are detailed in Section 2.2.

Method	d_1	d_2
TCI	39.7	0
MPC	28.2	75.9

In this scenario, we assume non-perfect model knowledge of the PKPD model and corresponding Hill function. The MPC model $\widehat{\text{PKPD}}$ and the Kalman filter assume nominal parameter values (the same as in Section 3), while the PKPD model that constitutes the true dynamics of the patient (see the patient block in Figure 2) is now different. The true patient model is created by drawing from the log-normal distribution for volumes and clearances that make up the A matrix, as explained in Section 2.1 and shown in Equation (4). For the Hill function, $\hat{h}$, we use popu-

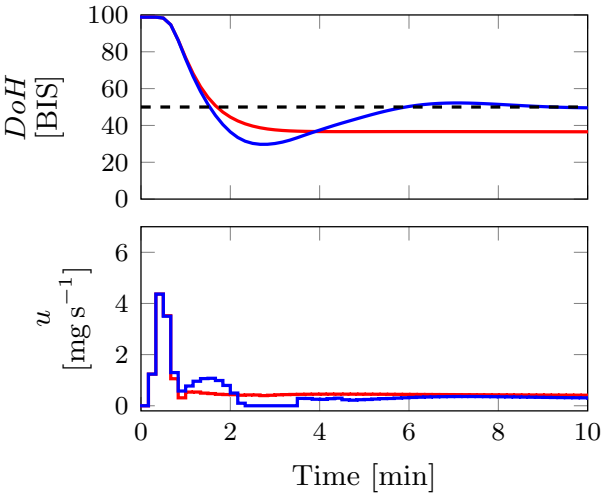

Figure 6. Induction phase *DoH* and corresponding infusion rate u with (blue) and without (red) integral action. The reference $r_{DoH} = 50$ BIS is shown in dashed.

lation averages $\hat{E}_0 = 95.9$ BIS, $\hat{C}_{e50} = 4.92$ mg L^{-1}, and $\hat{\gamma} = 2.69$, as provided in [Vanluchene et al., 2004].

The imperfect model would lead to a stationary error that can be eliminated in the closed-loop case by introducing integral action. This is done by adding a correction term to the control signal computed by the MPC, u_{MPC}, so that

$$u_k = (u_{\text{MPC}})_k + \beta (u_i)_k, \tag{16}$$

where the correction term is the sum of the integral error

$$(u_i)_k = \sum_{i=1}^{k-1} ((C_e)_i - r_{Ce})_i, \tag{17}$$

and β is a tunable parameter determining the amount of integral action. For this simulation scenario, we use $\beta = 0.2$, which was found to be a suitable value to eliminate the stationary error. Figure 6 illustrates the need for integral action with model errors during the induction phase, where a stationary error is obtained and is not corrected by the MPC without integral action.

To further increase realism, we superimpose a noise sequence presented in [Pawlowski et al., 2022] onto the measurement y used to drive the Kalman filter in the closed-loop case. As in [van Heusden et al., 2013] second-order filter with time constant 8 s, being the zero-order-hold discretization of

$$F(s) = \frac{1}{(8s+1)^2} \tag{18}$$

is employed to attenuate this noise.

During the induction phase, the patient goes from fully awake ($DoH \approx 100$ BIS) to a reference $r_{DoH} = 50$ BIS. We study a scenario where two disturbances affect the patient during maintenance. These are introduced at $t = 20$ min and $t = 40$ min and affect DoH and y, respectively, as specified in Section 3.

In this scenario, we assume that we have information about signal quality in terms of a signal quality index of 0-100 SQI. This index is provided in conjunction with the measurement by the most commonly used clinical monitors DoH, including the BIS monitor.

When the second disturbance d_2 affects the measurement, it is reflected as a drop in SQI from 100 (perfect measurement) to 50 (poor measurement). Then, the signal quality is poor until the disturbance disappears after five minutes. This simulates a scenario of using electrocautery devices, where electrical inference affects the BIS monitor and introduces measurement errors [Chan et al., 2012]. Details of how SQI is assumed to affect the measurement signal can be found in [Wahlquist et al., 2025].

In [Wahlquist et al., 2025], we developed a method to adjust R depending on the signal quality of the BIS signal, SQI, to seamlessly move between trusting the measurement or the model. Then, R was varied through an affine relationship between a minimum value $R_{\min}$ and a maximum value $R_{\max}$, so that

$$R(SQI) = R_{\min} + (1 - SQI/100)\,(R_{\max} - R_{\min}). \tag{19}$$

When $SQI = 100$, the signal quality is perfect, resulting in a small covariance $R_{\min}$. In contrast, a poor signal quality of $SQI = 0$ results in a large covariance $R_{\max}$.

The tuning of the Kalman filter ($R_{\min}$, $R_{\max}$, and Q) was performed by minimizing the mean square error (MSE) between the Kalman prediction of the DoH $\hat{y} = h(\hat{C}_e)$ and the true DoH over the simulation scenario with induction and the two disturbances. We assume that $R_{\min}$ and $R_{\max}$ are scalar and that Q is a diagonal matrix where the diagonal was identified in optimization. The MATLAB function `fmincon` with the interior-point algorithm was used for the optimization. The Kalman filter was initialized in $P_{0,0} = I_4$.

5. Results

Figure 7 shows the full simulation scenario of the induction and maintenance phase affected by disturbances as outlined in Section 4 The DoH, the measurement y, the infusion rate u, and SQI are presented. The signal quality is perfect ($SQI = 100$) throughout the time except at the time of the second disturbance d_2, which affects the measurement. The obtained values of $R_{\min}$, $R_{\max}$, and Q from optimization were $R_{\min} = 274, R_{\max} = 19706$, and $Q = \mathrm{diag}(0.85, 0.83, 2.5 \cdot 10^4, 1.4 \cdot 10^3)$.

As seen in Figure 7, the MPC can control DoH closely to the reference except when disturbances occur but is immediately able to regulate back. When SQI drops from 100 to 50 at $t = 40$ min, the MPC can instead run on the underlying (incorrect) PKPD model in the meantime to prevent overdosing.

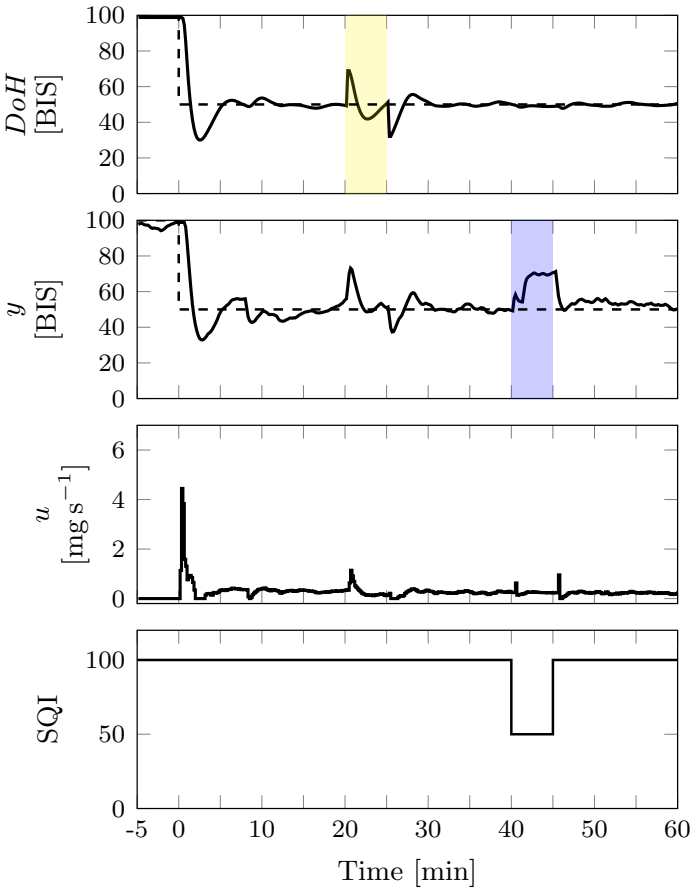

Figure 7. Simulation example with induction and maintenance phase, subjected to noise and two disturbances (yellow, affecting the *DoH*, and blue affecting the measurement). These correspond to d_1 and d_2 in Figure 2 and are detailed in Section 2.2. At the same time as the second disturbance takes place, the *SQI* drops from 100 to 50 (lower plot). A Kalman filter has been optimized and is detailed in Section 4. The reference $r_{DoH} = 50$ BIS is shown in dashed.

6. Discussion

TCI performs well when there are measurement errors, but struggles when errors directly impact the patient's *DoH*. This issue arises particularly in scenarios that involve disturbances and model-error mismatches. However, the opposite is true for MPC, which can manage measured changes in hypnotic depth through feedback, even when these changes are not accounted for in the model. This capability is

beneficial in situations where disturbances, noise, or patient-model mismatches are present. In summary, both regimens have strengths and weaknesses and are often complementary. In [Wahlquist et al., 2025], it was shown that the suggested method was robust to model uncertainties regarding inter- and intra-patient variability.

In this work we have introduced a control structure that seamlessly integrates TCI and closed-loop control, allowing for a continuous re-positioning between the two based on operating circumstances. This framework utilizes a measurement-driven state observer in the form of a Kalman filter, that is re-tuned to rely more or less on model and measurement respectively, thus moving seamlessly between TCI and closed-loop MPC behavior.

References

Absalom, A., D. Amutike, A. Lal, M. White, and G. N. C. Kenny (2003). "Accuracy of the 'Paedfusor' in children undergoing cardiac surgery or catheterization". *British Journal of Anaesthesia* **91**:4, pp. 507–513. DOI: 10.1093/bja/aeg220.

Absalom, A. R. and K. P. Mason, (Eds.) (2017). *Total Intravenous Anesthesia and Target Controlled Infusions: A Comprehensive Global Anthology*. Springer, Cham. DOI: 10.1007/978-3-319-47609-4.

Chan, M., S. S. Ho, and T. Gin (2012). "Performance of the bispectral index during electrocautery". *J Neurosurg Anesthesiol* **24(1)**, pp. 9–13. DOI: 10.1097/ANA.0b013e31823058bf.

Ionescu, C. M., R. De Keyser, B. C. Torrico, T. De Smet, M. Struys, and J. E. Normey-Rico (2008). "Robust predictive control strategy applied for propofol dosing using BIS as a controlled variable during anesthesia". *IEEE Transactions on Biomedical Engineering* **55**:9, pp. 2161–2170. DOI: 10.1109/TBME.2008.923142.

MathWorks (2024). *Quadprog*. https://se.mathworks.com/help/optim/ug/quadprog.html. Downloaded: 2024-09-18.

Pawlowski, A., M. Schiavo, N. Latronico, M. Paltenghi, and A. Visioli (2022). "MPC for propofol anesthesia: the noise issue". In: *2022 IEEE Conference on Control Technology and Applications (CCTA)*, pp. 1087–1092. DOI: 10.1109/CCTA49430.2022.9966102.

Sahinovic, M. M., M. M. R. F. Struys, and A. R. Absalom (2018). "Clinical pharmacokinetics and pharmacodynamics of propofol". *Clinical Pharmacokinetics* **57**:12, pp. 1539–1558. DOI: 10.1007/s40262-018-0672-3.

Schiavo, M., L. Consolini, M. Laurini, N. Latronico, M. Paltenghi, and A. Visioli (2021). "Optimized feedforward control of propofol for induction of hypnosis in general anesthesia". *Biomedical Signal Processing and Control* **66**, p. 102476. DOI: 10.1016/j.bspc.2021.102476.

Schnider, T. W., C. F. Minto, P. L. Gambus, C. Andresen, D. B. Goodale, S. L. Shafer, and E. J. Youngs (1998). "The influence of method of administration and covariates on the pharmacokinetics of propofol in adult volunteers". *Anesthesiology* **88**:5, pp. 1170–1182. DOI: 10.1097/00000542-199805000-00006.

Soltesz, K., K. van Heusden, and G. A. Dumont (2020). "5 - Models for control of intravenous anesthesia". In: Copot, D. (Ed.). *Automated Drug Delivery in Anesthesia*. Academic Press, Elsevier, pp. 119–166. DOI: 10.1016/B978-0-12-815975-0.00010-2.

Soltész, K. (2013). *On automation in anesthesia*. PhD thesis. Lund University, Lund, Sweden. ISBN: 978-91-7473-484-3.

van Heusden, K., J. M. Ansermino, K. Soltesz, S. Khosravi, N. West, and G. A. Dumont (2013). "Quantification of the variability in response to propofol administration in children". *IEEE Transactions on Biomedical Engineering* **60**:9, pp. 2521–2529. DOI: 10.1109/TBME.2013.2259592.

van Heusden, K., K. Soltesz, E. Cooke, S. Brodie, N. West, M. Gorges, J. M. Ansermino, and G. A. Dumont (2019). "Optimizing robust PID control of propofol anesthesia for children: design and clinical evaluation". *IEEE Transactions on Biomedical Engineering* **66**:10, pp. 2918–2923. DOI: 10.1109/TBME.2019.2898194.

Vanluchene, A., H. Vereecke, O. Thas, E. Mortier, S. Shafer, and M. Struys (2004). "Spectral entropy as an electroencephalographic measure of anesthetic drug effect: a comparison with bispectral index and processed midlatency auditory evoked response". *Anesthesiology* **101**, pp. 34–42. DOI: 10.1097/00000542-200407000-00008.

Vuyk, J. and M. Mertens (2003). "Bispectral index scale (BIS) monitoring and intravenous anaesthesia". *Advances in Modelling and Clinical Application of Intravenous Anaesthesia*, pp. 95–104. DOI: 10.1007/978-1-4419-9192-8_9.

Wahlquist, Y., A. Gojak, and K. Soltesz (2021). "Identifiability of pharmacological models for online individualization". *IFAC-PapersOnLine* **54**:15, pp. 25–30. DOI: 10.1016/j.ifacol.2021.10.226.

Wahlquist, Y., A. Gustafson, and K. Soltesz (2024). "Exploring the influence of patient variability on propofol target-controlled infusion performance". In: *2024 European Control Conference (ECC)*, pp. 3027–3032. DOI: 10.23919/ECC64448.2024.10590791.

Wahlquist, Y., N. Paolino, M. Schiavo, A. Visioli, and K. Soltesz (2025). "Kalman filter soft sensor to handle signal quality loss in closed-loop controlled anesthesia". *Biomedical Signal Processing and Control*. DOI: 10.1016/j.bspc.2025.107506.

Welch, G. and G. Bishop (1995). *An introduction to the Kalman filter*. Tech. rep. DOI: 10.5555/897831.

Läkemedelsdosering anpassad för dina behov

Ylva Wahlquist
Institutionen för Reglerteknik

Populärvetenskaplig sammanfattning av doktorsavhandlingen *Modeling and Control of Pharmacological Systems*, mars 2025.

Har du någonsin funderat över varför personer med olika kroppsvikt och kön ofta får samma läkemedelsdos? Om du går till läkaren kan du få samma dos smärtstillande som en person som väger betydligt mer än dig. Detta beror på att läkemedelsdoser oftast väljs för att passa de flesta, vilket inte alltid är optimalt. För smärtstillande kanske det inte är ett stort problem, men om du genomgår en operation och behöver bli sövd?

Narkosläkaren ansvarar för att du är tillräckligt sövd och justerar dosen kontinuerligt efter dina behov eftersom fel dosering kan få allvarliga konsekvenser. Underdosering kan leda till att du känner av smärta under operationen, eller i värsta fall vaknar upp, och överdosering kan leda till andningsuppehåll eller illamående vid uppvaket. Att hitta rätt dos kan vara en utmaning eftersom alla personer reagerar olika på läkemedel. Denna variation beror på underliggande sjukdomar och på faktorer som ålder, vikt och kön, och det är där vår forskning kommer in.

Vi har utvecklat matematiska modeller som beskriver hur läkemedelseffekten varierar mellan olika individer beroende på ålder, vikt och kön. Med hjälp av dessa modeller kan vi förutsäga hur en patient kommer att reagera på en viss dos. Genom att kombinera modellerna med mätningar av till exempel blodtryck och puls kan vi automatiskt dosera läkemedel på ett säkert sätt. Detta är särskilt viktigt inom intensivvården, där det är avgörande att ge rätt dos vid rätt tidpunkt. I vår forskning har vi studerat två tillämpningar, nämligen hjärttransplantation och narkos.

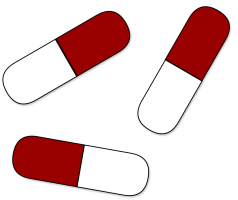

Läkemedeldosering, inte så enkelt som man kan tro.

Genom att noggrant dosera läkemedel för att hålla blodtryck och puls på stabila nivåer kan vi förbättra kvaliteten på donatorhjärtan och därmed öka antalet tillgängliga hjärtdonatorer. Inom narkos har vi visat hur vi kan beräkna en individanpassad dos av narkosmedel och sedan automatiskt justera doseringen, även under operationer där patientens tillstånd påverkas av exempelvis kirurgiska ingrepp. På lång sikt ser vi att individanpassad läkemedelsdosering blir en självklar del av sjukvården, vilket kan öka både patientsäkerheten och effektiviteten i behandlingarna.

Printed by Media-Tryck, Lund 2025 NORDIC SWAN ECOLABEL 3041 0903

Department of Automatic Control
P.O. Box 118, 221 00 Lund, Sweden
www.control.lth.se

PhD Thesis TFRT-1148
ISBN 978-91-8104-370-9
ISSN 0280–5316